Near Real-Time High-Rate GPS Data Analysis for Earthquake and Tsunami Early Warning

Heft 44
Schriftenreihe der Fachgebiet für Physikalische Geodäsie
Fachbereich Bau- und Umweltingenieurwesen
Technische Universität Darmstadt
ISBN 978-3-935631-33-4

Darmstadt, Juni 2015

TECHNISCHE
UNIVERSITÄT
DARMSTADT

Heft 44

Darmstadt, Juni 2015

Leonor Mendoza Malia

Near Real-Time High-Rate GPS Data Analysis for Earthquake and Tsunami Early Warning

Schriftreihe
Fachrichtung Geodäsie
Fachbereich Bau- und Umweltingenieurwesen
Technische Universität Darmstadt

ISBN 978-3-935631-33-4

Schriftenreihe Fachrichtung Geodäsieder Technischen Universität Darmstadt
Zugl.: Darmstadt, Technische Universität, Dissertation, 2015
D17

Online unter: http://tuprints.ulb.tu-darmstadt.de/4601

Verantwortlich für die Herausgabe der Schriftenreihe:

Der Sprecher der Fachrichtung Geodäsie
im Fachbereich Bau- und Umweltingenieurwesen
der Technischen Universität Darmstadt

Bezugsnachweis:

Technische Universität Darmstadt
Fachgebiet für Physikalische Geodäsie
Franziska-Braun-StraSSe 7
64287 Darmstadt

ISBN 978-3-935631-33-4

Near Real-Time High-Rate GPS Data Analysis for Earthquake and Tsunami Early Warning

Vom Fachbereich Bau- und Umweltingenieurwesen
der Technischen Universität Darmstadt
zur Erlangung des akademischen Grades eines
Doktor-Ingenieurs (Dr.-Ing.)

genehmigte Dissertation von
Lic. Leonor Mendoza Malia
aus Barbate, Spanien

Referent: Prof. Dr.-Ing Matthias Becker
1. Korreferent: Prof. Dr.-Ing José Martín Dávila
2. Korreferent: Prof. Dr.-Ing. Üwe Sörgel

Tag der Einreichung: 1. April, 2015
Tag der mündlichen Prüfung: 17. Juni, 2015

Darmstadt, Juni 2015
D17

Schriftenreihe Fachrichtung Geodäsie der Technischen Universität Darmstadt
Heft 44
ISBN 978-3-935631-33-4

Bitte zitieren Sie dieses Dokument als:
URN: urn:nbn:de:tuda-tuprints-46014
URL: http://tuprints.ulb.tu-darmstadt.de/4601

Preface

Some months before I finished my studies at the University of Cádiz, I was given the chance to become a researcher and write this Ph.D. I took this great opportunity and made the most of it, following a path in my life that is coming to an end with this dissertation. However, I am sure this is not the finishing line but a launch pad for further exciting projects in my life.

In the almost seven years it has taken me to finish the research, I have met great people and have had many amazing experiences which have broadened my horizons as a person and a researcher. Without them, I would never have become the woman I am today.

Foremost, I would like to acknowledge the help of my primary advisor, Prof. Dr.-Ing. Matthias Becker, and both Prof. Dr.-Ing. José Martín Dávila and Prof. Dr.-Ing. Jorge Gárate Pasquín from the San Fernando Naval Observatory. I cannot imagine having gone through this experience without their guidance and help. I would also like to thank my third advisor, Prof. Dr.-Ing. Uwe Sörgel, for the time he has spent commenting and correcting the draft.

My fellow colleagues at the Physical and Satellite Geodesy Department at Technische Universität Darmstadt and at San Fernando Naval Observatory in Spain also deserve recognition: without the sum of their knowledge and their patient explanations, this dissertation would not have been possible. I also owe a great debt to all the people who have helped me over the years, contributing with constructive comments, scientific curiosity and patience, asking and answering questions which also helped me gain a better understanding of the depth and details of this work.

Finally I would like to thank my very important support network of good friends and loved ones: all the people that accompanied me through these years, some of them from the beginning, some who arrived later, and others who are already gone. The combined efforts of all these people, through love, friendship and patience, is beyond measure.

To everybody who helped me in any way... which is all of you. Thanks.

Leonor Mendoza Malia
Darmstadt, 2015

Abstract

GPS has evolved lately in amazing ways: accurate surveying, financial transactions, precision agriculture and vehicle navigation, among others, are fields of study where GPS capabilities are highly involved. The use of GPS for earthquake magnitude determination and tsunami early warning has been introduced in the past years, along with an improvement in the accuracy of the solutions and an increase in processing speed. Earthquake magnitude determination is mainly achieved by using GPS as seismometers. Tsunami early warning is attained by estimating rupture parameters and comparing them with pre-computed models, obtaining an assessment of the threat. With further improvements in data obtention, transfer velocity and analysis methods, and the densification of GPS networks, warning times can be shortened and a better evaluation of the threat can be achieved, reducing or even eliminating false alarms.

The first goal of this Thesis is to validate the capability of the custom processing here presented for earthquake detection. In particular, the 2011 $M_w5.1$ magnitude Lorca Earthquake was successfully identified, and the recorded peak-to-peak displacement agreed with seismic observations. It is one of the few medium-magnitude earthquakes that have been observed by GPS to date.

The second and final goal of this Thesis is to introduce an approach for tsunami early warning, focused on the Iberian Peninsula and based on the load that a tsunami-induced redistribution of water imposes in the crust. This idea has not been observed in-situ due to the lack of real tsunami data in the area since the introduction of GPS. However, said approach has been tested for the stations in the Peninsula during two periods of extremely high tides in 2011. Also, a cyclone which hit the North Sea in December 2013 was successfully monitored by the use of GPS measurements, obtaining a good agreement between modeled and real surge data. This validates the detection capability and reveals the time that the crust takes to accommodate a big load. Some tsunami models have been later used to estimate the possible crustal deformation due to extreme events of specific characteristics.

In summary, it is demonstrated that the processing of GPS data presented here, which can be achieved in near real-time, is applicable to detect a neighbouring medium-size earthquake. It can be also utilized as a redundant method for tsunami early warning and alert validation for the Iberian Peninsula, even when only those GPS stations already available there are used.

Zusammenfassung

In den letzten Jahren hat GPS eine erstaunliche Entwicklung insbesondere in der Vielfalt der Anwendungen durchlaufen. Beispiele hierfür sind die genaue Vermessung, die Zeitzuordnung bei Finanztransaktionen, präzise Landwirtschaft und Fahrzeugnavigation. So ist in den letzten Jahren auch die Nutzung von GPS zur Bestimmung der Erdbeben-Magnitude und zur Tsunami-Frühwarnung aufgekommen, vor allem aufgrund auf einer verbesserten Genauigkeit und reduziertem Zeitaufwand zur Datenprozessierung. Die Bestimmung der Erdbeben-Magnitude geschieht durch die Nutzung von GPS als Seismometer, wärend die Tsunami-Frühwarnung durch die Bestimmung von Bruchparametern und deren Vergleich mit zuvor berechneten Modellen erreicht wird. Dies ermöglicht eine Einschätzung der Gefahrenlage. Durch weitere Verbesserungen in Bezug auf effizienten Datenfluss, Datenanalysenmethoden und Verdichtung von GPS-Netzen kann die Vorwarnzeit verlängert und die Gefahreneinschätzung verbessert werden. So können Fehlalarme reduziert oder gar ganz eliminiert werden.

Der erste Schwerpunkt der vorliegenden Arbeit ist die Validierung der Möglichkeit zur Erdbebenerkennung durch maßgeschneiderte Datenprozessierung. Das Lorca Erdbeben im Jahr 2011 mit einer Magnitude von $M_w5.1$ wurde erfolgreich erkannt und der geschätzte maximale Versatz stimmt mit der seismischen Beobachtung überein. Dies ist eines der wenigen Erdbeben mittlerer Magnitude, die bisher durch GPS erfasst wurden.

Den zweiten Schwerpunkt der Arbeit bildet die Untersuchung verschiedener Methoden zur Tsunami Früherkennung am Beispiel der Iberischen Halbinsel, wobei die Belastung der Erdkruste durch das vom Tsunami verdrängte Wasser analysiert wird. Dieser Effekt konnte nicht in-situ beobachtet werden, da es keine Daten zu Tsunamis in diesem Gebiet gibt. Stattdessen wurde die Methode für zwei Zeitpunkte 2011 mit extrem starken Flutereignissen getestet. Zusätzlich konnte das Modell durch den Vergleich von berechneten und gemessenen GPS-Daten während eines Sturms im Jahr 2013 in der Nordsee verifiziert werden. Anhand dieser Beispiele konnte die Modellierung der Anflasteffekte validiert und die Zeit untersucht werden, in der die Erdkruste auf die erhöhte Wasserlast reagiert. Einige Tsunamimodelle wurden zur Abschätzung der möglichen Deformation der Erdkruste bei derartigen extremen Ereignissen eingesetzt.

Zusammenfassend kann gesagt werden, dass mit der hier gezeigten Prozessierung der GPS-Daten, die auch in Echtzeit durchgeführt werden kann, die gezeigten nähergeliegenden Erdbeben mittlerer Stärke ermöglicht wird. Darüber hinaus kann diese Prozessierung als redundante Methode zu Tsunami-Frühwarnung und Alarmvalidierung für die iberische Halbinsel angesehen werden, sogar wenn nur die derzeit installierten GPS-Stationen verwendet werden.

Contents

7 Numerical Results 3. Comparison of GPS, Water Surge Models, Altimetry and Tide Gauges During a Storm Surge in Northern Germany 77

Introduction

Earthquakes and tsunamis are natural processes that represent an actual risk to the population all over the world, especially in places close to the boundaries of tectonic plates and on the coast. Earthquakes tend to be recurrent in most cases, and if they occur in the sea and are of sufficient magnitude, they have the potential to create a tsunami. Apart from earthquake magnitude, the generation of a tsunami strongly depends on the earthquake focal mechanism and hypocentral depth, among others. Landslides and volcanic eruptions are also deeply related to tsunamis: the abrupt movement of land can generate a dangerously big wave. Establishing a warning system which provides reliable expected arrival times is essential to mitigate the danger to the population.

Earthquake-prone area definition, magnitude determination, epicenter location and early warning have always been on the edge of scientific interest. On the other hand, as the recurrence of large tsunamis is of the order of several decades, they do not last long in the people's memory and the scientific interest has been negligible for a very long time. It was in 2004 where the interest arose, with the Sumatra tsunami on December 26 [*Geist*, 2007]. As the last known significant tsunami on the Atlantic coast of the Iberian Peninsula was in 1755 [*Martínez-Solares and López Arroyo*, 2004], the study of such events in the area and the establishment of a warning system has been long postponed [*Baptista et al.*, 2011].

The use of GPS as a seismometer has been widely studied. The earthquake parameters and characteristics can be derived with little error from GPS time series, helping in detection and early warning [*Blewitt et al.*, 1993]. However, GPS is not yet an active part of all the earthquake early warning systems in the world, although it is starting to be implemented. The detection of an earthquake with GPS is possible if the earthquake signal is big enough when reaching the receiver, due to its accuracy limitations. In this dissertation, the capability of some GPS stations in the selected network is validated through the recording of a $M_w5.1$ magnitude earthquake in the Province of Murcia, Eastern Spain. No magnitude determination or further data derivation has been attempted.

More recently, the use of GPS for tsunami monitoring and early warning has begun to be developed and tested. Most times, tsunami early warning relies on earthquake magnitude determination and rupture direction [*Blewitt et al.*, 2006]. Thanks to some pre-computed models, the characteristics of the possible tsunami are obtained and thus the risk can be assessed. GPS placed in buoys in the open sea can also measure the tsunami waves and, therefore, obtain an estimation of the waves expected to reach the coast [*Bressan and Tinti*, 2012]. The availability of both pre-computed tsunami models and GPS placed in buoys is restricted to areas marked as tsunami-prone.

Plag et al. [2006] stated that, during the 2004 Sumatra-Andaman tsunami, the redistribution of the water mass was comparable to that related to ocean tides. A peak-to-peak ground displacement amplitude up to 2 cm in height was reached, which is far above the noise level in the vertical component ($\sim$0.7 cm [*Bock et al.*, 2004]). No further research was published after that until 2013, when *Mitsui and Heki* [2013] found up to a 1 cm subsidence for the GPS coastal stations close to the epicenter in the 2011 Tohoku-oki tsunami in Japan. This proves that the load induced by some tsunamis can be detected by GPS. In this dissertation, the detection capability is tested for several GPS sites located on the Atlantic coast of the Iberian Peninsula. As there are no real tsunami recordings available from GPS, some tsunami scenarios based on simulations have been studied.

In summary, the main outcomes of this dissertation are the accurate detection of a medium magnitude earthquake, the study of tsunami detection capability of several GPS receivers on the Atlantic coast of Iberia and, above all, that these can be currently done with the infrastructure that is already available in the Iberian Peninsula.

Objectives and Approach of the Research

The goal of the investigation presented here is to assess the ability of a network consisting of already deployed GPS receivers in the Iberian Peninsula to monitor and warn about earthquakes and tsunamis that could endanger the population in the areas at risk. It could also be used as a complement to the traditional sensors (seismometers, mareographs), enhancing detection and alert capabilities.

In order to achieve this, the following requirements must be fulfilled:

- The processing method has to be analyzed and tested in terms of quality and processing time.
- The post-processing of the data must be such that no information is lost while most of the noise and uncertainties are eliminated.
- Results are to be compared with already available records in order to establish the sensitivity of the whole strategy.
- Finally, the relationship between recorded data, results and main aim of the study must be assessed.

Structure of this Thesis

This Thesis consists of nine Chapters, outlined as follows:

- Chapter 1 provides an overview of the satellite navigation systems available and the conventional GNSS analysis methods.
- Chapter 2 gives some information about the natural processes that are monitored in the following Chapters and the state of the art of earthquake and tsunami early warning achieved by the analysis of GNSS observations.
- Chapter 3 describes the Iberian Peninsula as the study area, focusing on the observability and occurrence of the different effects. It also lists the GNSS networks and stations available in the area.
- Chapter 4 explains the methodology and gives the details for the processing and post-processing of the recorded data, which is specified in the following Chapters.
- Chapters 5 to 8 are test cases where the methodology is customized, applied and tested for the different natural hazards. An earthquake is detected in Chapter 5, two periods of extreme tides are monitored in Chapter 6, a storm-induced surge is analyzed in Chapter 7 and some tsunami models are examined in Chapter 8 in order to assess their detectability in GPS recordings.
- Chapter 9 concludes the Thesis. It summarizes the dissertation research and gives an interpretation of the results. It also offers some recommendations for further investigation to be conducted on the matter.

1 GNSS and Analysis Methods

In this Chapter, a summary of the available Satellite Navigation Systems (SAT NAV) is provided along with an overview of the GPS satellite signal and observation equations. An explanation about reference frames and coordinate systems and a list of the products delivered by the International GNSS Service are given later. The usual analysis methods are explained, as well as a few examples of the most common software packages used nowadays. The post-processing strategies necessary to mitigate errors in the positioning are also listed. The Sections in this Chapter are very general, the actual methods used in this Thesis will be detailed in Chapter 4.

The goal in this study is not the development of any new methodology but the innovative application of several strategies in processing and post-processing, focusing on the Iberian Peninsula and obtaining useful results. Therefore, most of the literature, processes and methodology are treated as known. For further interest in GNSS and analysis methods, refer for example to [*Hofmann-Wellenhof and Moritz*, 2006].

1.1 Satellite Navigation Systems

A SAT NAV system is a constellation of satellites providing autonomous geospatial positioning. It allows any receiver to determine its location with a precision varying from a few meters to a submillimeter range. The receiver position is calculated using the signal transmitted by the satellites.

The first satellite navigation system, Transit, was deployed by the US military in the 1960's. It was operationally based on the Doppler effect. Since then, regional and global navigation satellite systems (RNSS and GNSS, respectively) have been deployed. RNSS are networks of satellites that do not provide a global coverage of geospatial positioning, but only in a defined region, country or continent. BeiDou (China) and IRNSS (India) are two examples of RNSS. Alternatively, GNSS do provide global coverage: a receiver anywhere on Earth can determine its location. GLONASS (GLObal NAvigation Satellite System, Russia, operational), COMPASS (China, in development), GALILEO (Europe, in development) and NAVSTAR GPS (NAVigation Satellite Timing And Ranging Global Positioning System, USA, operational) are the SAT NAV systems operational and under development at present time.

In this Thesis, only data from NAVSTAR GPS (referred as GPS from now on) is used. GPS is the most commonly used SAT NAV system and one of the two available during the time this Thesis was written. GLONASS was also available, but there is enough GPS data to carry out the investigation. However, if GLONASS (alone or in combination with GPS) –or even GALILEO when available– were to be used, the processing and post-processing strategies detailed in this Thesis would remain the same.

1.2 GPS Satellites Constellation. Observation Equations.

Nowadays, the GPS system is the most famous and used satellite constellation. It consists of up to 32 satellites in six different orbital planes, and it is globally operational since April 1995. GPS satellites continuously transmit signals that are measured and recorded by the GPS receivers. In order to obtain the position of each receiver, the signal must be analyzed. The transmitted signal contains a navigation message, including GPS date, time and health status; ephemeris data to calculate the position of the satellite in its orbit; and almanac data, with information related to the status and time of the whole constellation.

GPS signal includes also ranging signals, used to measure the distance between satellite and receiver. The two original ranging codes are C/A (Coarse/Acquisition), freely available to the public, and P (Precision), with limited access and reserved usually for military applications.

Navigation message and ranging signals are generated by modulating the carrier frequency. Modulation is the process of varying the properties of a periodic waveform, called carrier signal, with a modulating signal that contains the information to be transmitted. The original GPS design includes two frequencies: L1 (1575.42 MHz) and L2 (1227.60 MHz). C/A code is transmitted in L1, and P is transmitted in both frequencies. New GPS satellites (Block IIIA) will include a new frequency (L5, 1176.45 MHz) and will transmit other signals. Examples are L2C, which is a C/A signal transmitted in L2 carrier frequency, and M-code (or military code), which is a new military signal also transmitted in M1 and M2.

GNSS signals are circular polarized radio waves. The phase of the carrier signals is measured relative to the so-called initial phase ambiguities [*Remondi*, 1985], this is, containing an unknown number of phase cycles that occurred since the signal was transmitted until it first arrived to the receiver. This original number of cycles (N) is an integer and must be calculated in order to relate the phase measurement to the distance between satellite and receiver. The calculation of the number of ambiguities is not straightforward. Thus, in common practice, an estimation (float value, Nf) is used as a first approximation.

GPS receivers are able to measure pseudoranges for both modulated signals. Pseudoranges are defined as the signals biased by satellite and receiver clocks. From [*Dach et al.*, 2007], the observation equations for code (P) and phase (ψ) pseudoranges are as follows:

$$P_k^i = c((t+\delta_k) - (t - \tau + \delta^i)) \tag{1.1a}$$

$$\psi_{Fk}^i(t) = \phi_{Fk}(t) - \phi_F^i(t-\tau) + n_{Fk}^i \tag{1.1b}$$

where

i corresponds to the satellite,
k corresponds to the receiver,
c is the speed of light,
t is the signal reception time in GPS time (GPST),
δ_k is the error of the receiver clock at time t with respect to GPST,
τ is the signal traveling time from satellite to receiver,
δ^i is the error of satellite clock at signal emission time $t-\tau$,
ψ_{Fk}^i is the phase measurements (in cycles) at epoch t and frequency F,
ϕ_{Fk} is the phase generated by the receiver oscillator at signal reception time t,
$\phi_F^i(t-\tau)$ is the phase of the carrier at emission time $t-\tau$, and
n_{Fk}^i is an unknown integer number of cycles (the initial phase ambiguity).

The geometric distance between receiver and satellite, ρ_k^i ($= c\tau$) can be introduced in Equation 1.1a. Moreover, it can be further refined for both frequencies, obtaining:

$$P_{1k}^i = \rho_k^i + c\delta_k - c\delta^i + I_k^i + \Delta\rho_k^i \tag{1.2a}$$

$$P_{2k}^i = \rho_k^i + c\delta_k - c\delta^i + \frac{f_1^2}{f_2^2} I_k^i + \Delta\rho_k^i \tag{1.2b}$$

where

I_k^i is the ionospheric refraction (frequency-dependent),
$\Delta\rho_k^i$ is the tropospheric refraction (not frequency dependent), and
f_1 and f_2 are the different carrier frequencies.

Equation 1.1b can be developed and later multiplied by the wavelength of each frequency, λ_F where F=1,2. After refining it, we obtain the phase observation L_{Fk}^i (in meters) for each frequency:

$$L_{1k}^i = \rho_k^i + c\delta_k - c\delta^i - I_k^i + \Delta\rho_k^i + \lambda_1 n_{1k}^i \tag{1.3a}$$

$$L_{2k}^i = \rho_k^i + c\delta_k - c\delta^i - \frac{f_1^2}{f_2^2} I_k^i + \Delta\rho_k^i + \lambda_2 n_{2k}^i \tag{1.3b}$$

Equations 1.2 and 1.3 are the observation equations. By subtracting them, some biases can be eliminated or reduced. A single-difference between a pair of receivers k and l can be calculated (see Equations 1.4a). And later, a double-difference between a pair of receivers kl and a pair of satellites ij (in Equations 1.4b) can be computed.

$$P^{i}_{Fkl} = P^{i}_{Fk} - P^{i}_{Fl} \qquad L^{i}_{Fkl} = L^{i}_{Fk} - L^{i}_{Fl} \tag{1.4a}$$

$$P^{ij}_{Fkl} = P^{i}_{Fkl} - P^{j}_{Fkl} \qquad L^{ij}_{Fkl} = L^{i}_{Fkl} - L^{j}_{Fkl} \tag{1.4b}$$

The observation equations corresponding to the double differences presented in Equations 1.4b are:

$$P^{ij}_{1kl} = \rho^{ij}_{kl} + I^{ij}_{kl} + \Delta\rho^{ij}_{kl} \tag{1.5a}$$

$$P^{ij}_{2kl} = \rho^{ij}_{kl} + \frac{f_1^2}{f_2^2} I^{ij}_{kl} + \Delta\rho^{ij}_{kl} \tag{1.5b}$$

$$L^{ij}_{1kl} = \rho^{ij}_{kl} - I^{ij}_{kl} + \Delta\rho^{ij}_{kl} + \lambda_1 n^{ij}_{2kl} \tag{1.5c}$$

$$L^{ij}_{2kl} = \rho^{ij}_{kl} - \frac{f_1^2}{f_2^2} I^{ij}_{kl} + \Delta\rho^{ij}_{kl} + \lambda_2 n^{ij}_{2kl} \tag{1.5d}$$

As can be seen, double differencing a pair of receivers and a pair of satellites eliminates satellite and receiver clock errors, assuming that the receiver clock errors are known accurately enough to compute the distances ρ correctly [*Dach et al.*, 2007].

The linear combination of the measurements from the same epoch helps to mitigate errors, such as ionospheric delay, and helps with further corrections like multipath. Moreover, the generation of observations with different wavelengths facilitates the recovery of the integer ambiguities (refer to [*Blewitt*, 1989], for example).

1.3 International GNSS Service

The International GNSS Service (IGS) is a federation of agencies, universities and research institutions all over the world, that provides open-access to high quality data and precise products for GNSS [*Dow et al.*, 2005]. IGS also contributes to the definition of the International Terrestrial Reference Frame, see Section 1.4.

Apart from providing access to high quality GNSS observations, IGS generates several precise products, such as GNSS satellite ephemerides, Earth rotation parameters, station coordinates and velocities, satellite and tracking station clock information, zenith tropospheric path delay estimates and global ionosphere maps.

In this Thesis, data from several GPS stations from IGS is used, as detailed in Chapter 4. Also, the satellite orbits and the Earth rotation parameters are fetched from IGS.

Moreover, the IGS satellite orbits are provided with different latencies and accuracies, as listed in Table 1.1.

Orbit type	**Accuracy**	**Latency**
IGS Ultra Rapid Orbits (predicted)	∼5 cm	Real-time
IGS Ultra Rapid Orbits (observed)	∼3 cm	After 3-9 hours
IGS Rapid Orbits	∼2.5 cm	After 17-41 hours
IGS Final Orbits	∼2.5 cm	After ∼12-18 days

Table 1.1: Estimated quality of orbits in 2015. Information from [*IGS*, 2015].

1.4 Reference Systems and Frames

A reference system is a coordinate system with respect to an object, and is defined by an origin and two directions in a three-dimensional system. For the Earth, the reference system is three-dimensional, cartesian, Earth-centered and Earth-fixed, with a determined definition for x and z axis, see [*IERS Technical Note n. 36*, 2010a]. Since a reference system is an abstract coordinate system, it is necessary to uniquely locate and orient it. This process, called realization, gives a reference frame.

Reference frames allow to refer geodetic observations and estimated parameters with respect to a global and unique basis, and compare observations and results from different locations and times. In order to understand physical and geodynamic processes as positioning, plate tectonics, gravity, earth rotation parameters, etc., it is necessary to refer their change to a stable and precise frame of reference.

The International Terrestrial Reference System (ITRS) is the official reference system, recommended by the International Association of Geodesy (IAG) [*IERS Technical Note n. 36*, 2010a]. The International Terrestrial Reference Frame (ITRF) is the realization of the ITRS by a set of points with precise coordinates and velocities, estimated from observations [*ITRF*, 2015]. The GRS80 reference ellipsoid is adopted to transform 3D ITRS cartesian coordinates into ellipsoidal coordinates, latitude, longitude and ellipsoidal height.

The World Geodetic System (WGS) is a slightly different reference system to ITRS with a little less precision, realized by a subset of its reference points. Its realization in 1984, WGS-84, is the reference frame standard for GPS. The reference ellipsoid adopted, also called WGS-84, can be considered identical to GRS80 for positioning in the Earth.

IGS05 and IGS08 are the terrestrial reference frames realized by IGS using GNSS measurements from a subset of the ITRF reference points [*IERS Technical Note n. 36*, 2010a]. IGS05 was established in 2005, using the GNSS measurements of the reference points until that year. The coordinates of the stations used in Chapters 5, 6 and 8 are given in IGS05 coordinate frame. The coordinates from the stations used in Chapter 7 are referred to IGS08, that is the recomputing of IGS TRF in 2008. The transformation between the different reference frames can be done by a three-dimensional Helmert transformation, which is a similarity transformation consisting of seven parameters: a translation vector, a scale factor and a rotation matrix.

In this Thesis, the coordinates from several reference points used to realize the reference frames are selected for the processing, i.e. they are either fixed or strongly constrained. For the rest of the stations, the coordinates used a priori for the processing are those given by the different agencies they belong to. These are later transformed to the same date and reference frame as the reference stations. After processing, the difference between the initial coordinates and their estimated values is called residual, and is given in ellipsoidal coordinates for a better understanding.

1.5 Analysis Methods

The GPS receivers can directly process the recorded information to locate themselves, obtaining an estimated position with better or worse accuracy, depending on the quality of the components and the software within. For a higher accuracy, the signal obtained by more precise GPS receivers is processed by more elaborated software.

There is a wide variety of analysis methods from which two excel: Precise Point Positioning, and Precise/Phase Differential GPS or Double Differencing.

Precise Point Positioning (PPP). This analysis method relies on precise clock and orbit information for deriving site coordinates and receiver clock corrections independently for each analyzed station. PPP is based on undifferenced code and phase observations, as defined in Equations 1.2 and 1.3. Therefore, a very accurate knowledge of satellite and receiver clocks, attitude, etc., is needed. Its primary advantage is that the processing is much faster than for differential positioning. However, PPP strategy does not solve ambiguities, meaning that instantaneous positioning at a single epoch is not possible. Therefore, an extra module must be used to handle them in order to improve the positioning. PPP starts by determining precise GPS satellite positions and clock corrections from a globally distributed network of GPS receivers. Then, data from the stations to be processed is analyzed by estimating receiver-specific parameters with receiver-specific data; satellite parameters are held fixed at the values determined in the global solution, allowing a parallel solution to be obtained for all the stations at the same time [*Zumberge et al.*, 1997]. One example of software which uses this strategy is the open-source software RTKLib [*Takasu*, 2011].

Precise/Phase Differential GPS (PDGPS) or Double Differencing (DD). A differential (or relative) strategy allows estimating site coordinates simultaneously for a whole network, using double-differenced observations, as defined in Equations 1.5. Although this method is slower than PPP, full profit from ambiguity resolution can be obtained. As a set of stations is processed together by forming single and double differences of observations, there is no need of having precise clock data. Therefore, the highest accuracy is achieved for the relative geometry between the sites processed in a network solution. DD is the chosen strategy in this Thesis, and one of the highly-accurate scientific programs that implements this method is Bernese GPS-GNSS software [*Dach et al.*, 2007], which is used here.

1.6 Real-Time and High-Rate GPS

Nowadays, GPS receivers can record up to 100 samples each second (100 Hz). However, due to the storage capacity and the data transfer limits, as well as the arising problem of different uncertainties and errors, most of them store just 1 Hz data (one record per second, also defined as high-rate). 30-second data is valuable to get daily positions and is used in the study of plate tectonics over the years, and post-glacial rebound (see [*Segall and Davis*, 1997], for example). However, it has been found to be insufficient for short-period and/or short-duration motions. Currently, 1 Hz data is the most demanded one because of its value for precise analysis of short events like large magnitude earthquakes [*Miyazaki et al.*, 2004]. It has proven useful for detecting seismic wave fields for large-magnitude events [*Larson et al.*, 2003] as well as for modeling fault slips [*Ji et al.*, 2004] and volcanoes. Events which have been successfully observed with high-rate GPS networks include the 2002 Denali [*Kouba*, 2003; *Larson et al.*, 2003; *Bock et al.*, 2004], 2003 Tokachi-Oki [*Miyazaki et al.*, 2004; *Emore et al.*, 2007], 2003 San Simeon [*Ji et al.*, 2004; *Wang et al.*, 2007], and 2004 Sumatra-Andaman [*Ohta et al.*, 2006], among others.

Additionally, GPS data has been successfully applied to monitor events at higher frequencies [*Genrich and Bock*, 2006; *Zheng et al.*, 2012], and GPS networks are now able to stream 10 Hz data, yielding displacement waveforms with millimeter-level accuracy in real-time [*Bock et al.*, 2011]. Nevertheless, the tracking bandwidth of the receiver will ultimately limit the highest frequency signal amplitudes [*Ge et al.*, 2000b].

Lately, the problem of deriving displacements from seismic data in real-time is also being studied. For example, *Bock et al.* [2011] combine co-located high-rate GPS receivers and very high-rate strong-motion accelerometers. *Boebel et al.* [2010] use ocean bottom sensors to derive the load produced by an incoming tsunami. In [*Mendoza et al.*, 2012], the author of this Thesis also studies the near real-time earthquake monitoring capacity of GPS, which will be also detailed in Chapter 5.

1 Hz data is the highest and most common sampling rate available in near real-time in the stations within the region of interest for this study. Thus, it is chosen for the aims of this Thesis.

1.7 Bernese GPS-GNSS Software

The storage and management of large quantities of data are a burden for all sciences. The amount of data is rapidly growing, so a means to analyze such volumes in a consistent and robust manner is essential. Moreover, for real or near real-time applications, economizing processing time is crucial. An accurate positioning in real-time benefits the user with a rapid knowledge of the reality around him, being highly valuable for early warning of catastrophes such as landslides, earthquakes or tsunamis, among others.

The Bernese software is a very flexible geodetic tool developed at Bern University, Switzerland [*Dach et al.*, 2007]. It can provide the highest quality standards when processing data from both currently active GNSS systems (American GPS and Russian GLONASS), as well as Satellite Laser Ranging measurements to GNSS satellites. It has a user-friendly automation part and, thanks to its modular design, it can be tailored to the users needs. Bernese is capable of processing data using both PPP and DD strategies. Also, it has a very sophisticated tool for efficient combination and manipulation of analysis results on the normal equation levels (multi-session and multi-campaign) as well as kinematic analysis capability. Moreover, the latest release of Bernese, version 5.2, is also capable to process measurements from GALILEO satellites.

Bernese GPS software version 5.0 is chosen for the main purposes of this Thesis. Version 5.2 (renamed to Bernese GNSS software) is only used for a test case and is very similar to the previous version. Bernese is used to process 1 Hz GPS observations from three different networks: a permanent network of 39 stations in the Iberian Peninsula and surroundings (v. 5.0), a regional network in the South-East of Spain (v. 5.0) and a second regional network in the north of Germany (v. 5.2). Both regional networks are completed with far-away stations in order to gain stability in the positioning. The information about all the networks and stations is provided in Section 3.2. The details of Bernese custom setup and processing are given in Section 4.1.

1.8 Post-Processing

The accuracy of high-rate GPS positioning is influenced by the GPS measurement noise, the number and location of the satellites and the skill to model errors associated with orbits, satellite and receiver clocks, atmospheric delays, antenna effects, and multipath [*Choi et al.*, 2004]. Even when the same satellites, receiver types and software are used to compute positions, the differences in noise characteristics are significant at each site [*Larson et al.*, 2007]. In addition, to improve the accuracy of the displacements for geophysical applications such as seismology, it is essential to reduce systematic errors at seismic frequencies, this is, between 20 Hz and 54 minutes. Such errors can be attenuated by screening and filtering the processed data.

1 Hz kinematic time series obtained from Bernese sometimes contain clear outliers, occasionally over tens of centimeters. Such large residuals lead to significant uncertainties and errors, so they must be removed.

Errors generated due to the particulars of the individual GPS sites can be mostly attributed to multipath. Multipath is a systematic error at seismic frequencies, typically about 20 minutes, and is elevation angle dependent. It can be related to the location of the antenna with respect to reflecting surfaces. This particular error is not modeled in Bernese. Therefore, the baseline estimates can be corrupted by a station with significant multipath problems, especially in the vertical component [*Elosegui et al.*, 1995]. Such reflection problems can be mitigated by a Sidereal Filter, see Section 4.2.2.

Noises that are not related to multipath can be smoothed by a low-pass filter. Also, data time series are not always complete: data can be missing due to problems in the processing, or because it was eliminated during the first screening. In order to solve both problems at the same time, an elaborate sliding-window filter can be applied to the data: an exponentially weighted moving average filter. Such filter combines a low-pass filter with a data gap filling, weighting the data around the point to filter (or fill) following an exponential function. Its possible implementation and shortcomings are detailed in see Section 4.2.3.

2 GNSS and Natural Hazards Early Warning

This Chapter is divided into two Sections. The first one is related to seismology, and it comprises an overview of seismicity, GPS Seismology, and the state of the art of Earthquake Early Warning Systems in general and GPS-related methods in particular. The second Section is focused on loads: tides, surges and tsunamis are phenomena with the capacity of creating a load, which causes a crustal deformation recordable by GPS. Such events are further related to the crustal load they impose. In addition, some information about the state of the art in the investigation of Tsunami Early Warning Systems is provided.

2.1 Seismicity and Earthquakes

From the very beginning, mankind has developed methods to record earthquakes [*Ge et al.*, 2000a]. The first known device is the seismoscope, an instrument designed in 132 A.D. by the Chinese philosopher Chang Hêng. The device solely indicated the occurrence of an earthquake and the direction of the epicenter with respect to the device, not recording anything besides that. In the late 19^{th} Century, the seismograph was invented. Seismographs give a continuous record of the motion of the ground, also called seismogram, and provide accurate initial shock directions. In the mid 20^{th} Century, a more precise instrument called seismometer was created. A seismometer is a seismograph whose physical constants are so well known that the true ground motion can be calculated from the seismogram. Therefore, the magnitude is recorded. Lately, the use of GPS for the purpose of measuring earthquakes, by monitoring the true ground motion, has been discussed. This technique is best referred to as GPS Seismology.

2.1.1 Basics of Seismology

A sudden shaking of the crust can be produced not only by earthquakes but also by landslides and volcanic eruptions. Those unexpected quivers create waves that travel long distances through the Earth, dispersing and diverging as they cross it. They can be recorded by seismometers, independently of their nature. There are four types of seismic waves on Earth, divided into two main categories: P and S waves, also called body waves; and Love and Rayleigh waves, also called surface waves. As their names indicate, body waves travel through the interior of the Earth, propagating outwards in all directions from a source. P (primary or longitudinal) waves induce a particle motion in the same direction as the wave propagation, alternating compressions and dilations, thus called compressional waves. S (secondary or shear) waves, also called transverse waves, induce a particle motion perpendicular to the wave propagation. The surface waves propagate approximately parallel to the Earth's surface, and not directly through its interior, although surface wave motion penetrates to a significant depth in the Earth. The particles influenced by Rayleigh waves follow a retrograde ellipse movement. Love waves induce horizontal particle motion, perpendicular to the direction of propagation (transverse).

The velocity of seismic waves depends on the properties of the material they traverse. P-waves travel fastest and are non-dispersive, so they are the first-arriving signal on a seismogram; S-waves come later, as they move slower in a solid. On land, the surface moves as a P- or S-wave arrives, and this movement can be recorded by the seismometers.

In Figure 2.1, P, S, Rayleigh and Love waves are identified. As the surface waves velocity in rocks are lower than shear wave velocity, the surface waves arrive after S-waves. Surface waves spread over a long time interval because their propagation velocity is dependent on the frequency of the wave, and thus are dispersive. This dispersive character can be easily seen on the vertical (Z) component in the Rayleigh wave, in which the earliest wave energy has a longer period than the later arriving waves [*Shearer*, 2009].

If P-wave velocity is known, the location of the center of the shaking, the hypocenter, can be estimated by a simple triangulation. That is, by using the recording of its arrival time in a set of at least three seismometers, or four if they are collinear. The epicenter is the projection of the hypocenter in the surface, and is directly calculated from the latter.

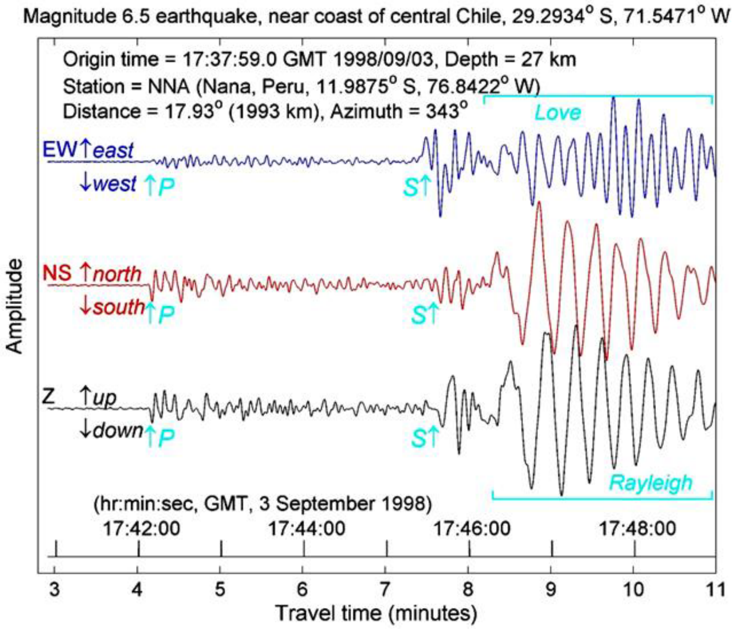

Figure 2.1: Example of a seismogram. Data recorded at Nana, Peru, for an earthquake occurred near the coast of central Chile on September 3, 1998. Figure taken from *Braile* [2004].

2.1.2 Earthquakes

An earthquake is defined as an abrupt movement in the Earth's crust resulting from a sudden release of energy. In a more general sense, "earthquake" is used to describe any seismic event that generates seismic waves, caused either by natural forces or human interaction.

Earthquakes are produced by the sudden release of energy accumulated between tectonic plates, which creates seismic waves that can be recorded by seismometers. These record the arrival times of the seismic waves as well as the shaking they induce in the Earth's surface. Thus, the true ground motion can be obtained from the recorded seismogram. The most common scale on which earthquakes are measured is the moment magnitude, M_w, which is an absolute scale. It is based on the rigidity of the Earth, multiplied by the average amount of slip on the fault and the size of the area that slipped, also called seismic moment [*Hanks and Kanamori*, 1979]. Earthquakes are divided into classes depending on their magnitude: M_w3-3.9, minor; M_w4-4.9, light; M_w5-5.9, moderate or medium; M_w6-6.9, strong; M_w7-7.9, major; and M_w>8, great earthquakes. Magnitude M_w3 or lower earthquakes are almost imperceptible, and over magnitude M_w7 can potentially cause severe damages over large areas [*Shearer*, 2009]. Alternatively, the intensity of shaking, that is the trembling felt, is measured on the modified Mercalli scale, which is the intensity scale used the most in Europe.

The main quake in a series of earthquakes is defined as the one with the largest magnitude shaking. Foreshocks are earthquakes which occur before the main shock, and they are some sort of preparation of the fault for the energy release. Aftershocks are quakes which occur after the main shock and are generated as the crust adjusts to its effects. If an aftershock is larger than the main shock, it is redefined as the main shock and the original shock is redesignated as foreshock [*Shearer*, 2009].

The energy released by an earthquake is proportional to the rupture length. Besides, the distance to the closest fault rupture and the direction in which the energy is released contribute also to the ground motion produced by a quake [*Boese et al.*, 2012]. There are earthquakes that release energy over hours, days or even months in a discontinuous way, called slow or silent earthquakes. They can also be detected by seismometers.

There are three main types of faults, and all of them can cause earthquakes. *Normal faults* include a vertical component and occur mainly on extension or divergent areas. *Reverse* or *thrust faults* also involve vertical motion in areas where the crust is shortening; that is, convergent boundaries. Finally, *strike-slip faults*, where the two sides of the fault move parallel to each other, in opposite directions. Not many faults are pure: the most common are a combination of normal and reverse (*dip-slip*) and strike-slip faults (*oblique-slip*). Thrust faults are associated with the most powerful earthquakes.

Research for predicting[1] the time and place in which earthquakes will occur has been conducted for many years. Despite considerable efforts, predictions cannot yet be made to a specific time. However, the probability that a segment may rupture within a reasonable period of time can be calculated [*Saradjian and Akhoondzadeh*, 2011] and the chances that a rupturing fault will evolve into a big earthquake can also be estimated [*Boese and Heaton*, 2010].

Nowadays in the scientific community, the existence of reliable earthquake precursors is both accepted by some ("the problem lies in conventional earthquake forecasting" [*Freund*, 2010]) and refuted by others ("earthquakes cannot be predicted" [*Geller et al.*, 1997]). For example, results related to ultra low frequency anomalies were presented by *Hayakawa et al.* [2009] and *Hayakawa* [2011], and were later refuted by *Masci* [2011]. Also, the increase in microseismicity is postulated by *Sobolev and Lyubushin* [2006] as one of the few seismic pre-earthquake signals. This contradicts *Rundle et al.* [2011], who state that an increase in the number of small earthquakes in a given area does not increase the occurrence probability of a larger earthquake (theory of nucleation).

Despite the current absence of an irrefutable proof for the existence of earthquake forecast parameters, several authors have developed short- and/or long-term forecasts. *Kagan and Jackson* [2010] base their forecasts on smoothed maps of past seismicity and assume spatial and temporal clustering. It has been demonstrated by *Astafyeva et al.* [2013] that ionosphere changes are directly related to earthquakes of different magnitudes (the larger the quake, the bigger the change). However, it is accepted as an earthquake consequence by the scientific community, not as a precursor. Some ionospheric disturbances are found when checking GPS data recorded prior to the 2007 Bengkulu and the 2005 Nias earthquakes in Sumatra [*Cahyadi and Heki*, 2013]. Nevertheless, *Yao et al.* [2012] analyze the ionospheric variation before the occurrence of seven earthquakes (for example, Chile 2010, Mexico 2010, positive; Japan 2010, negative), concluding that such anomalies are not bound to occur. Taking all this into account, the listed precursors are neither expected to be found all together prior to an earthquake, nor sufficient as an accurate stand-alone item for prediction [*Jing et al.*, 2013].

Available seismicity records are also used to evaluate future seismic occurrences. Statistical long-term worldwide forecasting based on earthquake catalogues is also a field of study. A downside of basing forecasting on recurrence is that they fail when earthquakes do not reset the stress field. A further main problem is that the likeliness of a big earthquake happening in an area is not bound to previous occurrences. This has been demonstrated to be a dangerous assumption: the 2011 Japan earthquake was nucleated in a subduction zone where an event with a magnitude bigger than $M_w{\sim}8$ was thought impossible to occur [*Geller*, 2011]. From that moment on, the theory declaring that the largest earthquakes typically are thrust fault events [*McCaffrey*, 2008] had to be discarded.

2.1.3 GPS Seismology

The improvement in data acquisition (sampling), storage and transfer velocity, as well as in processing time, has widened the reach of GPS into different research areas of geodesy and seismology. Nowadays, high-rate (1 Hz) and very high-rate (>1 Hz) GPS time series can essentially be treated like seismograms because of their ability to measure instantaneous geodetic positions over short timespans [*Bock et al.*, 2000; *Ge et al.*, 2000b], as well as large displacements near earthquake ruptures [*Larson*, 2009]. The main interest in the application of GPS Seismology is as a strong-motion recording method in the near field [*Larson*, 2009]. This enables the determination of earthquake source parameters where recordings from classical devices (broadband seismometers or accelerometers) either clip or saturate.

1 Hz GPS data has been successfully used to monitor seismic wave fields for large-magnitude events, directly measuring ground displacement. Processed and filtered GPS data can approach millimeter accuracy in the hor-

---

[1] A prediction is more accurate than a forecast: the former specifies a unique behaviour and the latter describes a statement's probability.

izontal direction and can be achieved within a few seconds. Despite the pioneering proposal of using GPS as a seismometer in 1994 [*Ge et al.*, 2000a] and a feasible methodology first described by *Bock et al.* [2000], the earliest demonstration of the agreement between ground displacement recorded by GPS and integrated from broadband seismometers was not achieved until 2003 by *Larson et al.* [2003], for the 2002 M_w7.9 Denali Fault earthquake. Many other examples of recorded dynamic displacements caused by earthquakes can be found in the literature, like the aforementioned 2002 Denali [*Kouba*, 2003; *Bock et al.*, 2004; *Bilich et al.*, 2008], 2003 Boumerdes in Algeria [*Yelles et al.*, 2006], 2003 Tokachi-Oki [*Emore et al.*, 2007; *Miyazaki and Larson*, 2007], 2003 San Simeon [*Wang et al.*, 2007], 2004 Sumatra-Andaman [*Ohta et al.*, 2006; *Gahalaut et al.*, 2008], 2008 Iwate-Miyagi Nairiku [*Yokota et al.*, 2009], 2010 Maule [*Vigny et al.*, 2011], and 2011 Tohoku [*Grapenthin and Freymueller*, 2011; *Wright et al.*, 2012] earthquakes. Moreover, the 2011 M_w5.1 Lorca earthquake is also recorded by GPS in this Thesis, see Chapter 5.

Apart from simple monitoring, GPS high-rate data has been inverted to resolve for rupture processes; either using a priori assumptions about location or mechanism, or not. Examples are the 2003 Tokachi-Oki [*Miyazaki et al.*, 2004], 2003 San Simeon [*Ji et al.*, 2004], 2003 Chengkung [*Ching et al.*, 2007], 2006-2007 Kuril [*Steblov et al.*, 2008], 2010 El Mayor-Cucapah [*O'Toole et al.*, 2012b], or the 2011 Tohoku [*Yue and Lay*, 2011] earthquakes, among others. Comparisons between records from high-rate GPS in the near field and strong-motion at regional to teleseismic distances (>1000 km) have been long published [*Allen and Ziv*, 2011; *Bock et al.*, 2011; *Zheng et al.*, 2012]. This shows the good agreement between both, thus validating the implementation robustness and possibilities of GPS Seismology. For the 2011 Lorca earthquake, a comparison between the GPS results obtained here and accelerograph recorded data is given by *Pro et al.* [2014].

In order to estimate the slip distribution and geometry of an earthquake, GPS data has been combined with several other geodetic and seismic records: Interferometric Synthetic Aperture Radar (InSAR) [*Pollitz et al.*, 2011], geologic surface offsets [*Hreinsdóttir et al.*, 2006], gravity [*Ergintav et al.*, 2007], strong-motion [*Cirella et al.*, 2008], seismic waveform [*Rolandone et al.*, 2006], or even with multiple recordings as teleseismic, surface wave and strong motion [*Thio et al.*, 2004].

It should be mentioned that the success of earthquake monitoring ultimately depends on the proximity between receiver and epicenter/rupture. Most of the medium-small earthquakes cannot be observed by high-rate GPS except for a handful of events. An example is the 2011 Lorca earthquake mentioned before, where the GPS receiver was located only 5 km away from the epicenter.

2.1.3.1 Evolution of the GPS as a Seismometer

As explained by *Ge et al.* [2000a], the use of a GPS as a seismometer, this is, real-time kinematic processing, has been long discussed:

- The use for a dynamic processing was first proposed in 1994, with an experiment carried out by the Disaster Prevention Research Institute from the Kyoto University in Japan, using 1 Hz data and achieving a horizontal accuracy of 1-2 cm in post-processing. This proves that GPS can be used as a strain seismometer to obtain large amplitude near-field ground motion.
- In the same year, a different study was published using 30 seconds data from the Japanese GPS Earth Observation Network to derive ground motion due to the 4 October 1994, M_w8.1 Hokkaido-Toho-Oki earthquake. The arrival of the P-wave was successfully resolved. It concludes that, even at 30 s sampling rate, GPS is able to detect slow earthquakes.
- The afterslip in the 1994 Sanriku-Haruka-Oki earthquake was a further example of slow earthquake detection by GPS with a 30 s sampling rate [*Heiki and Tamura*, 1997].
- 1 Hz sampling was later proposed as an ultra-long-period seismograph by *Miyazaki et al.* [1997].
- The idea was reintroduced by *Ge et al.* [2000b]. They showed that 20 Hz GPS data should be able to measure large displacements over short time intervals.

- After that, in 2003 the agreement between ground displacement integrated from broad-band seismometers and the recorded by GPS was achieved by *Larson et al.* [2003] for the 2002 M_w7.9 Denali Fault earthquake.
- Nowadays, high-rate and very high-rate GPS data is being used as long-period strong-motion displacement seismometers.

2.1.3.2 Advantages and Disadvantages of the GPS Used as a Seismometer

GPS positioning has many advantages and still some limitations despite all the new developments in the last few years. A list of pros and cons is detailed here, in comparison with classical seismological devices and recordings.

One of the main advantages of GPS is the direct determination of displacements without integration, as opposed to seismic data: accelerometers and velocimeters have to be double and single integrated, respectively, in order to recover ground displacements [*Emore et al.*, 2007]. There are various sources of errors in accelerometer records that are amplified when the acceleration is integrated. The three most common sources include large-scale tectonic tilt, local tilt due to ground failure, and non-linear behaviour of the seismometer itself.

Also, the GPS constellation can be considered completely independent from the influence of earthquakes on the Earth: a GPS measurement, after applying all the proper corrections, is only affected by the absolute position change, recording directly the Earth's surface movement [*Ge et al.*, 2000b]. Moreover, with no fine mechanical parts and no need for a temperature compensation system, a GPS is cheaper and easier to maintain than a traditional device. Furthermore, as GPS receivers record range measurements to the satellites, and the antenna position is estimated from these ranges, GPS positions are referenced to the earth-fixed terrestrial reference frame, whereas seismographs produce direct measurements in an inertial reference frame: the signal recorded is the relative motion between a pendulum and its frame.

Another advantage of GPS is the ability to remain on scale whatever the amplitude of ground displacement. They can measure large events with significant displacements, both dynamic and static [*Bock et al.*, 2004]. On the contrary, seismometers have nearly the opposite behavior, potentially clipping or saturating under the extreme accelerations associated with very large earthquakes.

The main task after recording an earthquake is to determine the arrival time of the different seismic waves in order to locate the epicenter, as well as their periods and amplitudes. For that, accurate timing and calibration are of utmost importance. Using a GPS as a seismometer does not need additional timing system since all the measurements are taken together and related to GPS time. Also, GPS do not require any calibration. On top of that, while many different instruments are necessary to recover the diverse kinds of seismic waves, GPS seismometers have the potential to cover the whole seismic wave spectrum.

On the other hand, the use of a GPS as a seismometer has some disadvantages with respect to traditional methods and devices. Such shortcomings are either resolved by different methods or used as compelling reasons to design multisensor approaches to benefit from all types of recordings. This is a critical aspect when setting up early warning systems for earthquakes and tsunamis, as it will be detailed in Sections 2.1.4.1 and 2.2.4.1.

The sensitivity of the seismometers makes them capable of measuring moderate to large distant earthquakes, while GPS are better when they are placed near the source because they do not clip. Also, the noise floor of high-rate GPS measurements, about 5 cm, limits their detection capability to large-magnitude or nearby events [*Ge et al.*, 2000b; *Bilich et al.*, 2008]. For example, in this Thesis, the 2011 Lorca earthquake is observed by GPS in Chapter 5. Its epicenter was located 2 km from the GPS receiver, and its magnitude was of M_w5.1. There was no signal visible in the closest GPS site, placed 49 km away. Neither was the foreshock visible in the closest GPS, with a magnitude of M_w4.5.

Furthermore, despite 1 Hz GPS data is more than adequate to study some earthquakes, recorded data would be far more valuable if the receivers sampled at 10 Hz or higher [*Larson et al.*, 2003]. Nowadays, some GPS networks are able to stream 10 Hz data [*Bock et al.*, 2011] but, as mentioned, the farthest to the epicenter, the more GPS measurements approach the GPS noise level.

Another shortcoming of GPS is that the signal that is observed strongly depends on the direction and depth of the rupture: the receivers must be situated in the direction of the maximum rupture propagation, also called directivity, in order to measure the maximum amplitude of the event. If they are located perpendicularly, smaller displacements are observed [*Larson et al.*, 2003].

Finally, GPS and traditional seismic records can be merged in order to benefit from the advantages and to decrease the shortcomings of both systems. For example, while strong motion seismometers are designed to detect the large ground accelerations, GPS receivers are more suitable to detect longer period and steady state signals [*Zheng et al.*, 2012]. By using GPS and seismographs altogether, the whole frequency band is covered if both devices record an event. Moreover, in areas where there is no seismic information available, either because there are no receivers or because the instruments clips, high-rate GPS observations may serve as a supplementary data source.

2.1.4 Earthquake Early Warning Systems

To be effective, an Earthquake Early Warning System (EEWS) must be people-centered and must integrate several elements: knowledge of the risk, technical monitoring and warning service, dissemination of warnings and public awareness and preparedness to act [*Basher*, 2006]. EEWSs ideally predict future hazard based on presently available data, providing sufficient lead times, accurate source parameters, and reliable predictions of the potential final dimensions of the event at the target area [*Boese and Heaton*, 2010].

To provide the best warning times, most EEWS estimate earthquake magnitude from the earliest P-wave arrivals, using empirical relationships to magnitude. For the 2011 Tohoku-oki earthquake, a successful first early warning was issued within thirty seconds after the nucleation, when the estimated magnitude exceeded the M_w7.0 threshold. However, the final magnitude was significantly underestimated, due to the saturation of the seismometer 120 seconds after the earthquake began. This led to a magnitude estimation of M_w8.1 instead of 9.0 [*Wright et al.*, 2012].

Earthquake travel times strongly depend on the properties of the materials they traverse. Thus, warning times can vary from a few seconds to several minutes, depending mainly on the distance between epicenter and target area, and the type of soil the seismic waves traverse. Even when having only several seconds between warning and shaking arrival, heavy machinery and dangerous processes can be automatically stopped, e.g. trains, generators or chemical reactions. With a warning several minutes ahead, population can leave buildings and move away from dangerous locations.

The improvement of technology has made possible to implement EEWSs in many active seismic regions of the world. EEWS are currently running in Japan [*Kamigaichi et al.*, 2009], Taiwan [*Hsiao et al.*, 2009] and Mexico [*Suárez et al.*, 2009]. Other systems are under development or being tested in California [*Koehler et al.*, 2009], China [*Peng et al.*, 2011], Italy [*Zollo et al.*, 2009], Romania [*Boese et al.*, 2007] and Turkey [*Fleming et al.*, 2009]. In Istanbul, an earthquake rapid response and early warning system was implemented in 2002 [*Erdik et al.*, 2003]. Such systems are grounded in results related to the properties of seismic waves and strong ground motion.

Two different configurations for EEWSs are widely used: regional (network-based) and on-site (station-based) [*Colombelli et al.*, 2013]. In a network-based EEWS, event location and magnitude are estimated directly. Later, an existing empirical ground-motion prediction equation is used to rapidly derive intensity at distant sites in order to release an alarm. It benefits from the source-to-site distance. The data in such configuration is continuously updated, so the estimations are refined as the different sensors in the network acquire new data. In a station-based EEWS, the first recordings of the P signal are used to predict ensuing peak ground motion at the same site.

Nowadays, new strategies are emerging to complement traditional seismic monitoring, mainly consisting of broadband seismometers and accelerometers. Their goal is to set more complete and reliable multisystem EEWS, providing a more dense coverage of both land and seismic frequencies. For example, in Japan the so-called *home seismometers* are under testing, which are inexpensive seismometers that are being added to the already-set EEW receiving/alarm units in many homes. This way, the current $\sim$1000 seismic stations network is increased drastically, enabling a calculation of hypocenter parameters within 0.1 seconds [*Horiuchi et al.*, 2009].

2.1.4.1 GPS for Earthquake Early Warning: State of the Art

After detecting and locating potentially significant events by seismic data, a rapid determination of earthquake magnitude can be achieved by using measurements from already-existing GPS permanent networks [*Blewitt et al.*, 2006; *Song*, 2007; *Occhipinti et al.*, 2008; *Blewitt et al.*, 2009]. In addition to that, if real-time high-rate continuous GPS data is available, the position of GPS stations can be tracked with a latency of about a couple of seconds and with cm-level accuracy [*Genrich and Bock*, 2006]. This is, the permanent co-seismic deformation of the crust can be measured by GPS [*Blewitt et al.*, 1993]. As it is directly related to the seismic moment magnitude (M_w) of an earthquake, the latter can be calculated without any saturation. The probability for an earthquake to evolve into a big event is largely controlled by the characteristics of the rupturing fault [*Boese and Heaton*, 2010]. Therefore, an EEWS for large earthquakes will benefit from the real-time recognition of the fault (location, geometry and orientation), carried out while the rupture occurs.

For example, using static displacements measured in the near-field from a network of GPS receivers, and using a crustal model and approximate source location, *Allen and Ziv* [2011], *Melgar et al.* [2011] and *O'Toole et al.* [2012a] successfully determine the final static displacements taking approximately 10 minutes. To speed up such process, *Ohta et al.* [2012] determine an evolving slip model while the earthquake rupture is still progressing, estimating also its magnitude for the 2011 Japan earthquake. The magnitude obtained is $M_w8.8$, still below the final $M_w9.0$, and is obtained less than 2 minutes after the nucleation. *Crowell et al.* [2012] obtain reasonable models in terms of slip and magnitude estimates using near-source real-time GPS measurements for two test events also less than 2 minutes after the earthquake begun. *Bock et al.* [2011] show that GPS and accelerometers can be combined in real-time with sufficient accuracy to detect near-source P waves for $M_w>6.0$ earthquakes. *Blewitt et al.* [2006] postulate that, if near real-time GPS data were processed during the 2004 $M_w9.2$ Sumatra-Andaman earthquake, a proper warning could have been issued within 15 minutes, potentially saving thousands of lives.

Only seismic data is currently utilized in running EEWS. Nevertheless, the ability of GPS to complement seismic records, as detailed in Section 2.1.3.2, has motivated the investigation of its implementation in already-existing seismic networks. Regional GPS networks are able to directly measure displacements close to the source during large earthquakes in real-time. Projects following such idea are being developed in Cascadia and California [*Hammond et al.*, 2011].

2.2 Crustal Loads and Tsunamis

Earth's crust can experience a load by different agents. The most relevant for this Thesis are ocean tides, storm surges and tsunamis. They impose a load on the crust that can be measured by GPS, but their origin is different: ocean tides are an astronomical effect, surges are anomalous water rise, usually due to storms, and tsunamis are huge waves due to a redistribution of a big amount of water, usually generated by an earthquake and sometimes also by a landslide.

The change in the volume of water close to a place is traditionally measured by mareographs, also called tide gauges (TG). This change creates a difference in load. In the past years, the use of satellite altimetry has been developed in order to measure the water level changes all over the world, even in places where no mareographs can be installed. Also, ocean bottom pressure devices and GPS placed on buoys are used to calculate the water column above or below them, respectively. Tides are very accurately predicted because of their direct relationship to changes in the positions of Moon and Sun. Non-periodical (non-tidal) water level changes, such as storm surges or tsunamis, are predicted using different models of different accuracies and spacing.

2.2.1 Tides and Tidal Loading. Observation by GPS

The combined actions of the gravitational effects caused by the Moon and Sun, added to the Earth's centrifugal force, originate a response of the solid, gas and liquid parts of the Earth. They are known as terrestrial (solid), atmospheric and oceanic loads, respectively [*Benavent-Merchán*, 2010].

The part of the tide in the solid Earth that is due to its yielding to the body forces exerted by the Sun and the Moon is called solid tide. The atmosphere also produces surface loads from the pressure variations associated with atmospheric tides and weather.

Oceanic masses, perturbed by the combination of the gravitational forces exerted by the Sun and the Moon in addition to the centrifugal force related to both Earth-Sun and Earth-Moon systems, produce a periodic vertical displacement of the sea surface called oceanic tide. The tide at a point in the ocean at an instant is defined as the elevation of the surface of the ocean with respect to its mean position, due to the lunisolar attraction effect. Although oceanic tides are the greatest source of sea-level changes, external forces such as wind, barometric pressure changes and gravitational attraction from other celestial bodies also influence the sea level. Moreover, the oceanic tide is influenced by several other factors, such as the oceanic bottom topography, the coastline shape and the ocean dynamics, among others [*Benavent-Merchán*, 2010].

Tides are constantly predicted. The ocean tidal coefficient is the magnitude that indicates the amplitude of the forecast, defined as the difference in height between the consecutive high tides and low tides in any given area. The highest possible tidal coefficient is 118 cm, corresponding to the greatest high or low tide possible excluding meteorological effects. Observed tides at the mareographs are usually compared with the predictions, improving further predictions. The water surge, this is, the results from eliminating the prediction from the observations, is used to study several other natural processes as landslides, storms (see Chapter 7) and tsunamis (Chapter 8).

As a consequence of the tides in the ocean, an indirect response of the terrestrial crust is originated, called indirect oceanic effect or, most commonly, Ocean Tide Loading (OTL). If the Earth were completely rigid, the forces generated by the tides would produce no deformation. As this is not the case, there are deformations expected with an associated redistribution of mass. This response is determined by the elasticity of the crust and the structure of the upper mantle [*Baker*, 1984].

Tides are not directly observed by GPS per se, but the OTL affects GPS measurements. They need to be known very accurately, in order to correct GPS for them. A clear example of the effect of an extreme astronomical tide in GPS data as occurred in September 2011 can be seen in Figure 6.2. This vertical displacement (peak-to-peak up to 10 cm) and East-West tilt (up to 4 cm) strongly influences the GPS measurements. Some information about how OTL is computed for this Thesis can be found in Section 4.3.

2.2.2 Storm Surges. Surge-Induced Loading. Observation by GPS

Storms are natural processes that occur very often, originating when low pressure develops inside a system of high pressures. The opposition of the forces creates winds and results in the formation of storm clouds. Storms are successfully predicted by weather forecasting.

A strict meteorological definition of a storm is a wind speed of 24.5 m/s (89 km/h) or more [*Harris*, 1963]. There are several types of storms, such as ice, snow, ocean, fire, wind, thunder and hail storms, as well as blizzards, dust devils, squalls, gales, cyclones and tornados. Their labeling depends on the effects they produce, like the kind of precipitation or wind speed.

A storm surge is an abnormal rise of water generated by a storm, above the predicted values due to astronomical tides. The increase of water height is due to the push of the water toward the shore by the force of the winds circling around a storm, in combination to the low-pressure-induced dome of water drawn up under it [*Harris*, 1963]. When a storm surge coincides with high tide, the water quickly adds up, being able to cause extreme flooding in coastal areas.

Storm surges have always been recorded by tide gauges. Nowadays, with the development of ocean-bottom pressure sensors, the amount of water over them is measured as well. Also, a couple of storms have been recorded by altimetry satellites, for example, Hurricane Sandy [*Scharroo et al.*, 2005] and Xaver cyclone [*Scharroo and Fenoglio*, 2013]. With the increase of precision in GPS data, several storm surges have been successfully recorded by GPS, either co-located with tide gauges and ocean-bottom pressure sensors, or placed on buoys in the water.

According to *van Dam et al.* [2012], the North Sea is very sensitive to non-tidal loading because it is a storm surge prone area. A subsidence of up to 2-3 cm at some geodetic sites around the southern part of the North Sea in response to a storm surge was predicted by *Fratepietro et al.* [2006]. Later, *Williams et al.* [2009] and *Geng et al.* [2012] studied GPS data recorded during a storm surge in November 2007, obtaining a vertical subsidence of up to 3 cm related to a surge of up to a meter, the latter with a sub-daily (2 hourly) output rate. In this Thesis, cyclone Xaver induced water surge is studied by GPS, altimetry and tide gauge data in Chapter 7. A subsidence of up to 4 cm is measured by GPS in some coastal stations co-located with TG.

Despite the fact that storm surge is not a natural hazard that can be early-warned by GPS in general, the observation of the December 2013 storm surge in the German Bight and further comparison with modeled data, altimetry and tide gauges, is of great importance. The obtained relationships provide a very valuable information for the use of GPS for tsunami early warning by the study of tsunami models, with the current processing strategy and software utilized in this Thesis.

2.2.3 Tsunamis. Tsunami-Induced Loading. Observation by GPS

A tsunami is defined as a series of waves caused by the displacement of a large volume of water. Most of the known tsunamis sources are either giant megathrust earthquakes [*Hiroo and Kanamori*, 1972; *Okal and Synolakis*, 2004] or landslides [*Synolakis et al.*, 2002; *Sarri et al.*, 2012]. However, moderate-size submarine seaquakes, inland earthquakes [*Newman et al.*, 2011; *Roger et al.*, 2011], volcanic eruptions, glacier calvings, meteorite impacts and natural or human-induced underwater explosions have the potential to generate a tsunami as well. Depending on the volume of water displaced, near-field tsunamis can devastate nearby coasts in only a few minutes [*Roger et al.*, 2011].

Tsunami waves range from a few centimeters to tens of centimeters in the open ocean, traveling at about 600 to 700 km per hour [*Wu and Ho*, 2011]. As they approach the coast and the waters become shallow, their speed decreases down to about 10% and the amplitude grows enormously. For example, a 2-meter wave can wash away a house [*Balcerak*, 2011]. On top of that, the approaching wave is not likely to break, resembling a big wall of water reaching up to tens of meters for extreme events like the 2011 Japan earthquake. A large tsunami may involve multiple waves arriving over several hours with a typical wave period between 10 and 40 minutes [*Occhipinti et al.*, 2008]. The first wave to reach land may not be the ridge (positive peak) but the trough (negative peak). This would resemble a dramatic receding of the shoreline, like a sudden low tide with a drawback of the water line of up to hundreds of meters.

There are two types of tsunami forecasting, either based on earthquake forecasting (see Section 2.1.2) or directly by computing the probability of a tsunami nucleation once an earthquake has occurred, which is the most robust method.

The first method is based on the relationship between the energy released by an earthquake, thus its magnitude, and its ability to create a tsunami [*Blewitt et al.*, 2006; *Rosenau et al.*, 2010], as well as the distance to the coast [*Roger et al.*, 2011] and the shoreline bathymetry, which affect the tsunami size. It must be pointed out that a tsunami cannot be precisely predicted in all cases, even if the magnitude, location and depth of the earthquake are known [*Hiroo and Kanamori*, 1972; *Song*, 2007]. There are records of earthquake-generated tsunamis much larger than expected based on the seismic magnitude, like the M_w7.8 2010 Mentawai, Indonesia, earthquake [*Hill et al.*, 2012] or the 2006 Java earthquake, followed by a tsunami with 21 meters run-up despite its relatively moderate magnitude [*Fritz et al.*, 2007]. Later, *Song* [2010] demonstrated that the total tsunami energy can be written as a function of the seafloor displacement, including the horizontal motions of a faulting continental slope because it also transmits kinetic energy to the ocean. Unfortunately, the ocean floor topography can also interact with the wave paths, both complicating the prediction of the target areas and even causing two tsunami waves to merge into a larger wave, as it has been hypothesized for the 2011 Japan tsunami [*Balcerak*, 2011].

The second method is mainly used for near-shore sources. The forecast is carried out using pre-computed scenarios and tsunami catalogues. This approach is incomplete for the high end of the magnitude scale [*Rosenau et al.*, 2010] because tsunamis triggered by giant megathrust earthquakes (M_w∼9) are very rare, between one and three events per century [*McCaffrey*, 2008]. Nevertheless, compendiums of available seismological information are created in order to propose tsunami models for a correct forecasting, including all tsunamis referenced in historical documents and catalogues. For example, *Matias et al.* [2013] integrate the available seismotectonic information for the Gulf of Cádiz. The main problem of this approach is that there are no models or catalogues for new active areas, where no earthquakes or tsunamis have been generated yet.

On the other hand, trans-oceanic tsunamis can take hours to reach the coast [*Titov*, 2009]. Hence, they can be forecasted, and the alert can be validated by using deep-ocean pressure data: measuring the change in height of the deep ocean or checking the recordings in mareographs in places where the wave has already arrived [*Bressan and Tinti*, 2011]. This can assist the establishment of a tsunami model in real-time [*Tang et al.*, 2012] thus both far-field and teleseismic tsunamis can be alerted before they reach the target coasts.

Ionospheric disturbances, mainly total electron content, have been related to several tsunamis, e.g. 2004 Sumatra [*Liu et al.*, 2005], 2010 Chile and 2011 Japan earthquake-generated tsunamis [*Kakinami et al.*, 2012]. As for the earthquake forecast, this is a strategy not fully spread neither fully accepted in the seismological and geodetic communities.

Up to the time of this research, the load of only one tsunami has been successfully recorded by GPS: the March 11^{th}, 2011 Tohoku earthquake [*Mitsui and Heki*, 2013]. The crustal subsidence due only to the tsunami-induced load reaches up to 1 cm and is almost instantaneous. Before that, only *Plag et al.* [2006] introduces this possibility for the M_w9.2 December 26^{th}, 2004 Sumatra earthquake-induced tsunami, but the research carried out to obtain such statement was never published.

Separating tsunami-induced loading in the solid earth and co- and post-seismic crustal displacements is critical. Using only water height models for such events, as it will be done in Chapter 8, can be of help to be aware of the possible signals that can be detected by GPS in case of events of similar magnitude.

2.2.4 Tsunami Early Warning Systems

A Tsunami Early Warning System (TEWS) must be designed to allow operators to receive the necessary information, interpret it and send the alarm fast enough to initiate evacuation procedures. The communications infrastructure is likely to be affected by the disaster itself. Hence, its design is particularly challenging [*Angermann et al.*, 2010]. Data centers must be placed in buildings that are not threatened by the impending waves, and reliable power supplies for all components involved are crucial. Inundation maps [*Baptista et al.*, 2011] and water run-up models [*Liu et al.*, 2005; *Muhari et al.*, 2011], threatened areas [*Atillah et al.*, 2011; *Renou et al.*, 2011] and safe evacuation roads [*Muhari et al.*, 2011] are also valuable pieces of information that must be available.

Current TEWSs rely on earthquake magnitude determination and rupture parameters estimation. It was already pointed out that tsunami waves travel 600-700 km/h and their speed decrease down to a 10% as they approach the coast. Thus, if a tsunami alert is issued several minutes after nucleation and the tsunami source is located far enough from the coast, the population can have sufficient time to evacuate and make it to safety. For example, if the tsunami is generated close to the fault where the 1755 Lisbon earthquake was nucleated (approximately 160 km away from the nearest point in Portugal), the first increase of water would arrive about15 minutes after the nucleation. If the warning were issued 5 minutes after the earthquake, population would have up to 10 minutes to make it to safety. Unfortunately, the tsunami generated by the past Japan quake (March 11^{th}, 2011) was only a few kilometers away from the coast thus the warning time was too short.

This means that, if a tsunami is nucleated near to a coast, its first wave may reach land in a few minutes. This is the timespan available for analyzing the recorded data, setting a warning and evacuating the population in danger. Therefore, as it can be very short, the best option would be a completely automatized system that, in a few minutes, could check the veracity of the alarm and send proper warnings according to the impending risk. Despite the difficulty of designing a TEWS for tsunamis generated close to shore (near-field tsunamis), lives can at least be saved in more distant places.

Before 2005, real-time seismic data processing was rare. Following the tsunami generated by the great December 26^{th}, 2004 Sumatra-Andaman earthquake, the population awareness with respect to their vulnerability when facing such extreme events arose [*McCloskey et al.*, 2008]. After 2004, several TEWSs are developed and implemented in the regions exposed to tsunamis. For example, there are systems already operational in the Pacific (PTWS, [*Titov*, 2009]), Australia (ATWS, since 2009 [*Allen and Greenslade*, 2010]) Indian Ocean (IOTWS, since the end of 2011), Japan (JTEWS, [*Kamigaichi*, 2009; *Wang et al.*, 2012]) and Indonesia (GITEWS, German Indonesian Tsunami Early Warning System [*Rudloff et al.*, 2009]). TEWSs are being installed and tested in the Caribbean area (CARIBE EWS), North America's West Coast and Alaska (WC/ATWC) and in the North Eastern Atlantic, the Mediterranean and Connecting Seas (NEAMTWS, [*Olivieri and Scognamiglio*, 2007; *Hanka et al.*, 2010]). Such projects are designed to cover large areas, but in many places there is a need to establish a regional warning system arising from the short time available for an effective response. For example, Portugal is developing a national TWS (Portuguese Tsunami Warning System - PtTWS), based on the 1755 Lisbon experience [*Matias et al.*, 2013].

Several parallel research projects are also carried out, focusing on Europe (Mediterranean and NE-Atlantic basins, mainly). Among others, SCHEMA (SCenarios for Hazard-induced Emergencies MAnagement [*Valencia et al.*, 2011]) is centered on tsunami hazard and vulnerability assessment. Examples for Rabat and Salé areas are found in [*Atillah et al.*, 2011; *Renou et al.*, 2011]. A wider example for European-Mediterranean coast is given by *Valencia et al.* [2011].

In order to issue an alert, two methods are usually followed: either a decision matrix [*Tinti et al.*, 2012] or precomputed scenarios, calculated by suitable tsunami numerical models [*Behrens et al.*, 2010]. A decision matrix is a routine that links the main parameters of an earthquake (magnitude, location, depth) and the possible ensuing tsunami. Its goal is to make a quick decision on the type of alert to trigger, which may be improved or cancelled on the basis of updated seismic information and/or data supplied by other means, like tide gauges, or buoys where available [*Behrens et al.*, 2010]. For the tsunami precomputed scenarios and in Indonesia by GITEWS [*Rudloff et al.*, 2009], the necessary parameters are the same as for the decision matrix. All the available sensor data, including seismic and ocean measurements, is integrated within and a tsunami prediction is generated based on the collected observations. To provide such a prediction, an inverse problem is solved: find the best-fitting tsunami generation and propagation model on a set of models. A similar strategy is used in the Pacific Tsunami Early Warning System, where such best-fit models are constructed on-the-fly from precomputed components [*Titov*, 2009].

Unfortunately, none of the methods mentioned above is completely reliable. The "tsunami earthquakes" are greater than expected from their seismic magnitudes [*Hiroo and Kanamori*, 1972], e.g. the 2010 M_W7.1 Solomon Islands earthquake, [*Newman et al.*, 2011]. There is also the possibility of the occurrence of a big earthquake that does not produce a tsunami [*Kreemer et al.*, 2006]. Other limitations for precomputed models are that tsunamigenic earthquakes are modeled only arising from known subduction zones. Also, the number of pre-computed sources and scenarios is finite, not being able to estimate all possibilities. It must be pointed out that both decision-making strategies are tools that only handle tsunamis of seismic origin. This is especially dangerous for the Mediterranean Sea, where volcanic activity has triggered tsunamis in the past.

Nowadays, tsunami detection in real-time can be also achieved by instrumental sea-level data recording [*Omira et al.*, 2009; *Falck et al.*, 2010; *Bressan and Tinti*, 2011, 2012; *Wang et al.*, 2012]. With the information and methodology currently available, the only way to know if a tsunami has been generated in the open-ocean is to obtain a measurement in ocean sensors, both coastal[2] and offshore [*Bressan and Tinti*, 2012]. For example, the 2010 Solomon Islands earthquake-generated tsunami produced waves in open-ocean of 1-2 cm, which were measured by deep-ocean sensors [*Newman et al.*, 2011]. In addition to that, satellite altimetry data can be very helpful to both detect tsunamis in the open ocean and improve predictions made by models: by using satellite altimetry observations, the tsunamis of 2004 in Sumatra [*Godin et al.*, 2009], 2010 in Chile [*Hamlington et al.*,

---

[2] The detection of tsunami waves in coastal sensors could seem like a too late approach, but detecting a tsunami at one place is useful for all other locations that are more remote and thus reached later. This information can be used to update or even cancel tsunami alerts.

2011] and 2011 in Japan [*Hamlington et al.*, 2012] could have been detected in near real-time. Unfortunately, this would only be possible if an altimeter satellite was recording the water height in the right place at the right time, and if the data was processed in real-time.

2.2.4.1 GPS for Tsunami Early Warning: State of the Art

TEWSs are based on the general knowledge of the incoming wave before it reaches the coast. In this scheme, the robustness of the warning highly depends on the quality of real-time data, as well as on the quality of modeling for the strategies based on a decision matrix and tsunami models.

After a quick detection by seismic data, GPS measurements can be used for a rapid determination of the earthquake's magnitude [*Blewitt et al.*, 2006; *Song*, 2007; *Occhipinti et al.*, 2008; *Blewitt et al.*, 2009]. If real-time high-rate continuous GPS data is available, the permanent co-seismic deformation of the Earth's surface can be estimated. Static displacements take 2-5 min to establish after an event [*Sobolev et al.*, 2007; *Falck et al.*, 2010], which makes near real-time GPS a very valuable component of any TEWS. *Blewitt et al.* [2006] demonstrated that for the 2004 Sumatra earthquake, a 15 or 30 seconds data rate is sufficient to resolve the permanent displacement for ocean-wide tsunamis of similar characteristics. However, to provide the initial conditions for near-field tsunamis models, higher sampling rates are necessary [*Blewitt et al.*, 2009].

Different projects are currently underway to merge GPS into TEWSs. In Japan, the Earthquake Research Institute has deployed a GPS tracked tsunami warning buoy network (Deep-ocean Assessment and Reporting of Tsunamis "DART" [*Kato et al.*, 2005]) that is currently running in demonstration mode [*Foster et al.*, 2012]. Japan's Geographical Survey Institute is also deploying a very dense GPS network with a real-time capability [*Yamagiwa et al.*, 2006]. Moreover, GITEWS (see Section 2.2.4) is the first and currently the only tsunami warning system that explicitly introduced a multi-sensor approach into TWS [*Behrens et al.*, 2010]. It is expected to issue a warning in just 2-3 minutes after an event [*Kamigaichi*, 2009; *Hanka et al.*, 2010]. Continuous near real-time GPS arrays are integrated into this system, providing averaged surface displacements in two-minutes intervals [*Falck et al.*, 2010]. Such displacements, together with seismic data, are directly inverted to obtain detailed source parameters [*Sobolev et al.*, 2006, 2007]. Later on, other sensor systems such as ocean bottom pressure sensors [*Boebel et al.*, 2010] and GPS-buoys ("GPS Shield", [*Sobolev et al.*, 2007; *Schoene et al.*, 2008]) assist to track the wave propagation. Finally, a network of coastal tide gauges helps to constrain forecasting uncertainty by directly checking the incoming leading wave depression or ascension, and thus measuring tsunami height [*Babeyko et al.*, 2010; *Schoene et al.*, 2011].

3 The Study Area and Infrastructures. Observability of Effects

In this Chapter, an overview of the tectonic structure in the study zone is presented. The threats derived from possible events are discussed in Sections 3.1.2 and 3.1.3 according to their target areas. The GNSS networks deployed are detailed in Section 3.2.

It is important to remark that this Thesis is focused on the use of GPS data for natural hazards early warning in the Iberian Peninsula and surroundings. Thus, the GNSS networks presented here correspond to those available in this region and whose data has been used for the several test cases. However, some other GPS networks outside this region, seismographs and tide gauges are utilized in this Thesis, and they will be introduced at the beginning of each corresponding Chapter.

3.1 Geological and Tectonic Description of the Study Zone

The area of interest for this Thesis is the so-called Iberia-Maghreb region. From North to South, it consists of the Iberian Peninsula, Gulf of Cádiz, Alborán Sea and Northern parts of Morocco and Algeria. This region is located at the convergent African-Eurasian plate boundary, see Figure 3.1.

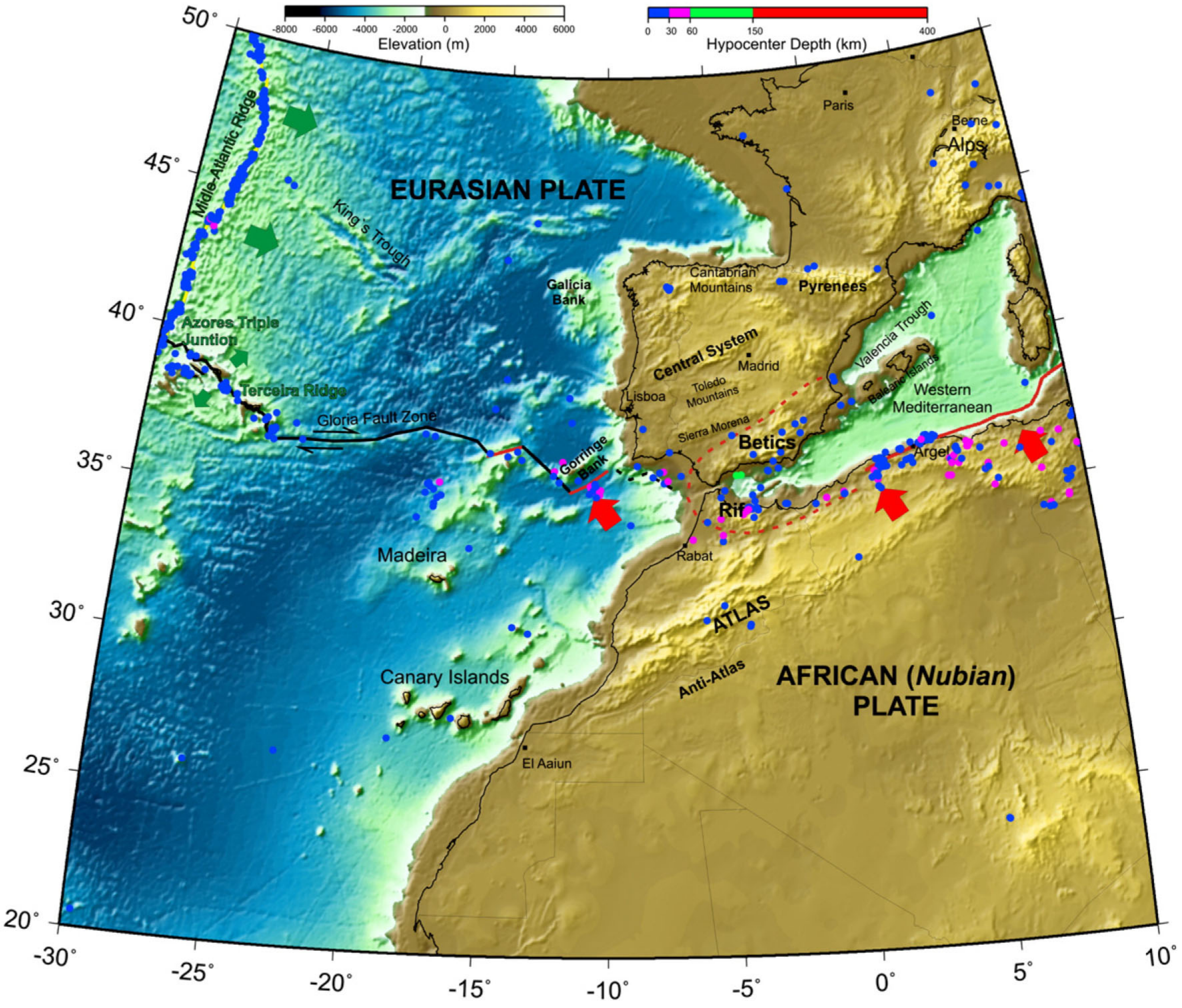

Figure 3.1: Simplified tectonic map of the Western Africa-Eurasia plate boundary from [*Muñoz-Martín et al.*, 2010].

In this Section, a short description of the tectonic structure of the Iberia-Maghreb region is given, as well as an overview of seismicity and seismotectonic and the possible threats due to impending tsunamis. The study zone is separated into the different areas of interest. From West to East: Atlantic Ocean (specially near Iberia) and Gulf of Cádiz, Iberian Peninsula focusing on Southern (Guadalquivir basin and Betic Cordillera) and Eastern (Province of Murcia) regions, and also Western Mediterranean area, emphasizing Alborán Sea and Northern Algeria.

3.1.1 Description of the Study Zone

Presently, the overall convergence between Nubian (African) and Eurasian tectonic plates near the Iberian Peninsula occurs at rates of approximately 5-6 mm/year, shortening in WNW-ESE direction [*Stich et al.*, 2006; *Vissers and Meijninger*, 2011]. In the Western Mediterranean sector, tectonic deformation complexity is enhanced by extensional processes [*Comas et al.*, 1999; *Jolivet and Faccenna*, 2000]. Furthermore, Western Iberia is located near the confluence of oceanic, active continental and stable continental crust [*Vilanova et al.*, 2012], entangling a general description.

3.1.1.1 Atlantic Ocean and Gulf of Cádiz

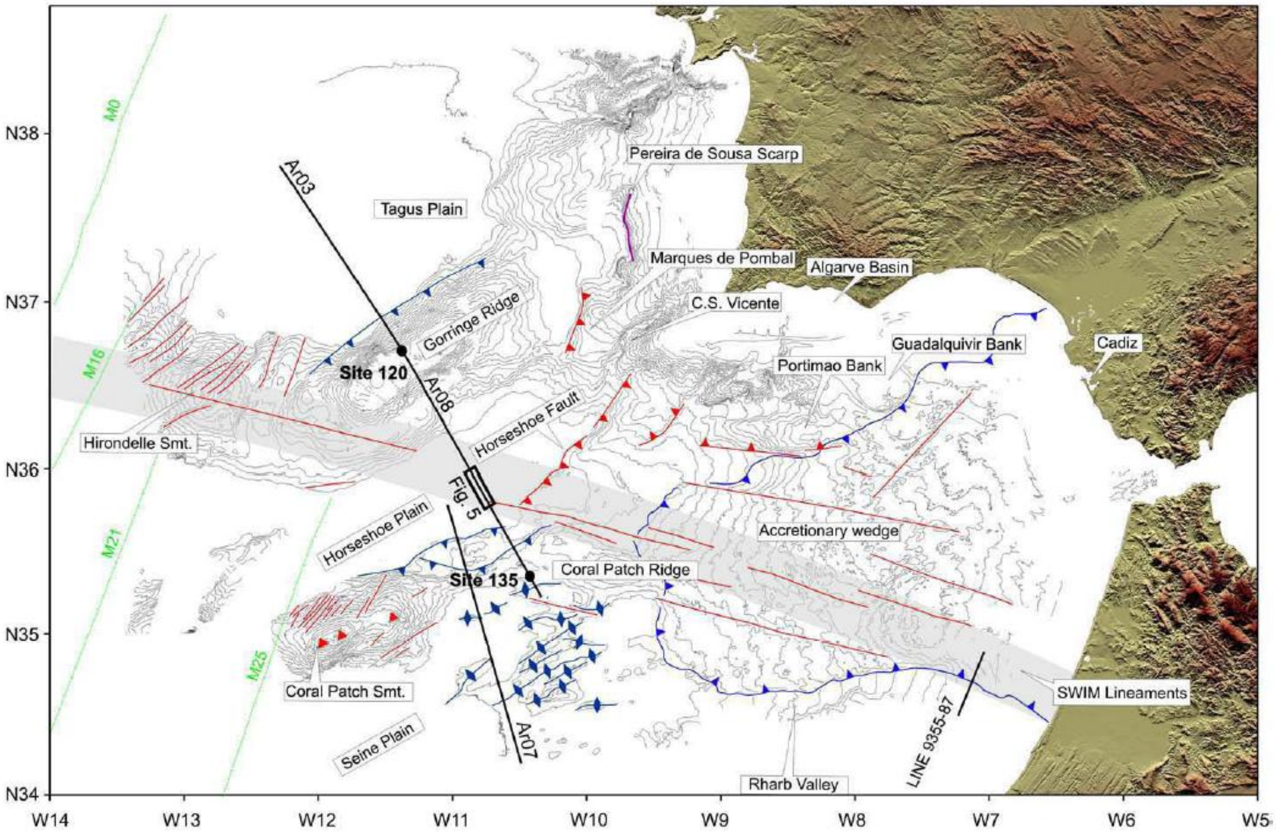

Figure 3.2: Tectonic map from [*Zitellini et al.*, 2009]. Red line with triangle: active reverse fault; purple line with triangle: external limit of the accretionary wedge; blue line with triangle: inactive reverse fault; blue lines with rhombus: axis of inactive anticline; short, close-spaced red line: lineament related to accretion of oceanic crust; violet line: Cretaceous normal fault; long, WNW-ESE oriented, red lines: SWIM lineaments.

The plate boundary between Northwest Africa and Southwest Eurasia connects the Betic-Rif orogenic arc (West Alpine orogen termination) to the Gloria Fault Zone, a transform faults area in the central part of the Azores-Gibraltar plate boundary, see Figure 3.2. West of the Gloria Fault, the Terceira Ridge is an oceanic transtensional plate boundary where oceanic crust accretion occurs nowadays. East of the Gloria fault towards the Gulf of Cádiz, a plate boundary is not well established: the deformation is distributed over a wide area of about 200 km width [*Morel and Meghraoui*, 1996].

According to *Zitellini et al.* [2009] and following the map in Figure 3.2, two different plate-driving mechanisms in the Gulf of Cádiz are evident. First, subduction associated with the Westward emplacement of the Gibraltar Arc and formation of the Gulf of Cádiz accretionary wedge. And second, oblique lithosphere collision between Iberia and Nubia causes thrusting in the Horseshoe Abyssal Plain and SW Portuguese Margin. Such a collision also induces dextral wrenching along the SWIM fault zone. SWIM faults are a set of recently found WNW-ESE trending vertical faults, almost linear and sub-parallel. They form a narrow band of deformation over a length of 600 km, connecting the Gloria Fault to the Rif-Tell plate boundary.

3.1.1.2 Iberian Peninsula

Iberia is mainly formed by the Hesperic Massif, consisting of Precambrian and Paleozoic terrains accreted during the Variscan continent-continent collision [*Benito et al.*, 2010]. It is located in the Western part of the Eurasian-African plate boundary, near the Azores-Gibraltar fracture zone. In this area, transition from oceanic to continental boundaries occurs from West to East. The oceanic part extents from the Azores along the Azores-Gibraltar fault to the West of the Strait of Gibraltar (12°W). Across the Western part of Algeria, from 12°W to 3.5°E, the boundary gets more diffuse and forms a wider area of deformation. Bathymetry, seismicity, stress regime and tectonics are a proof of this complexity.

The interaction between Iberia and Africa has been subject of study for a long time, and still several new results come up every year. For example, see [*Buforn et al.*, 2004; *Khazaradze et al.*, 2007; *Benito et al.*, 2010; *Muñoz-Martín et al.*, 2010; *Nocquet*, 2012; *Sørensen et al.*, 2012; *Vilanova et al.*, 2012], among others.

3.1.1.2.1 Southern Spain: As it can be seen in Figure 3.3, the main geological structures in the South of Spain include the Southern boundary of the Iberian Massif, the Betics and the Guadalquivir Basin.

The plate boundary between Africa and Iberia in the Betics range (Northern Alborán) is not clear due to the complex Neogene deformation that led to its formation. It stretches more than 500 km wide, from the High Atlas in Morocco to the Betics in Spain [*Calvert et al.*, 2000].

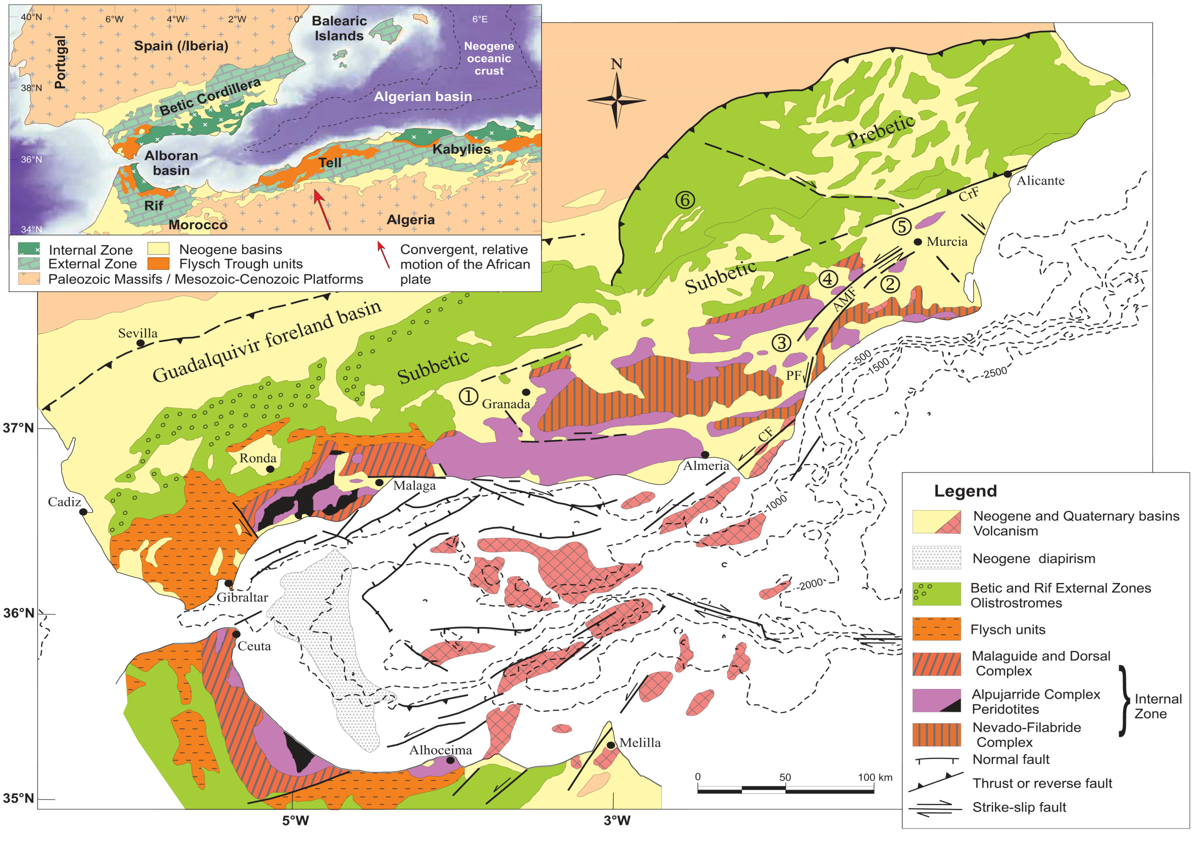

Figure 3.3: Geological structures in Southern Spain. Figure taken from [*Meijninger*, 2006].

The Betic Cordillera has been generated by a series of collisions and separations between the Eurasian and Nubian plates (fold-and-thrust belt), with an overall deformation in the order of up to 4 mm each year [*Khazaradze et al.*, 2007; *Benito et al.*, 2010]. Such a complex history leads not into a major contact fault but to a dense network of secondary faults. Because of the diffuse plate boundary, the stress diverges to several small faults. Hence, small magnitude earthquakes are predominant [*Buforn et al.*, 1995]. Several basins developed while the Betics rose: the Guadalquivir Depression, widening Southwesternwards, is the most important one. Strike-slip faults determine other small basins located within the Betics, accommodating strong internal deformation, like Granada Basin [*Vilanova et al.*, 2012].

3.1.1.2.2 Eastern Spain: the Region of Murcia: Murcia is located in the Southeast of Spain, directly in the Eastern part of the Betic Cordillera and close to the convergence between Eurasian and Nubian plates [*Dewey et al.*, 1973]. The Eastern Betic Zone is a NE-SW transpressive fault system.

The interest in the Region of Murcia is linked to Chapter 5, where the M_w5.1 Lorca earthquake that occurred on May 11th 2011 is analyzed. It took place 5 km away from the city of the same name. It is located immediately adjacent to a main fault zone, called the Lorca-Totana fault, or more commonly, Alhama de Murcia fault (AMF in Figure 3.4). It forms part of the aforementioned NE-SW trending network of prominent faults. It is associated with the contact between basement rocks and mostly Quaternary basin sediments, and defined by a steep NW dipping fault [*Vissers and Meijninger*, 2011]. The Alhama de Murcia fault has a strike between N45°E and N65°E and a maximum slip rate of 0.3 mm/yr, measured in recent trenches. Besides, it is located close to the convergent plate limit between Eurasian and African plates, with a total regional motion rate of 4 to 5 mm/yr [*Masana et al.*, 2004].

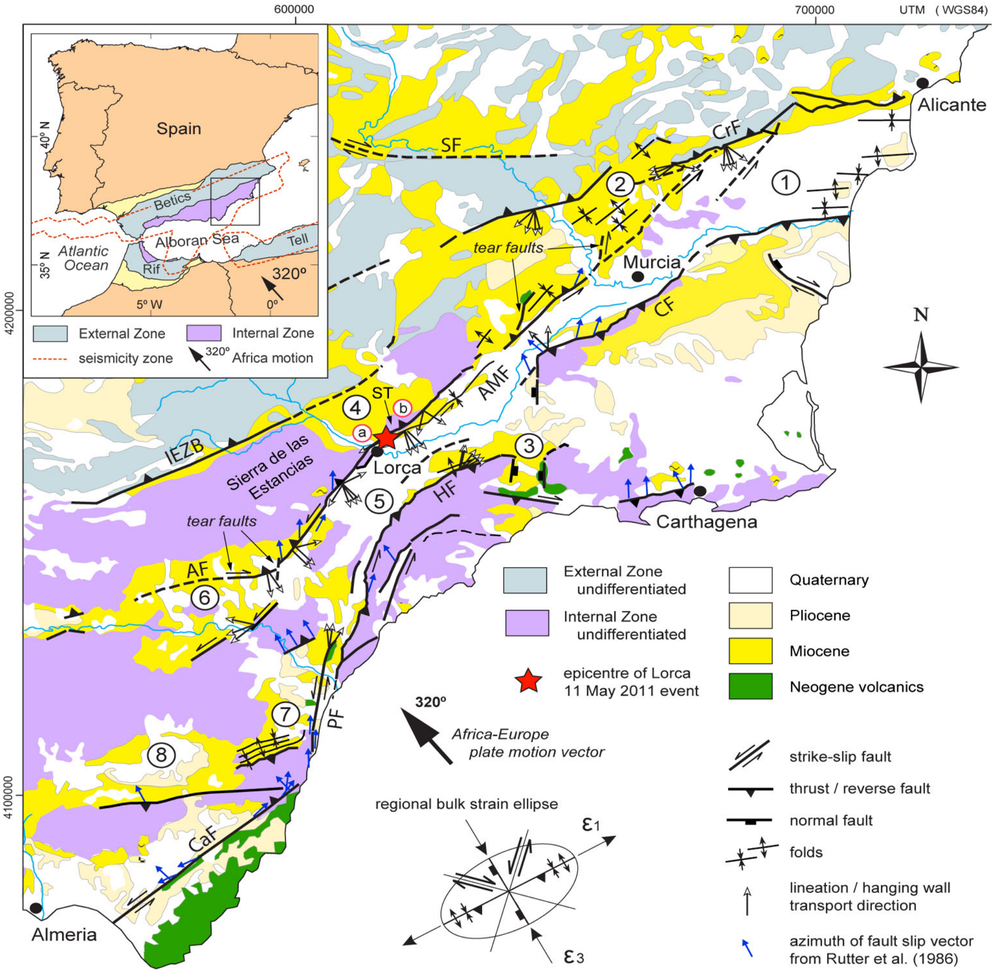

Figure 3.4: Geological structures in the Region of Murcia. Main individual faults, from North to South: Carrascoy (CrF), Alhama de Murcia (AMF), Palomares (PF) and Carboneras (CaF). Number (4) corresponds to the Lorca basin. Map taken from [*Vissers and Meijninger*, 2011].

3.1.1.3 Western Mediterranean: Alborán Sea and Northern Algeria

In North-Central Algeria, the dominant active tectonic structures are NE-SW to E-W trending fold and thrust system [*Maouche et al.*, 2011]. In this area, plate convergence and extensional processes interact to produce complex tectonic deformation over the Iberia-Maghreb region. East to the Strait of Gibraltar, the Nubia-Iberia plate boundary is roughly defined by a right-lateral transpressive shear area (Rif-Tell fault zone) [*Morel and Meghraoui*, 1996].

Results published by *Borges et al.* [2001] and *Mancilla et al.* [2002] state that Northern Algeria is characterized by predominantly reverse faulting under ∼NNW-SSE compression. Moreover, at the SE-Iberian margin (Alborán Basin and Southern Spain), compression in ∼NW-SE direction along reverse and strike-slip faulting is predominant [*Buforn et al.*, 2004], see Figure 3.3. Such results suggest extensional tectonics added to Nubia-Eurasia plate convergence along this section of the plate contact [*Mezcua and Rueda*, 1997; *Bezzeghoud and Buforn*, 1999; *Stich et al.*, 2003].

3.1.2 Seismicity and Seismotectonics. Earthquake Recurrence

A map showing the seismicity in the Peninsula and its surroundings until 2006 can be found in Figure 3.5. It represents earthquake epicenters with local magnitudes $M_w \geq 3$ projected onto a map of active and potentially active faults. Summing up, seismicity is relatively focused at the Algerian and SW-Iberian margins but more diffuse between Morocco and Spain. Relevant seismicity is also observed in the Pyrenees and in several intraplate areas on and around the Iberian Peninsula. According to *Buforn et al.* [1995], in the zone where Iberia and Africa connect, seismicity is distributed over a belt of 400 km width, and comprises lower magnitude events compared to the adjacent areas. Most of the earthquakes in Iberia have a shallow depth (0<h<40 km) foci, and the corresponding magnitudes are mostly smaller than $M_w 5.5$ [*Buforn et al.*, 2004]. Intermediate and deep seismicity (h ∼600 km) is also present in this region, where several high magnitude events are well documented too.

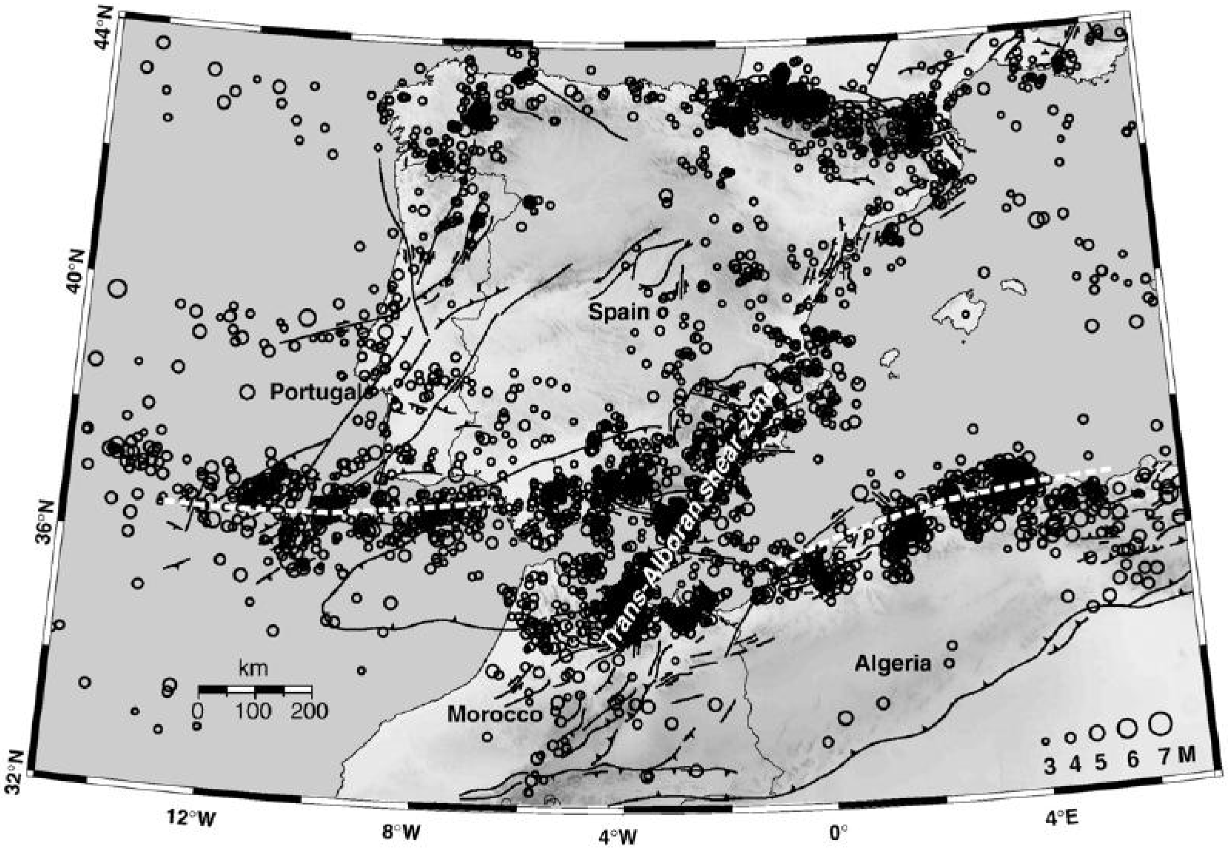

Figure 3.5: Seismicity in the Iberian Peninsula until 2006 [*Stich et al.*, 2006].

3.1.2.1 Atlantic Ocean and Gulf of Cádiz

The area offshore Cape St. Vicente (Portugal) and the Gulf of Cádiz are part of the plate boundary between Eurasia and Africa. The material conforming this region is relatively rigid, and the stresses are released by large earthquakes. As a result, it is one of the most important tsunamigenic areas in Europe [*Benito et al.*, 2010].

The Gorringe Bank is the area located SW St. Vicente Cape. It is known for some big events like the large earthquakes in 880, 1356, 1755, 1761, 1969 (M_w7.8) and 2007 (M_w6.0), all sharing the same characteristics [*Buforn et al.*, 1988; *Benito et al.*, 2010]. The 1755 Great Lisbon earthquake, with estimated magnitudes between M_w8.5 and 8.7 [*Martínez-Solares and López Arroyo*, 2004], generated the largest and highest destructive tsunami ever experienced in Western Europe [*Zitellini et al.*, 2009]. More information about this tsunami will be given in Section 3.1.3.1. Despite earthquakes of this magnitude are only related to plate boundaries, either at subduction zones, intracontinental orogenic sutures or conservative borders, the source location of this event is not determined accurately [*Buforn et al.*, 1988]. Its closest plate boundary is found in the Western part of the Eurasian-Nubian Plates, extending from the Azores islands through the Gulf of Cádiz into the Mediterranean [*Zitellini et al.*, 2009].

3.1.2.2 Iberian Peninsula

According to *Vilanova et al.* [2012], the largest magnitude estimates for past earthquakes in Iberia are in the range of M_w6.9-7.1 from historical data, and between M_w7.1-7.3 from paleoseimological evidence. Excluding the Betics and Pyrenees, Iberia is classified as a stable continental region. Nevertheless, it is located near the Azores-Gibraltar plate boundary, a complex area with potential to nucleate very strong earthquakes.

3.1.2.2.1 Southern Spain: Andalucía (Andalusia), located in Southern Spain, is considered a moderate seismic area in a worldwide context, but it is one of the Spanish regions with the highest seismic activity according to historical and instrumental seismic data [*Benito et al.*, 2010]. In this zone, intermediate deep shocks are concentrated at 4.5°W, between 40 and 120 km depth within a zone trending southward from the Spanish coast into the Alborán Sea. As seen in Figure 3.5, the earthquakes in Northern Algeria and Eastern of the Atlantic Ocean tend to a WSW-ENE direction, showing two convergence segments between Eurasia and Africa. Such partition is diffuse, comprehending a large number of small faults, which and clearly complicates the definition of a plate boundary.

Along the Betics, the existence of such small faults compels the accumulated stress release by frequent small to moderate earthquakes [*Grimison and Chen*, 1986], the latter more common. Besides, during 19^{th} Century, at least two earthquakes took place with magnitudes M_w>6, in years 1829 and 1884. It is believed that the lack of large earthquakes between 1900 and 2015 is due to an anomalous quiet period. The only two exceptions are the 1910 Adra coast earthquake (M_w6.2) and the 1954 Dúrcal earthquake (M_w7.9).

3.1.2.2.2 Eastern Spain: the Region of Murcia: The Alhama de Murcia Fault is approximately 85 km long [*Benito et al.*, 2007]. It is characterized by marked seismicity, stretching into the Alborán Sea in a belt of equally high seismic activity. According to *Vissers and Meijninger* [2011], kinematic indicators consistently show that the Alhama de Murcia fault has an oblique-slip (reverse-sinister) movement. This contradicts *Stich et al.* [2006], who state that a complex variety of faulting styles, going from pure normal to pure reverse faulting for small and moderate events, is found on significant parts of the Alhama de Murcia fault zone. Furthermore, the existence of large faults with late Quaternary activity indicates that the occurrence of major earthquakes ($M_w \geq 6.0$) cannot be dismissed [*García-Mayordomo et al.*, 2007].

Over the last years, seismic hazard in this area began to be considered, mainly due to the occurrence of several low to medium magnitude earthquakes [*Buforn et al.*, 2005; *Gaspar-Escribano et al.*, 2008]. In 1930, the recording of events began. Since then, more than 2,200 earthquakes have been registered in this area, almost 1,500 of them with magnitudes lower than M_w2.0. On the other hand, some events that occurred in the last 20 years have generated huge damage to the population and structures, like the Mula 1999, the Bullas 2002, the La Paca 2005 and the Lorca 2011 earthquakes, with magnitudes $4.7 \leq M_w \leq 5.2$ [*Buforn et al.*, 2006; *Cabañas-Rodríguez et al.*, 2011]. Such closeness in space and time led to the proposal of a link between triggering processes of several seismic series [*Benito et al.*, 2007]. This is, the occurrence of an event in a fault can trigger a second event in a neighboring fault. In addition to the pure seismic hazard, the population is located very close to the Alhama de Murcia faulting belt, increasing the possible risk of loss of lives.

3.1.2.3 Western Mediterranean: Alborán Sea and Northern Algeria

Sporadic events with magnitudes $M_w \geq 6.5$ have taken place in the Western Mediterranean region during the last half century: 1954, 1980 and 2003 in Northern Algeria, and 2004 in Northern Morocco. Their high magnitude and their emplacement near or in the Sea lead to an increase of the seismic hazard in Alborán Sea and Northern Algeria, and also in Southern Spain and Balearic Islands [*Benito et al.*, 2010]. In the West of the Strait of Gibraltar, a diffuse spatial distribution is found. On the contrary, the Eastern part presents a different configuration, according to *Stich et al.* [2006]. In Granada, very near to the coast, there have been some earthquakes at a great depth (around 600 km), being the deepest earthquakes in the Mediterranean coast region and with undecided origin [*Buforn et al.*, 2004]. *Stich et al.* [2006] demonstrate that seismicity in Alborán is consistent with nearly N-S average compression and $N240^oE$ extension. Such extension orientation is parallel to the central Betics as well as to the Alborán stretching direction.

3.1.3 Tsunami Threats

Europa's awareness of the risk associated with tsunami occurrences started to grow after the 2004 Indian Ocean tsunami [*Ribeiro et al.*, 2011]. In particular, and due to the broad coastal exposure as well as the population density and the importance of tourism infrastructure, Spain is one of the countries with a higher tsunami risk within the European continent [*Álvarez-Gómez et al.*, 2011].

Tsunami catalogues are a very relevant tool to compute the tsunami potential of a given area and to determine the risk. The use of catalogues provide the identification of the tsunami sources and the related tsunamigenic mechanism, as well as the determination of the tsunami offshore- and nearshore-propagation [*Tinti et al.*, 2001]. Despite tsunamis usually take place in seismically active regions (earthquake-generated), other possible triggering mechanisms are landslides and volcanic eruptions. However, tsunamis occur less frequently than floods, landslides or earthquakes. Hence, there are records of only a few, which is the reason they are not usually as studied as the rest of the hazards mentioned above.

The Western coast of Iberia presents a greater risk than the Mediterranean coasts of the Peninsula. This is due to the capability of the faults in the Atlantic for generating higher magnitude earthquakes and, therefore, tsunamis, in comparison to the Mediterranean. Moreover, tsunami and tide interaction can be locally relevant [*Dao and Tkalich*, 2007]. Thus, the impact of a possible tsunami on the Atlantic coastal areas of Iberia is directly related to tide amplitude at the time of the tsunami [*Lima et al.*, 2010].

3.1.3.1 Atlantic Ocean and Gulf of Cádiz

Some of the earthquakes that stroke Andalucía in the past (see Section 3.1.2) also produced a devastating tsunami that hit the coast of Iberia. The $M_w8.5$ Lisbon earthquake generated the greatest tsunami in the area up to now, causing an enormous destruction in Lisbon downtown and the city coastal village of Setúbal. There, the earthquake destroyed almost every building, and the sea inundated the city up to three times [*Ribeiro et al.*, 2011]. The waves even reached the coast of Cádiz and Huelva, causing more than 1,200 casualties in the Spanish territory. The Western coast of Morocco was also damaged, including the destruction of parts of Tangier, Rabat and Casablanca [*Renou et al.*, 2011]. According to *Carreño Herrero* [2005], the extent of generated deposition suggests that the waves were between 12 and 15 meters high. Moreover, the 1755 Lisbon earthquake does not correspond to the worst-case tsunami scenario: given the high range between spring and neap tides, the flooding related to this event could have been worse if combined with a higher tidal amplitude [*Baptista et al.*, 2011; *Matias et al.*, 2013].

Other tsunamis have been registered on the Atlantic coast of the Iberian Peninsula: *Lario et al.* [2011] have identified at least five catastrophic tsunami events generated by strong earthquakes affecting this area during the last 7000 years, with a recurrence interval between 1200 and 1500 years. The last of them was on February 28^{th}, 1969, reaching the coasts of Portugal, the Azores, Spain, Canary Islands and Morocco. It was generated by a magnitude M_w7.9 submarine earthquake, whose epicenter was located near the Azores-Gibraltar fracture zone, South of Gorringe Bank [*Renou et al.*, 2011].

The consequences related to a tsunami in Cádiz city and its Province are severely negative, although the probability of a tsunami is relatively low [*Birkmann et al.*, 2010]. The research summarized in [*Jelínek and Krausmann*, 2009] details a tsunami risk analysis applied to the city of Cádiz. It involves scope definition, tsunami risk analysis, estimation of the potential hazard consequences, and risk evaluation. This research is part of the TRANSFER project and is based on tsunami risk assessment. Figure 3.6 shows an inundation map for the Province of Cádiz, depending on the height of the incoming wave [M.Sc. Carmen María Martorell Edreira & Dr. Marina Murillo Arcila; personal communication].

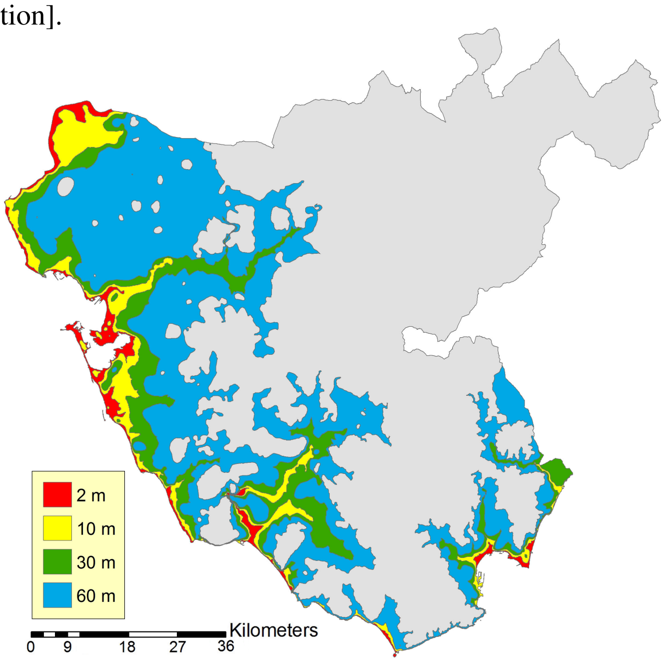

Figure 3.6: Inundation map due to a tsunami reaching Cádiz coasts. Colors depend on wave height. Figure handed over by M.Sc. Carmen María Martorell Edreira & Dr. Marina Murillo Arcila [personal communication].

The most probable areas for a tsunami nucleation are the South and Southwest coasts of the Iberian Peninsula. A wave generated there takes less than 15 minutes to reach the Portuguese Southern coast [*Ribeiro et al.*, 2011]. For the worst-case scenario, the published travel times (minutes) and wave height (meters) during high and low tides are summarized in Table 3.1. For Marqués de Pombal Fault (MPF), and Gorringe Bank Fault (GBF) correspond magnitudes of M_w8.1 and 8.2, respectively, see Figure 3.2. Also, in Chapter 8, the travel time obtained from two tsunami models (without considering tides) is listed as well, considering both best- and worst-case scenarios.

		High tide		**Low tide**	
Scenario	**Area**	**Travel time (min)**	**Wave height (m)**	**Travel time (min)**	**Wave height (m)**
MPF	Huelva	70	5.2	71	3.2
	Cádiz	70	6.5	71	4.6
GBF	Huelva	81	4.4	82	2.4
	Cádiz	80	4.9	81	3.0

Table 3.1: Computation of travel times and wave height of an incoming tsunami during high and low tide for the worst-case scenario, obtained from [*Ribeiro et al.*, 2011].

According to *Birkmann et al.* [2010] and *Álvarez-Gómez et al.* [2011], two additional faults are possible candidates for magnitude $M_w \sim 8$ events: the Horseshoe and the Portimao Bank faults.

3.1.3.2 Alborán Sea

Having the Boumerdes-Zemmouri (2003) and El Asnam (1980) earthquake-generated tsunamis as a proof of faith, it can be accepted that even moderate events can produce sea waves powerful enough to cause significant losses. Both events, with magnitudes around M_w7.3, were originated at the Northern African coast. Although the potential to generate destructive waves in the Mediterranean is lower than in the Atlantic, those past events caused serious damage. Further examples are the Djijelli event (1856), recorded in the Balearic Islands, and some tsunamis generated in the Alborán Sea during 1790, affecting Spanish and African coasts.

For the Mediterranean littoral of Iberia, as well as for the Balearic Islands, some risk assessment studies can be found in [*Tinti et al.*, 2001, 2005; *Álvarez-Gómez et al.*, 2011]. The danger on the coast of Iberia due to an earthquake-induced tsunami generated in the northern Algeria zone is directly linked to the water uplift of 1.25 m and subsidence of -0.31 m expected in the computed simulations [*Tinti et al.*, 2005].

The model for the Balearic Islands agrees with the information recorded during the May 21^{th} 2003 tsunami, with waves up to 2 m and the strongest observed effects located in Majorca and Minorca islands [*Tinti et al.*, 2005; *Herbert and Alasset*, 2003].

More recently, *Álvarez-Gómez et al.* [2011] computed a set of 22 seismic tsunamigenic sources obtaining maximum wave elevations and tsunami travel times by numerical modeling. The Alborán Sea sources only threaten the peninsular coast. On the other hand, North Algerian sources are the most dangerous to the Spanish littoral as well as to the Western Balearic Islands. There, possible run-ups of 4 meters in Formentera and Ibiza, and up to two meters locally in Majorca and Minorca islands are derived. Moreover, travel times are found to be between 30 and 45 minutes, depending on the island. This agrees with the propagation travel times calculated by *Tinti et al.* [2005]. Eastern and even Southern coasts of the Iberian Peninsula are also threatened by potential events generated in the Northern Algerian sources. They are found to be hit within 30 minutes after the earthquake nucleation and with waves locally higher than 1 meter, especially on the coast of Granada.

3.2 GNSS Networks

Permanent GPS stations provide continuous geodetic data. The data can be obtained in real-time by streaming or in near real-time from files containing 15, 30 or 60 minutes of observations available shortly after being recorded. In some cases, GPS data is only published after several hours or even days. This delivery time depends on the station and the network it belongs to. Nowadays, in the Iberian Peninsula and surroundings (Ibero-Maghrebi region), more than a hundred permanent stations installed and managed by different official organisms and private institutions exist. Most of them supply GPS observations in real or near real-time, as well as differential corrections for real-time positioning.

A geodetic network consists of a set of control points positioned in a defined reference frame. *Dong and Bock* [1989] demonstrate that, with proper network design, there is an accuracy improvement in the results for pairs of stations (baselines) hundreds of kilometers apart. Moreover, adding shorter baselines to the network improves the ability to resolve ambiguities on the longer baselines [*Zumberge et al.*, 1997]. This is, the accuracy of the computed deformation of a region strongly depends on the network geometry. Thus, to accurately monitor deformations with GPS, the design of the network is the first issue to be addressed.

The chosen GPS network should serve the main purpose in this Thesis, this is, earthquake monitoring and tsunami early warning. For the former, stations located in the direction of maximum displacement of the fault are the ones that record the biggest amplitudes [*Blewitt*, 2000]. Moreover, for a reliable magnitude determination of big events, *Ohta et al.* [2012] find that stations placed 100 km away from each other are enough, and that additional sites help only for redundancy. For the latter, the availability of GPS stations along the littoral is necessary to set a proper alert because there are no GPS buoys deployed in the western coasts of Iberia. Thus, a custom GPS network is defined for this Thesis. This network comprises many stations in the Iberian Peninsula and surroundings. They belong to ROA (Real Instituto y Observatorio de la Armada, San Fernando Naval Observatory, Spain, [*Pazos et al.*, 2010]), EUREF (Reference Frame Sub-commission for Europe, [*Bruyninx et al.*, 1996]) and IGS (International

GNSS Service, [*Dow et al.*, 2005, 2009]). They are shown in Figure 3.7, ROA in yellow circles, EUREF in red stars, IGS in blue circles. It must be pointed out that the stations selected for this study were not deployed specifically for it. The sites within the Iberian Peninsula have been chosen according to their open access and high-rate data availability. To gain stability, this compendium of stations has been complemented with several IGS and EUREF receivers placed far away from Iberia, as proposed by *Dong and Bock* [1989].

For the different aims of the test cases in this work, several regional networks are used. They are shown on the map in Figure 3.7, in green circles for the regional network in Murcia (Meristemum) used in Chapter 5 and pink squares for RAP (Red Andaluza de Posicionamiento, positioning network in Andalusia) network, utilized in Chapters 6 and 8. The regional network used in Chapter 7 is outside the area of interest in this Thesis and will be detailed in the correspondent Chapter.

3.2.1 San Fernando Naval Observatory Network

In the Geophysics Department in San Fernando Naval Observatory (ROA), geomagnetism, seismology, geodesy and meteorology are the main research topics. A geodetic network has been deployed by ROA researchers, consisting of several triangulation stations placed in South and Eastern of Spain, and Northern Africa. Most of the receivers from ROA network are co-located with accelerometers and broad-band seismic stations, in order to study the sensitivity of GPS to co-seismic displacements. A map with the stations used in this Thesis from the ROA GPS permanent network can be found in Figure 3.7, yellow circles.

The most relevant station in this network is SFER, included in EUREF network and IGS since 1996. Its oscillator is monitored by a Cesium atomic pattern from the "Sección de Hora" in ROA. 30 second RINEX data in daily packages are available publicly. ROA provides 1 Hz data in 15 minutes packages for each station specifically for this research. ROTA receiver, in Rota city, is also a very relevant GPS station because it is co-located with a mareograph. The data from this device is also available for this research with 1 Hz sampling rate.

In the tables from Appendix D, a compilation of receivers and antennas, and a list of their approximate IGS05 Cartesian coordinates from GPS stations used from ROA network are provided.

3.2.2 Andalusian Positioning Network

The Andalusian Positioning Network (Red Andaluza de Posicionamiento, RAP) is a geodetic network deployed by the Consejería de Obras Públicas y Transporte of the Junta de Andalucía, through the Andalusian Cartography Institute. The Astronomy, Geodesy and Cartography Laboratory of the University of Cádiz is responsible for the design, development, quality control and geodetic maintenance of the network. The primary objective of RAP is to provide GPS data from the stations within the network both in RINEX format for static positioning and differential corrections for real-time positioning. The RAP consists of 22 permanent stations homogeneously distributed in order to solve the positioning problem in the whole Andalusian territories, as well as in the coastline. More information about RAP can be found in [*Berrocoso et al.*, 2006]. From this network, only stations UCAD and ALGC are used in Chapter 6. In Figure 3.7, RAP stations are plotted in pink squares.

RINEX data for this network is available in http://rap.uca.es/ in three different formats: 24-hour files with 30 seconds observations; hourly files with measurements every 30 seconds; and also hourly files with 1 Hz data. The latter are utilized in this study. A list of their approximate IGS05 Cartesian coordinates, receivers and antennas are given in Appendix D.

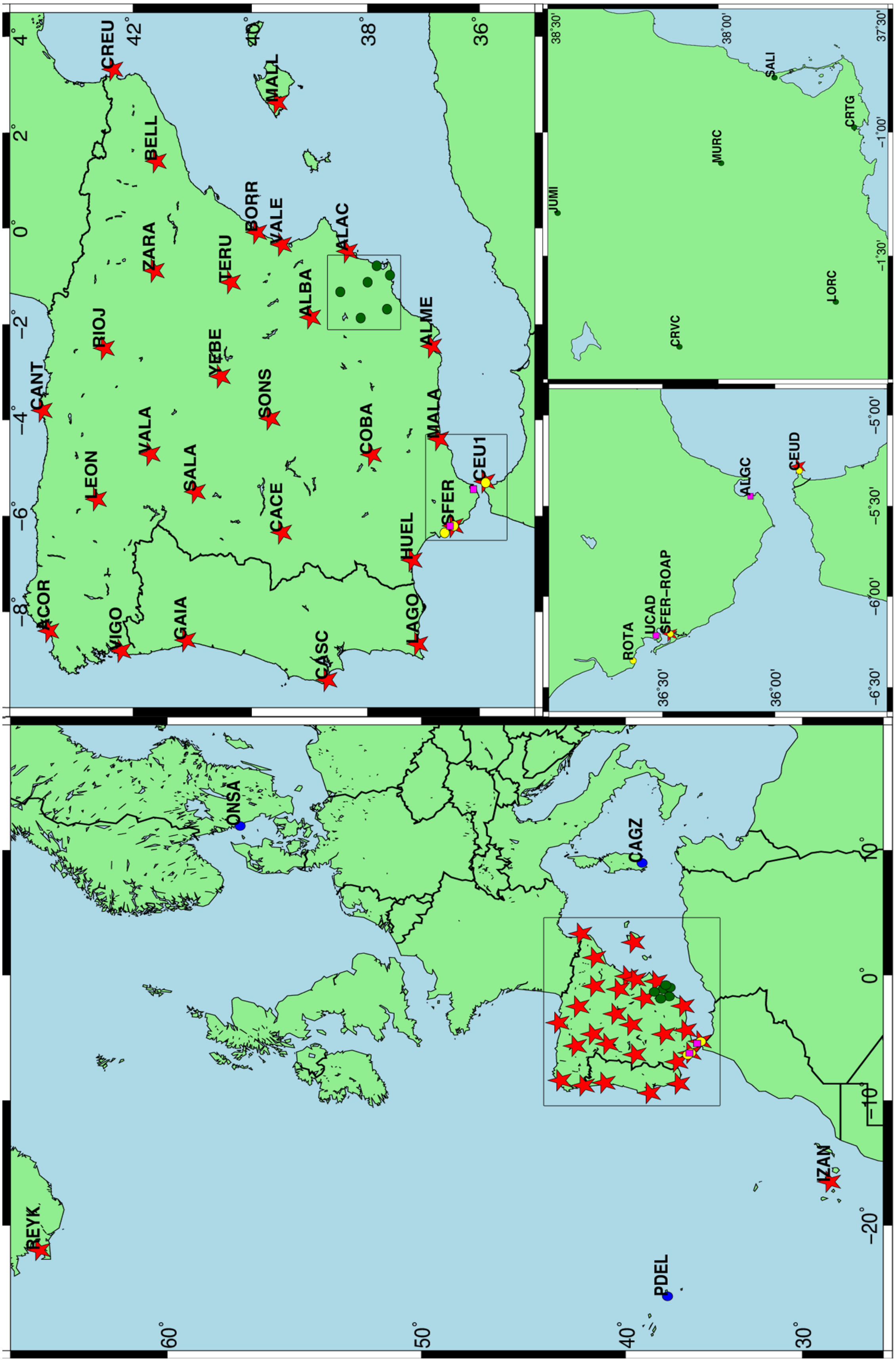

Figure 3.7: Map showing all the stations belonging to EUREF (red stars), IGS (blue dots), Meristemum (green dots), RAP (pink squares) and ROA (yellow dots) GNSS networks. A compendium of all the information about each station (name, 4-character identification, receiver and antenna types, and coordinates) can be found in Appendix D.

3.2.3 GPS Network in the Region of Murcia

Meristemum is a geodetic network for satellite tracking, developed by the Consejería de Agricultura y Agua of the Region of Murcia. It was deployed to satisfy needs arising from the environmental management: land boundary definition, public field area protection and hydrological and forest working projects elaboration. In Meristemum network, the location of each station was chosen in order to optimize available resources and coverage, accessibility and vigilance of the stations to have a control over them, and telecommunications availability to send the recorded data to the operations center. All the stations from this network are used in Chapter 5, and are plotted in green dots in Figure 3.7.

RINEX raw data and differential corrections are accessible by WEB and FTP, providing a higher precision in the positioning. Hourly RINEX data packages with 1 Hz sampling rate and daily packages of 30 seconds are available for each station in the network in their public FTP: ftp://meristemum.carm.es/. Moreover, users can also benefit from NTRIP data flow for a real-time processing.

In Appendix D, a compilation of receivers and antennas as well as a list of their approximate IGS05 Cartesian coordinates from Meristemum network GPS stations is provided.

3.2.4 IGS and EUREF Permanent Networks

Several stations from IGS (International GNSS Service) and EUREF (Reference Frame Sub Commission for Europe) networks are used to densify the coverage in the Iberian Peninsula and surroundings. The quality of the data available from such institutions is guaranteed to its correct use for scientific post-processing [*Dow et al.*, 2005].

Raw data is available by FTP from ftp://ftp.epncb.oma.be/, in packages with 15 minutes and 1 second sampling, or daily 30 seconds sampling. NTRIP data flow for most of the stations in the network is also available for real-time purposes.

See Appendix D for a compilation of receivers and antennas, as well as a list of their approximate IGS05 Cartesian coordinates, from both IGS and EUREF networks. In Figure 3.7, EUREF stations are plotted in red stars and IGS receivers in blue dots.

4 Computational Procedures. Data Analysis

The goal in this Chapter is to provide a detailed explanation of a Bernese GPS software version 5.0 processing and a posterior post-processing of its results developed here. A a step-by-step methodology for near real-time processing in a custom GPS network with receivers from IGS, EUREF and ROA (see Figure 3.7) is provided. The characterization of the different test cases developed in this Thesis will be detailed in each corresponding Chapter for each GPS subnetwork and objective.

In the first Section, an overview of Bernese 5.0 and the processing and post-processing strategy followed is given. The Bernese 5.2 software, released in December 2012, is used in one of the test cases in this work (see Chapter 7) but its setup is similar to Bernese 5.0. The post-processing of Bernese output is later detailed in Section 4.2, focusing on screening method and used filters. In the last part of this Chapter, another software (SPOTL) utilized in this Thesis is introduced to prepare the data for its use in loading computation.

4.1 Bernese Software

Bernese GPS software v. 5.0 is used to process the data from a set of stations by a DD strategy. Bernese can be customized for the user's needs thanks to its modular design. For this Thesis, the standard processing is an automatic near real-time processing using up to 34 GPS stations providing 15 minutes observation files.

Bernese Processing Engine (BPE) is a tool that runs Bernese in a fully automatic mode and has been used for the GPS data analysis. Individual scripts are set-up and processed, allowing for a much faster analysis of the data. Parallelization of some scripts also decreases the processing time. The data fed to BPE must be downloaded to the corresponding folders and pre-processed. The output is safely stored in different places to avoid overwriting.

Detailed information about the software can be found in the manual provided by *Dach et al.* [2007]. A list of the input parameters for a near real-time processing in Bernese are summarized in Table E.1. The specific Bernese setup for the test cases will be further detailed in the corresponding Chapters (5, 6, 7 and 8).

4.1.1 Data Provision

Before starting with the analysis, preparations must be made. Necessary data is obtained from the on-line services provided by different organizations. Observation files are downloaded as well as available orbit and Earth rotation parameters (ERP) data files, all automatic and on a near real-time basis:

RINEX (Receiver Independent Exchange) observation files are obtained with 15 minutes latency and 1 Hz sampling rate from the corresponding FTP servers at ROA, IGS and EUREF.

IGS Ultra-Rapid products are fetched from [ftp://cddis.gsfc.nasa.gov/gps/products/WWWW], where WWWW refers to the corresponding GPSWeek. Orbits and ERP files are automatically downloaded every 6 hours, at 04:07, 10:07, 16:07 and 22:07. It must be pointed out that minute 07 has not been chosen randomly: this way it is unlikely that, for a daily near real-time continuous processing, the main process is overlapped. This is because the main process is set up to begin every 15 minutes starting in the minute 10 of each hour, and takes around 10 minutes to finish (see Section 4.1.3.2).

From CODE database [ftp://ftp.unibe.ch/aiub/CODE], ionospheric information for each day is also downloaded.

4.1.2 Data Evaluation and Documentation

Evaluation strategy and observation interval, as well as the reference station selection, must be verified for the process. Once achieved, two steps are needed in order to determine sub-daily movement for each receiver. First, static coordinates are estimated, using atmospheric parameters and fixing ambiguities, see Section 1.2. After that, the kinematic analysis is performed. In the end, a Perl script stores the estimated kinematic (cartesian and ellipsoidal) coordinates and residuals with respect to the initial coordinate into a plain text file for each station for the further processing.

Every 15 minutes, a file is downloaded for each station, containing 1 Hz GPS observations for the last 15 minutes. Such measurements files in RINEX format are aggregated into 6 hour packs, because it is mandatory to process more than 6 hours of data in order to obtain a suitable ambiguity resolution [*Dach et al.*, 2007]. No more than 6 hours is advised for this number of stations and the current strategy and machine in use because running the whole process must take less than 15 minutes to avoid overlapping with the following execution. This number has been obtained after testing several options, looking for the best ratio ambiguity resolution/time consumed. The aforementioned packages are then transformed into Bernese binary format. After that, clocks are synchronized with GPS time and approximated station coordinates are calculated using zero-difference measurements. Polar motion information is transformed into Bernese format. Orbital data also needs to be processed before its information is integrated into the subsequent steps, generating tabular orbits and clock files. Tabular orbits are combined with the pole motion data, obtaining the so-called standard orbits. In the following step, single-difference baselines are formed. Optimal results, in terms of resolved ambiguity ratio, are reached when baselines are defined by the maximum number of observations between two stations[3] (OBS-MAX[4]). This procedure of single differencing eliminates the satellite clock error terms in the model. Tropospheric and ionospheric effects are also reduced through single differencing, especially for those stations close to each other. The last step in preprocessing consists of searching and correcting for cycle slips. Finding cycle slips formed during single differencing allows further determination or even the elimination of ambiguities. In addition to the data cleaning process, this step can be used to determine a first coordinate solution without fixing ambiguities.

In order to obtain kinematic coordinates, good static coordinates must be estimated first, as well as troposphere parameters. In the main processing part, residuals in the observations (Section 1.4) based on Double Differences are estimated according to the standard proceeding, as explained in Bernese 5.0 manual, pages 172-183 [*Dach et al.*, 2007]. In this step, an ionosphere-free linear combination (L3) is used. With this combination, the ionospheric path delay is cancelled, because of the linear combination using zero- (L1, 1.2) and double-difference (L2, Equations 1.2) phase observables. Inconsistent observations are marked so that they are not used in further processing. This is, a first order ionosphere-free equation is formed with unknown ambiguities. Later, ambiguities are fixed. The resolution strategy depends on the length of the baseline considered: Short-Lane strategy for baselines up to 50 km, Widelane-Narrowlane (WL-NL) for baselines from 50 to 200 km and Quasi-Ionosphere-Free (QIF) for baselines longer than 200 km. For each session, the static solution is found after solving the ambiguities in the phase observations (see Equations 1.5). Such ambiguities are applied later for the calculation of kinematic coordinates from the last 15 minutes. Troposphere parameters are also required for the kinematic processing, so they are estimated as well.

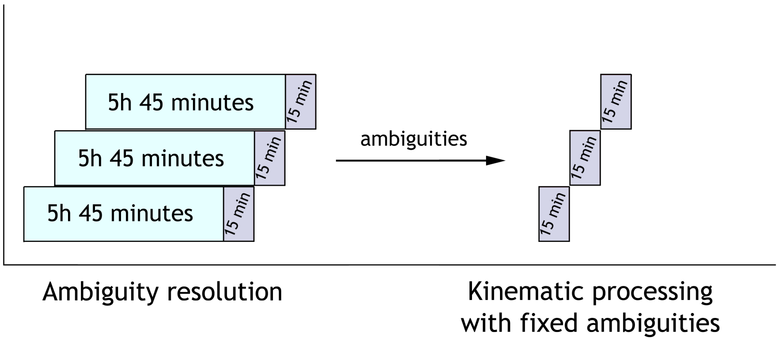

Figure 4.1: Scheme for the 6 hours Bernese processing. First, ambiguities are resolved in a 6 hours processing. Ambiguities are extracted from the 6 hours and fixed for the last 15 minutes, from which and a kinematic time series is computed.

Finally, a 1 Hz kinematic processing is carried out for the last 15 minutes dataset and one of the stations in each selected baseline. By convenience, the receiver considered as fixed is the first in the baseline, and the

---

[3] Sometimes it is necessary to fix baselines in order to obtain specific results. This will be explained in Section 5.5.

[4] Other strategies, like STAR, are used in this Thesis, see Section 6.3. STAR baseline selection uses one defined station as the center and connects the rest of the stations in the network to it.

second is treated as kinematic. The evaluation is performed as an ionosphere-free combination with fixed (known) ambiguities. If baselines are short, tropospheric parameters are very similar for each station in the baseline, but for longer baselines, such parameters must be considered. They are taken from the last 6 hours of output data. Resulting kinematic coordinates are saved for further analysis. The whole procedure is summarized in Figure 4.1.

In the Chapters where an a posteriori analysis is indicated, a similar procedure to the previous is followed, with a small modification: 15 minutes GPS data are aggregated into daily packages, ambiguities are fixed for the whole period and later 1 Hz kinematic coordinates are estimated for the same whole day.

4.1.3 Automated Processing by Bernese Processing Engine

GPS receivers are prepared to measure a vast amount of data during surveys that can last weeks or months, and also from continuous observations. Such volume of data clearly demands an automated analysis. Bernese software can execute all possible tasks in batch mode, using parallel processing where feasible. Its evaluation procedure can be defined by the so-called "Process Control Files". In this Section, the procedure for a continuous processing of a network of 34 stations is detailed. Kinematic coordinates are estimated every 15 minutes for the last 15 minutes data available, by using the observations from the previous 6 hours.

4.1.3.1 Parallelization

The objective of parallelization is shortening the duration of the processing. Subprograms related to baseline or single station processing run once for each baseline or station, so if they run in parallel the processing time highly decreases. Hence, as long as the computer has more than one core, parallelization allows running one baseline or station in each computer core, without overlapping.

Time saved by parallelizing depends on the number of stations to be processed and the number of cores available. The machine used in this analysis has two processors and eight cores. Ambiguity resolution subprogram parallelization reduces up to 7 minutes out of 10. The rest of the subprograms parallelized (aggregate 15-minutes files into 6-hours packs, transformation into Bernese format, clock synchronization and search and erase cycle slips after single-differencing) save around one minute each. Therefore, after parallelization the processing time is shortened by almost the half, from 23 to 12 minutes.

4.1.3.2 Timeline

- Minute 0-15: GPS receivers record the data.
- Minute 15-25: The agencies that own the data (EUREF, IGS, ROA) change the format, compress the datasets and upload them to an FTP server.
- Minute 25: A script is launched to download the data files. They are uncompressed and stored in the designated folder for the campaign.
- Minute 26-37: The data files are processed, and the kinematic coordinates of the selected stations are derived.
- Minute 38-39: Data is screened and filtered when necessary.
- Minute 40: Results are stored for the selected stations.

4.1.3.3 Date Change

Bernese standard session is 24 hours; in this case, a non-standard session of a 6 hours sliding window needs some boundaries. To process a timespan of 6 hours belonging to two consecutive days, some considerations must be taken into account and the change of date must be handled carefully. To solve it, the *Session Table* in Bernese needs to be forced to consider data from two different days. Also, orbits, ERP and ionosphere files must be prepared for the change of the day. This is done by concatenating the old with the new ones that are uploaded every six hours in case of IGS Ultra-Rapid products, or daily in case of ionosphere files.

4.2 Preparation of the Kinematic Coordinates Time Series

From now on, the residuals from the ellipsoidal coordinates estimated during a Bernese kinematic procedure are going to be used. They will be simply referred as kinematic time series.

Kinematic time series need to be screened and adjusted. Outliers are eliminated when possible, according to a maximum allowable dispersion estimator (3-sigma screening). The gaps in the remaining data are filled in with an interpolation of the surrounding data. Finally, the data is filtered. For near real-time results, a Sidereal Filter (SF) is applied to the data in order to eliminate periodicities. For some applications where periodicities are of interest, an exponential moving average filter is chosen to smooth the data instead of a SF. It is important to remark that smoothing data for earthquake detection must be done carefully to not to attenuate the signal. The application of a Regional Filter (RF, see [*Mendoza et al.*, 2012]) is not necessary because it eliminates regional common biases in a set of stations, and double-differencing during the Bernese processing also cancels such errors.

4.2.1 Residual Screening

Time series built directly from Bernese output are made of by the so-called *residuals*. As it was already mentioned in Section 1.4, a residual is the difference between the reference coordinate and the obtained coordinate after the data processing. Residual time series sometimes have outliers, some of them over tens of centimeters. Such large residuals lead to great uncertainties and errors. Therefore, they must be removed.

In order to eliminate outliers, a simple approach consists of finding epochs with very large residuals, as applied by *Nikolaidis et al.* [2001] for example. A possible alternative consists of using the kinematic coordinate file and the residuals Root Mean Square (RMS): timespans with excessively large residuals can be found by screening the data's RMS. The problem arising is that, when the mean value of the data is not close to zero, a rejection method based in RMS can eliminate valuable data. Therefore, the dispersion estimator Sigma, this is, the empirical standard deviation S_N, is of interest and a 3IQR[5] screening method is therefore utilized. Eliminating results outside 3IQR is a very common screening method: values outside [mean - $3 \cdot S_N$, mean + $3 \cdot S_N$] are considered outliers [*Nikolaidis et al.*, 2001]. It is important to remark that this procedure is not always advisable because non-constant and sudden effects can be canceled by the application of this screening method. A clear example is the loading due to a storm surge, see Chapter 7.

4.2.2 Sidereal and Modified Sidereal Filters

Multipath is a site-dependent systematic error at seismic frequencies and is elevation angle dependent. It can be related to the location of the antenna with respect to reflecting surfaces. This particular error is not modeled in Bernese. Therefore, the baseline estimates can be corrupted by a station with significant multipath problems, particularly in height [*Elosegui et al.*, 1995]. It is attenuated by using GPS observations above a cutoff angle. For this Thesis, the cutoff angle is set to 7-degree elevation.

GPS multipath occurs when the signal reaches an antenna not along the direct path. For example, it can arrive by reflections from nearby objects. Then occurs a superposition of the direct and reflected signal. The signal reflected has a longer path length than a direct signal, influencing the measurements and introducing errors which propagate to the final solution [*Choi et al.*, 2004]. See Figure 4.2: for an infinite horizontal reflector such as the ground (shaded) the relevant parameters are the height (h) of the antenna above the ground and the satellite elevation angle (θ). These can be related to the additional path length (grey arrows) of a reflected signal.

The geometry of the GPS satellite constellation is designed to repeat exactly after half a sidereal day, as this corresponds to their orbital period. However, in practice, it deviates slightly for the different satellites. For a

---

[5] 3 times Interquartile Range, being the interquartile range the difference between its 75th and 25th percentiles.

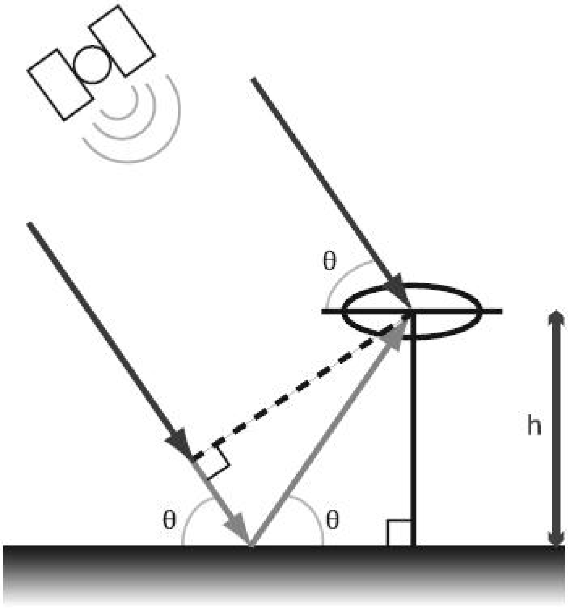

Figure 4.2: Multipath geometry for a classical GPS monument. Figure obtained from [*Larson et al.*, 2007].

point on the Earth, satellites visible in the sky at a given moment should be visible in the exact same direction 23 h 56 m 4 s, a sidereal day, later. Over such period, the Earth would experience one revolution, and the satellites would have completed exactly two revolutions in their orbits in inertial space. This brings everything back to the same geometry.

The position of the observed GPS satellite is responsible for the incoming signal direction. It implies that the signal will reflect surfaces in the same way every time the satellite occupies the same position and the level of interference depends on the reflective properties of the surface and its distance from the antenna. This is, the reflections occur at the same epoch every time that the geometry of the constellation is repeated. In fact, each GPS satellite has a distinct orbit repeat period that itself varies approximately 8 s throughout the year. Furthermore, satellites being maneuvered can differ from the sidereal orbit repeat period by over 100 s. The filter that takes advantage of the simple day-to-day highly repeatable error source is called sidereal filter (SF) and was first suggested by *Bock* [1991] and *Genrich and Bock* [1992].

It was just pointed out that each satellite has a different orbit repeat period. So a modification to this filter was proposed: the so-called modified sidereal filter (MSF) [*Larson et al.*, 2007; *Larson*, 2009]. A MSF is based on the period of the satellite constellation or Aspect Repeat Time (ART) [*Agnew and Larson*, 2007]. ART is the time the satellite needs in an Earth-fixed reference frame to return to a position of minimal distance to the starting point, i.e., same azimuth and elevation. ART varies for each satellite and each station, so a software called ASPREP [*Agnew and Larson*, 2007] is used to calculate each satellite repetition rate seen in each station. A mean of each satellite's repetition rate is estimated and, finally, satellite constellation period is calculated as the arithmetic mean of the individual satellite periods rounded to an integer number of seconds.

A MSF cannot be applied under near real-time conditions because the ASPREP program is based on precise orbits made available only 12 days after the observation took place [*Agnew and Larson*, 2007]. Despite the S_N of the results after applying a MSF is better, the difference to a classical SF is small [*Choi et al.*, 2004]. Thus, for near real-time processing, only a sidereal filter is implemented. For data processed a posteriori, MSF can be utilized.

A near real-time SF is applied considering the data from the last three processed days, schematically shown in Figure 4.3. The filter for one station is based on its position time series for the previous three sidereal days. First, the last epoch of the time series is considered as the end of a sidereal day span. Three epochs in intervals of integer multiples of a sidereal day ($(t-n\cdot T)$, where T=23h 56min 4s) are searched. These corresponding

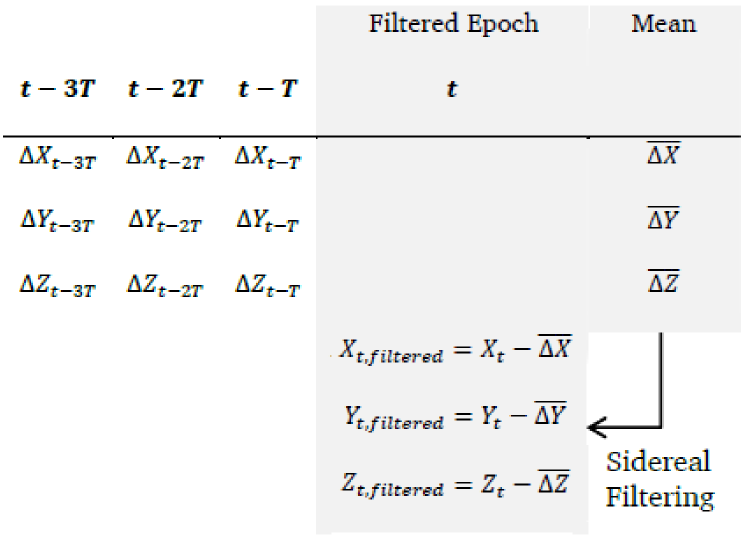

Figure 4.3: Scheme of a Sidereal Filter for one station and one epoch in near real-time.

epochs' residuals are arithmetically averaged and subtracted from the epoch t value. It is important to remark that the days that have less than 85% of the observations (73239 observations or less) are not included in the filter. The scheme for a MSF is similar, fixing T as the mean value of the repetition rate.

4.2.3 Exponentially Weighted Moving Average Filter

As stated before, a sidereal or modified sidereal filter cancels systematic errors that repeat every sidereal day. Sometimes, periodical effects are the goal to be analyzed, so they must not be eliminated. Therefore, neither a SF nor a MSF should be applied (see Chapter 6 for example).

A multipoint boxcar filter is one of many filters used for GPS results without eliminating common-mode errors, as applied by *Bilich* [2006] for example. This strategy averages together a series of points (epochs) and their mean value is assigned to the center point of the window. The main disadvantage of such a filter for a near real-time application is that the last seconds of the time series are impossible to filter: the bigger the interval, the more seconds left unfiltered. The advantage is that high frequencies are removed and, although computationally intensive for high-rate data, no phase shift is introduced. However, a multipoint boxcar filter application to a time series where gaps are present leads to an output filtered time series with the same gaps.

Therefore, a different moving average filter is applied, in order to fill in the gaps obtained after data screening as well as filter the data. It uses the so-called Exponential or Poisson window [*Gade and Herlufsen*, 2013], which increases exponentially towards the center of the window and decreases exponentially in the second half. A simplification of the function that defines the window implemented in this filter is as follows:

$$f(t) = e^{-\left|\frac{t-t_0}{t_c}\right|} \tag{4.1}$$

where t_0 is the point to filter and t_c is the so-called characteristic time. This latter value indicates the decrease ratio of the exponential function, as can be seen in Figure 4.4.

The values of the limits in the windows are non-zero because the exponential function never reaches zero. In order to produce a finite filter, this exponential function is multiplied by a rectangular window. Then, the weighting for each point decreases exponentially with distance, until the edges of the window. This means that the importance (weight) of the points in the filter is bigger the nearer to the point to filter, and decreases exponentially according to their relative distance. Usually, data outside three times t_c is considered negligible. Therefore, it is advised

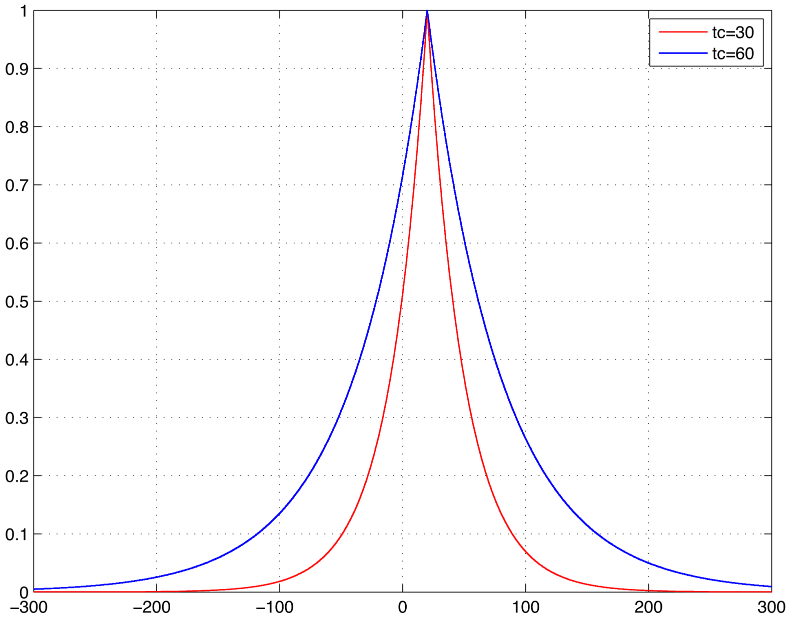

Figure 4.4: Exponential or Poisson function for two different values of t$_c$.

to set the window length above such value. This filter is called Exponentially Weighted Moving Average Filter (EWMA).

So as to set up a sensitive characteristic time, a visual comparison of different values is shown in Figure 4.5. For the first five hours of DOY 269 of 2011 in station ROTA, a gap of 15 minutes is introduced. Data is filtered in three different ways: filters with t$_c$=200, 400 and 600 seconds, and respective window lengths of 600, 1200 and 1800 seconds. The behaviour of the filtered data when there is no gap is almost identical. For unavailable data (gaps) it is clear that the bigger the characteristic time (and thus window length), the smoother the jump.

According to Figure 4.5, a characteristic time of 600 seconds is chosen. It provides a sufficient smoothness and the computation time is not excessive, up to a minute when using a 1800 points (seconds) window.

In addition to the setup of the weighted moving average filter, the reductions in S_N are detailed in Table 4.1 for stations ALGC and UCAD on DOY 78 and 79 of year 2011, respectively. The time series considered are corrected from OTL-related effects. The improvement in S_N is clear after filtering for both stations. S_N reduction rises with the increase in t$_c$ and window length, and seems to be close to its limit for a characteristic time of 600 seconds and a window length of 1800 seconds.

The visual comparison of the obtained results in Table 4.1 for UCAD corrected by OTL on DOY 79 of 2011, for characteristic times of 25, 50, 100, 200, 400, 600 and 900 seconds and window lengths of 3 times the characteristic time (3·t$_c$), are presented in Figures F.1, F.2 and F.3. In addition, to (visually) check the performance of the filter, the stations that were processed without ocean loading corrections are filtered as well. ROTA station is shown as the example, for days from 262 to 277 of year 2011. A window length of 1800 seconds is set here, and different characteristic times are applied: 25, 50, 100, 200, 400, 600 and 900 seconds. Figure 4.6 shows vertical GPS data time series, raw and filtered. North and East components are displayed in Figures F.4 and F.5.

The attenuation of the signal noise is very distinctive, and the elimination of high-frequency components is seen clearly. If the filter is correctly applied, there should be no bias between the raw and filtered signals, and the gaps in the raw data are filled with new information that follows the nearby data trend. Note that some authors, like *Langbein and Bock* [2004], use linear interpolation for gap filling. The goodness of this filter will be confirmed by Figure 6.6, where a fast Fourier transform is applied to the filtered data from ROTA on DOY 265 to 271 of 2011. Raw data is plotted, compared with a window length of 300, 1800 and 2700 seconds filtered data and a fixed

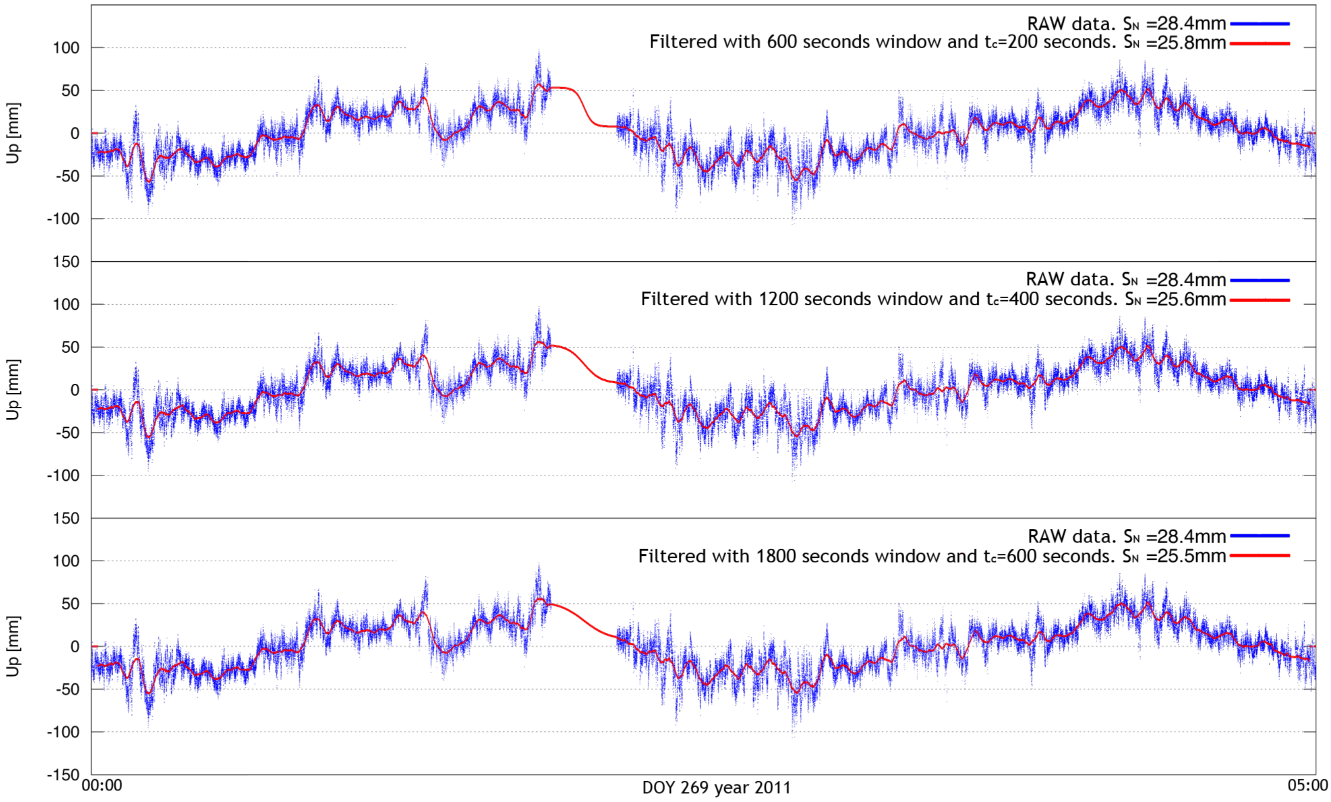

Figure 4.5: Data before (RAW) and after filtering using different characteristic times and 3·t_c seconds window lengths. Station ROTA, height component. DOY 269 year 2011. Empirical standard deviation (S_N) also shown.

ALGC **DOY 78**	**Raw**	**t_c=25 s** **w=75 s**	**t_c=50 s** **w=150 s**	**t_c=100 s** **w=300 s**	**t_c=200 s** **w=600 s**	**t_c=400 s** **w=1200 s**	**t_c=600 s** **w=1800 s**	**t_c=900 s** **w=2700 s**
S_N**N (mm)**	5.1	4.8	4.7	4.6	4.3	4.3	3.8	3.7
S_N**E (mm)**	5.5	5.1	4.9	4.5	3.8	3.6	2.8	2.8
S_N**U (mm)**	10.8	9.7	9.2	8.9	8.6	8.5	8.1	7.9
UCAD **DOY 79**	**Raw**	**t_c=25 s** **w=75 s**	**t_c=50 s** **w=150 s**	**t_c=100 s** **w=300 s**	**t_c=200 s** **w=600 s**	**t_c=400 s** **w=1200 s**	**t_c=600 s** **w=1800 s**	**t_c=900 s** **w=2700 s**
S_N**N (mm)**	8.4	5.1	4.3	4.1	3.7	3.6	3.3	3.3
S_N**E (mm)**	5.8	3.6	3.0	2.9	2.6	2.5	2.2	2.1
S_N**U (mm)**	13.4	11.9	11.5	11.4	11.1	10.9	10.6	10.5

Table 4.1: Empirical standard deviation (S_N) reduction after using different characteristic times (t_c) for a filter with a window length (w) of 3·t_c seconds. ALGC and UCAD stations, DOY 78 and 79 of year 2011, respectively.

characteristic time of 600 seconds. The elimination of the highest frequencies is clear, and the amplitude of the signal is almost unchanged for the filters with 300 and 1800 seconds windows. Using a 300 seconds window is not advisable, some of the data outside the window is not negligible. A 2700 seconds window length filter is neither the best option, amplitude is reduced by >10% (peak-to-peak amplitude in the vertical component), processing time is doubled and the reduction in S_N is not much higher than for a 1800 seconds window.

According to the results presented before, the optimal choice for an EWMA filter has a window of 1800 seconds and a characteristic time of 600 seconds. It gives a sufficient empirical standard deviation reduction (see Table 4.1) and almost does not decrease the amplitude in the signal, as can be seen in Figure 4.6 for vertical component and F.1 and F.2 for North and East components, respectively.

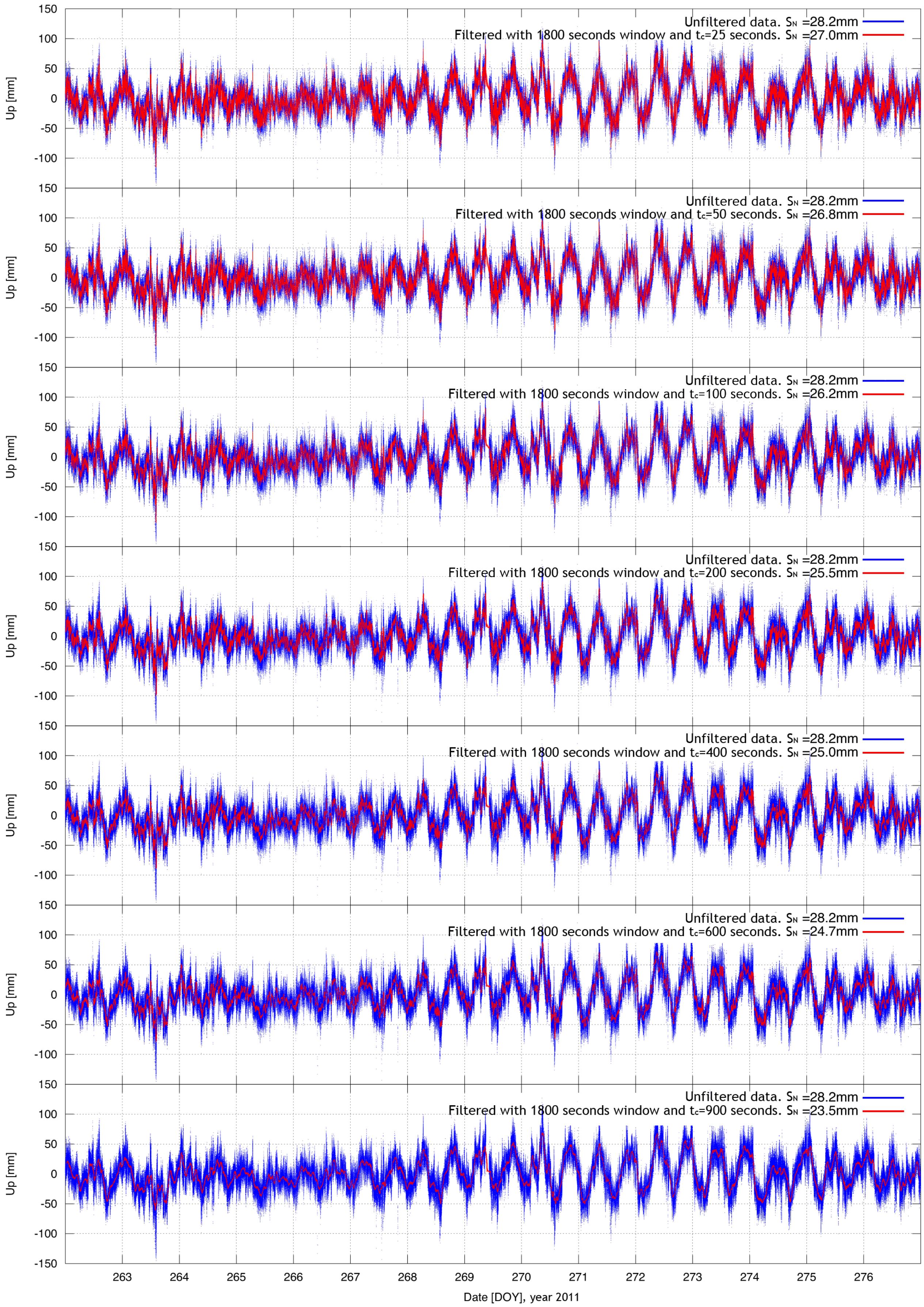

Figure 4.6: Different characteristic times for the EWMA filter with a window length of 1800 seconds. Station ROTA, vertical component not corrected by OTL. DOY 262-277, 2011. t_c = 25, 50, 100, 200, 400, 600 and 900 seconds.

A common concern when applying a filter is the processing time, but for an a posteriori data processing, this is not a burden. For the purposes addressed in this study, the size of the sliding window used for the filter needs to be taken into account. This is, for example, a 30 minute (1800 seconds) filter would use 15 minutes of data before and after the epoch to filter. Therefore, for applying it to the data in near real-time, which comes every 15 minutes and contains 15 minutes of data, this last processed data would not be filtered until the following run. This could be solved by using data only before the epoch to filter, shortening the second half of the window while arriving at the limiting epoch. However, this approach also has a severe shortcoming: using only data before big gaps can lead to false results, as a downwards trend in the last 15 minutes does not necessary mean a downwards movement in the following missing 15 minutes. Thus, this filter is only advisable for small data gaps and a processing not in near real-time.

4.3 SPOTL

SPOTL (Some Programs for Ocean Tidal Loading) package [*Agnew*, 2013] is, as its name indicates, a set of programs related to Ocean Tide Loading computation. It uses an integration mesh consisting of concentric rings around the point considered, with width and number of subdivisions depending on the distance from the site. In particular, given an ocean tidal model, SPOTL can compute in any location the effects produced by the load tides, i.e., gravity, induced potential, displacement, tilt and strain load tides. SPOTL is also able to predict tides from harmonic constituents.

SPOTL is used in this Thesis to obtain the vertical displacement that a given GPS site would undergo, depending on the water mass load in its surroundings. In particular, SPOTL is used to estimate the vertical subsidence a GPS station would experience if a tsunami of fixed characteristics was approaching to it. In Chapter 7, the subsidence computed by SPOTL from selected models that predict real water conditions are compared to GPS estimated vertical motion to validate the latter. Later, in Chapter 8, some tsunami models are processed by SPOTL to compute the expected vertical subsidence.

4.3.1 Input Preparation and Subprograms Used

NLOADF [*Agnew*, 1997] is a subprogram from SPOTL that calculates ocean loadings at a site. It needs the coordinates of the site to be considered (latitude, longitude, height), the ocean tide model selected and a specification of the distribution of land and sea in the area that the model covers. It also needs the loading functions for the deformation of the Earth's surface, called Green Functions [*Farrell*, 1972]. NLOADF uses a polar grid centered on the site with grid dimensions increasing with distance from the center. It outputs gravity, induced potential, displacement, tilt and strain load tides.

The models to be fed to SPOTL must be reshaped into SPOTL format conventions and then converted to binary format and stored in the corresponding folder. The conventions for the format can be found in the SPOTL manual [*Agnew*, 2013]. In order to compute a certain area of vertical subsidence, a custom script is run calling NLOADF for all the points in a grid.

The SPOTL land-sea mask has a 1/64 degree resolution, approximately 1.7 km at the equator. NLOADF uses Green functions to estimate the load. The Green functions chosen in this case for the Earth model are the "Gutenberg-Bullen Model A average Earth", computed and tabulated by *Farrell* [1972]. For these Green functions, NLOADF calculates the load only on points marked as sea in the land-sea mask. However, it can be forced to calculate the load also in points that correspond to land. This way, NLOADF can estimate the subsidence related to a particular flooding if water height data is available.

The selected Green functions have a resolution depending on the radial distance to the point where the load is to be computed. From the point to a radius of 0.02 degrees, 95 subintervals are considered, spaced by 0.0002 degrees. From 0.02 deg to 0.05, there are 30 subintervals spaced 0.001 degrees. From 0.5 to 1 degree far from the point, the 95 subintervals are spaced 0.01 degrees. From 1 to 10 degrees, 90 subintervals are defined, spaced 0.1 degrees. From 10 to 90 degrees away from the point, the spacing of the 160 subintervals is of 0.5 degrees. And from 90 to 180 degrees away from the point, the 90 subintervals are spaced 1 degree. Each subinterval is divided into sections, defined by the following *adaptative* equation:

$$max(150, 360 \cdot sin\psi) \tag{4.2}$$

where ψ is the spherical distance in radians.

This is, the closer the subinterval to the point where the load is to be computed, the smaller the sections it is divided into. The minimum of divisions is 150, and the maximum corresponds to the last subinterval, which is divided into 360 sections.

4.3.2 Used Models

SPOTL pre-defines several ocean tide models, both local and global, like the global FES2004 model [*Lyard et al.*, 2006]. FES2004 is also used by Bernese to correct GPS time series, and OTL from FES2004 will be used in Chapter 6. Also, different ocean model can be introduced to SPOTL. In this Thesis, the used water height models depend on the aim of each test case.

In Chapter 7, three surge models are used. First, two model simulations of water heights are considered. The first is the ocean model BSHcmod (hereafter called DWD/BSH), the regional operational numerical circulation model of the German Federal Maritime and Hydrographic Agency (BSH) [*Dick et al.*, 2001]. It is driven by the meteorological models GME and COSMO-EU of the German weather service (DWD). Its output is the predicted sea level. The surge is computed by subtracting from the model output the tide predicted by BSH. Wind speed data from COSMO-EU/DWD and wave height data from the Local Wave Model (LSM, hereafter DWD/BSH) are used, the latter also driven by the DWD winds [*Behrens and Schrader*, 1994]. The second model (hereafter ECMWF/JRC) is the JRC Storm Surge Calculation System, called Hyflux2 [*Probst and Franchello*, 2012]. It uses meteorological forecasts produced by the European Centre for Medium-Range Weather Forecasts (ECMWF) to estimate with a 3-day lead-time potential storm surges due to cyclones or general storm events. Wind speed data from ECMWF, six-hourly surface pressure and wind speed data from the NOAA/NCEP Global Forecast System (GFS) model and from the ECMWF Interim Reanalysis model (ERA Interim), and sea wave height data from ERA Interim, are used as well. The third surge model is obtained by a simulation using the DWD COSMO-EU wind field as forcing for the JRC code HyFlux2 (hereafter DWD/JRC).

The three models show the surge of the seawater during a storm generated by Cyclone Xaver in December 2013 in northern Germany, and are available with a 15 minutes (DWD/BSH) and 60 minutes (DWD/JRC, ECMWF/JRC) sampling. DWD/JRC and ECMWF/JRC models have a spatial resolution of 0.033 degrees (3.7 km). They cover an area from 48.5166 to 62.983 degrees Latitude and from -12.8833 to 24.9833 degrees Longitude. For DWD/BSH model, the spacing is of 0.05 deg in Latitude and 0.08 deg in Longitude, corresponding to 5.56 and 9.26 km, respectively. This model covers an area from 48.575 to 65.875 degrees Latitude and -4.0417 to 30.375 degrees Longitude. The three models were reshaped to cover a region from 49 to 62 degrees Latitude and from -3 to 15 degrees Longitude.

In Chapter 8 several tsunami models are used:

A worst- and best-case scenarios representative of the SW Iberian coast were kindly handed over by M.Sc. Ricardo Tavares da Costa [personal communication]. They include the Gulf of Cádiz and the West of the Strait of Gibraltar, with models adopted from the Joint Research Centre of the European Commission [*Annunziato*, 2007]. The mesh resolution goes from 60 arc-seconds in the open ocean (0.017^o, about 1.8 Km) to 15 arc-seconds close to the coast (0.004^o, about 0.46 Km). For each scenario, a tsunami surge model is given for every two minutes in the 3 hours after the earthquake origin. The best-case scenario corresponds to a quake generated in the MPF with epicenter in [36.895, -10.067] and a $M_w 8.5$ magnitude, as computed by *Lima et al.* [2010]. The worst-case scenario is a multi-fault scenario, including two epicenters in two different faults, HSF and MPB, as computed by *Matias et al.* [2013]. The epicenter coordinates are [35.796, -9.913] and [36.574, -9.890] respectively, and both have the same magnitude, M_w8.6. These models cover the area between 39 and 33 degrees latitude and between -6 and 12 degrees longitude. The unstructured grid was transformed into a mesh with 1201x1201 points, this is, 0.005^o spacing (about 0.55 Km).

Also, several tsunami models for the maximum credible earthquake, or worst-case scenario, comprising only the city of Cádiz and surroundings were handed over by Prof. Mauricio González and Prof. Luis Otero, from the University of Cantabria [personal communication]. Such models were created for the TRANSFER project [*UCA and IGN*, 2009] in order to study the effect of a possible tsunami in the Western part of Andalucía in terms of personal and economic losses, and is focused on the risk related to flooding. The models show the state of the sea at the point where the highest values are found near the city of Cádiz and surroundings. Each model corresponds to the different tsunami source zones: GBF (Gorringe Bank Fault, M_w8.2), HSF (Horseshoe Fault, M_w8.3), MPF (Marqués de Pombal Fault, M_w8.1), PBF (Portimao Bank Fault, M_w8.0) and CWF (Cádiz Wedge Fault, M_w8.6) (see Section 3.1.3.1). The models only comprise a small area, 36.37355 to 36.64105 deg Latitude and -6.40696 to -6.11946 deg Longitude (536x576 points). Opposite to the best- and worst- case models introduced in the previous paragraph, these models include the astronomical tide corresponding to the mean equinoctial high tide. It is of 3.55 meters in the harbor of Cádiz [Moreno, S. personal communication], and this value is subtracted from the models thus only the surge is considered for further studies.

4.4 Error Assessment

In the last decades, many advances in modeling errors influencing the GPS signal have been made. Tropospheric [*Niell*, 1996] and ionospheric [*Kedar et al.*, 2003] delays, antenna phase center variation [*Schmid et al.*, 2005] as well as reference frame [*Altamimi et al.*, 2002; *IERS Technical Note n. 36*, 2010a] affect the position determination. The processing strategy developed in this study is based on the relative position between stations and focused on the difference between consecutive residuals. Hence, the last error source listed does not affect the main aim in this Thesis. Nonetheless, for the test case in Chapter 7, the accuracy in the reference coordinates is of utmost importance.

The Bernese software [*Dach et al.*, 2007] corrects GPS coordinates for different effects through modeling of site displacements. Tectonic plate motion, or propagation of site coordinates by velocities, deforms networks and affects IGS satellite orbits consistency. Solid Earth, pole and permanent tides are also corrected for. Ocean tidal loading effects deform the crust by the changing mass distribution due to ocean tides (ocean tidal loading). Vertical and horizontal OTL corrections are applied in the processing, based on FES2004 tide model. Other effects causing site displacements, like atmospheric loading, non-tidal ocean loading, post-glacial rebound or varying ground water levels are not corrected by Bernese GPS Software Version 5.0. This is because either they are rather small, change position very slowly or no conventional models are available. Nevertheless, these effects are above the noise level thus measurable with GNSS. Note that Bernese GNSS Software Version 5.2 includes the possibility to correct data by atmospheric loading.

Tropospheric and ionospheric errors are addressed within Bernese processing. Tropospheric delay is estimated by wet-Niell model, ionosphere-free observable combination is directly used within processing strategy, eliminating to the first order. Also, antenna phase center variations are handled within Bernese by using the PCV (antenna phase center variation) correction tables [*Dach et al.*, 2007].

After incorporating satellite orbits and Earth rotation parameters, some terms of the observable equations remain, e.g. satellite and receiver clocks, multipath, receiver noise and integer phase ambiguity. Both satellite and receiver clocks are eliminated by double differencing, and integer phase ambiguities are solved by Bernese [*Dach et al.*, 2007].

Thus, it can be stated that all the aforementioned errors are eliminated or reduced in the Bernese computation. The biggest error source that remains is multipath. Multipath-based errors are first reduced within Bernese by only using observations above 7 degrees elevation, and afterwards corrected or smoothed through a Sidereal or a Modified Sidereal Filter, where admissible, resulting in a lower noise floor and less structured noise characteristics

[*Bilich*, 2006]. For example, a MSF reduces noise in approximately 50, 45 and 30% in empirical standard deviation (North, East, Vertical) for Lorca, see Section 5.3.4.

Although it has not been analyzed for a real tsunami, the noise and empirical standard deviation reduction has been estimated for the 2011 Lorca earthquake in Chapter 5. For a real tsunami, a MSF does not eliminate a tsunami imprint in the GPS time series because tsunamis are not a repeating signal.

When the application of a MSF is not possible, an exponentially weighted moving average filter (with a 1800 second window and 600 seconds characteristic time) can be applied. The noise in empirical standard deviation is reduced by approximately 55, 60 and 20% (North, East, Vertical), see Table 4.1. The main disadvantage is that such filter introduces time correlations in the results. As an alternative, a simple sliding window filter can be applied as in Chapter 7. The reduction in empirical standard deviation is 47 and 71% in height for all the stations considered (also after a SF).

In addition to GPS observations, also some other data sources are used in this Thesis. Tide gauges and altimetry (Chapter 7) include errors as well, that are addressed in the correspondent bibliography. Also, the hydrodynamic models used by SPOTL (Chapters 7 and 8) include several errors as physical simplifications (scaling, grid resolution, parameterization), numerical methods (analytical solutions are not possible, so numerical methods imply errors like shortening or rounding), and external data (bathymetry or magnitudes like water density) among others. The single error that can be directly validated within SPOTL is the input model grid resolution: a vertical subsidence of only 12 mm is reached when computing an homogeneous 1-meter water circular region with 111 km radius which corresponds to a circular 38707 km^2 surface. Hence, a layer of 1-meter water in 100 km^2 would only deform the crust vertically by 0.03 mm. This means that, if the model used as an input to SPOTL had a mismatch of 500 meters close to the coast, and if that surface was loaded by one meter of water, the total vertical displacement error derived to SPOTL would be of less than 1 mm. Note that the oceanic coastline of Andalucía measures approximately 340 km. Water density is also a systematic error source related to SPOTL and accounts for less than a 1%. It is reduced by not using a constant water density [*Agnew*, 2013]. Displacement loads computed by SPOTL differ less than a 5% with respect to other similar programs, and the discrepancies are probably caused by differences in the gridding [*Agnew*, 1997].

The empirical standard deviation of the different stations used for the processing in the various Chapters of this Thesis is shown in the correspondent Section. There, the information is focused on the specific error sources. Also, a weekly combination is computed to assess the daily repeatability of the station coordinates for the different daily solutions, which is an estimation of the precision. The repeatability is defined by the weighted mean square scatter of individual coordinate components (north, east, up) about a linear trend. This helps with the identification of errors in the particular stations, due to environmental, receiver or processing problems. Note that it may also be caused by geophysical phenomena like earthquakes.

Based on the results obtained, and the subjective experience working with the different dataset, a summary of the typical GPS accuracy for EWS in near real-time is given in Table 4.2:

		S_NN (mm)	S_NE (mm)	S_NU (mm)
1 second DD kinematic output rate	Unfiltered	9.4	7.3	14.6
	SF	5.3	4.7	9.6
1 second PPP kinematic output rate	Unfiltered	12.0	8.5	27.3
	SF	6.3	5.8	13.0
	SF+RF	3.8	7.4	10.1

Table 4.2: Error assessment for near real-time processing using the procedure explained in Chapter 4.

5 Numerical Results 1. Earthquake Monitoring by GPS: the Lorca Earthquake

In order to study the earthquake detection capacity of the custom processing and post-processing described in Chapter 4, the data measured by several GPS receivers during the May 2011 Lorca earthquake is used as a test case. A subset of stations from a regional network is processed, and its output is later filtered, studied and compared with publicly available seismic records. Also, a near real-time processing is achieved, using only data available at the moment of the earthquake. Moreover, precise GPS baseline processing is compared with a different software and strategy, namely RTKLib PPP processing, with very similar results. A part of this research was published in [*Mendoza et al.*, 2012].

5.1 Introduction

On May 11^{th}, 2011, at 16:47 UTC, a M_w5.1 magnitude earthquake occurred near the town of Lorca (Murcia, Spain) [IGN, 2011]. The reported location of the epicenter (37.699^{o}N, -1.673^{o}W) was approximately 2 km East-Northeast of the city, with a hypocentral depth of only about 4 km [*Cabañas-Rodríguez et al.*, 2011; *Pro et al.*, 2014]. It has been suggested by *Gonzalez et al.* [2012] that the shallow depth during the earthquake could have been caused by the extraction of groundwater in a nearby basin aquifer. Such mass redistribution was able to produce an unloading stress at the upper levels of the crust, affecting seismic activity [*Bettinelli et al.*, 2008].

Lorca is placed in the Eastern Betics Shear Zone (see Figure 3.4), a region that has suffered a significant number of moderate-to-large magnitude earthquakes in the past 500 years, as explained in Section 3.1.1. According to *López-Comino et al.* [2012], the locations of the 149 events within the earthquake sequence show no discernible pattern. However, detailed seismic relocation leads to the Alhama de Murcia Fault as the generator.

In this region, the GNSS network "Meristemum" is deployed, including six stations (see Table 5.1 and green dots in Figure 3.7) and providing 1 Hz observations.

4-CHAR	Location	Distance to the epicenter (km)
LORC	Lorca	5
CRVC	Caravaca de la Cruz	49
MURC	Murcia	58
CRTG	Cartagena	62
SALI	San Pedro del Pinatar	80
JUMI	Jumilla	91

Table 5.1: Considered stations from Meristemum GPS network.

Stations from Meristemum network are included in the custom network defined in Chapter 3, in addition to GNSS receivers from EUREF, IGS and ROA (Figure 3.7) which are deployed in the Iberian Peninsula and its surroundings. Using Bernese v. 5.0 software, a kinematic Double Differences (DD) analysis of the data is performed and the earthquake signal within the time series from LORC, one of the Meristemum stations, is successfully detected.

A first evaluation of the data from station LORC (the nearest to the epicenter, see Table 5.1) shows that some periodical oscillations with peak-to-peak amplitudes of about 2 centimeters in the North-South (N-S) direction are detected in a timespan of 20 seconds, as will be shown in Figure 5.6. In the same figure, but for East-West (E-W) direction as well as in height, displacement with peak-to-peak amplitudes up to a centimeter are manifest.

To work out the effect of the influence of seismic waves on the station positions a Modified Sidereal Filter (Section 4.2.2) is applied. It removes most of the periodic influence (temporal correlation) due to the satellite constellation recurrence and especially multipath effects. Even if this event may be identified without applying such attenuation methods, the real amplitude of the movement can be better obtained after improving the data.

The five remaining stations in the network were processed as well, and they were found to be stable. The distance to the hypocenter seems to be too large to get any discernible motion above the noise level. This result is in agreement with *Gonzalez et al.* [2012].

Moreover, a near real-time kinematic analysis is carried out in order to test the procedure's capability to work under real-time conditions. Only data available at the moment of the event is used.

5.2 GPS Data Availability

Gaps in the data interfere with its accuracy after processing. If there are only a few observations available from a certain station, the processing would not be trustworthy, and the results should not be considered. Therefore, before starting running Bernese, RINEX files from Meristemum network during the day of the earthquake have been screened in order to monitor gaps in the recorded data.

On the day of the event (DOY 131), there is a data gap discernible in stations MURC, LORC and CART during the first four hours of the day. As the earthquake occurs at 16:47 UTC, such gap will neither interfere with the processing (6 hours sliding window) nor the results.

5.3 A Posteriori GPS Analysis

Double Differencing solutions are shown for two hours of data around the time of the earthquake. MSF is performed for the timespan from 15:30 to 17:30 GPST on May 11^{th}, 2011. A comparison between unfiltered and filtered results is also given.

5.3.1 Data Provision

The GPS measurements used are provided by Meristemum network. 1 Hz RINEX observations of the stations listed in Table 5.1 are downloaded. Other GPS data is fetched from ROA, IGS and EUREF.

To carry out the MSF, all GPS data available for GPSWeek 1635 was downloaded. This week includes the days 128 to 134 in the year 2011. The earthquake occurred at DOY 131.

IGS final products are used for the main analysis. The orbital data in SP3-c format is downloaded from the CDDIS FTP server, needed to calculate the aspect repeat time (ART, see Section 4.2.2).

5.3.2 Ambiguity Fixing Strategy

The 1 Hz RINEX GPS data for each day is aggregated into a daily package. For the medium-length baselines considered (CRVC-MURC, MURC-LORC, MURC-CRTG, MURC-CRVC, CRVC-JUMI and CRVC-SALI, see Table 5.2 and red lines in Figure 5.1) the best-fit ambiguity resolution strategy is Widelane-Narrowlane (WL-NL) [*Dach et al.*, 2007]. The processing strategy follows the explanation from Chapter 4 for a posteriori settings, using IGS final products. The ambiguities resolved are above 89% for all the sites.

For the purposes of this Chapter, the first station in each baseline is held fixed and the second is defined as kinematic with a 1-meter a priori sigma. Such loose constraint allows the movement of the receiver within the time series.

Baseline	Strategy	Ambiguities resolved
CRVC-MURC	WL-NL	96%
MURC-LORC	WL-NL	89%
MURC-CRTG	WL-NL	96%
MURC-CRVC	WL-NL	93%
CRVC-JUMI	WL-NL	93%
CRVC-SALI	WL-NL	91%

Table 5.2: Ambiguity resolution ratio for the baselines considered.

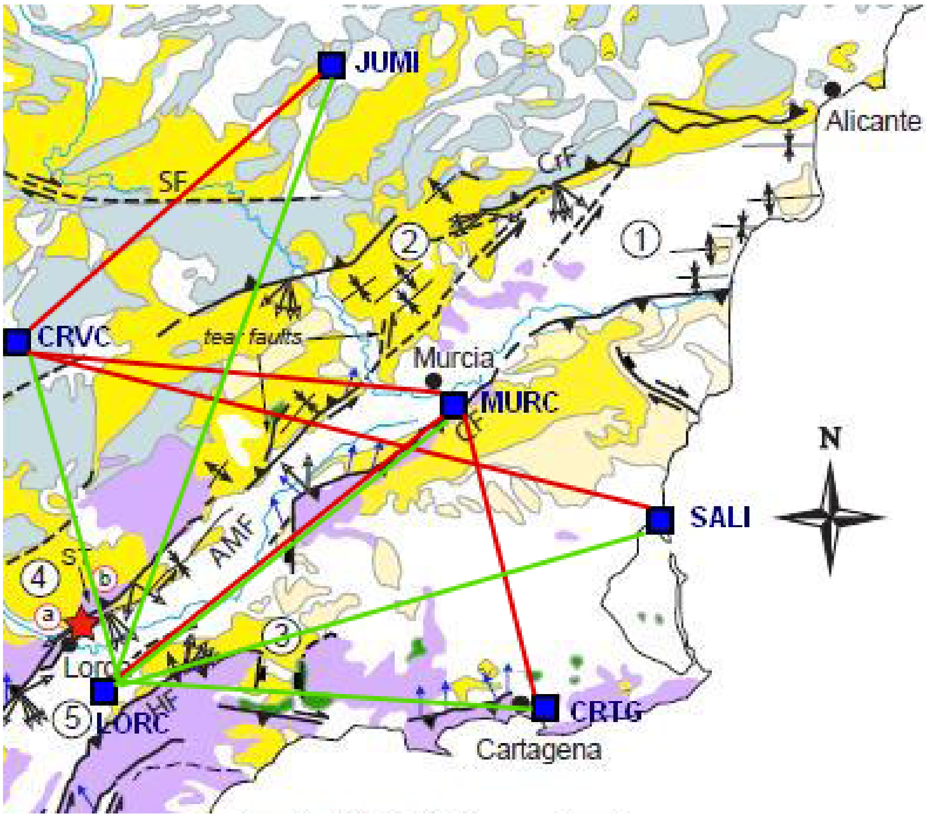

Figure 5.1: Baselines considered in the processing in red. Baselines including station LORC, in green. Map modified from [*Meijninger*, 2006].

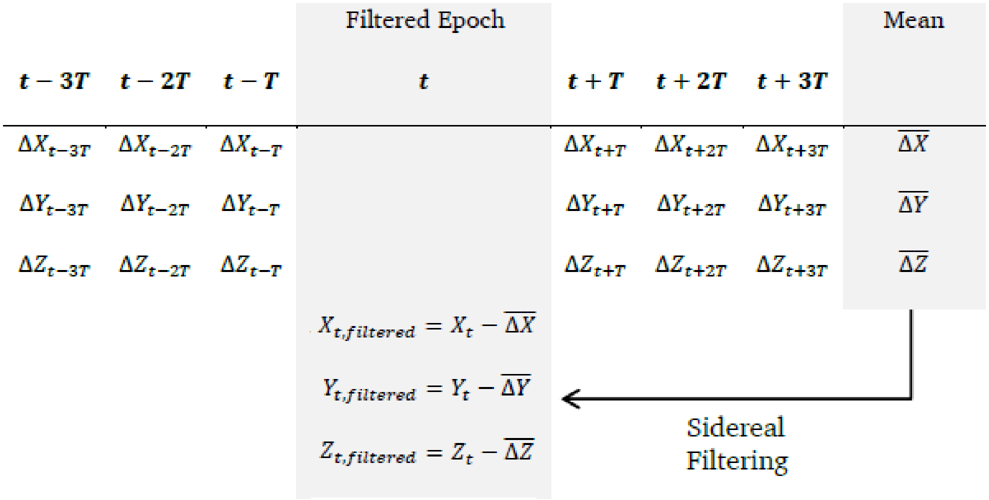

$t-3T$	$t-2T$	$t-T$	Filtered Epoch t	$t+T$	$t+2T$	$t+3T$	Mean
ΔX_{t-3T}	ΔX_{t-2T}	ΔX_{t-T}		ΔX_{t+T}	ΔX_{t+2T}	ΔX_{t+3T}	$\overline{\Delta X}$
ΔY_{t-3T}	ΔY_{t-2T}	ΔY_{t-T}		ΔY_{t+T}	ΔY_{t+2T}	ΔY_{t+3T}	$\overline{\Delta Y}$
ΔZ_{t-3T}	ΔZ_{t-2T}	ΔZ_{t-T}		ΔZ_{t+T}	ΔZ_{t+2T}	ΔZ_{t+3T}	$\overline{\Delta Z}$

$$X_{t,filtered} = X_t - \overline{\Delta X}$$

$$Y_{t,filtered} = Y_t - \overline{\Delta Y}$$

$$Z_{t,filtered} = Z_t - \overline{\Delta Z}$$

Figure 5.2: MSF scheme for one station and one epoch.

5.3.3 Post-processing of the Results

A modified sidereal filter is used in this case. The ART (see Section 4.2.2) was calculated for a single satellite and reference station positions LORC and MURC, at the reference time DOY 131, 16:47 GPST (the time of the earthquake). The satellite constellation period was calculated as T = 86155 s (rounded to an integer number of seconds). It was the same for both stations.

Using the advantage that the a posteriori run of the data provides, the sidereal filter is applied here as indicated in Figure 5.2. In this case, MSF for one station is based on its position time series for the whole GPSWeek 1635. The filter setup is as follows: first, for every epoch t of day 131, epochs in intervals of integer multiples of the ART $(t \pm n \cdot T)$ are searched within GPSWeek 1635; afterwards, a stacking is done and the residuals corresponding to each epoch are arithmetically averaged and subtracted from each epoch t residual. As solutions for DOY 134 were found to be of bad quality, they were not used for this filter.

DD results indicate a short-period noise and partially long-periodic fluctuations. They are efficiently eliminated by sidereal filtering, as one can see in the empirical standard deviation decrease. This is particularly well visible for MURC station in Table 5.3. However, high-frequency noise is not reduced. The position accuracy after filtering presents a homogeneous reduction in S_N for N-S and E-W residuals of 43-55%. A reduction of 30-40% is achieved for the height component.

In the Figures corresponding to Meristemum stations (5.3, G.1, G.2, G.3, G.4 and G.5) the improvement in the time series is also visible, as well as in Table 5.3. It is clear that the data is less scattered, and the empirical standard deviation is reduced from 20 to up to a 56%.

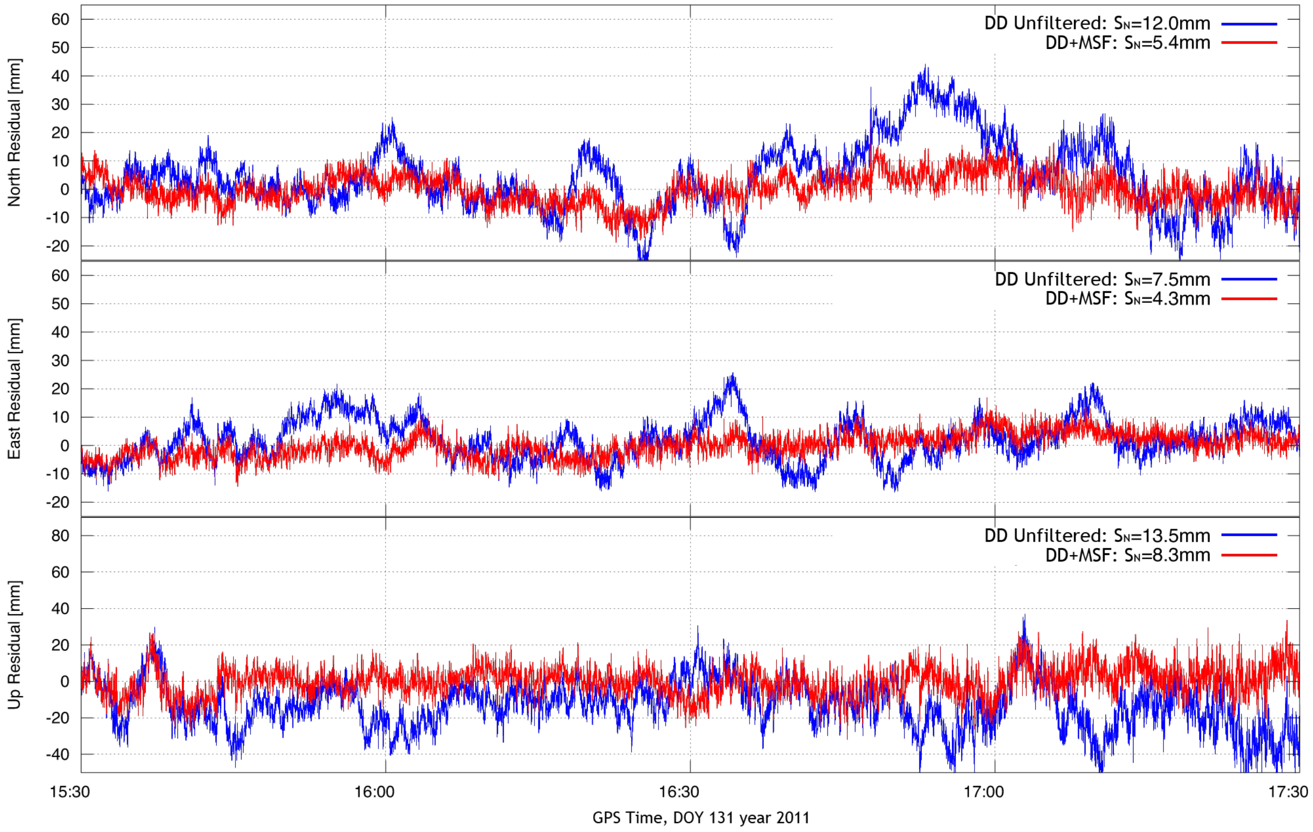

Figure 5.3: Time series for station LORC, DD unfiltered (blue) and DD filtered by a MSF (red) for DOY 131.

5.3.4 DD and PPP Comparison

Precise Point Positioning (PPP) strategy is an alternative to Double Differencing for GNSS data positioning, see Section 1.5. Sidereally filtered DD data is compared with sidereally and regionally filtered solutions derived from a PPP approach using RTKLIB software. As a regional filter eliminates errors common to an area, its use is recommended because PPP does not benefit from double differencing, which eliminates such errors.

After applying only a sidereal filter for every coordinate in both stations, the reduction in S_N is bigger for DD than for PPP, except E-W for MURC. It can be seen in Figures 5.4 here and G.6 in the Appendix, as well as in

		DD Raw	**DD MSF**	**Improvement ratio**
LORC	S_N N-S (mm)	12.0	5.4	**55%**
	S_N E-W (mm)	7.5	4.3	**43%**
	S_N Up (mm)	13.6	8.3	**39%**
MURC	S_N N-S (mm)	11.7	6.0	**49%**
	S_N E-W (mm)	10.0	5.5	**45%**
	S_N Up (mm)	14.3	9.9	**31%**
CRTG	S_N N-S (mm)	11.4	5.6	**51%**
	S_N E-W (mm)	8.4	5.1	**39%**
	S_N Up (mm)	16.6	11.6	**30%**
CRVC	S_N N-S (mm)	11.7	5.9	**50%**
	S_N E-W (mm)	10.1	5.6	**44%**
	S_N Up (mm)	14.2	10.2	**29%**
JUMI	S_N N-S (mm)	10.2	4.5	**56%**
	S_N E-W (mm)	9.2	4.6	**50%**
	S_N Up (mm)	21.0	9.9	**53%**
SALI	S_N N-S (mm)	7.5	5.9	**21%**
	S_N E-W (mm)	5.7	4.2	**26%**
	S_N Up (mm)	13.0	10.4	**20%**

Table 5.3: Empirical standard deviations (S_N) for Meristemum network stations, before and after applying MSF. Improvement ratio between unfiltered and filtered solutions. Time interval considered: 15:30 to 17:30 GPST year 2011.

LORC	**DD Raw (mm)**	**DD MSF (mm)**	**Improv. ratio**	**PPP Raw (mm)**	**PPP MSF (mm)**	**Improv. ratio**	**PPP MSF+RF (mm)**	**Improv. ratio**
S_N N-S	12.0	5.4	**55%**	7.8	6.4	18%	3.8	**51%**
S_N E-W	7.5	4.3	**43%**	5.9	6.5	-10%	5.6	**5%**
S_N Up	13.6	8.3	**39%**	14.1	13.6	3%	12.0	**15%**
MURC	**DD Raw (mm)**	**DD MSF (mm)**	**Improv. ratio**	**PPP Raw (mm)**	**PPP MSF (mm)**	**Improv. ratio**	**PPP MSF+RF (mm)**	**Improv. ratio**
S_N N-S	11.7	6.0	**49%**	16.7	6.1	63%	3.9	**77%**
S_N E-W	10.0	5.5	**45%**	10.9	5.1	53%	3.5	**68%**
S_N Up	14.3	9.9	**31%**	44.5	13.7	69%	9.2	**79%**

Table 5.4: Empirical standard deviations for LORC and MURC stations, and applied filters. Ratio of improvement between unfiltered and filtered solutions. Time interval considered: from 15:30 to 17:30 GPST, DOY 131 year 2011.

Table 5.4. However, when comparing MSF applied to the data with MSF+RF applied to the same, the improvement in PPP solutions is evident. Nevertheless, comparing DD + MSF and PPP+MSF+RF strategies, there is no general advantage visible for one of both. For MURC station, PPP results are clearly better. However, for LORC station, DD empirical standard deviation of the results is better for E-W and height components. This means there is no absolute indicator of a "best strategy" related to the reduction of the residuals scatter.

In Figure 5.5, a polar plot for the data shown in Figure 5.4 is given, comparing DD corrected by a SF and PPP corrected by both MSF and SF. The scatter reduction after filtering PPP results seems bigger for N-S component than for E-W. On the other hand, for DD results, the scatter in both components is similar. Such results are consistent with Table 5.4.

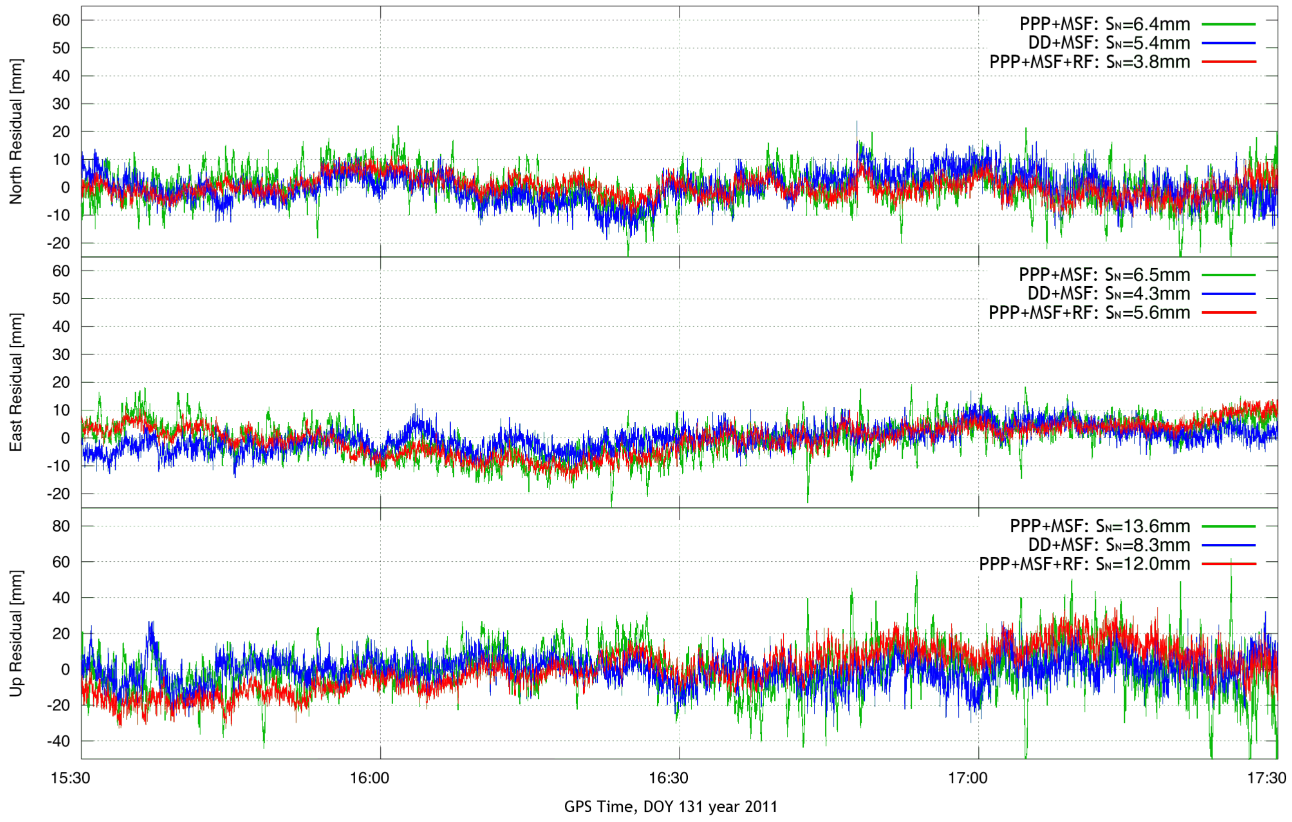

Figure 5.4: Time series for station LORC, MSF results from PPP (green PPP+MSF, red PPP+MSF+RF) and DD (blue, DD+MSF).

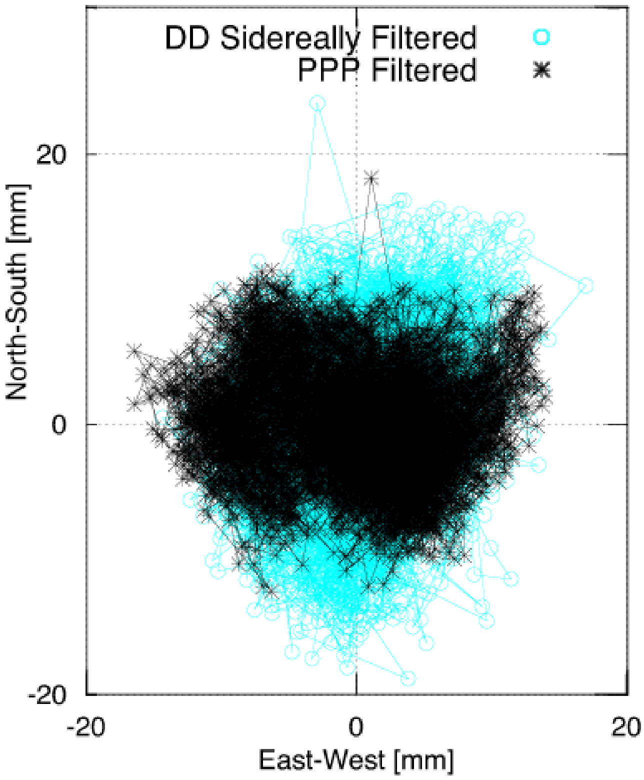

Figure 5.5: Polar plot comparing residuals from DD after MSF and PPP after MSF+RF for station LORC. Note that both directions are equally scaled.

5.4 Near Real-Time Analysis

Achieving real-time processing is the ultimate goal of the research on EWS. In order to set up an EWS, the best-case scenario is obtaining the station position at the moment it changes, i.e., real-time movement. The strategy followed here is the same as was introduced in Sections 4.1 and 4.2 for near real-time specifications.

Data processing and post-processing are necessary, and such processing time must be added to the delay in the obtention of RINEX data from the GPS receivers plus the time it takes recording and uploading the data files to the Internet (currently around 1 minute). Meristemum delivers hourly packages, so an event could be detected between 1 hour 10 minutes and 1 hour 25 minutes after it occurred if using the current processing explained here.

In an ideal case using streaming data, the absence of hourly data packages reduces the delivery of the solution by 1 hour. Thus, for the current processing technique, the event could be identified less than 10 minutes after nucleation. The use of streaming data by NTRIP data flow and PPP real-time processing was studied in [*Koppert*, 2011; *Mendoza et al.*, 2012]. Streaming raw data arrives less than three seconds after the measurement is done [*Dettmering and Webber*, 2004; *Liu and Stuerze*, 2013]. The positions are determined by RTKLIB, and are sidereally and regionally filtered, which takes only a fraction of a second for one station and 1 Hz sampling, if a continuous data streaming is provided. IGS ultra-rapid orbits and clock predictions are used. The results present an empirical standard deviation of 3 cm in horizontal components and 5 cm in the vertical, matching the results computed by *Genrich and Bock* [2006], for example.

5.4.1 Data Provision

As the goal in this Section is a simulation of a near real-time procedure, only data available at the time of the event was considered: IGS Ultra-Rapid products (see Section 1.3) were downloaded. Hourly 1 Hz RINEX data packages were fetched from the Meristemum FTP server.

5.4.2 Ambiguity Fixing Strategy

The ambiguity fixing strategy follows the explanation in Chapter 4 with a small modification: every hour and for each station, an hourly 1 Hz RINEX package is downloaded from Meristemum FTP site and merged with the previous 5 hours. Bernese runs using a MAX-OBS baseline selection strategy. Kinematic results are computed for the last hour of data and appended to the existing ones.

5.4.3 Post-processing of the Results

For this example, the setting of a 3-sigma outlier screening is tested. A slight improvement of up to 3 mm in the vertical component for both LORC and MURC stations in the empirical standard deviation of the data is found after screening. However, if the amplitude of the earthquake signal were bigger than $3S_N$, it would have been eliminated from the time series. Thus, this procedure is not advisable for earthquake observation.

As mentioned in Section 4.2.2, the design of a MSF is not possible due to the lack of precise orbits under real-time conditions. Therefore, a sidereal filter is applied to the data as in Figure 4.2.

5.5 The Lorca Earthquake

Calculations for the earthquake parameters, including location, were carried out by *Pro et al.* [2014] using data from all seismic stations available in the vicinity. The accelerometer in Lorca, placed very close to the epicenter, allowed the calculation of the hypocenter with small error margin. The biggest events in the seismic series are very close and approximately 2 km North of Lorca city, see Table 5.5.

One of the goals of this Thesis is to improve the results in order to make possible the seismic waves recognition and amplitude determination, which perturb the GPS time series. Significant periodic oscillations, especially in

Date	Time (UTC)	Latitude (^{o})	Longitude (^{o})	Depth (km)	Magnitude (M$_w$)
11^{th} May 2011	15:05:13	37.7041	-1.6812	2	4.5
11^{th} May 2011	16:47:25	37.6946	-1.6756	4	5.1

Table 5.5: Biggest foreshock and main shock from Lorca earthquake series. Information from [*Cabañas-Rodríguez et al.*, 2011; *Pro et al.*, 2014].

N-S direction, may be visible shortly after the specified time of the earthquake (16:47:25 UTC, 16:47:42 GPST) for LORC time series (see Figure 5.6). A peak-to-peak amplitude displacement of approximately 30 mm is found for North-South and vertical components, and in East-West, the displacement obtained is close to 20 mm.

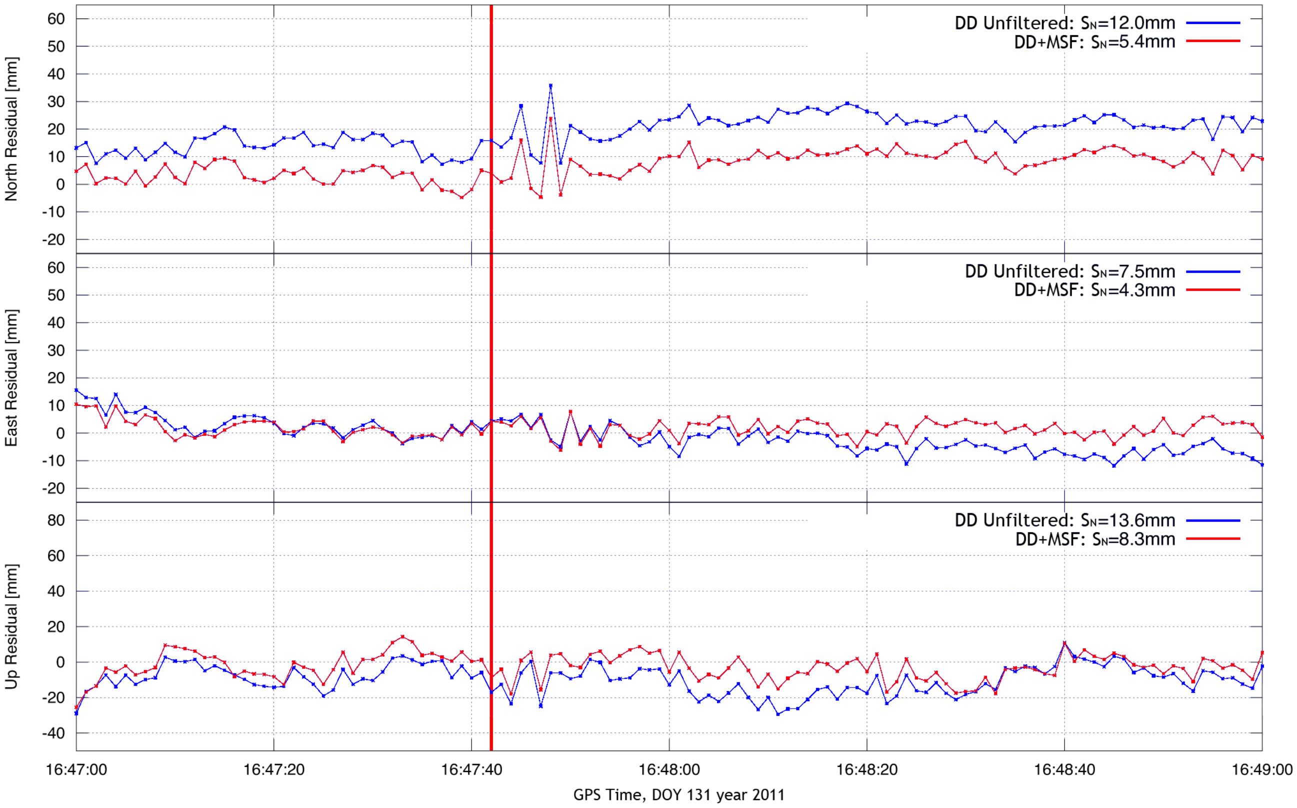

Figure 5.6: LORC time series, DD unfiltered (blue) and after SF (red), for the estimated time of arrival of the earthquake at 16:47:42 GPST (red vertical line).

Results obtained with data available a posteriori and in near real-time are similar. In Figure 5.7, a comparison of both evaluations is shown for the two minutes around the earthquake in station LORC. Despite the fact that the Ultra-Rapid orbits (see Section 1.3) may deteriorate the results and increase the empirical standard deviation in near real-time analysis, the behaviour of the time series around the moment of the earthquake remains the same, including the peak-to-peak amplitude of the shaking. The difference between both time series gave a difference of about 1 mm for the three components and the whole period.

For a further examination of the earthquake-induced movements of the station LORC, the ground track of the computed positions from the PPP processing is visualized in Figure 5.8. The plots corresponding to DD results are almost identical. Only horizontal displacements are considered here over a timespan of 15 seconds. This view helps to study the properties of the seismic waves and it ideally allows the identification of their type. In order to do that, the station motion has to be related to the direction of propagation of the seismic waves. Assuming a direct radial propagation of the seismic waves (because of the closeness to the epicenter and the minor depth of the

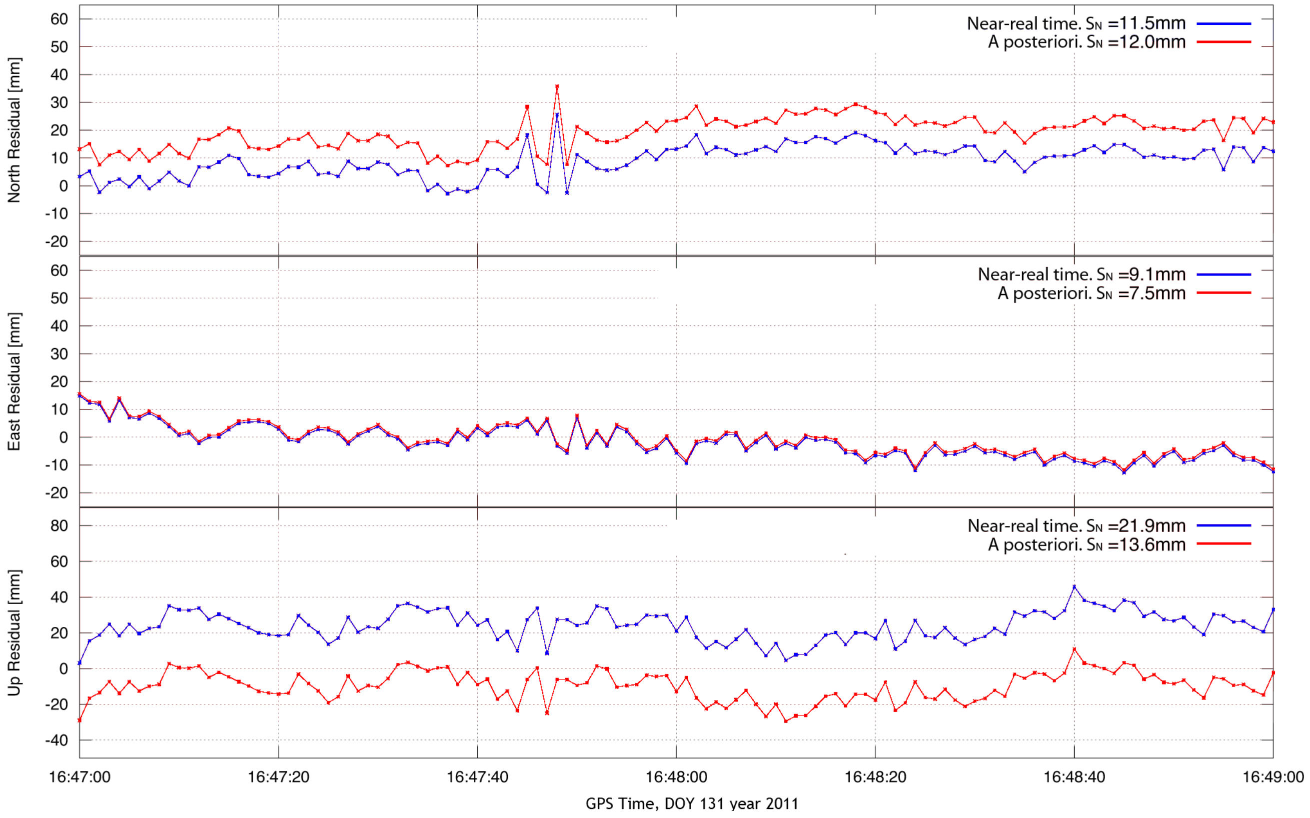

Figure 5.7: LORC time series around the moment of the earthquake. Raw results from a posteriori and near real-time analysis of the data from baseline MURC-LORC.

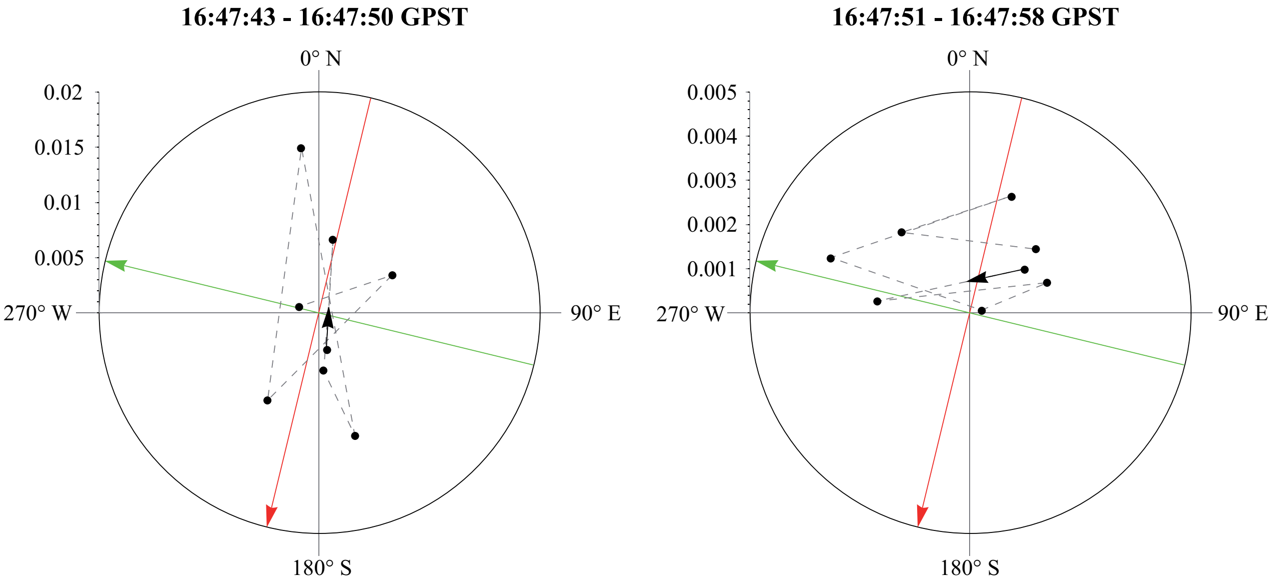

Figure 5.8: Polar plots from station LORC, PPP results. DOY 131 year 2011.

hypocenter), the direction of propagation can be approximated by the azimuth between the earthquake epicenter and the station site, 193.6^o.

Between 16:47:43 and 16:47:50 GPST the station mainly undergoes movements in radial direction with amplitudes up to 20 mm. After 5 seconds also a smaller perpendicular movement becomes visible. During the following

8 seconds (16:47:51 - 16:47:58 GPST) the main direction of movement is perpendicular to the computed direction of wave propagation, this is, perpendicular to the radial direction. However, there is also a noticeable radial movement. The displacements during this period are generally smaller than during the period before (note the different scaling of the two figures).

There are obviously systematic displacements of the station LORC which can be related to the assumed direction of propagation of the seismic waves. The displacements before and after this period do not show this systematic nature (see Figure 5.8). Radial and tangential displacements are observed, so the waves studied here can be identified as surface waves. This observation is consistent with the minor depth of the hypocenter which lead to big surface waves [*Vissers and Meijninger*, 2011]. The body waves have been too small to be identified in the computed position time series neither for PPP nor for DD.

5.5.1 Other Shocks in the Seismic Series

The Lorca earthquake is, in fact, the biggest event in a series of 149 tremors over three days [*López-Comino et al.*, 2012]. The second biggest shaking had a magnitude of M_w4.5 and occurred at 15:05:13 GPST on the day of the main event (see Table 5.5). The analysis of the station LORC for the foreshock produced a time series shown in Figure 5.9. The peak in N-S component two to three seconds after the estimated arrival time could be considered as an earthquake indicator. Nevertheless, shaking due to an earthquake has a smaller period than what Figure 5.9 shows. Moreover, as there are no more signs of anomalous behaviour within, it can be concluded that this event is not visible in the corresponding time series.

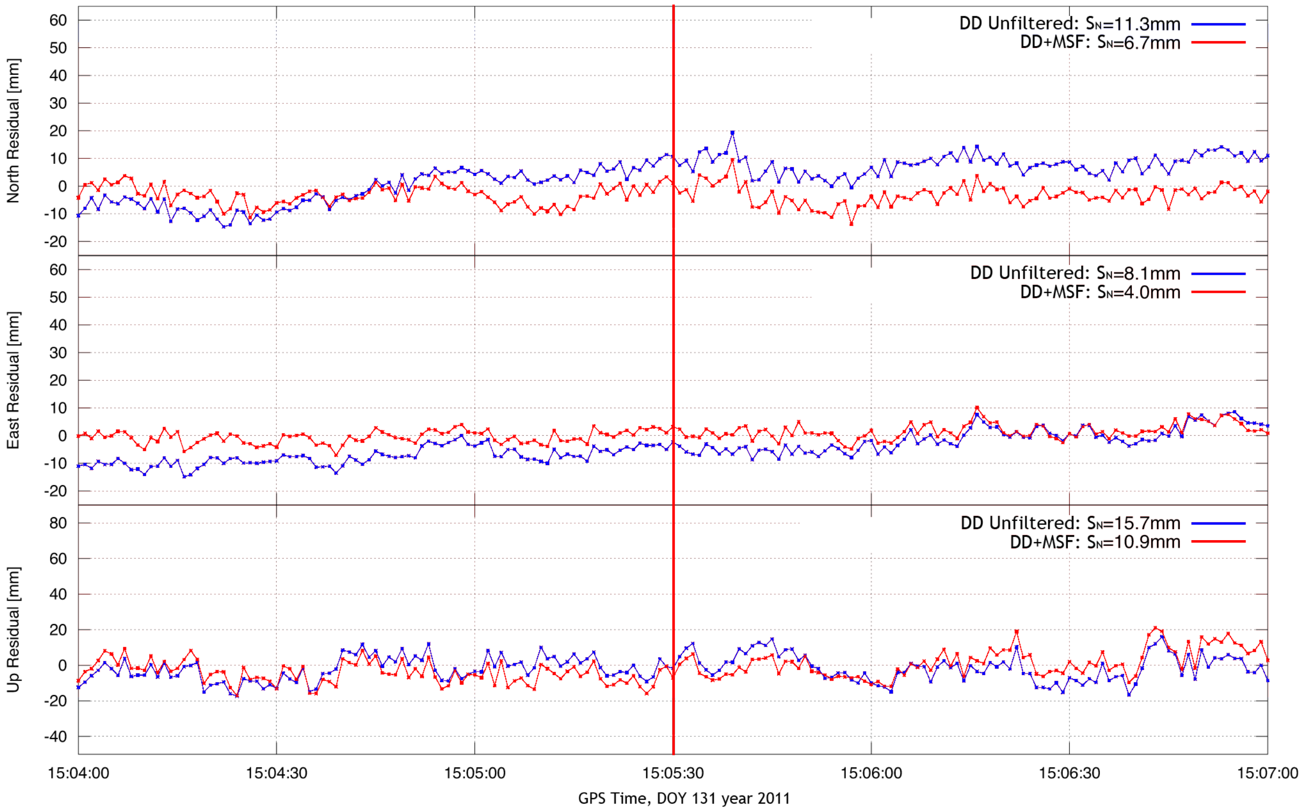

Figure 5.9: LORC time series, DD unfiltered (blue) and after SF (red), for the estimated time of arrival of the second biggest event in the seismic series at 15:05:30 GPST (red vertical line).

5.5.2 Comparison of Different Baselines

The behaviour of the coordinates registered during an event depends on the position of the considered station with respect to the fault. In addition, slight changes between the stations in the network can influence the goodness of the results. In this Section, solutions obtained after analyzing all possible baselines containing LORC station are studied. Time series around the instant of the earthquake are compared depending on the baseline considered and statistics are derived from data recorded within one hour before and after the event. LORC station position is set as kinematic while the rest of the stations are held static.

Figure 5.10 shows the graphical representation of the solutions using all the baselines mentioned before, for a minute before and after the event. One of the most interesting results found here is that station LORC overall behaviour is definitely different depending on the baseline used to obtain its position, mainly due to the noise related to each baseline. Nevertheless, the movement of LORC station during the earthquake (starting at 16:47:42 GPST) is almost identical for each baseline: amplitudes are very similar and the duration of the shaking is also alike. As a consequence, for this particular event, all the baselines can be used for the shaking detection and amplitude estimation.

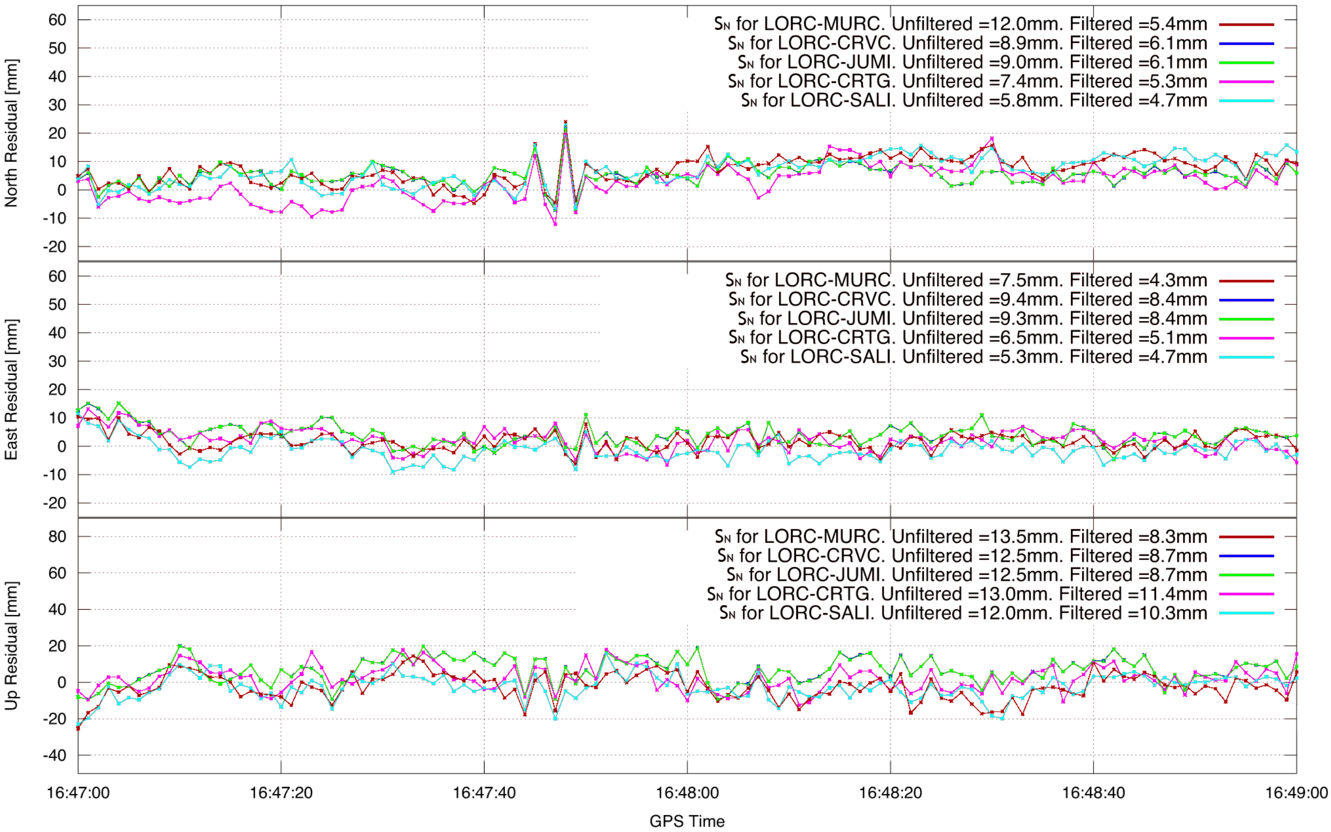

Figure 5.10: Time series around the time of the earthquake for station LORC (kinematic, MSF applied) and the rest of stations (static) in the network. DOY 131 year 2011.

It is also interesting to consider the orientation of the baselines with respect to the fault (see green lines in Figure 5.1). LORC-MURC baseline is almost parallel to the fault while LORC-CRTG and LORC-CRVC are almost perpendicular to it. LORC position time series derived from LORC-SALI baseline shows the best performance in terms of ratio of ambiguities resolved (98%, see Table 5.6). The smallest S_N values are found for LORC in LORC-MURC baseline, where the filtered data has a S_N of 5.4, 4.3, 8.3 mm in North, East and Up components, and 91% of the ambiguities were resolved. The theory states that the most significant displacements are found in baselines parallel to a fault. In Figure 5.10 it is clear that the signal for this event is seen in all baselines considered. Nevertheless, the solutions for station LORC are here always derived from LORC-MURC baseline, to follow the theory: this baseline is the closest to the fault direction. This has also been proved by *Larson et al.* [2003] for the 2007 July 16^{th} Chuetsu-Niigata earthquake (M_w6.5).

It must be remarked that the kinematic displacement of the rest of the stations during the event (see next Section) is in the order of the recorded noise level, therefore their movement does not spoil the signal registered in LORC.

		DD Raw	DD MSF	Reduction ratio	Ambiguities resolved
LORC-MURC	S_N N-S (mm)	12.0	5.4	**55%**	91%
	S_N E-W (mm)	7.5	4.3	**43%**	
	S_N Up (mm)	13.5	8.3	**39%**	
LORC-CRVC	S_N N-S (mm)	8.9	6.1	**3%**	94%
	S_N E-W (mm)	9.4	8.4	**11%**	
	S_N Up (mm)	12.5	8.7	**30%**	
LORC-JUMI	S_N N-S (mm)	9.0	6.1	**32%**	96%
	S_N E-W (mm)	9.3	8.4	**10%**	
	S_N Up (mm)	12.5	8.7	**30%**	
LORC-CRTG	S_N N-S (mm)	7.4	5.3	**28%**	96%
	S_N E-W (mm)	6.5	5.1	**21%**	
	S_N Up (mm)	13.0	11.4	**12%**	
LORC-SALI	S_N N-S (mm)	5.8	4.7	**19%**	98%
	S_N E-W (mm)	5.3	4.7	**11%**	
	S_N Up (mm)	12.0	10.3	**17%**	

Table 5.6: Empirical standard deviations for the different baselines with LORC. DD solutions before and after applying the MSF. Ratio of improvement between unfiltered and filtered solutions. Ratio of ambiguities resolved. Time interval considered: from 15:30 to 17:30 GPST, DOY 131, year 2011.

5.5.3 The Earthquake at Other Stations

Since earthquake waves propagate radially from the hypocenter and they travel in different ways through the layers of the ground depending on the type of material they cross, an approximation of the propagation velocity may be calculated. The given earthquake origin time is 16:47:40 GPST and the movement in the station LORC begins at 16:47:42 GPST, placed 5.1522 km away from the epicenter. As the hypocenter was shallow, the distance between it and each station is taken as the linear distance in the surface. Then, the estimated arrival times to the different stations for the earthquake waves are as given in Table 5.7.

Station	Distance to the epicenter (km)	Estimated arrival time (UTC)
LORC	5	16:47:27
CRVC	49	16:47:42
MURC	58	16:47:45
CRTG	62	16:47:47
SALI	80	16:47:56
JUMI	91	16:47:58

Table 5.7: Distance to the epicenter and estimated arrival times from the different GPS locations. Note that GPST=UTC+15 seconds in 2011.

In Figures G.9 and G.10 from the Appendix, MURC and CRTG time series from DD after MSF applied are shown for the time span between 16:47:00 and 16:49:00 GPST, analogue to Figure 5.6. The expected arrival time is marked by a vertical red line for each station. Despite the fact that the sites mentioned above are the nearest to the epicenter except LORC, it turns out that they do not show any distinct change in the time series of any coordinate. No displacement is detectable in the rest of stations either, see Figures G.11, G.12 and G.13.

5.5.4 The Earthquake in Seismic Sensors

Accelerometers, as the name suggests, measure acceleration, which must be integrated twice to obtain ground movement. For comparison with the results from GPS data, the accelerograms from Lorca station, placed 3 km from the epicenter, were recovered.

In Figure 5.11, N-S displacement is shown as computed by *Cabañas-Rodríguez et al.* [2011] from the Lorca accelerometer data. Integration from acceleration to velocity, and from velocity to displacement, smoothens the high-frequency peaks. This reduces the signal to almost a unique long-period pulse. Its maximum peak-to-peak displacement is 30 mm, in agreement with the results obtained by GPS in the previous Sections. *Cabañas-Rodríguez et al.* [2011] show that the maximum amplitude registered during the event is found in N30^{o}W direction.

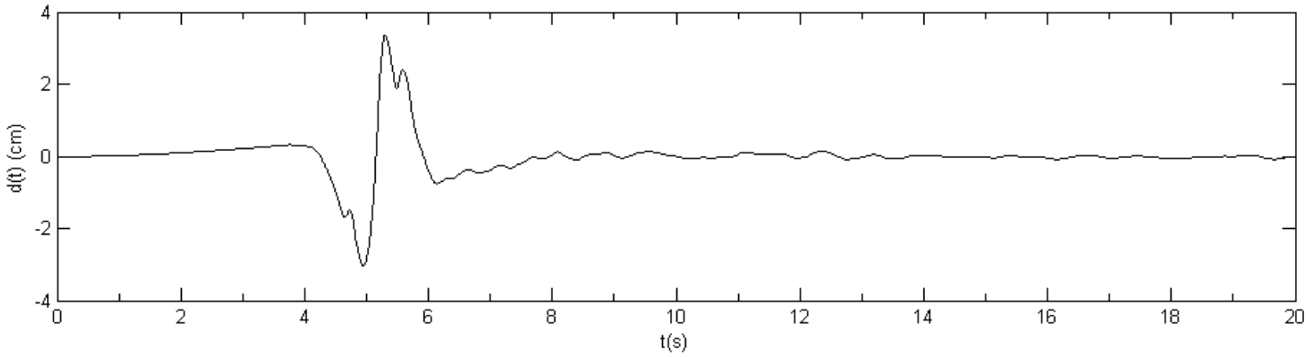

Figure 5.11: N-S displacement over time of the accelerometer near Lorca (station Lorca), after double integration from the signal. Filter 0.1-50 Hz. Taken from [*Cabañas-Rodríguez et al.*, 2011].

The strong motion data has also been processed by *Pro et al.* [2014] in order to derive the ground motion. The resulting peak-to-peak displacements are 11.8, 6.2 and 8.2 mm for vertical, East and North directions, very close to the results obtained here. A more detailed comparison can be found in the paper mentioned earlier.

5.6 Error Assessment

The combination of daily coordinate estimates in Bernese shows a repeatability below 1.5, 0.9 and 3.4 mm in North, East and height, respectively, for all the stations considered in this network and days 128 to 133 in 2011, excepting DOY 131. This indicates that the daily solutions are of good quality.

	LORC		MURC	
	DD MSF	**PPP MSF+RF**	**DD MSF**	**PPP MSF+RF**
S_N N-S (mm)	4.0	3.8	5.2	3.8
S_N E-W (mm)	4.1	5.5	4.3	3.6
S_N Up (mm)	7.5	10.1	8.9	9.1

Table 5.8: Empirical standard deviations for kinematic time series from LORC and MURC stations, and applied filters. Time interval considered: DOY 128-133 of 2011, except 131.

On the other hand, for the kinematic 1 second time series, the empirical standard deviation obtained during the days around the earthquake ranges between 4.9 and 5.2 mm for horizontal components in DD, and between 3.6 and 5.5 mm for PPP in the same components. For the vertical, DD shows a smaller scatter than PPP: 7.5 and 8.9 mm for DD in LORC and MURC for DD, respectively, and 10.1 and 9.1 for PPP and the same stations. Those results are summarized in Table 5.8 and they do not differ much from the results obtained for the time of the earthquake (Table 5.4), as it was small and did not last long. The rest of the stations show similar statistics, and all are within the expected values for 1 Hz kinematic GPS solutions.

The solutions obtained for raw data in days 128-133 except 131 are also similar to those obtained for DOY 131 (Table 5.4) and are not shown here.

Moreover, the earthquake signal (peak-to-peak amplitude of 30 mm in N-S and vertical and 20 mm in E-W directions) lies above the noise level as seen in Table 5.8.

5.7 Summary

The GPS data available for the week of the earthquake is sufficient to analyze it. However, results for DOY 134 were of bad quality and thus not used for an a posteriori modified sidereal filtering.

The improvement after applying the MSF is manifest in Table 5.3, with a reduction in empirical standard deviation between 30 and 55%. The periodicities in the data are eliminated as well, and the peak-to-peak amplitude of the earthquake is not reduced.

The comparison between DD and PPP methodologies does not lead to any "best strategy": both methods can be used with similar achievable accuracy. Data processed by both strategies and filtered afterwards have similar empirical standard deviations (scatter) and show the same peak-to-peak amplitude of the earthquake.

The results obtained with Ultra-Rapid orbits and the near real-time processing strategy presented in Section 4.1, are similar to those obtained with the precise orbits and the a posteriori settings. The comparison between both signals, without any post-processing, is very good in terms of shape. Moreover, the time series are almost identical for the two minutes around the earthquake, showing a difference of only S_N1 mm in the whole period.

Earthquakes of magnitudes up to M_w4.2 can not be detected by GPS using the current strategy, as the analysis of the foreshock shows. Also, if the GPS receivers are located more distant to the epicenter (the second closest GPS receiver was placed 49 km away from the epicenter), the seismic signal becomes too weak to be seen.

If the earthquake were detected by other GPS stations, having the arrival time of the signal in each receiver, a rough estimation of the location of the epicenter could have been achieved using a plain triangulation method, as mentioned in Section 2.1.1.

Obtained results are in good agreement with smoothed accelerometer data computed by *Cabañas-Rodríguez et al.* [2011] and *Pro et al.* [2014]. This, added to the similarities to PPP processing, validates the DD data processing and post-processing strategies defined for this Thesis.

6 Numerical Results 2. Sensitivity of GPS Time Series to Extreme Tides

In this Chapter, GPS and mareograph data in the littoral of the Province of Cádiz from two periods of extreme tides that occurred in 2011 is used. First, GPS recordings are checked to detect either anomalies or large gaps that could affect the result. Afterwards, the displacements derived from extreme tides in the GPS coastal stations are processed. Moreover, the delays between the waves recorded by co-located GPS and mareographs are computed by a correlation of both signals. A further research is done to study the subsidence decay patterns through a profile from the coast to the center of the Peninsula. A second profile is set using GPS coastal stations from West to East to estimate wave travel times.

6.1 Introduction

The Province of Cádiz is placed in the southernmost region of Spain. Its eastern part is bathed by the Mediterranean Sea and its western part faces the Atlantic Ocean, presenting bigger tides than the Mediterranean. In this region, there are several mareographs deployed by the Spanish Hydrographic and Oceanographic Institutes. Their coordinates and locations are detailed in Table H.1 and Figure 6.1 together with the GPS available in the area.

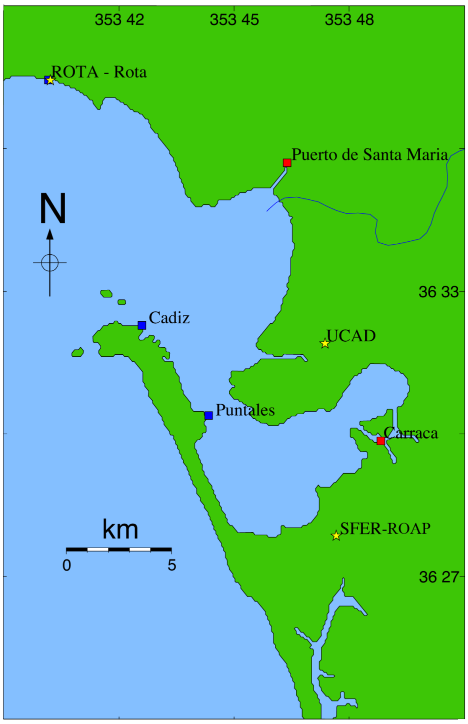

Figure 6.1: Mareographs (squares) and GPS stations (stars) close to the city of Cádiz.

The maximum theoretical value for the ocean tide coefficient is 1.18 meters (see Section 2.2.1). According to the information provided by the Spanish Hydrographic Institute [Moreno, S. & Quijano, J.; personal communication], a tide coefficient of 1.17 meters was reached on March 19^{th} 2011 (DOY 78) at 12:00 UTC and on March 20^{th} 2011 (DOY 79) at 00:00 UTC in ROTA mareograph. Also, a tide coefficient of 1.15 was reached on September 27^{th} 2011 at 12:00 UTC (DOY 270) in the same station. The same coefficient of 1.15 meters has been reached several times since year 2000.

In March 2011, the extreme values were produced by Moon and Sun declination angles close to zero. If the Earth had been in its perihelion (January), the maximum theoretical value for the tide coefficient would have been reached. However, the Moon was full and placed in its minimum annual perigee. For the situation observed in September 2011, both Moon and Sun had very low declination angles, but the Moon was in new Moon phase. Also, the lunar perigee was slightly larger than in March 2011 but very close to the annual minimum. The Earth was also far from its perihelion.

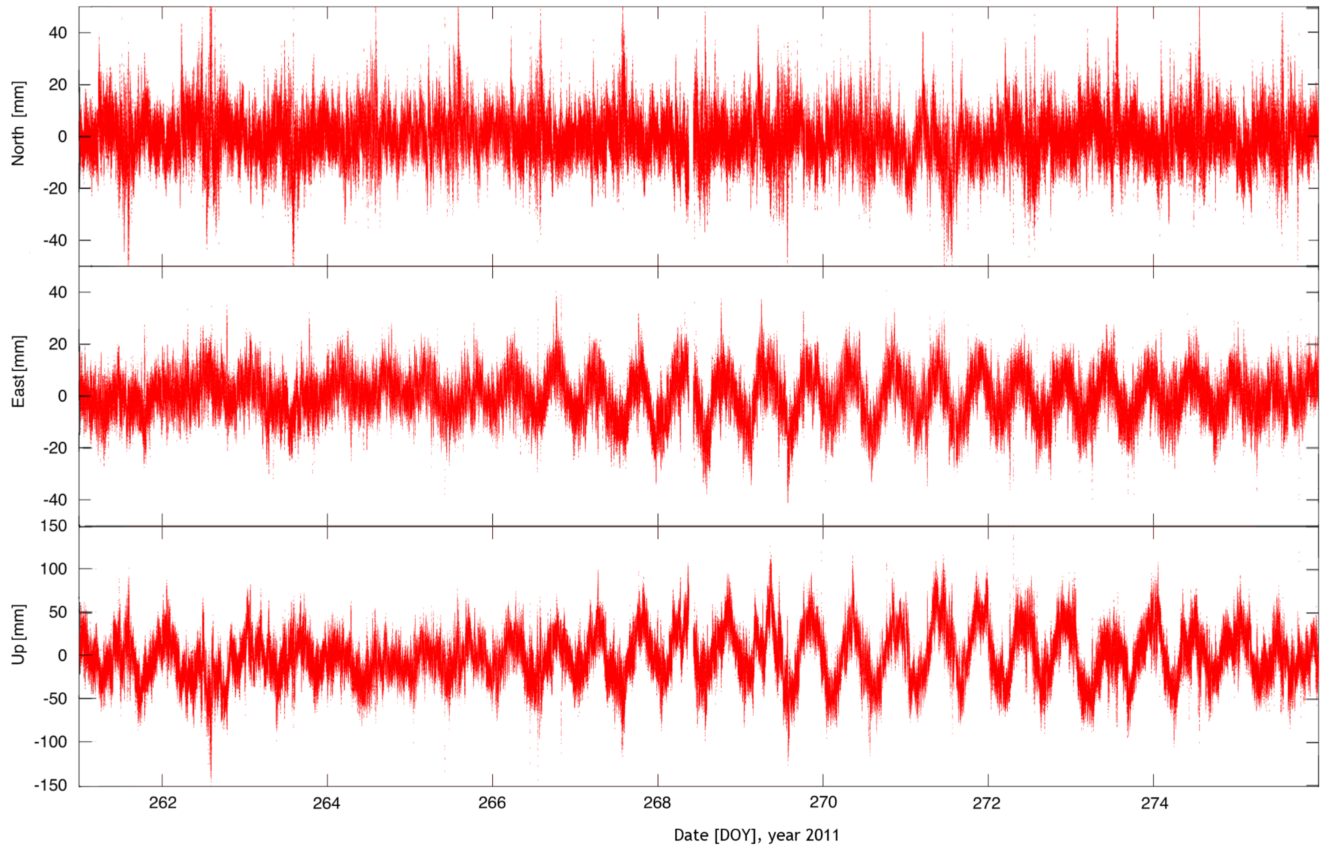

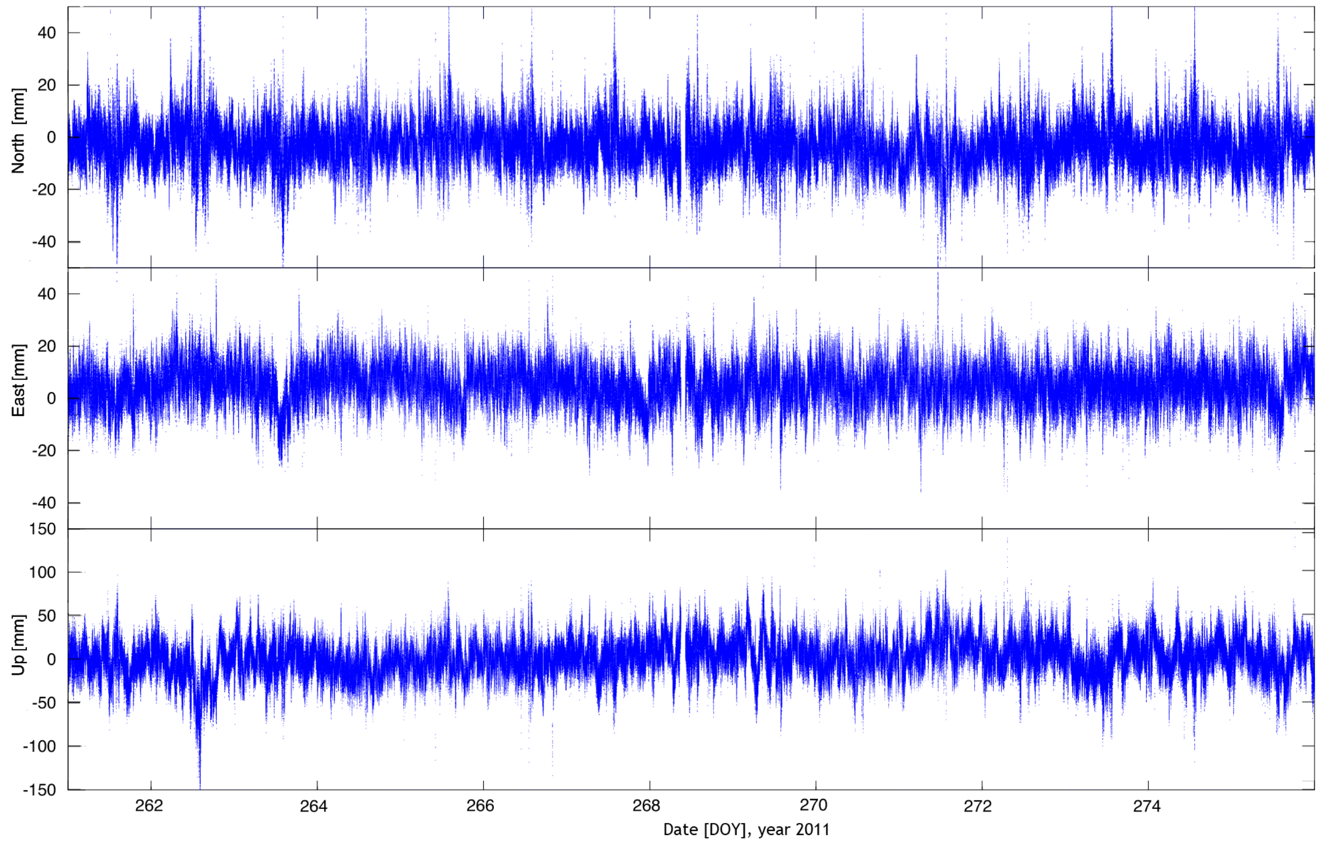

Figure 6.2: GPS time series for ROTA station in September 2011. Unfiltered data. OTL corrections not applied (red, top) and applied (blue, bottom) by Bernese.

In both study cases, the meteorological conditions in the Province of Cádiz were favorable: neither wind nor barometric changes influenced the water level. If a big storm or strong winds had accompanied the phenomena, it would have been dangerous for the population due to the highly increased water level in the area, as is the case in Chapter 7. On the other hand, In September 2011 the difference between predicted and observed mareograph water level reached 20 cm in ROTA, which could be related to the low atmospheric pressure recorded during that week.

PUNTALES and ROTA mareograph data has been provided by the Spanish Hydrographic Institute. CADIZ mareograph recordings have been handed over by the Spanish Oceanographic Institute. The data has a sampling of 1 minute for ROTA and 5 minutes for CADIZ and PUNTALES. The extreme tides in March were recorded by CADIZ and PUNTALES mareographs; in September, only data from CADIZ and ROTA was available. The mareographs that did not register any data during these time periods are marked with red squares in Figure 6.1. Also, predicted data with 10 minute sampling has been provided for the mentioned mareographs.

There are four GPS receivers placed in the vicinity of the mareographs under study in Cádiz: UCAD, SFER, ROAP and ROTA. As explained in Section 3.2, UCAD belongs to the RAP network and the rest belong to the ROA. ROTA mareograph and GPS receiver are co-located. The distances between mareographs and GPS in the Province of Cádiz are detailed in Table 6.1.

	ROAP - SFER	**ROTA**	**UCAD**
CADIZ	11 km	9 km	7 km
PUNTALES	7 km	14 km	5 km
ROTA	20 km	0 km	14 km

Table 6.1: Distance between mareographs and GPS that recorded data during the periods of extreme tides in March and September 2011.

HUEL GPS station is located within 5 km of HUELVA mareograph from REDMAR network (Puertos del Estado, Spain). Despite they are not in the Province of Cádiz, their observations are also used. Data has been provided for both extreme events by Puertos del Estado, Spain. Their location can be checked in Figure 6.4.

The GPS stations presented before are complemented with GNSS receivers from EUREF, IGS, RAP and ROA, deployed in the Iberian Peninsula and surroundings (see Figure 3.7). Using Bernese v. 5.0 software, a kinematic Double Differences (DD) analysis is performed, obtaining the GPS time series corresponding to the extreme tide periods in 2011.

Data recorded in ROTA GPS receiver during two weeks around the high tide period in September is processed by Bernese and the residuals with respect to IGS05 coordinates (see Section 1.4) are shown in Figure 6.2. In the time series on the upper part (red), OTL corrections are not applied. They clearly show that tidal amplitudes increase around the day with the biggest tidal coefficient, DOY 270, 2011. The vertical subsidence related to oceanic tides is above the noise level for GPS (uncorrected) recordings in ROTA during the periods of extreme tides. Consequently, if a tsunami signal reached the same magnitude, or above, it could also be detected. The periodic oscillation in E-W direction in Figure 6.2 is due to the load that the ocean exerts on the crust, which produces a tilt in the GPS antenna.

In the time series on the lower part from Figure 6.2 (blue), the data has been corrected for FES2004 modeled ocean tides within Bernese. The residuals plotted show no periodical signal, implying that the ocean tide loading corrections applied by Bernese remove the subsidence to a level that is below the noise in the GPS signal, even for extreme tides. This is, the ocean tidal model FES2004 represents accurately the water state in this region. This is going to be checked analytically in the following Sections.

6.2 GPS Data Availability

Ambiguity resolution is intrinsically related to data availability. Data to be processed must not have substantial gaps. Completeness of data for stations SFER, UCAD, ROTA and HUEL are the foremost concern for their closeness to the mareographs, and it can be checked in Figure 6.3.

Figure 6.3: Missing RINEX data for the stations of interest in March (top) and September (bottom) 2011, indicated by blue dots. SFER data could not be retrieved for the period of interest in March.

A large amount of data is missing from stations ROAP and HUEL, which could lead to unreliable results. Moreover, ROAP antenna was found unstable [Gárate Pasquín, J.; personal communication], thus it will not be considered in the processing. SFER 1 Hz data could not be retrieved.

6.3 GPS Data Analysis

The residuals from a kinematic Double Differences processing is given with 1 Hz rate for DOY 70 to 86 (March) and DOY 262 to 275 (September), 2011. Such periods contain the days when the maximum tidal coefficients were predicted and observed. The goal is to monitor the vertical load of the crust in several stations, so the baseline selection is critical for this test case. The residuals are filtered by the exponentially weighted moving average (EWMA) filter introduced in Section 4.2.3, whose performance is also checked.

6.3.1 Data Provision

GPS measurements are provided by IGS, EUREF, ROA and RAP, and downloaded from their servers with a 1 Hz sampling for days 70 to 86 and 262 to 275 (all included) of year 2011. IGS final products are used.

6.3.2 Baseline Selection

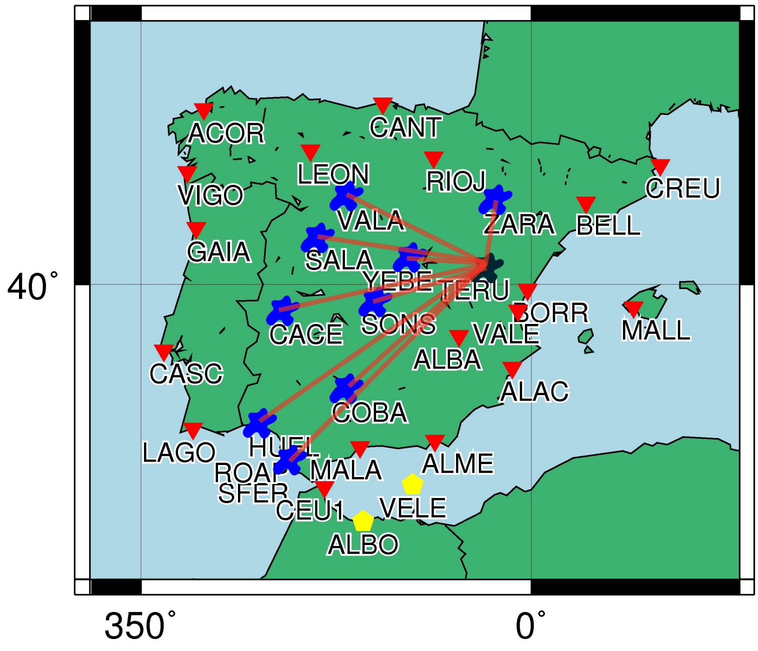

Figure 6.4: Baselines centered in TERU.

Baseline selection for this Chapter is crucial in order to achieve the highest accuracy in the results. To monitor the subsidence of several GPS stations due to tides, the point fixed in each baseline must be stable. The stations of interest are ROTA, SFER and UCAD. A test proposed by *Ge et al.* [2000a] is carried out, using a STAR baseline configuration with ROTA as the central station for a first Bernese run, OTL corrections applied. The station that is less prone to be influenced by ocean load tides (more to the center of the Peninsula) and showing the best ambiguity resolution ratio and lowest scatter (S_N) is selected to be the central station for the following Bernese processing. For DOY 77 and 81 of 2011, the stations that matched such requirements were CACE and TERU (highlighted in bold in Table H.2). For consistency, the same test was performed for baselines with UCAD at an edge (Table H.3), and the outcome was similar. TERU GPS receiver is chosen due to its location farther away from the Atlantic littoral, thus theoretically less influenced by ocean loadings.

A small modification has been added to the strategy proposed by *Ge et al.* [2000a]: the baseline selection for the Bernese run is a combination between STAR and OBS-MAX strategies. This is, only the baselines from Figure 6.4 are fixed, and the rest are free for Bernese to combine them according to the maximum number of observations in each run. It increases ambiguity resolution ratio and decreases S_N in most of the cases that have been tested. This result can be checked in Table 6.2, for baselines with CACE and TERU at an end and connected with SFER, UCAD, ROTA and ALGE. COMB. (combined) indicates the combination of strategies STAR and OBS-MAX.

The advantages of a combination of both strategies are clear: if the data from the center station was missing or is of bad quality, STAR strategy would not be affordable. In that case, the rest of the network (OBS-MAX) provides a more stable result.

			19 March (DOY 78)				**20 March (DOY 79)**				**27 Sept (DOY 270)**			
			Amb	S_N**N**	S_N**E**	S_N**U**	**Amb**	S_N**N**	S_N**E**	S_N**U**	**Amb**	S_N**N**	S_N**E**	S_N**U**
			%	**(mm)**	**(mm)**	**(mm)**	**%**	**(mm)**	**(mm)**	**(mm)**	**%**	**(mm)**	**(mm)**	**(mm)**
ALGC	**CACE**	**STAR**	93%	5.1	5.5	10.8	89%	4.9	3.2	11.5	80%	5.8	5.7	17.8
		COMB.	95%	5.2	5.8	12.1	91%	5.0	3.2	11.1	78%	5.9	5.7	18.0
	TERU	**STAR**	89%	5.0	4.4	11.0	89%	5.1	3.2	11.8	81%	5.9	5.3	17.3
		COMB.	90%	5.1	4.4	11.1	89%	5.2	3.2	11.6	81%	6.0	5.4	18.6
ROTA	**CACE**	**STAR**	95%	6.8	5.3	15.8	92%	6.8	5.2	16.4	89%	8.5	6.5	23.1
		COMB.	95%	6.8	5.3	15.7	92%	7.0	5.2	16.1	89%	8.5	6.5	23.2
	TERU	**STAR**	94%	6.9	5.4	16.6	88%	6.9	5.2	15.9	85%	8.7	6.7	21.4
		COMB.	94%	7.0	5.3	16.3	88%	7.1	5.2	17.1	79%	8.8	6.7	22.7
SFER	**CACE**	**STAR**	-	-	-	-	-	-	-	-	88%	9.8	6.7	33.9
		COMB.	-	-	-	-	-	-	-	-	86%	10.2	7.0	32.0
	TERU	**STAR**	-	-	-	-	-	-	-	-	84%	16.3	17.3	79.0
		COMB.	-	-	-	-	-	-	-	-	86%	10.1	6.9	31.4
UCAD	**CACE**	**STAR**	88%	8.9	3.5	11.8	86%	8.4	5.8	13.4	83%	10.3	5.5	25.1
		COMB.	88%	8.9	3.4	12.1	87%	8.5	5.8	11.8	84%	10.2	5.5	24.5
	TERU	**STAR**	91%	8.9	3.5	12.4	89%	8.5	5.8	13.1	80%	10.1	5.5	27.0
		COMB.	92%	8.9	3.4	11.8	91%	8.4	5.8	13.8	82%	10.3	5.5	24.5

Table 6.2: Tests to check the best center station for STAR strategy in baseline selection. Also a combination of strategies (COMB.) is provided: STAR for the stations in the profile towards the center of the Peninsula and maximum number of observations (OBS-MAX) for the rest of the stations in the network. Ratio of ambiguities resolved (Amb.) and empirical standard deviation (in mm) for North, East and up components.

6.3.3 Ambiguity Fixing Strategy

The only modification in Bernese processing is the baseline selection. The rest follows the steps detailed in Chapter 4 with the setup for a posteriori data: 1 Hz RINEX data is aggregated into daily packages and the ambiguity resolution strategy is chosen by Bernese depending on the length of the baseline considered.

6.3.4 Post-processing of the Results

Applying a modified sidereal filter (see Section 4.2.2) as implemented for the Lorca earthquake (Section 5.1) is possible but not desirable in this context. Filtering in such a way would lead to a common behaviour elimination in the data. As tides affect the observations on a periodic basis, almost synchronous to a sidereal day (slightly less than two tides per day, see Figure 6.2 for example), such effects would be erased by a MSF. Therefore, an exponentially weighted moving average filter (see Section 4.2.3) was chosen, since it would reduce high-frequency noise and not the daily periodicities. Also, it fills in possible gaps in the data.

In Figure 6.2 the time series for the two weeks chosen in September 2011 are plotted. The upper part of the Figure shows the residuals obtained by Bernese processing, not corrected by OTL. On the lower part of the Figure, the same data is plotted, corrected by FES2004 model. After a visual comparison, the periodicities from the upper plot disappear from the lower plot. This means that the OTL corrections applied by Bernese from FES2004 model eliminate the signal related to the tides that is above the noise level in the time series. However, modeled data and observed data sometimes differ. As mentioned in the introduction of this Chapter (Section 6.1), the difference between predicted and observed mareograph data in ROTA station was up to 20 cm in September 2011. This difference could impose a load not visible in the time series that is detected in its power spectrum.

A discrete (or fast) Fourier transform is applied to OTL corrected and not corrected ROTA GPS data during the selected period in September 2011. Welch method [*Welch*, 1967] allows a Fourier transformation of discrete data as the currently processed. This transformation sometimes reveals spectral content even among data that appears noisy in the time domain.

The resulting time series from the fast Fourier transform application are displayed in Figure 6.5 for the whole spectrum (top) and for a zoom to the lower frequencies (bottom). As expected, the biggest amplitude is found for the frequency related to 12.42 hours. This period coincides with the main semidiurnal period of the tides, M_2 [*IERS Technical Note n. 36*, 2010b]. Note that there is a peak in the same frequency for the corrected data, but it is not significant among the rest of peaks. This is, it is known that such peak is bound to exist, but it would not outstand if it was not looked for.

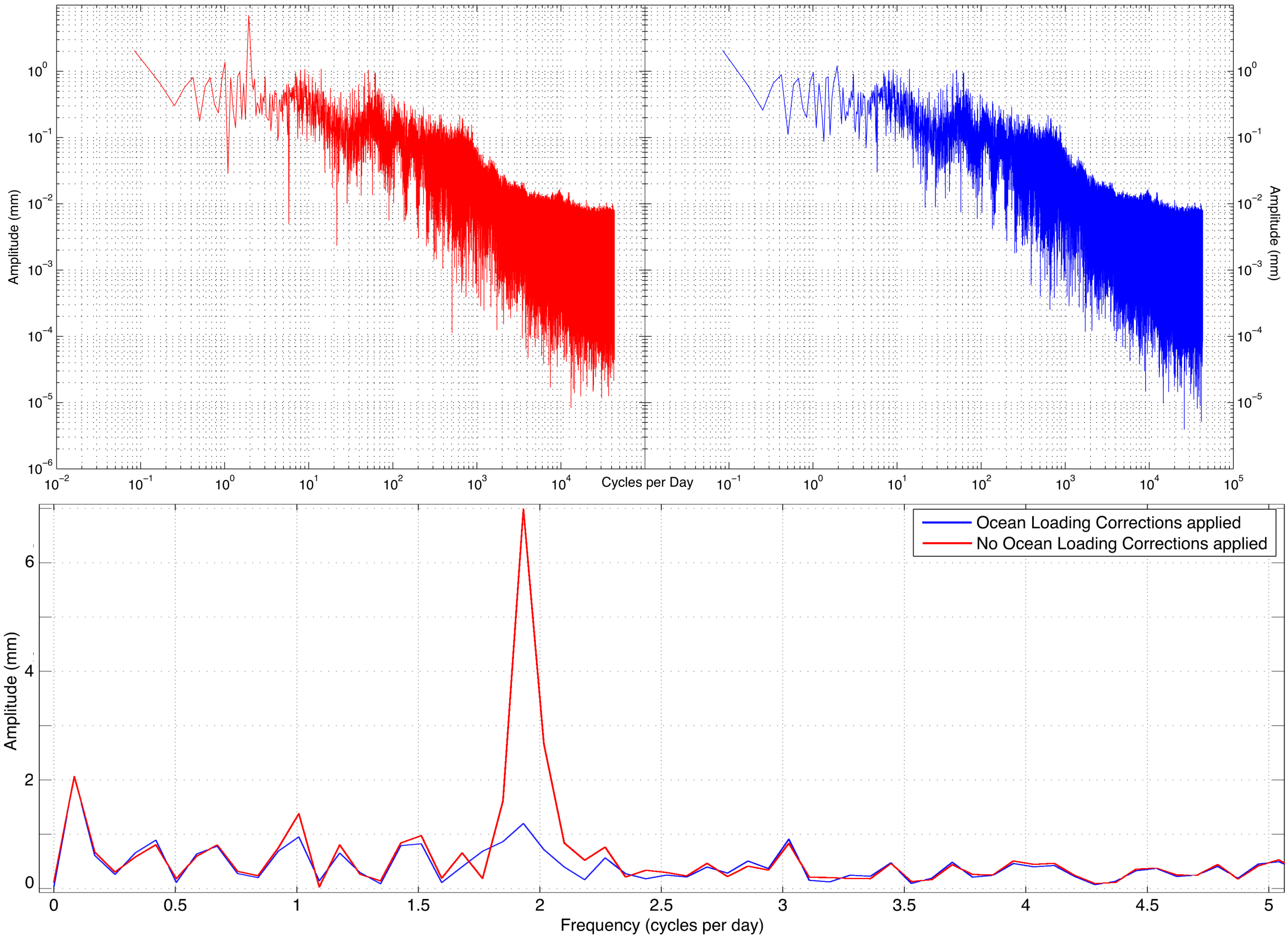

Figure 6.5: Power Spectrum for station ROTA GPS in the two weeks of data in September 2011 (DOY from 262 to 277). Zoom to the lower frequency terms (bottom).

As the records from extreme tides in March show bigger amplitudes than in September 2011, the possibility of obtaining a peak for the 12.42 hours frequency in the March OTL corrected data is higher than in September. However, its power spectrum does not show any distinct frequency for OTL corrected time series from stations HUEL, ALGC and UCAD. Therefore, data not corrected by OTL will be used for the comparison between mareograph and GPS (Section 6.4.2).

For the filters studied in Section 4.2.3, a power spectrum analysis of the data after filtering with different time windows is also computed. The results after a fast Fourier transformation of ROTA time series are plotted in Figure 6.6. The upper part side shows results for unfiltered and three versions of filtered data. The plot on the lower part shows a zoom to the lower frequencies. The decrease of higher frequencies gives the confirmation of the goodness of the filter. Furthermore, the filter does not eliminate the tidal periods and barely reduces the amplitude of the signal. The behaviour of SFER and UCAD is almost identical.

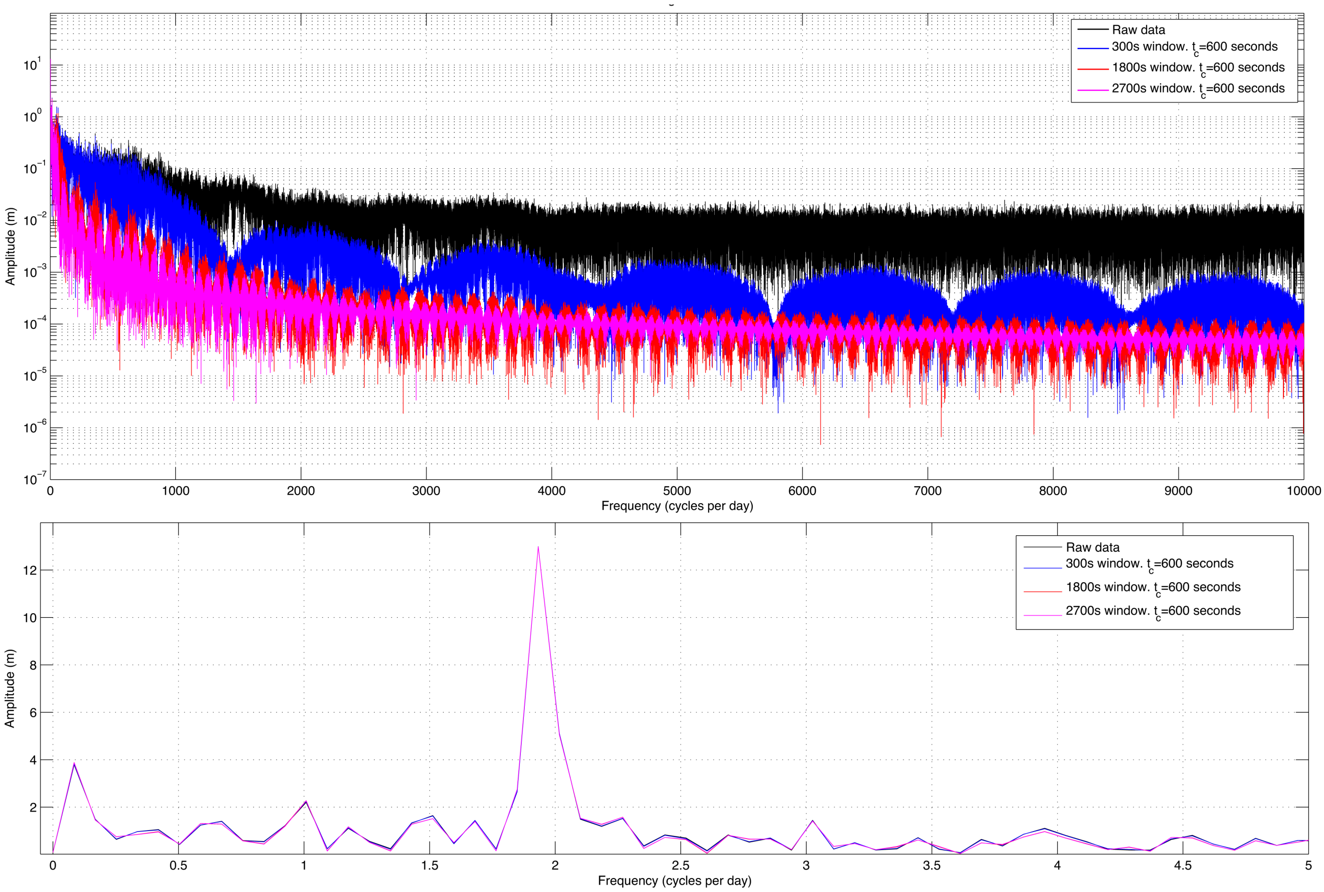

Figure 6.6: Power spectrum of four different datasets obtained from ROTA GPS up coordinate on DOY 270 2011: Raw data (black), 300 seconds window (blue), 1800 seconds window (red) and 2700 seconds window (magenta). t_c= 600 seconds. Zoom to the lowest frequencies (bottom).

6.4 Extreme Tides during March and September 2011

One of the goals of this dissertation is to set up an early warning system for tsunamis in the Iberian Peninsula. The area that is more endangered by tsunamis is the southwestern part of Iberia. As there are no GPS records available for any past tsunami, the extreme tides observed in March and September 2011 are used as a test case.

Water loads the crust enough to be visible in GPS time series, as in Figure 6.2. The extreme tides were also recorded by several mareographs placed on the western coast of Andalucía. The difference between the time when the maximum water height and the minimum GPS height (maximum subsidence) occurred is of interest. It helps to estimate the accommodation time of the crust in the area. Also, the relationship between recorded water height and measured vertical subsidence in the devices co-located could lead to a possible estimation of the surge due to an incoming tsunami. This must be analyzed carefully because loading does not have to be directly related to water height only, but with the total amount of water in the surroundings.

6.4.1 Mareograph Time Series

During the two extreme tide events in 2011, the mareographs of Figure 6.1 recorded the water height. The devices in Cádiz and Huelva documented both periods. PUNTALES recorded only the event in March, and ROTA only in September.

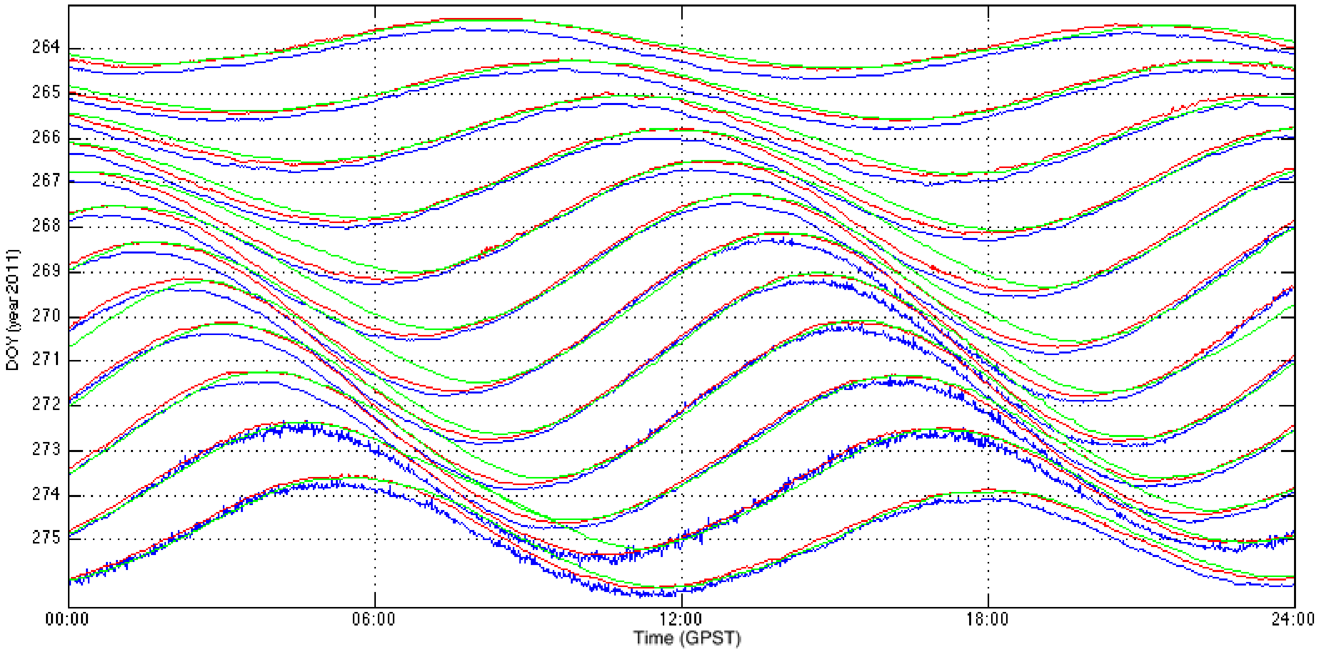

Figure 6.7: Stacking for September data from ROTA (in blue), CADIZ (in green) and HUELVA (in red) mareographs. DOY 270, year 2011. Scale in Y axis is 1 meter.

ROTA and HUELVA mareographs recorded data each minute. The rest of the devices were set up with 5 minutes sampling rate. The predicted values have a 10 minutes sampling. A linear interpolation is applied to the data to increase the sampling to 1 Hz, matching the GPS kinematic output rate.

The data from the different mareographs is stacked in Figure 6.7 for September 2011. The correlation ratio and lag between CADIZ and ROTA are given in Table 6.3. The Figure and Table mentioned before show that the tides recorded by CADIZ mareograph are shifted by 7 to 23 minutes with respect to the tides observed by ROTA. CADIZ mareograph is located inside the Cádiz bay, see Figure 6.1; the mareograph in ROTA is closer to open ocean. The obtained correlation is above 98% for all the days considered, and the lag between both mareographs is up to 23 minutes, with ROTA ahead of CADIZ. A similar procedure was carried out for HUELVA recordings. The correlation ranges between 95 and 97% and the lag reaches up to 15 minutes. This matches the theory that states that waves travel from West to East.

	264	**265**	**266**	**267**	**268**	**269**	**270**	**271**	**272**	**273**	**274**	**275**
Correlation	99%	99%	99%	98%	98%	99%	99%	99%	99%	99%	98%	99%
Lag (min)	19:06	18:18	12:04	12:09	15:46	17:18	23:06	21:12	19:20	16:10	17:50	07:20

Table 6.3: Correlation ratio and lag in minutes and seconds between Cádiz and Rota mareographs in September 2011.

The data recorded in March 2011 is plotted in Figure H.7. Table 6.4 shows a 99% correlation between CADIZ and PUNTALES for all the days considered. For this dataset, the lag between both sites reaches up to 13 minutes, with PUNTALES ahead of CADIZ. The tides in CADIZ are always a few minutes after Puntales in March, which does not follow the fact that tidal waves travel West to East. This can explained by the location of the mareographs: the complex bathymetry and water flow within the bay alters the behaviour of CADIZ and PUNTALES data.

According to a personal communication by M.Sc. S. Moreno from the Spanish Hydrographic Institute, data from CADIZ mareograph always presents some irregularities, including a small delay in time of approximately 3 minutes. Therefore, only data from ROTA and HUELVA mareographs will be used from this point on.

	72	**73**	**74**	**75**	**76**	**77**	**78**	**79**	**80**	**81**	**82**	**83**	**84**	**85**
Correlation	99%	99%	99%	99%	99%	99%	99%	99%	99%	99%	99%	99%	99%	99%
Lag (min)	4:35	4:14	4:38	0	2:37	5:54	9:43	12:36	13:15	9:52	6:29	1:56	0	0

Table 6.4: Correlation ratio and lag in minutes and seconds between Cádiz and Puntales mareographs in March 2011.

6.4.2 Comparison between Mareograph and GPS Observed Data

The co-location of GPS and mareograph in Rota city give the best opportunity to compare the different datasets. Both devices were functional in September 2011: the mareograph recorded data every minute, and the GPS gave measurements every second.

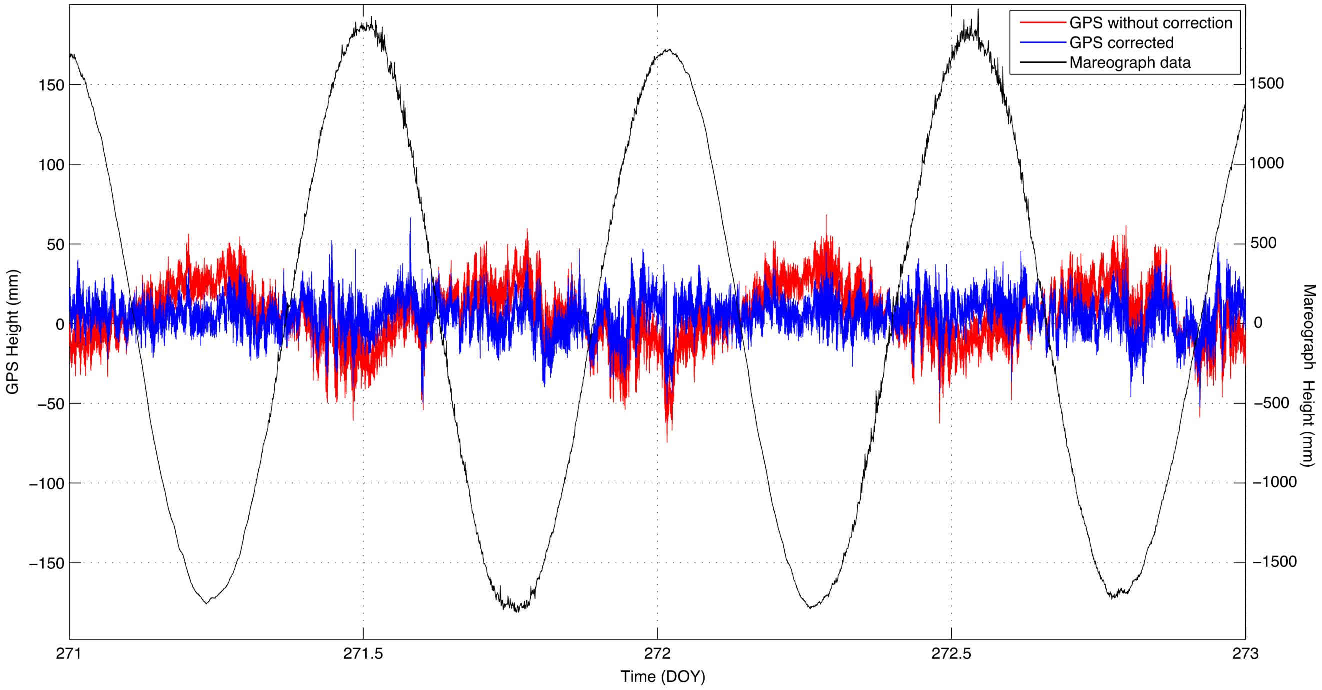

Figure 6.8: ROTA mareograph recordings and GPS estimated signals in September 2011. Unfiltered signals, demeaned. In blue, GPS data not corrected by OTL. In red, GPS data corrected. In black, Mareograph data.

A visual comparison between ROTA mareograph and GPS data is displayed in Figure 6.8. The residuals of the GPS kinematic time series corrected (red) and uncorrected (blue) from ocean tide loading are plotted together with the mareograph recordings. The main information that can be obtained from this Figure is that the increase in the recorded water height and the subsidence measured by GPS are almost in phase. Nevertheless, there is a time lag between both signals, either due to the accommodation time of the crust from the weight of the water or due to the global accumulation of water in the vicinity of the GPS.

Periodicity in the signals from ROTA is clear in Figure 6.8. Theoretically, their frequency should be equal, as both perturbations are tide-related. This is demonstrated in Figure 6.9.

Figure 6.9 shows the power spectrum obtained from ROTA mareograph (black) and uncorrected GPS (red) during DOY 262 to 276 in 2011, The first peak is found at 0.1 cycles per day and indicates the number of samples. The second peak is close to 1 cycle per day, and coincides with the main diurnal harmonic (K_1=23.93 h). And the third peak, close to 2 cycles per day, corresponds to the the dominant semidiurnal wave (M_2=12.42 h) [*IERS Technical*

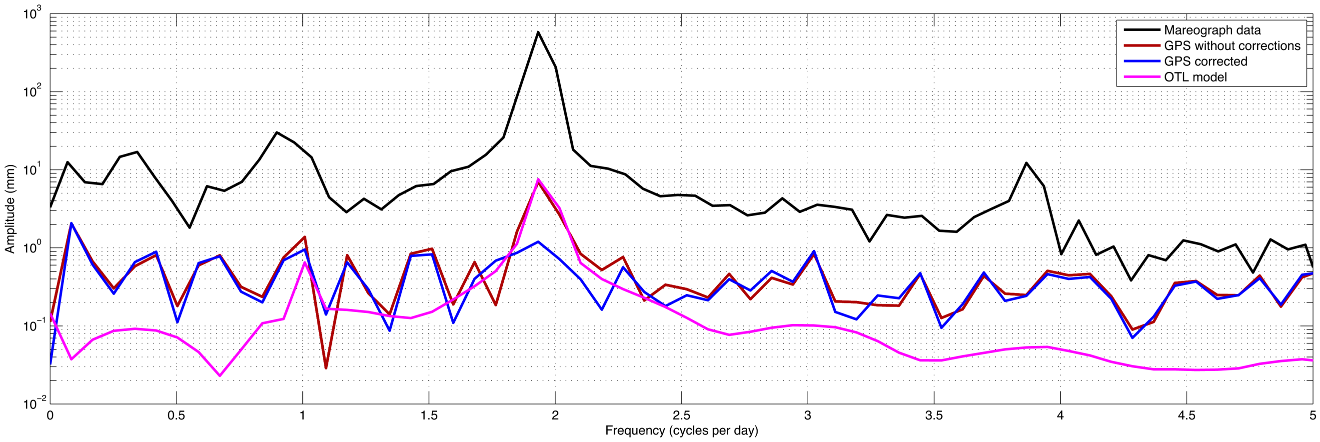

Figure 6.9: Power spectrum from ROTA mareograph and GPS recorded signals during September 2011. GPS data not corrected by Ocean Loading in red, corrected in blue. Mareograph data in black. FES2004 OTL model in magenta.

Note n. 36, 2010b]. Longer period waves are not found in the data because the sample is not long enough. This is, the shortest long period wave that is bigger than a day has a 13.66 days periodicity (M_f, lunar fortnightly), and the samples processed here are only 16 days long. In order to obtain other periodicities as O_1 or S_2, at least 328 and 355 hours are necessary, respectively [*Godin*, 1972].

The residual computed from GPS signal after OTL correction does not show any discernible power related to the semidiurnal harmonic M_2. This indicates that the correction of OTL made by Bernese using the FES2004 model is good, eliminating the signal above noise level. In other words, the FES2004 models accurately the tides in the region.

The calculation of the time lag between mareograph recordings and GPS measurements is also of interest. However, it has been attempted without a clear outcome. A correlation between mareograph and filtered GPS signal has been computed as well. An exponentially weighted moving average filter does attenuate the amplitudes in a subtle way, but the relative maximums and minimums remain in the same position in the signal. The inverse correlation ratio between mareograph and GPS in Rota is less than 40%, which is not very significant. A parallel computation was carried out for the data from the devices in Huelva, obtaining similar results: the inverse correlation between signals reached only a 35%. Moreover, the time lag between maximum water height and subsidence ranged from -2 to 3 hours, depending on the day, which is not plausible.

6.4.3 OTL Deformation Profiles

The propagation direction of the oceanic tide is monitored and evaluated here by studying the crustal subsidence induced by the tides. Two different profiles have been chosen to calculate the subsidence in the GPS stations, induced by the extreme tides in September 2011. The first profile follows the coast of Southern Iberia from West to East: LAGO, HUEL, ROTA, SFER, UCAD, ALGC, CEU1 and MALA, see Figure 6.10. The second profile begins in ROTA and moves towards the center of the Peninsula: ROTA, COBA, SONS, YEBE, ZARA.

The results from correlating ROTA GPS residuals from the filtered kinematic time series to the rest of the stations in both profiles can be checked in Table 6.5, for each day in the selected period from September 2011. The lag between the absolute maximum subsidence of ROTA and the closest local maximum subsidence for the second station is also computed for each day. The last three columns correspond to the profile towards the center of the Peninsula. The rest, to the profile from West to East. As expected, the biggest correlations are found for the days with higher tides, DOY 270-272 in 2011. The time lag between the stations does not follow any discernible pattern for any of the profiles.

The same procedure has been performed for unfiltered GPS time series not corrected by OTL, with similar results. Moreover, a parallel computation was carried out with GPS data corrected by OTL. As seen in Section 6.3.4, the correction of GPS data by OTL completely eliminates this signal. As expected, the kinematic time series obtained for the dataset does not present any pattern at all, only showing the undisturbed GPS kinematic time series behaviour as it would occur in any other normal day.

		Profile W-E							Profile to the center			
		LAGO	**HUEL**	**UCAD**	**SFER**	**ALGC**	**CEU1**	**MALA**	**COBA**	**SONS**	**YEBE**	**ZARA**
km to ROTA		-232	-83	14	20	97	178	237	203	398	518	729
264	**Lag (s)**	-500	-123	0	-39	2816	537	123	10727	-7692	3815	19614
	Correlation	20%	40%	40%	39%	31%	28%	34%	21%	33%	13%	23%
265	**Lag (s)**	10	-3235	25520	-7	416	1029	978	-999	271	-1956	676
	Correlation	34%	32%	40%	47%	32%	20%	52%	21%	25%	14%	30%
266	**Lag (s)**	-672	-6036	-9220	-10128	11973	887	16122	14116	-22146	N/A	17488
	Correlation	39%	23%	12%	29%	26%	40%	34%	24%	21%	N/A	30%
267	**Lag (s)**	-2290	-26802	-193	-74	7173	3256	6201	1616	3244	N/A	-84
	Correlation	15%	26%	59%	63%	25%	38%	29%	26%	33%	N/A	37%
268	**Lag (s)**	-124	846	17151	0	-116	3410	2376	37	5997	3965	6024
	Correlation	24%	51%	17%	70%	45%	42%	39%	56%	38%	34%	51%
269	**Lag (s)**	-244	711	1508	-1893	5289	6198	654	330	1776	5764	6338
	Correlation	49%	38%	31%	61%	41%	42%	51%	52%	50%	29%	45%
270	**Lag (s)**	-3351	5151	-345	5373	0	864	1428	362	5780	5567	5895
	Correlation	67%	62%	62%	58%	75%	60%	49%	46%	58%	50%	52%
271	**Lag (s)**	120	877	2963	1012	-581	1002	9912	1155	2017	3315	1661
	Correlation	72%	68%	29%	80%	56%	71%	68%	63%	50%	38%	67%
272	**Lag (s)**	-1009	761	-1695	-211	-177	314	1873	304	3371	-262	5678
	Correlation	65%	70%	33%	72%	68%	45%	29%	69%	57%	43%	44%
273	**Lag (s)**	98	-340	-1612	-506	-93	3179	252	1053	1794	3245	6499
	Correlation	51%	63%	26%	60%	59%	36%	56%	58%	45%	30%	30%
274	**Lag (s)**	-10	-877	1755	-1491	3257	2291	863	-1478	4306	-7527	-6686
	Correlation	28%	31%	23%	54%	29%	27%	42%	24%	19%	13%	21%
275	**Lag (s)**	341	875	-1739	1786	684	992	3187	-1436	-2083	4163	1423
	Correlation	35%	40%	18%	50%	29%	34%	41%	28%	21%	12%	15%

Table 6.5: Lag in seconds between ROTA GPS absolute maximum and the closest local maximum from the rest of the GPS stations in September 2011, for both profiles. Correlation ratio is also listed.

The unclear comparison from Table 6.5 could be due to the water redistribution around the Peninsula, with some piling-up due to the local bathymetry and topography. However, it can be also due to the high noise in the time series, or the occurrence of gaps in the data, as seen in Figure 6.3. In order to check this, the load estimated by SPOTL from FES2004 model in the locations of the two profiles from Table 6.5 is also computed. The results are summarized in Tables 6.6 and 6.7, showing the maximum subsidence estimated (Subsidence) and the time difference between the occurrence of both maximums (Lag). They include the subsidence estimated at the moment where the maximum in ROTA occurs (Subsidence 2).

The information in Table 6.6 for the profile from West to East is plotted in Figure 6.11. For this profile, the maximum subsidence diminishes as the profile goes to the East, except for HUEL. The epoch when the maximum is found for each station does not follow a clear pattern. In LAGO, the maximum occurs 2 minutes 26 seconds before than in ROTA, but in HUEL the maximum is estimated about 4 minutes after ROTA. Also, the results show that the maximum is found in UCAD and SFER before than in ROTA. The latter can be explained for the water redistribution close to the coast, that affects the loading in different manners. On the other hand, the subsidence expected for each site at the time where the maximum is found in ROTA is very close to its maximum subsidence, due to the fact that they are very close in time (up to only 13.5 minutes for MALA).

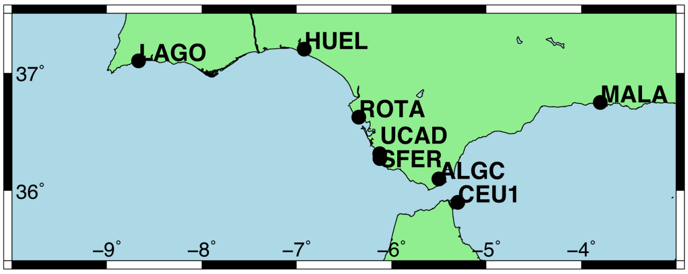

Figure 6.10: Map showing the locations of the GPS receivers in the profile from West to East.

	LAGO	HUEL	ROTA	UCAD	SFER	ALGC	CEU1	MALA
Subsidence (mm)	54.5	37.5	41.9	39.9	41.3	31.4	29.5	26.2
Lag (min)	-2:26	3:49	0:00	-0:36	-1:36	5:07	5:41	13:31
Subsidence 2 (mm)	54.5	37.5	41.9	39.9	41.3	31.3	29.5	26.0

Table 6.6: SPOTL computed FES2004 vertical subsidence for the stations in the profile from West to East. Sorted by longitude. Distance and time difference with respect to ROTA. Data plotted in Figure 6.11.

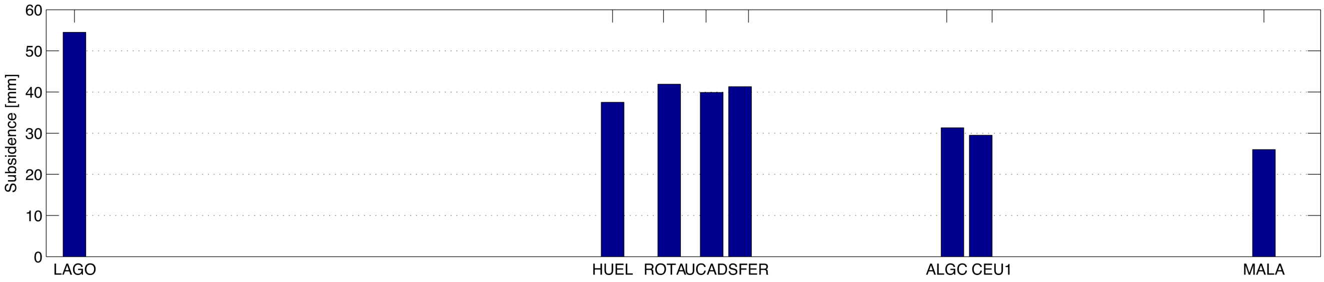

Figure 6.11: Subsidence (mm) at the time where the maximum subsidence is found in ROTA. Results computed by SPOTL using FES2004 model. Profile West to East, stations sorted by longitude. Data from Table 6.6.

SPOTL computed subsidence from FES2004 model at the GPS locations chosen for the profile inside the Peninsula are listed in Table 6.7. The expected decay pattern towards the center of the Peninsula is clear. In order to see this pattern in more detail, another profile is set from LAGO towards ZARA. Both stations are 1000 km away, and nine auxiliary points are chosen between them, separated 100 km. This profile is plotted in Figure 6.12. The results from SPOTL computations can be checked in Table 6.8, and can be seen in Figure 6.13. The maximum subsidence decreases towards the center of the Peninsula until ZARA. The evolution of the time it happens follows a parallel path: the maximum is found later from one station to the next. The subsidence found at the different stations at the time it occurs in LAGO also diminishes the closer it gets to ZARA, which matches the evolution of the maximums, as mentioned before.

A further research could be done, comparing SPOTL computed subsidence from FES2004 model and GPS time series not corrected by OTL. However, the FES2004 corrections applied by Bernese were compared with the subsidence computed from SPOTL, and the difference between both signals does not rise above a 2%. Therefore, they can be considered equal.

	ROTA	COBA	SONS	YEBE	ZARA
Subsidence (mm)	41.9	24.8	23.8	24.3	31.5
Lag (h)	0	0:53:46	1:09:46	1:16:31	2:09:39
Subsidence 2 (mm)	41.9	23.7	21.7	21.8	19.1

Table 6.7: SPOTL computed FES2004 vertical subsidence output for the locations of the GPS in the profile towards the center of the Iberian Peninsula. Maximum in the time series (Subsidence), and time difference with respect to ROTA. Value of the computed subsidence at the time ROTA reaches its maximum (Subsidence 2).

Figure 6.12: Map showing the points chosen for the profile from LAGO to ZARA.

	LAGO	100 km	200 km	300 km	400 km	500 km	600 km	700 km	800 km	900 km	ZARA
Subs. (mm)	54.5	40.5	33.4	29.4	26.9	25.3	24.2	23.4	23.1	22.6	22.2
Lag (h)	0:00:00	0:06:30	0:43:12	0:53:12	1:01:07	1:08:05	1:13:11	1:18:33	1:23:12	2:08:44	2:12:05
Subs2 (mm)	54.5	40.5	33.1	28.4	25.4	23.4	22.1	20.9	20.4	19.7	19.1

Table 6.8: SPOTL computed FES2004 vertical subsidence for the stations in the profile from LAGO to ZARA. Maximum in the time series (Subs), and time difference with respect to LAGO. Value of the computed subsidence at the time LAGO reaches its maximum (Subs2). Data plotted in Figure 6.13.

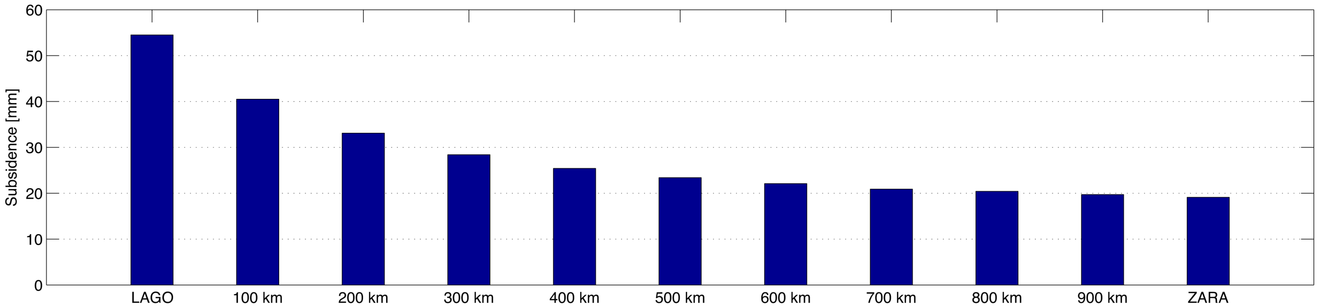

Figure 6.13: Subsidence (mm) at the time where the maximum subsidence is found in LAGO. Results computed by SPOTL using FES2004 model. Profile from LAGO to ZARA. Data from Table 6.8.

6.5 Error Assessment

The combination of the daily results for days 262-268 of year 2011 corrected by OTL shows a repeatability of 1.45, 1.13 and 4.19 mm in North, East and height, respectively, for the stations considered in the network. Those days are not influenced by the extreme tides studied here. This indicates that the solutions in those days are of good quality.

	Unfiltered			**EWMA filter, 1800 s window, t_c=600 s**		
	S_NN (mm)	S_NE (mm)	S_NU (mm)	S_NN (mm)	S_NE (mm)	S_NU (mm)
ALGC	5.5	4.2	11.3	4.2	3.1	7.1
ROTA	7.5	6.2	15.2	5.1	4.0	8.8
SFER	8.4	7.5	13.0	3.2	2.6	10.0
UCAD	8.0	4.2	14.2	4.9	4.0	7.3

Table 6.9: Empirical standard deviation (in mm) of the different solutions obtained for 1 second GPS data (corrected by OTL) for unfiltered and filtered data during days 262-268 in year 2011.

The statistics related to 1 second OTL corrected GPS data during the days 262-268 of year 2011 are summarized in Table 6.9.

The reduction in S_N between direct Bernese output and final post-processed data is detailed in Table 6.9. The final scatter is within the expected values for 1 Hz kinematic GPS data (∼0.7 cm, [*Bock et al.*, 2004; *Larson et al.*, 2007]). Filtering the data with a weighted average sliding window filter reduces the noise but does not decrease the signal amplitude as demonstrated in 6.3.4.

6.6 Summary

Water loads the crust vertically, even inducing a lateral tilt in some stations, as seen in Figure 6.2. If not eliminated, the tidal signal is detectable in the GPS recordings (see power spectrum from ROTA GPS station uncorrected in red, Figure 6.5). This deformation, evident in coastal sites, also pushes the crust downwards inland. However, this deformation is not clear in GPS time series, but the OTL at inlands locations can be checked for the theoretical subsidence calculated with SPOTL from FES2004 tidal model.

Baseline selection is crucial for this test case. Some baselines were fixed between TERU and the rest of the stations forming a profile towards the center of the Peninsula. The rest of the baselines are organized by Bernese, attending to the maximum number of observations in each one of them. TERU was chosen because of its large amount of data recorded, because of its distance to the Atlantic Ocean (less influenced by oceanic tides) and because of the big ambiguity resolution provided when tested in baselines with ROTA and UCAD in an end, two important GPS sites for this example. Results are summarized in Table H.2 in the Appendix.

A modified sidereal filter can be implemented for this case, but it is not advisable because the loads studied correspond to tides, which are periodical and would be eliminated if filtered by a MSF. However, it must be pointed out that a modified sidereal filter could be implemented for a near real-time approach when applying for a standard data processing, because the tsunami load is not related to tides (despite it could resemble a very extreme and quick tide, see Section 2.2.3) and it would not repeat each day under any circumstances.

The FES2004 model used for ocean tidal loading in Bernese correct GPS signals by loads in a way that the periodical residuals are always below noise level. There are no periodicities visible in the power spectrum of the time series from Bernese processing output, see blue line in Figure 6.5. The contribution of the FES2004 to the vertical GPS time series is computed by SPOTL and can be checked in Section 6.4.3. It agrees with the Bernese OTL corrections within a 98%.

After checking the performance of the mareographs, only data from ROTA and HUELVA was decided to be used. Mareographs in Puerto de Santa María and Carraca did not record any data during the weeks of interest. PUNTALES and CADIZ mareographs are placed inside the Cádiz Bay, so the water waves are affected by local effects, spoiling the records due to the interferences with themselves. Moreover, CADIZ mareograph presents irregularities and a small delay in time.

Information obtained from tide gauges are compared with the results derived from GPS data processing. An estimation of the time shift between a wave and the induced crustal response is a relevant information leading to a more accurate tsunami arrival time forecast. This is, knowing the time needed for the crust to respond to a loading induced by the tide, an estimation of the distance to a wave (or load) produced by a tsunami could be obtained, as well as its height (related to the load imposed). Unfortunately, the correlation between mareograph and GPS data computed in Section 6.4.2 does not lead to a satisfying solution. It is important to remark that the accommodation time obtained could be misleading, as it could be induced by the accumulation of water in the vicinity more than the arrival of the maximum water height.

Moreover, the results concerning the profile towards the center of the Peninsula studied in 6.4.3 show no distinguishable loading pattern for GPS time series, neither in vertical displacement nor in time lag. However, the load computed by SPOTL by using FES2004 model does show a decay pattern towards the center of Iberia. Similar results are found for the profile set from West to East, where coastal GPS receivers are located. The results obtained from GPS recorded data (Table 6.5) in September 2011 show many correlations below 50%, which is not significant: it is not advisable to derive conclusions from it. Nevertheless, the correlation between ROTA and several stations in the days of the maximum tides rise up to 80% for SFER in DOY 271, for example.

To sum up, the most valuable result from this Chapter is that the OTL corrections applied by Bernese are of good quality and there is no remaining periodicities related to tides in the corrected data.

7 Numerical Results 3. Comparison of GPS, Water Surge Models, Altimetry and Tide Gauges During a Storm Surge in Northern Germany

In this Chapter, GPS data recorded during the cyclone Xaver on 5^{th} and 6^{th} of December 2013, which stroke the North Sea, is analyzed and compared with observations from altimetry and tide gauges. The predicted surge given by three different ocean models is compared to several tide gauges records. Moreover, the predicted surge in the models is processed by SPOTL, and the vertical subsidence obtained is compared to GPS estimations.

7.1 Introduction

On December 4^{th}, 2013, Cyclone Xaver (a very intense winter storm) formed south of Greenland. The propagation direction, after entering North Sea on the 5^{th}, was along the East coast of Scotland and England from North to South, continuing then anti-clockwise along the coast and later moving over Southern Norway and Sweden [*Willetts*, 2013]. Its lowest pressure (thus highest water surge) was reached on the 6^{th}. The wind from NW direction created an accumulation of water in the vicinity of the Elbe estuary, which added up to the water surge related to the Cyclone.

Cyclones like Xaver impose a big threat to the population along the coast of the North Sea, especially in the lower regions. The extreme low pressures, combined with the wind-generated waves and with the direction of the wind towards the coast, created a huge water surge [*Scharroo and Fenoglio*, 2013] reaching up to 4.2 meters.

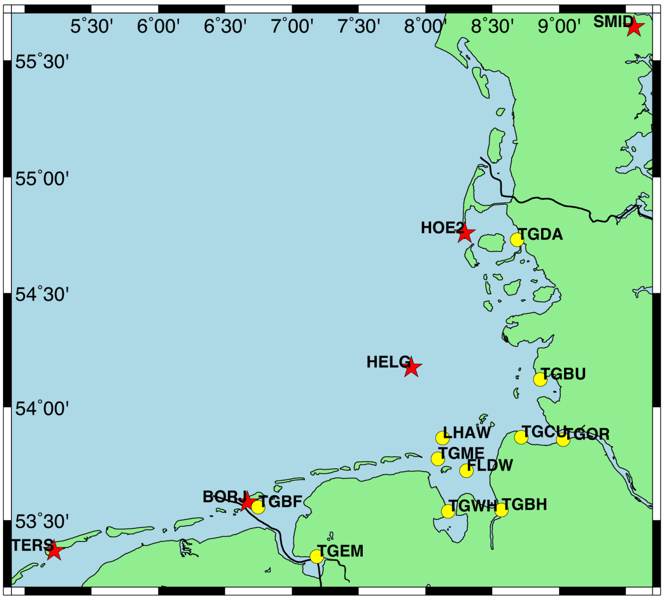

Figure 7.1: EUREF (red) and BfG (yellow) permanent GNSS stations co-located with TG in the region of interest. The grey line indicates AltiKa satellite ground track.

The GPS network used in this test case includes GPS stations belonging to IGS, EUREF and the German Federal Institute of Hydrology (Bundesanstalt für Gewässerkunde, Germany, BfG). 4-char ID, station names, IGS08 Cartesian coordinates (see 1.4), receiver and antenna types can be found in Table D.2. The maps showing all the stations used for the processing are given in Figure I.1. The region of interest is seen in Figure 7.1, including the available GPS receivers co-located with tide gauges (GPS@TG). The coordinates of the tide gauges are listed in Table D.3 and the distance between TG and the closest GPS receiver is given in Table 7.1.

	BORJ	FLDW	HELG	HOE2	LHAW	TGBF	TGBH	TGBU	TGCU	TGDA	TGEM	TGME	TGWH
Dist.(m)	200	1	150	182	1	1	1	2	1	1	1	1	1

Table 7.1: Distance between co-located GPS and tide gauges.

At the time of the maximum surge (December 6th, 5:45 UTC), satellite altimeter AltiKa (Ka-band satellite radar altimeter) on board the SARAL satellite was crossing the North Sea from North to South. Its ground track can be seen in Figure 7.1 (grey line). The surge recorded by the altimeter compares well with nearby tide gauges, within 10 cm for Helgoland [*Scharroo and Fenoglio*, 2013].

The non-tidal loading detected by GPS data analysis is mainly due to the water surge. Effects like pressure also influence the GPS measurements, which are corrected by OTL. However, they are below centimeter level. GPS measurements are compared with the storm surge loading deformation calculated by SPOTL (see Section 4.3). It uses the surge predicted by three different models and calculates the corresponding deformation at the GPS locations. Moreover, the surge height recorded by satellite altimetry and tide gauges, and the predicted by the water surge models, are compared. Some more details about the surge models used for this computations are given in Section 4.3.2.

7.2 GPS Data Availability

Due to the high number of GPS receivers selected for this project (see Table 7.1), only the screening for gaps for stations co-located with tide gauges (GPS@TG) is shown here.

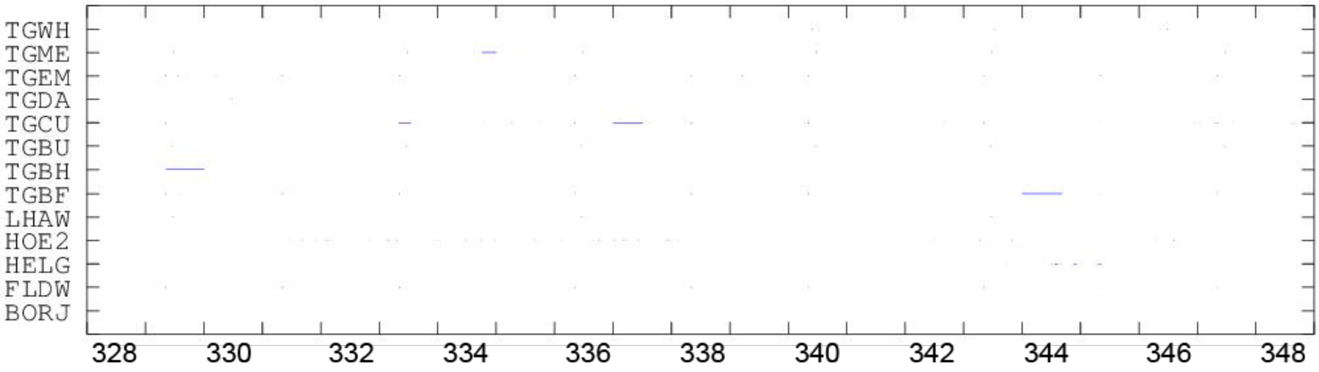

Figure 7.2: Missing RINEX data for the stations of interest, from 28th November to 15th December 2013 (DOY 328-348).

According to Figure 7.2, no big gaps are found in the observation files for the stations in the German Bight co-located with tide gauges.

7.3 GPS Data Analysis

Kinematic Double Differenced solutions in 1 minute steps are obtained for the stations listed in Table 7.1 and for each day. A modified sidereal filter (MSF) is applied, as well as a simple moving average 6 hours window filter. Bernese GNSS software version 5.2 is used for this test case. This version of Bernese can compute S1 and S2 atmospheric tidal loading displacements and also center of mass corrections for ocean and atmospheric tidal loading. However, they are not applied here, see Section 7.4.3. Note that the data is corrected by OTL.

7.3.1 Data Provision

GPS data from the 12 GPS@TG was provided by BfG. 37 additional IGS and EUREF stations are selected to complete the network (listed in Table D.2). Days 328 to 348 of year 2013 are chosen for this study, corresponding to the time interval from 28th November to 15th, 2013.

IGS final products are used, as well as the ionospheric data from CODE.

7.3.2 Ambiguity Fixing Strategy

A classic Bernese processing is run for this test case with IGS final products. RINEX data is downloaded in daily packages with a 30 seconds sampling rate, and baselines are chosen by Bernese depending on the maximum number of observations for each run. The ambiguity resolution strategy is automatically set-up according to the baseline length, as explained in Section 4.1. As the input data rate is 30 seconds, the kinematic output from Bernese is set-up for 1 minute sampling.

Stations HOE2, TGCU, TGDA, TGEM and TGWH were found extremely noisy, with residuals bigger than a meter for the kinematic solution in more than a 50% of the points in the time series. This is validated by a PPP processing, with the same results. Thus, the stations are eliminated from the network and Bernese is re-run.

7.3.3 Post-processing of the Results

Bernese kinematic output is firstly screened for outliers. As the data is highly influenced by the water load in the area, a plain 3-S_N outlier rejection would eliminate valuable data. Therefore, to clean the data, points with residual differences between Bernese output time series and 1 hour moving average filtered data bigger than 3-times S_N are canceled.

A MSF is applied to the resulting time series using all the days available except those from the days influenced by the Cyclone (5^{th} and 6^{th} of December). The strategy is similar to what was explained in 4.2.2, but increasing the time interval used for the filter. Later on, a 6 hours moving average filter is applied. The output is kept at 1 minute sampling for further analysis of the time series; it is downsampled to 15 and 60 minutes time series to match surge models sampling and allow further comparisons.

7.4 The Cyclone Xaver

Cyclone Xaver was a winter storm that reached its maximum around the German Bight on the 5^{th} and 6^{th} of December 2013.

The comparison between the subsidence estimated by GPS and predicted by the surge models and SPOTL is given. The water surge heights recorded by altimetry and tide gauges, and predicted by surge models, are compared as well.

7.4.1 Models of the Cyclone

The predicted surge derived from DWD/BSH, DWD/JRC and ECMWF/JRC models is used here (see Section 4.3.2 for more details about the models). The first is given in 15 minutes sampling; the other two, with 1 hour sampling. The region covered by the models includes the whole North Sea, comprising from -3 to 15 degrees longitude, and from 49 to 62 degrees latitude.

In order to select the model which best fits the observations, the methodology explained by *Geng et al.* [2012] is followed. The best surge model is chosen according to the highest empirical standard deviation (S_N) reduction when correcting the measurements for the predicted quantities (subtracting the latter from the former). In addition to that, a second criterion is selected here for the same purpose: the correlation between measured and predicted quantities.

Both criteria are applied to the comparison between estimated and predicted subsidence, and between observed and predicted water surge height, i.e., observed TG surge against water height derived from surge models.

7.4.2 Xaver Observed by Altimetry and Tide Gauges

The SARAL satellite, carrying the AltiKa satellite radar altimeter, has a ground track repetition of 35 days. In December 2013, it was flying over the German Bight during the day of the maximum water surge (6^{th} December at 4:47 UTC). AltiKa measured wind speed and wave height, with maximums of 18 m/s and 13 m, respectively.

Tide gauge data from the sites listed in Table 7.1 was provided by the German Wasser- und Schiffahrtsverwaltung des Bundes (WSV) in real-time and with 1 minute sampling rate. Additionally, data from two tide gauges in UK, Aberdeen and Lowestoft was downloaded from the National Oceanography Center, Liverpool [http://www.ntslf.org], with a 15 minutes sampling. The surge was obtained by subtracting the predicted tides grin the recorded data. The predicted tides were downloaded for Aberdeen and Lowestoft and computed for the rest of the TG using recordings from 2010 to November 2013, also provided by the WSV.

The sea level surge computed from AltiKa observations is compared by *Scharroo and Fenoglio* [2013] with two tide gauges in the German Bight, in Norderney and Borkum, where the highest surge levels of 3.4 and 3.2 meters were found just after the SARAL overflight. The comparison between AltiKa and the surge modeled along-track is also good, with a S_N of the difference of 0.31, 0.29 and 0.21 meters for DWD/BSH, ECMWF/JRC and DWD/JRC models, respectively.

7.4.3 Comparison Between the Different Strategies

In order to compare data from the different observations, they must correspond to the same physical effect. As an example of the importance of the corrections applied, in Figure 7.3 one can see that the correction by OTL in Bernese shifts the maximum of the subsidence by almost six hours.

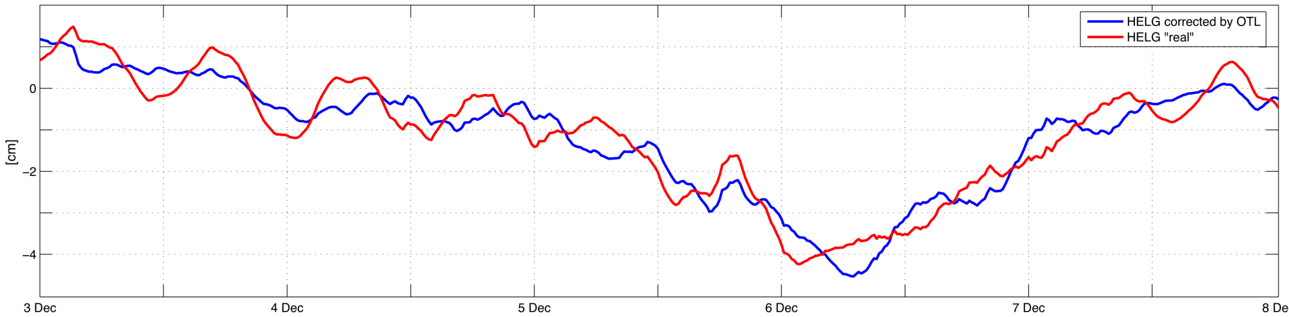

Figure 7.3: 15 minutes sampled GPS data after a 6 hours moving average filter. Results from Bernese, including OTL corrections (blue) and without applying them (red). December 2013.

In Table 7.2, the corrections to the different observations (TG, altimetry), measurements (GPS) and predictions (models, SPOTL) are listed. Note that the goal is to compare the water surge, which is defined as the difference between measured surge and predicted values. Earth Tide correction has been applied to altimetry in order to compare to TG. OTL corrections have been applied to GPS and altimetry, and TG, altimetry data and models have been corrected for ocean tides. None of the data has been corrected by atmospheric loading effects. It is important to mention that any correction applied to the predicted surge models also affects to the predicted load calculated by SPOTL, as the latter is directly derived from the former.

Correction	GPS	TG	Altimetry	Surge models
Earth tide	Y	N	Y	N
Ocean tidal loading	Y	N	Y	N
Ocean tide	N	Y	Y	Y
Atmospheric loading on sea level	N	N	N	N
Atmospheric loading on land	N	N	N	N

Table 7.2: Different corrections applied to GPS, tide gauges, altimetry and surge models.

The surge derived from altimetry and tide gauge recordings can be compared directly with the values predicted by surge models after applying the corrections from Table 7.2. Also, the subsidence estimated by GPS and the predicted loading can be compared as well.

It must be taken into account that the analytical comparison between TG and GPS is not always completely reliable in terms of the time where the maximum surge height and subsidence are found. This is because a rise in TG surge data can be due to a big wave reaching it, but this does not necessary imply that it comes with a big mass of water that could deform the crust and be therefore visible in GPS. And vice-versa, it is possible that the extreme winds push a considerable water mass towards the coast, but the water surge is small at the tide gauge.

However, the scale in time of five days allows just a rough visual comparison between GPS estimated subsidence (red) and TG observed surge (orange) in Figure 7.4 for Helgoland (HELG). In the same figure, the surge predicted by the three surge models is plotted as well, along with the predicted subsidence from DWD/BSH surge model. One can see that the loading predicted by the models and estimated by GPS are very similar in terms of shape and time where the maximum value is found. They show a similar amplitude as well.

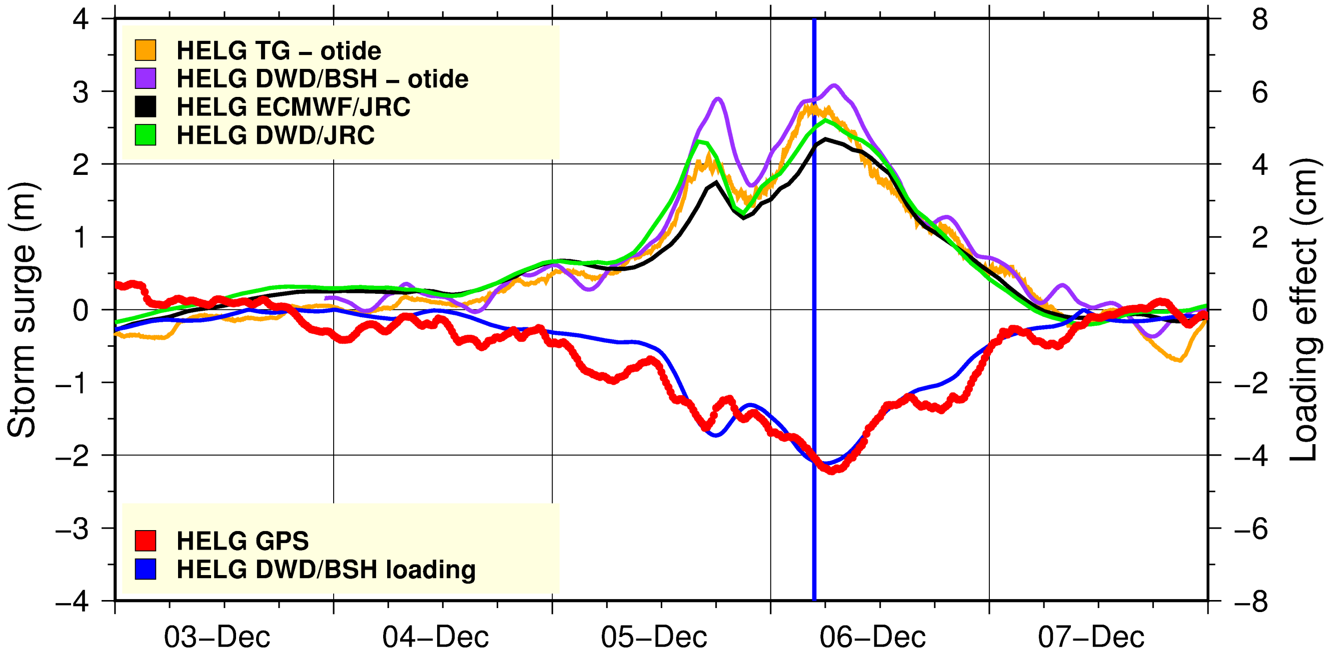

Figure 7.4: Comparison of the different observations in HELG. December 2013.

The comparison between TG observed surge and GPS estimated subsidence is shown in Figure 7.5 for stations TGDA, TGBU, HELG and TGBF with a 15 minutes sampling. The data compares well in most of the stations in terms of shape. Exceptions are TGBH and TGBU, probably due to local topography and bathymetry. Only for HELG, the maximum surge observed was reached around the same moment as the maximum subsidence was estimated. This was also shown in Figure 7.4. For the other three stations, the highest water surge occurred several hours after the maximum subsidence estimated by GPS. As aforesaid, this can be explained by the distribution of the water masses in the area, which affects the total load computed for the point.

7.4.3.1 Comparison Between Estimated GPS Data and Predicted Subsidence

In Tables 7.3 and 7.4 the analytical comparison between GPS estimated and model predicted subsidence can be found, the latter obtained by SPOTL from the three surge models (ECMWF/JRC, DWD/BSH and DWD/JRC). The sampling of the data used is 1 hour in both Tables. Both Tables show, up to down and model by model, the empirical standard deviation (S_N) corresponding to the subsidence estimated by GPS, the S_N of the subsidence predicted, S_N of GPS estimations corrected from the predictions, ratio of S_N reduction (estimated with respect to corrected) and correlation ratio between estimated and predicted data. Moreover, for each GPS site, the maximum ratio of S_N reduction and correlation ratio are highlighted.

Table 7.3 shows that correcting GPS estimated data for the predicted subsidence from the three models does not cause a reduction in S_N during the week previous to the arrival of the Xaver Cyclone to the German Bight. The data S_N can even increase in up to a 44% for some models and stations (e.g.: DWD/JRC model, station BORJ). Despite the values of S_N are similar for the estimated and predicted data, their correlation does not rise above 68% for any of the three models. Yet, the S_N obtained from estimated GPS time series is within the expected (usual) limits. This can be explained by the fact that both estimated and predicted signals are small compared to the noise (small signal to noise ratio). The reduction in S_N can not be used as an estimator of the best-fit model [*Geng*

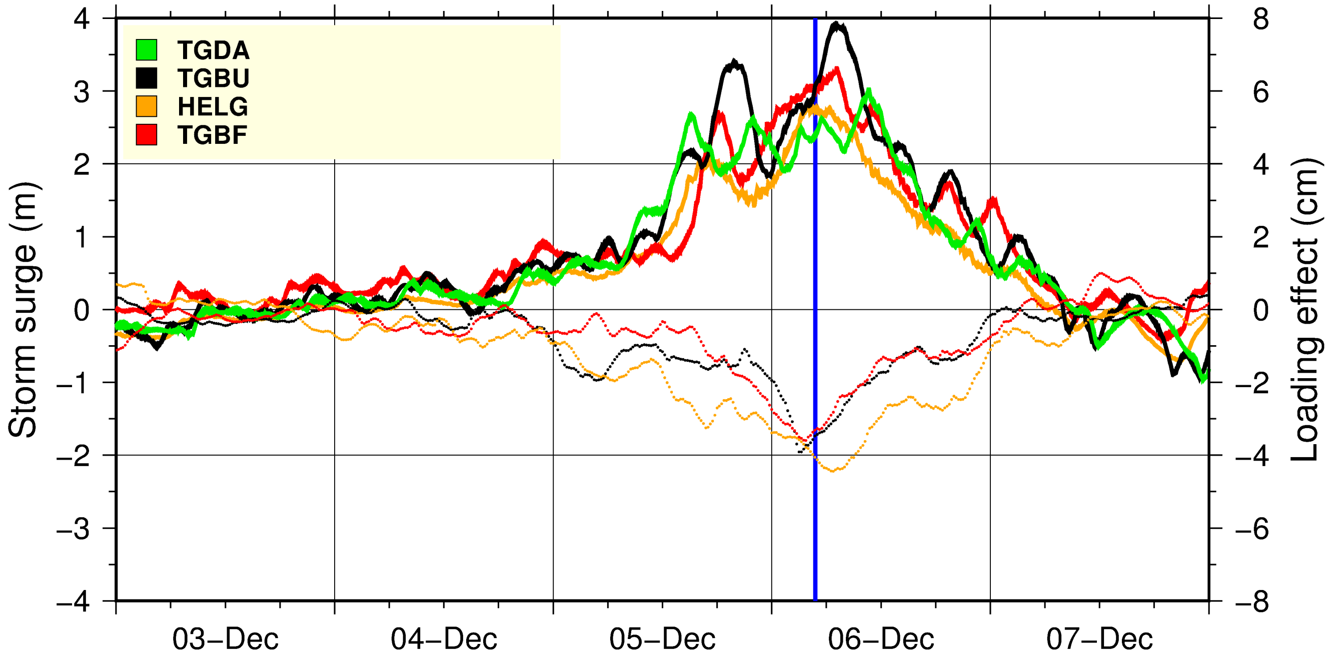

Figure 7.5: Comparison between TG recorded surge (thick lines) and GPS estimations. December 2013.

	BORJ	**FLDW**	**HELG**	**LHAW**	**TGBF**	**TGBH**	**TGBU**	**TGME**
GPS S_N(mm)	4.0	4.7	6.2	5.5	4.9	11.6	3.6	4.3
ECMWF/JRC S_N(mm)	4.3	3.6	4.4	4.0	4.2	2.5	3.2	3.8
GPS-Model S_N(mm)	5.5	4.2	4.8	5.0	5.0	10.7	4.3	4.0
S_N Reduction GPS-Model	-36%	10%	23%	10%	-2%	7%	-18%	7%
Correlation GPS and Model	14%	50%	64%	49%	41%	41%	20%	52%
DWD/JRC S_N(mm)	4.6	3.9	4.8	4.3	4.5	2.7	3.5	4.2
GPS-Model S_N(mm)	5.8	4.1	4.6	4.9	5.1	10.6	4.5	4.1
S_N Reduction GPS-Model	-44%	13%	25%	11%	-4%	8%	-24%	2%
Correlation GPS and Model	12%	56%	67%	53%	41%	43%	-19%	51%
DWD/BSH S_N(mm)	4.3	3.6	4.5	4.0	4.2	2.5	3.1	3.8
GPS-Model S_N(mm)	5.4	4.4	4.5	5.0	5.0	10.5	4.2	4.3
S_N Reduction GPS-Model	-35%	7%	27%	9%	-1%	8%	-15%	0%
Correlation GPS and Model	15%	47%	68%	48%	42%	49%	24%	45%

Table 7.3: Empirical standard deviation S_N of the subsidence estimated (GPS) and predicted (Model) from the different surge models, based on a week uninfluenced by Xaver cyclone (28^{th} November at 00:00 to 4^{th} December at 23:00). Comparison between subsidence estimated and predicted. The correlation between estimated and predicted data is also given. 1 hour sampling.

et al., 2012]. On the other hand, the maximum of the correlation between estimated and predicted subsidence corresponds to DWD/BSH model, except for stations FLDW, LHAW and TGME.

In parallel to Table 7.3, Table 7.4 shows the statistics during the two days where Xaver Cyclone hit the German Bight. During that period, the S_N obtained for estimated and predicted data is much higher than for the previous week. This can be explained by the the vertical subsidence accompanying the water surge and should not be used for a statistical comparison. The values of S_N obtained after correcting estimated from predicted values are similar to those obtained for the estimated subsidence during the week not influenced by Xaver Cyclone. The reduction in S_N when correcting the estimated from the predicted subsidence is higher for model DWD/JRC in all the locations. Therefore, following the criterion described by *Geng et al.* [2012], DWD/JRC is the model that adjusts better to the storm conditions. Moreover, the correlation between estimated and predicted subsidence ranges between 65 and 96% for all the models, which indicates that all of them predict correctly the subsidence. The maximum correlation in almost all the GPS sites, except on HELG, TGBH and TGBU, corresponds to DWD/BSH model.

	BORJ	FLDW	HELG	LHAW	TGBF	TGBH	TGBU	TGME
GPS S_N(mm)	9.4	9.4	9.1	10.7	8.6	5.2	7.5	9.1
ECMWF/JRC S_N(mm)	9.6	7.8	9.5	8.7	9.4	5.3	6.5	8.4
GPS-Model S_N(mm)	4.8	4.3	3.6	6.2	4.5	2.9	5.9	3.4
S_N Reduction GPS-Model	49%	54%	61%	42%	47%	44%	21%	63%
Correlation GPS and Model	87%	89%	93%	81%	88%	85%	65%	93%
DWD/JRC S_N(mm)	8.4	7.1	8.6	8.0	8.2	4.8	6.1	7.6
GPS-Model S_N(mm)	4.2	3.9	3.6	5.6	3.6	2.9	5.8	2.9
S_N Reduction GPS-Model	55%	59%	61%	47%	58%	44%	22%	68%
Correlation GPS and Model	89%	93%	92%	86%	91%	84%	65%	96%
DWD/BSH S_N(mm)	10.9	9.6	11.7	10.8	10.7	6.2	7.9	10.3
GPS-Model S_N(mm)	5.2	5.2	4.1	7.2	5.2	3.8	6.5	4.3
S_N Reduction GPS-Model	45%	45%	54%	32%	40%	27%	13%	53%
Correlation GPS and Model	88%	85%	95%	77%	88%	80%	64%	91%

Table 7.4: Empirical standard deviation S_N of the subsidence estimated (GPS) and predicted (Model) from the different surge models, based on the two days of Xaver Cyclone maximum (5^{th} and 6^{th} December 2013). Comparison between subsidence estimated and predicted. The correlation between estimated and predicted data is also given. 1 hour sampling.

		1 min	**15 min**		**1 hour**			
Station	**Longitude**	**GPS**	**GPS**	**DWD/BSH**	**GPS**	**DWD/BSH**	**DWD/JRC**	**ECMWF/JRC**
BORJ	6.653^o	-36.3	-36.0	-36.8	-35.1	-36.8	-31.4	-35.7
TGBF	6.736^o	-38.5	-38.3	-36.8	-37.3	-35.6	-30.7	-35.0
HELG	7.903^o	-44.6	-44.4	-42.3	-44.0	-42.3	-34.3	-38.1
TGME	8.097^o	-39.8	-40.0	-35.7	-39.2	-35.7	-30.0	-33.2
LHAW	8.125^o	-47.2	-47.1	-37.8	-46.6	-37.8	-31.4	-34.8
FLDW	8.319^o	-42.3	-42.1	-32.7	-41.7	-32.7	-28.0	-31.0
TGBH	8.569^o	-21.4	-21.2	-21.3	-21.1	-21.3	-18.7	-20.8
TGBU	8.847^o	-39.4	-39.1	-28.0	-37.9	-27.9	-24.6	-26.8

Table 7.5: Maximum subsidence for GPS sites, corresponding to estimated GPS and predicted subsidence by surge models. Stations sorted by Longitude. Different samplings: 1, 15 and 60 minutes.

From Table 7.4 it can be concluded that the subsidence predicted by DWD/JRC model gives the best fit for hourly GPS estimated subsidence. However, Table 7.5 shows that the subsidence predicted by DWD/JRC model underestimates the maximum subsidence estimated by GPS by up to 15.8 and 15.2 mm for station LHAW, when compared to 1 and 60 minutes GPS solutions (lines black and red from Figure 7.6). This accounts for 33% of the total displacement estimated by 1 minute GPS. Moreover, despite DWD/JRC gives the most similar time series to GPS in terms of shape (correlation), it is also the model that most miscalculates the subsidence. The model that compares better to GPS estimations in terms of maximum subsidence is DWD/BSH (even exceeding the prediction in 0.5 mm at BORJ, see Figure 7.7). Similar plots for the rest of the GPS sites can be found in Figures I.2, I.3, I.4, I.5, I.6 and I.7.

7.4.3.2 Comparison Between TG Recorded and Predicted Water Surge

A parallel comparison to the analysis of the subsidence from measurements and models is here presented for surge height recorded by tide gauges and predicted by surge models.

Table 7.6 considers two time intervals. The upper part side shows the statistics corresponding to the week previous to the arrival of Xaver Cyclone to the German Bight (28^{th} November at 00:00 to 4^{th} December at 23:00) and the lower part of the Table shows the same results concerning to the days where the Cyclone hit Northern Germany

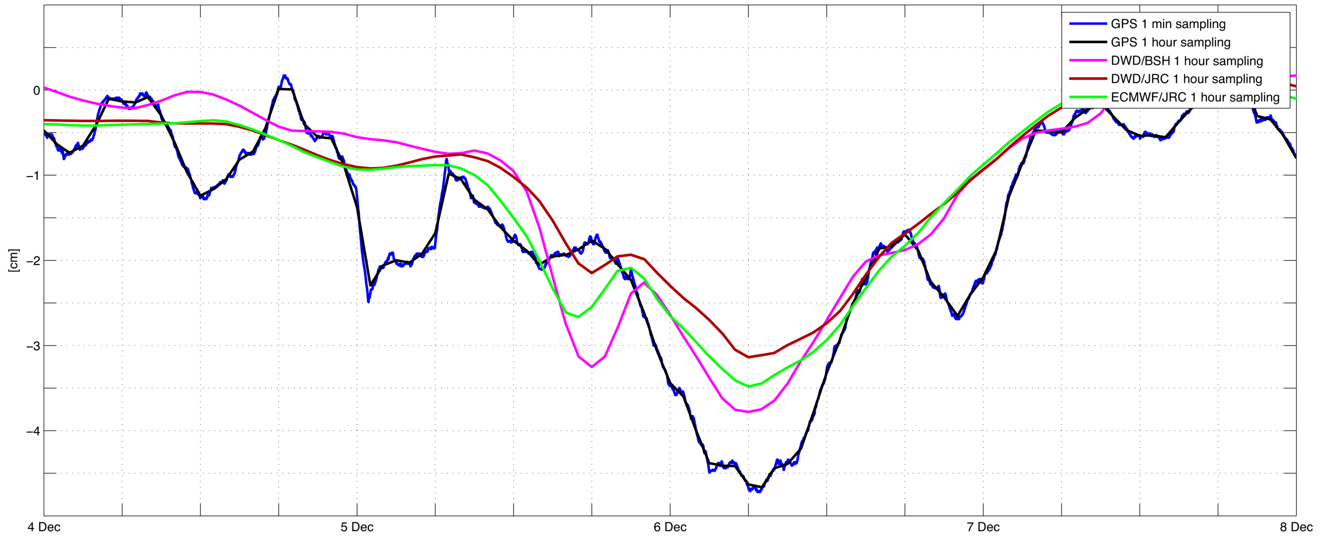

Figure 7.6: Comparison for the different models in LHAW, also for 1 and 60 minutes GPS vertical residuals. December 2013.

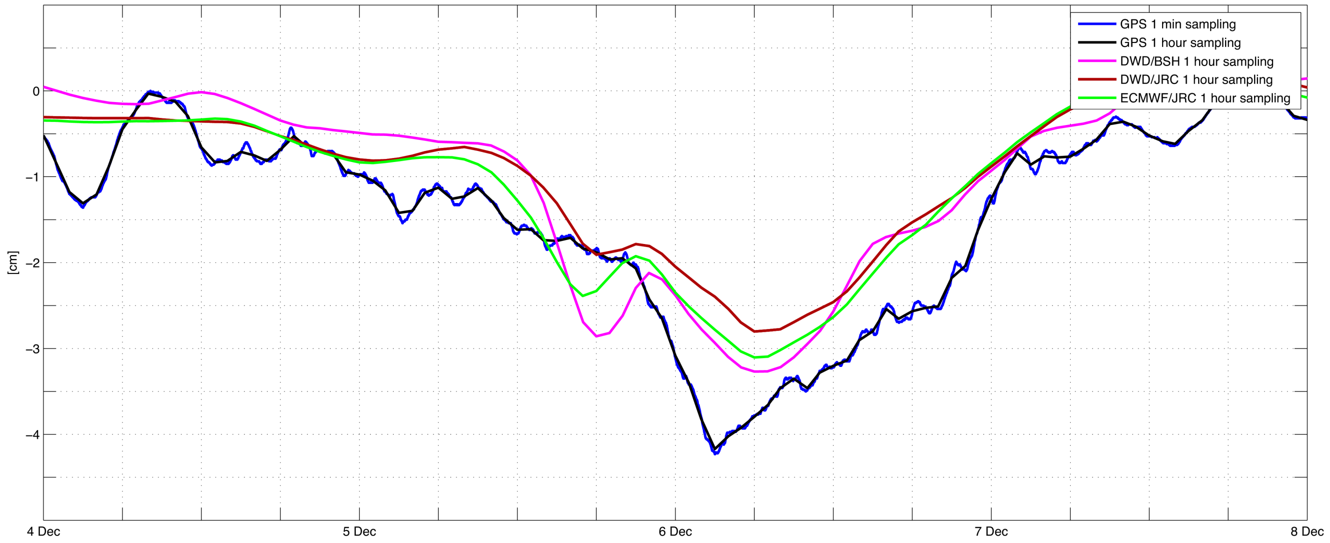

Figure 7.7: Comparison for the different models in FLDW, also for 1 and 60 minutes GPS vertical residuals. December 2013.

(5^{th} and 6^{th} of December). For both time intervals, the analytical comparison between the surge height recorded by TG and predicted by the three surge models (ECMWF/JRC, DWD/BSH and DWD/JRC) is shown. The sampling of the data used is 1 hour. The Table shows, up to down and model by model, the empirical standard deviation (S_N) of the surge height recorded by TG, predicted surge and TG recorded surge corrected from the predictions. Moreover, the ratio of S_N reduction (recorded with respect to corrected) and correlation ratio between recorded and predicted data is given, and for each TG site, the maximum ratio of S_N reduction and correlation ratio are highlighted. This Table is similar to Tables 7.3 and 7.4.

Over the interval not influenced by the Cyclone, (Table 7.6), the best-fit for the TG recorded data is obtained for the ECMWF/JRC model. This is because the S_N reduction of the TG recorded surge corrected by the predicted surge is the highest for almost all the TG sites (excepting Aberdeen, Lowestoft, HELG, HOE2 and TGDA), following the criterion from *Geng et al.* [2012]. Moreover, the correlation between both recorded and predicted surge heights for this model are the largest for almost all the sites, excepting Aberdeen, Lowestoft, HELG, HOE2, TGDA and TGBU. This contradicts the results obtained from the equivalent for GPS (Table 7.3), where the best-fit model is found to be DWD/BSH for the same time period.

		Abe	Low	BORJ	TGBF	TGEM	HELG	TGME	LHAW	TGWH	FLDW	HOE2	TGBH	TGDA	TGCU	TGBU
A week uninfluenced by Xaver	TG S_N(m)	0.16	0.32	0.33	0.33	0.35	0.30	0.32	0.32	0.34	0.34	0.27	0.35	0.28	0.34	0.34
	ECMWF/JRC S_N(m)	0.16	0.40	0.34	0.35	0.36	0.31	0.33	0.33	0.35	0.35	0.29	0.36	0.30	0.35	0.33
	TG-Model S_N(m)	0.09	0.13	0.15	0.16	0.19	0.15	0.15	0.15	0.17	0.16	0.13	0.19	0.16	0.16	0.18
	S_N Reduction TG-Model	45%	59%	54%	53%	44%	50%	54%	52%	49%	52%	50%	47%	45%	53%	47%
	Correlation TG and Model	85%	95%	90%	90%	85%	88%	90%	89%	88%	89%	89%	87%	86%	89%	85%
	DWD/JRC S_N(m)	0.17	0.22	0.35	0.36	0.31	0.33	0.35	0.35	0.37	0.36	0.31	0.37	0.32	0.36	0.35
	TG-Model S_N(m)	0.09	0.29	0.16	0.17	0.23	0.16	0.16	0.16	0.19	0.17	0.14	0.21	0.15	0.17	0.18
	S_N Reduction TG-Model	45%	11%	51%	50%	33%	47%	52%	49%	44%	48%	47%	41%	45%	51%	46%
	Correlation TG and Model	87%	49%	89%	88%	75%	88%	89%	89%	86%	88%	89%	83%	87%	89%	86%
	DWD/BSH S_N(m)	0.16	0.36	0.33	0.30	0.37	0.31	0.34	0.33	0.36	0.35	0.27	0.41	0.26	0.37	0.32
	TG-Model S_N(m)	0.07	0.10	0.17	0.18	0.20	0.14	0.18	0.17	0.22	0.19	0.12	0.28	0.19	0.21	0.24
	S_N Reduction TG-Model	58%	69%	49%	45%	43%	53%	45%	46%	35%	43%	54%	21%	33%	38%	31%
	Correlation TG and Model	92%	96%	87%	84%	85%	89%	86%	86%	80%	84%	90%	74%	76%	83%	75%

		Abe	Low	BORJ	TGBF	TGEM	HELG	TGME	LHAW	TGWH	FLDW	HOE2	TGBH	TGDA	TGCU	TGBU
Two days influenced by Xaver	TG S_N(m)	0.33	0.85	0.83	0.84	1.11	0.72	0.88	0.82	1.03	0.96	0.64	1.15	0.75	0.97	0.98
	ECMWF/JRC S_N(m)	0.36	0.97	0.42	0.43	0.40	0.34	0.38	0.38	0.41	0.40	0.29	0.41	0.30	0.36	0.34
	TG-Model S_N(m)	0.11	0.26	0.50	0.51	0.77	0.43	0.56	0.49	0.69	0.62	0.41	0.84	0.50	0.64	0.71
	S_N Reduction TG-Model	67%	70%	40%	39%	31%	41%	37%	40%	33%	35%	36%	27%	33%	34%	28%
	Correlation TG and Model	95%	97%	88%	87%	91%	92%	91%	92%	90%	91%	87%	84%	89%	93%	88%
	DWD/JRC S_N(m)	0.31	0.80	0.64	0.66	0.68	0.60	0.70	0.68	0.77	0.76	0.53	0.82	0.57	0.76	0.70
	TG-Model S_N(m)	0.09	0.49	0.31	0.31	0.77	0.25	0.28	0.28	0.46	0.34	0.27	0.49	0.35	0.37	0.47
	S_N Reduction TG-Model	72%	43%	62%	63%	31%	65%	68%	66%	55%	64%	57%	58%	54%	62%	52%
	Correlation TG and Model	96%	83%	94%	94%	73%	94%	96%	95%	91%	94%	91%	93%	90%	94%	90%
	DWD/BSH S_N(m)	0.34	0.93	0.94	0.85	1.14	0.92	1.10	1.05	1.17	1.15	0.83	1.35	0.96	1.22	1.06
	TG-Model S_N(m)	0.11	0.19	0.35	0.24	0.50	0.29	0.34	0.34	0.50	0.34	0.35	0.64	0.50	0.47	0.48
	S_N Reduction TG-Model	66%	78%	58%	71%	55%	59%	61%	59%	52%	64%	45%	45%	33%	51%	51%
	Correlation TG and Model	95%	98%	93%	96%	90%	96%	96%	96%	90%	96%	92%	88%	86%	93%	89%

Table 7.6: Empirical standard deviation S_N of the water surge recorded (TG) and predicted (Model) from the different surge models, based on a week uninfluenced by Xaver cyclone (28^{th} November at 00:00 to 4^{th} December at 23:00) (top) and the two days of Xaver cyclone maximum (5^{th} and 6^{th} December 2013) (bottom). Comparison between surge recorded and predicted. The correlation between recorded and predicted data is also given. 1 hour sampling.

On the other hand, the results for the two days during the storm are listed on Table 7.6 (below). Here, the empirical standard deviation (S_N) is higher than in the week uninfluenced by the Cyclone, due to the increase of the surge related to the storm. Following again the paper from *Geng et al.* [2012], the model DWD/JRC is chosen. It gives the maximum number of TG sites where the reduction in S_N is bigger when correcting the recorded surge heights by the predicted data in the same location. For this timespan, the maximum number of sites with the maximum correlation between recorded and predicted data corresponds also to model DWD/JRC. This result matches the outcome from the previous comparison between estimated GPS and predicted subsidence due to the surge (Table 7.4).

The maximum surge height from models is found on the 5^{th} of December at most of the TG sites. This maximum is predicted by the models for all the sites except Aberdeen and Lowestoft. The predicted maximum on the 5^{th} can be explained by a slight mismodeling of the surge due to the complex bathymetry and topography of the German Bight. There is also a local maximum in the TG recordings on that day, but the global maximum is found in the following day. In consequence, the maximum of the surge are calculated for the predicted data after 00:00 UTC on the 6^{th} of December for all the sites except Aberdeen and Lowestoft. The results of this calculation are found in Table 7.7. The downsampling from 1 to 60 minutes does not attenuate the signal more than a 5%. The difference between recorded and predicted surge at TG are higher than 1 meter in a few cases, as in TGBF. DWD/BSH model overestimates the surge maximum for more than the half of the sites, and ECMWF/JRC and DWD/JRC underestimate it for all the TG but Aberdeen and Lowestoft.

		1 min	**15 min**		**1 hour**			
Station	**Longitude**	**TG**	**TG**	**DWD/BSH**	**TG**	**DWD/BSH**	**DWD/JRC**	**ECMWF/JRC**
Aberdeen	-2.080^o	N/A	0.74	0.97	0.74	0.97	1.04	1.10
Lowestoft	1.751^o	N/A	2.18	2.13	2.18	2.07	2.22	2.78
BORJ	6.653^o	3.39	3.33	2.96	3.28	2.96	2.33	2.66
TGBF	6.736^o	3.44	3.39	2.72	3.37	2.64	2.36	2.73
TGEM	7.186^o	3.87	3.82	3.60	3.78	3.60	2.25	2.95
HELG	7.903^o	2.73	2.73	3.20	2.72	3.20	2.34	2.64
TGME	8.097^o	3.30	3.28	3.51	3.21	3.51	2.71	3.00
LHAW	8.125^o	3.09	3.06	3.43	3.02	3.43	2.64	2.91
TGWH	8.181^o	3.78	3.78	3.71	3.75	3.58	2.87	3.22
FLDW	8.319^o	3.36	3.31	3.70	3.26	3.69	2.88	3.18
HOE2	8.319^o	2.46	2.45	2.80	2.42	2.78	2.21	2.36
TGBH	8.569^o	4.23	4.22	4.66	4.19	4.64	2.97	3.37
TGDA	8.681^o	3.04	2.97	3.13	2.87	3.04	2.30	2.53
TGCU	8.708^o	3.74	3.71	3.90	3.68	3.88	2.88	3.19
TGBU	8.847^o	3.90	3.90	3.41	3.90	3.41	2.78	3.02

Table 7.7: Maximum surge recorded by TG and predicted by surge models. Stations sorted by longitude. Different samplings: 1, 15 and 60 minutes. The data downloaded for Aberdeen and Lowestoft has a 15 minutes sampling. The maximum is calculated for TG recordings from the 28^{th} of November to the 15^{th} of December 2013. For Aberdeen and Lowestoft predicted values, the same timespan is considered. For the rest of the predicted sites, the maximum is calculated after the 5^{th} of December.

7.4.4 Propagation Direction of the Storm

One minute post-processed (filtered and smoothed) GPS estimated data is analyzed here to detect the time of maximum subsidence, for all the stations at the German Bight that are co-located with tide gauges. This helps to assess the temporal evolution of the storm, related to the surge loading effects. It has been previously done in the same region by *Geng et al.* [2012], with a 2 hours sampling GPS data and during a storm in 2007. However, the highest temporal sampling of this test case should enhance the solution. The storm temporal evolution is also studied by checking the surge recorded by the several tide gauges placed in the same area.

The closeness between stations within the German Bight and the quick spread of the storm does not allow for a detailed monitoring if using 60 or even 15 minutes data. From the columns corresponding to 15 and 60 minutes sampling in Table 7.8 it can be concluded that all the models and GPS data with different samplings monitor the temporal evolution of the storm correctly at almost each station, except FLDW and TGBU. As an example, Figure 7.7 gives the comparison between estimation and prediction for FLDW. The 3 hours shift of the minimum GPS estimation in FLDW with respect to the minimum predicted by all the models can be explained by a mismodeling of the local topography and bathymetry, which contribute to the accumulation of water in the area.

		1 min	15 min		1 hour			
Station	**Longitude**	**GPS**	**GPS**	**DWD/BSH**	**GPS**	**DWD/BSH**	**DWD/JRC**	**ECMWF/JRC**
BORJ	6.653^{o}	3:38	3:45	5:00	4:00	5:00	6:00	6:00
TGBF	6.736^{o}	3:42	3:45	4:45	4:00	5:00	6:00	6:00
HELG	7.903^{o}	6:38	6:45	6:00	7:00	6:00	6:00	6:00
TGME	8.097^{o}	6:40	6:45	6:00	7:00	6:00	6:00	6:00
LHAW	8.125^{o}	6:43	6:45	6:00	7:00	6:00	6:00	6:00
FLDW	8.319^{o}	3:00	3:00	6:30	3:00	6:00	6:00	6:00
TGBH	8.569^{o}	9:09	9:15	6:15	9:00	6:00	8:00	8:00
TGBU	8.847^{o}	3:05	3:00	5:45	3:00	6:00	8:00	8:00

Table 7.8: Time (UTC of 6th December 2013) of the maximum subsidence for GPS sites, corresponding to estimated GPS and predicted subsidence by surge models. Stations sorted by longitude. Different samplings: 1, 15 and 60 minutes. 6th December 2013.

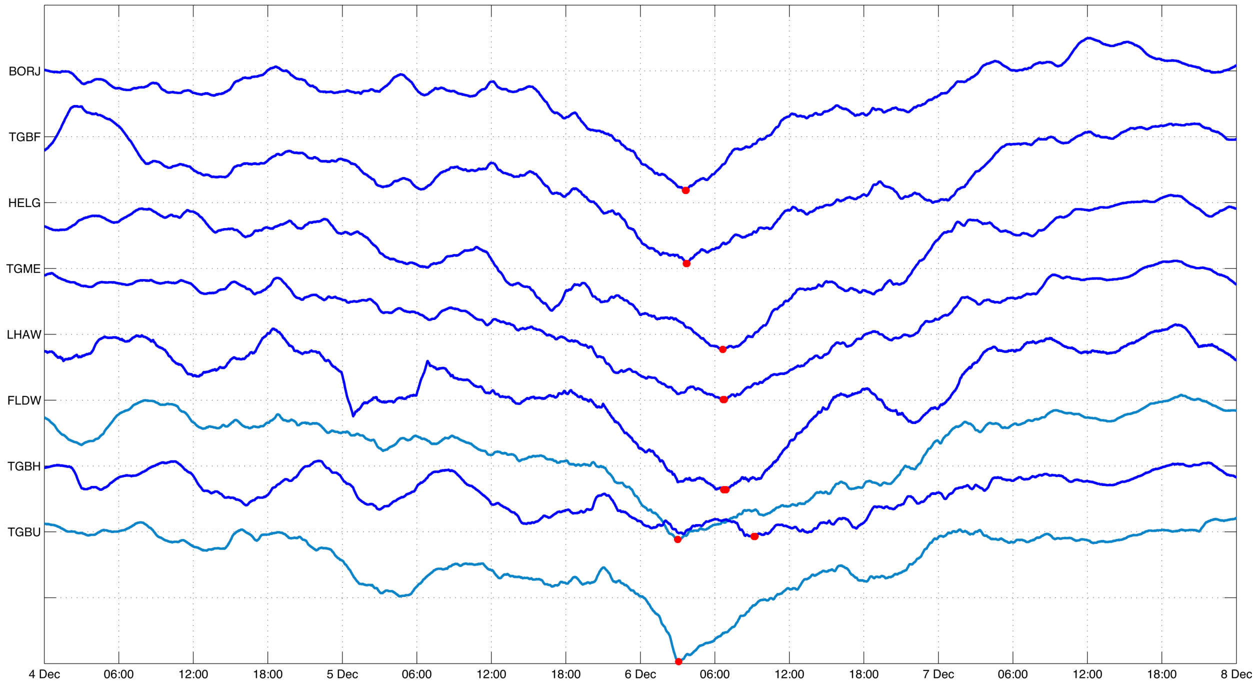

Figure 7.8: 1 minute GPS time series of the stations from Table 7.8, sorted by longitude. Red dots show the minimum value of each station. Scale in Y axis is 2 centimeters. December 2013.

Besides, a much more impressive outcome is obtained when checking the 1 minute sampled GPS estimations (column highlighted in grey, Table 7.8) for the times of the maximum subsidence. Stations FLDW and TGBU are again found outside the expected temporal evolution. The rest of the stations behave exactly as awaited, the maximum subsidence is found following the observed anti-clockwise movement of the storm. A plot showing the maximum subsidence in 1 minute GPS time series of the stations sorted by longitude can be found in Figure 7.8. In it, the maximum subsidence estimated is highlighted with a red dot and it is clear from it that the water displaced by the storm reaches its maximum from smaller to bigger Longitudes (from BORJ to TGBH sites). This is, following an anti-clockwise direction, which is detected by GPS recordings.

On top of that, a one minute GPS time series in TERS (see map in Figure 7.1) was estimated as well. TERS is located westward of BORJ and east of Lowestoft (5.219^o Longitude), and experiences its minimum at 02:50 UTC of the 6^{th} December 2013, according to what is to be expected due to its location.

Similar to the comparison between GPS estimated and predicted subsidence, the time of occurrence of the maximum surge has been estimated from the tide gauges readings and the predicted from the models. As it was already pointed out, the maximum is calculated for TG recordings from the 28^{th} of November to the 15^{th} of December 2013. For Aberdeen and Lowestoft predicted values, the same timespan is considered. For the rest of the predicted sites, the maximum is calculated after the 6^{th} of December. The results are summarized in Table 7.9. Unfortunately, the temporal evolution of the storm in the German Bight cannot be extracted from the Table. Only the arrival of the Cyclone is recorded in Aberdeen and Lowestoft before than in the rest of the sites in Northern Germany. Note also that the downsampling of TG HOE2 from 1 and 15 minutes to 60 minutes leads to a shift in the maximum of 5 hours and 15 minutes. This is because the two local maximums in the time series were of similar value (2.46 and 2.42 meters) but not close in time, see Table 7.7.

	1 min	**15 min**		**1 hour**			
Station	**TG**	**TG**	**DWD/BSH**	**TG**	**DWD/BSH**	**DWD/JRC**	**ECMWF/JRC**
Aberdeen	N/A	5/12 12:15	5/12 19:00	5/12 13:00	5/12 19:00	5/12 14:00	5/12 14:00
Lowestoft	N/A	5/12 22:00	5/12 22:30	5/12 22:00	3:00	5/12 22:00	5/12 22:00
BORJ	5:47	5:45	4:15	6:00	4:00	6:00	6:00
TGBF	6:08	6:15	8:15	6:00	8:00	6:00	6:00
TGEM	7:24	7:15	10:00	7:00	10:00	9:00	8:00
HELG	4:51	4:45	6:15	6:00	6:00	6:00	6:00
TGME	7:28	7:30	5:45	7:00	7:00	6:00	6:00
LHAW	4:41	5:15	6:00	5:00	6:00	6:00	6:00
TGWH	7:15	7:15	9:30	7:00	10:00	8:00	7:00
FLDW	5:12	5:15	7:45	5:00	8:00	6:00	7:00
HOE2	3:44	3:45	9:15	9:00	9:00	11:00	6:00
TGBH	7:46	7:45	11:15	8:00	11:00	8:00	8:00
TGDA	9:38	9:30	12:15	10:00	12:00	11:00	6:00
TGCU	5:07	5:15	8:45	5:00	9:00	8:00	7:00
TGBU	5:59	6:00	11:00	6:00	11:00	6:00	7:00

Table 7.9: Time (UTC of 6^{th} December 2013) of the maximum surge for each station, corresponding to the different datasets: TG recorded surge and surge predicted by models. Different samplings, 1, 15 and 60 minutes. Stations Aberdeen and Lowestoft are downloaded with 15 minutes sampling. Stations sorted by longitude.

A plot similar to 7.8 can be found in in Figure 7.9 for TG recorded surge heights (black lines). It shows that the maximum surge recorded (red dots) is not reached at the same time as the storm arrives at the different locations. If the first local maximum for each time series were highlighted, the arrival of the first surge rise at 18:00 on December the 5^{th} would be clearer.

The surge predicted by DWD/BSH model compares well in terms of shape with TG recorded surge heights, for some stations like HELG, TGME, LHAW, TGWH and FLDW, see Figure 7.9. The difference in height reaches up to 1-meter. Alas, the discrepancies in surge and arrival times for recorded and predicted data are bigger for other stations where the water might interfere with itself or the coast, or where the storm is not correctly modeled. The difference between predicted and recorded surge in HELG (Figure 7.4) is of about 1 meter. Similar plots comparing JRC/DWD and JRC/ECMWF predictions with respect to TG recorded surge can be found in Figures I.8 and I.9 in the Appendix.

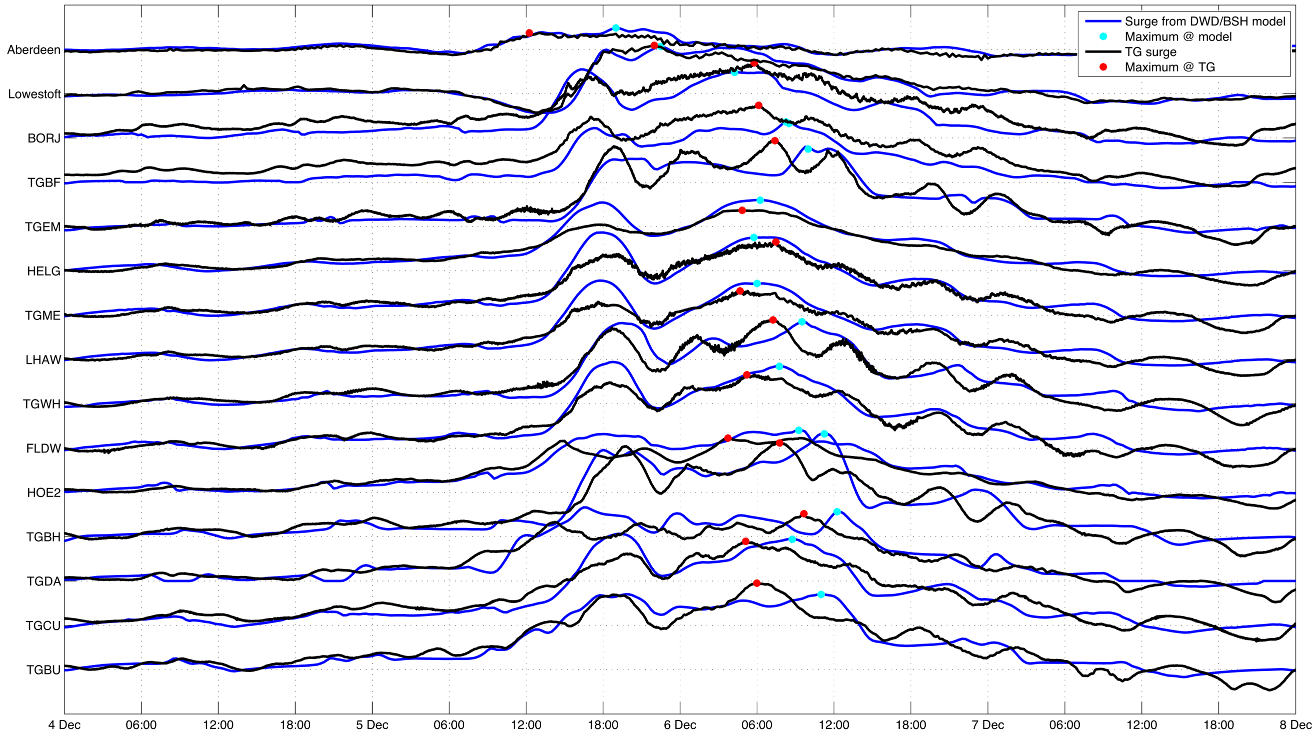

Figure 7.9: Stacking of 1 minute tide gauge time series (except for Aberdeen and Lowestoft whose sampling is 15 minutes), in black. Red dots show the maximum value for each station. In blue, DWD/BSH predicted surge with 15 minutes sampling. Cyan dots show the maximum value for each station. Stations sorted by longitude. Scale in Y axis is 2 meters. December 2013.

7.5 Error Assessment

Daily GPS results are combined within Bernese. The internal consistence of the 22 days combined solution (except the maximum surge days, 339 and 340) is very good, with a repeatability of 1.02, 0.92 and 3.39 mm in North, East and height, respectively, for the 48 stations considered in the network. However, the kinematic solutions for stations HOE2, TGCU, TGDA, TGEM and TGWH reached one meter in more than the 50% of the epochs, thus they were eliminated from further calculations.

The empirical standard deviations (S_N) of the GPS estimations are listed in Table 7.10 for the stations used in this Chapter. It is calculated for the direct Bernese output (R), after a sidereal filter (SF), and for the final estimations (F) which also have a 6 hour sliding window filter applied. The reduction ratio of the different steps with respect to the unfiltered data has also been computed. Final GPS data scatter is reduced between 47 and 71% with respect to the raw Bernese output. The final S_N ranges between 3.7 and 11.7 mm. Those values are within the limits for vertical sub-daily kinematic GPS data (about 7 mm, [*Bock et al.*, 2004]).

According to Table 7.10, downsampling from 1 to 15 minutes reduces very slightly the data scatter (compare columns corresponding to final data), which could be seen as an indicator of improvement in the time series, and does not eliminate much of the signal amplitude (less than 1 mm for all the GPS stations in Table 7.5). However, the accuracy in arrival times for the maximum subsidence can be diminished by up to 7.5 minutes. Likewise, the decrease in sampling from 1 to 60 minutes cancels up to 1.5 mm in the recorded signal (for station TGBU), which accounts for approximately a 4% of the total. Also, the uncertainty in the arrival times of the maximum displacement rises up to 29 minutes. Note that the reduction in S_N between 1 minute and 1 hour sampled data (Table 7.3) is significant, up to 90% for station TGBH.

The S_N for the TG recordings sampled to 15 minutes in Aberdeen and Lowestoft and 1 minute for the rest of the stations is shown in Table 7.11. It ranges between 0.16 and 0.35 meters.

	Raw without outliers (R) S_N (mm)	**Sidereally filtered (SF)** S_N (mm)	**Reduction (R, SF)** S_N (mm)	**Final data (F)** S_N (mm)	**Reduction (R, F)** S_N (mm)	**Final data 15 min sampling** S_N (mm)
BORJ	12.5	11.3	10%	4.1	68%	4.1
FLDW	13.7	11.2	19%	4.7	65%	4.7
HELG	15.4	12.3	20%	6.2	60%	6.2
LHAW	26.8	17.9	33%	5.6	79%	5.5
TGBF	17.0	13.5	21%	5.0	71%	5.0
TGBH	34.4	33.8	2%	11.7	66%	11.6
TGBU	11.6	10.6	9%	3.7	68%	3.7
TGME	11.8	10.2	13%	4.3	63%	4.3

Table 7.10: Empirical standard deviation of the different solutions obtained for 1 minute GPS data. Reduction in S_N of each solution with respect to raw data. Statistics calculated for days 28/11 to 4/12, 2013 (not influenced by the Xaver cyclone). The last column indicates the empirical standard deviation of the final results downsampled to 15 minutes. The results for 60 seconds downsampled data can be found in Figure 7.3

	Abe	**Low**	**BORJ**	**TGBF**	**TGEM**	**HELG**	**TGME**	**LHAW**	**TGWH**	**FLDW**	**HOE2**
S_N (m)	0.16	0.33	0.33	0.33	0.35	0.30	0.32	0.31	0.33	0.34	0.27
	TGBH	**TGDA**	**TGCU**	**TGBU**							
S_N (m)	0.35	0.28	0.34	0.34							

Table 7.11: Empirical standard deviation of the different solutions obtained for 15 minutes TG recordings for Aberdeen and Lowestoft, and 1 minute for the rest of the sites. Statistics calculated for days 28/11 to 4/12, 2013 (not influenced by the Xaver cyclone).

7.6 Summary

Cyclone Xaver produced a water surge up to 4.2 meters at the site TGBH, corresponding to a subsidence of up to 21 mm in the same station. The biggest subsidence is found in LHAW (47 mm), where the maximum surge height was 3 meters. The comparison between observed surge heights and estimated subsidence is not recommended, as a maximum in the surge in a TG does not have to be directly related to a big accumulation of water in the vicinity, which creates a subsidence in GPS.

For events where a big difference in coordinates is expected (earthquake or big subsidence, for example), a 3-sigma screening is not advisable as an outlier rejection strategy. For this case, where a big subsidence is experienced during several hours and even days, the most suitable rejection method is eliminating the points in the unfiltered time series with residual differences between unfiltered and 1 hour (or more) moving average filtered data bigger than 3-times empirical standard deviation.

Stations HOE2, TGCU, TGDA, TGEM and TGWH have a good daily solution repeatability (approximately 1, 1 and 4 mm in North, East and height), and also the repeatability of the final kinematic results combination is always below 1.3 mm. However, the kinematic solutions obtained from all the stations is highly noisy, from both DD and PPP methods. Thus, those GPS time series are removed from the current study.

In order to compare data obtained from different methodologies, one must assure that the same data is being compared by applying different corrections to each dataset (see Table 7.2). Applying OTL corrections in Bernese shifts the maximum subsidence in the estimated time series up to 6 hours (Figure 7.3). Surge heights recorded by AltiKa (satellite) and predicted by surge models compare well, showing an empirical standard deviation of the difference of 0.31, 0.29 and 0.21 meters for DWD/BSH, ECMWF/JRC and DWD/JRC models, respectively.

The subsidence predicted by DWD/BSH, DWD/JRC and ECMWF/JRC models does not compare well with GPS estimations during one week uninfluenced by the storm. This is mainly due to the small signal to noise ratio.

However, for the days during the Xaver Cyclone, the correlation between estimated and predicted subsidence reaches up to a 96% (Table 7.4). DWD/JRC (with 1 hour sampling) is the model that gives the best-fit, following the criterion explained by *Geng et al.* [2012], where the S_N reduction of the corrected data is chosen as the indicator. Also, the correlation between estimated and predicted signals is high, ranging between 65 and 96%. However, it is also the model that most underestimates the maximum subsidence produced by the storm (see Table 7.5), accounting for up to a 33% of the total subsidence in station LHAW. On the other hand, the model that compares better to GPS estimations in terms of maximum subsidence is DWD/BSH. Note that the correlations between estimated and predicted subsidence for such model also vary from 64% to up to 95%.

The subsidence predicted by the three surge models, and also the GPS estimations (1, 15 and 60 minutes sampling) can be used to monitor the temporal evolution of the storm, except for GPS in FLDW and TGBU. By using 1 minute sampled GPS estimations, the results obtained fit perfectly to the expected arrival direction of the storm, which was observed anti-clockwise (Figure 7.8, except for stations FLDW and TGBU). When the data is downsampled, the arrival times of the maximum subsidence begin to overlap, as seen in Table 7.8.

The comparison between surge recorded by TG and predicted by surge models is done parallel to the comparison between estimated and predicted subsidence. During the period where the storm occurred, the best-fit model is DWD/JRC; on the other hand, for the week uninfluenced by the storm, the best-fit model is ECMWF/JRC. The decision is based again on the criteria introduced by *Geng et al.* [2012]. The results obtained are not as straightforward as for the subsidence estimated and predicted in terms of storm direction: the maximum in water surge does not follow a clear temporal pattern neither for recordings nor for predictions. Apart from that, the greatest surge value is usually overestimated by DWD/BSH and underestimated by the other two models.

8 Numerical Results 4. Vertical Load of the 1755 Lisbon Tsunami

To assess the potential of a GPS tsunami early warning system for the Iberian Peninsula, several tsunami models are studied in this Chapter in terms of water surge and vertical subsidence derived from these models. Arrival times of the maximum subsidence and water height are compared, in order to establish the possible warning time available for each scenario. This accommodation time is a key information for the early warning of an incoming tsunami, because such deformation and the amount of water traveling toward the coast are intrinsically linked.

8.1 Introduction

Tsunami early warning can be triggered by several means: relating a surge in the TG records to the incoming tsunami water height [*Bressan and Tinti*, 2011], obtaining seismic parameters and slip distribution by classical methods [*Blaser et al.*, 2011], monitoring open-ocean sea height by satellite altimetry [*Hamlington et al.*, 2012] or by GPS located in buoys, and even by using GPS data to look for the tsunami signature in the ionosphere [*Occhipinti et al.*, 2008]. Moreover, *Song* [2007] proposes a GPS derived seafloor motion on the fault and relates it to an estimation of the tsunami source energy. However, the most used strategy is a rapid determination of earthquake magnitude using data from existing GPS networks. Computed rupture parameters by a fault model are then related to tsunami nucleation and its wave form and size [*Sobolev et al.*, 2006; *Blewitt et al.*, 2006; *Ohta et al.*, 2012]. This is done by deriving the tsunami waveforms using pre-computed tsunami scenarios [*Behrens et al.*, 2010; *Hanka et al.*, 2010], which helps to estimate arrival times and maximum height.

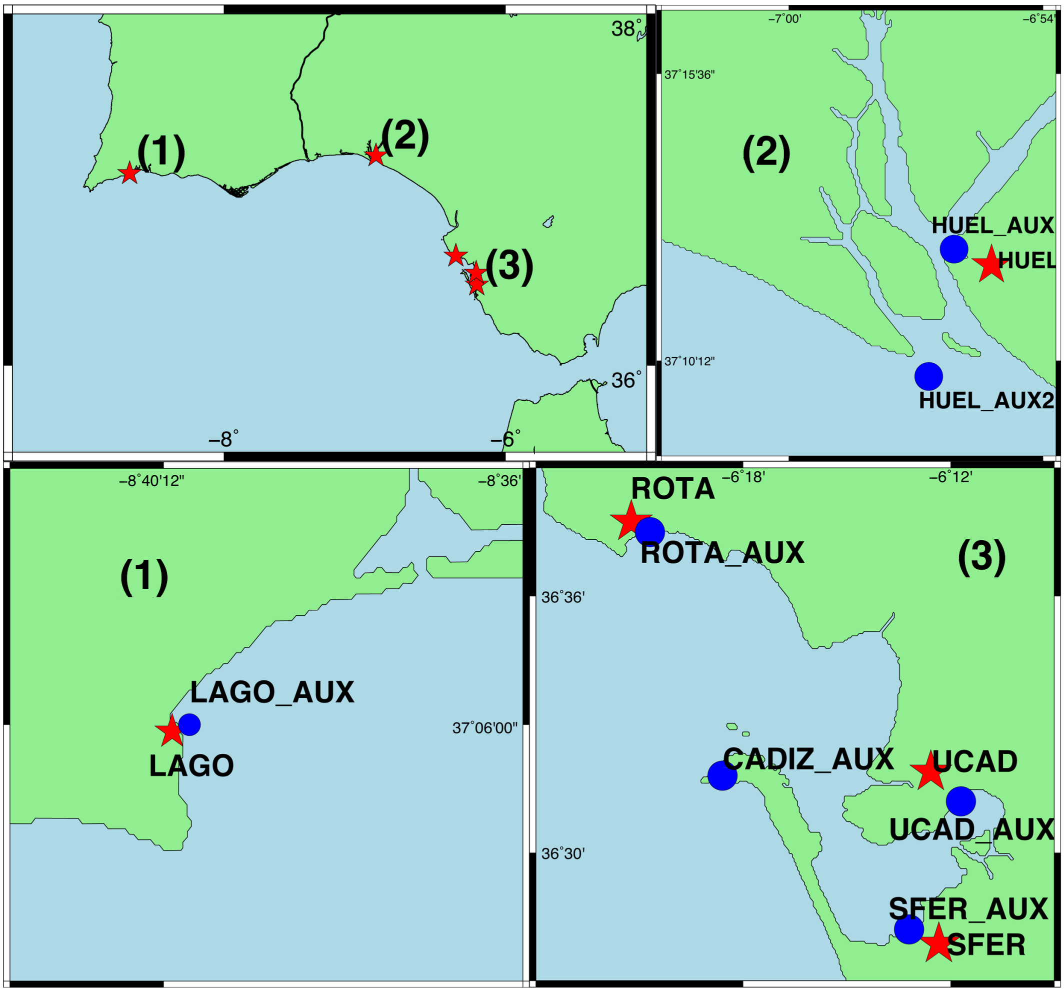

Figure 8.1: Points chosen to calculate the vertical subsidence (red stars), and the water height from tsunami models (blue circles).

The approach followed in this Chapter was first introduced (but not demonstrated) by *Plag et al.* [2006] and lately applied by *Mitsui and Heki* [2013] for the 2011 Japan earthquake-induced tsunami. The basic concept relies on the vertical load that a large water mass exerts in the crust, and in the similarities between ocean tides and tsunamis. This is, tsunamis create a subsidence that, if detectable by GPS, could be integrated into an EWS. Moreover, if several scenarios were used to predict the subsidence induced by different tsunamis, a real estimation of the incoming water height could be obtained to alert the population according to the threat.

The only known event that could have caused a subsidence detectable by GPS in the Iberian Peninsula was the 1755 San Vicente earthquake and tsunami, from which there is neither GPS nor mareograph data available. Therefore, a prediction of the subsidence in several GPS stations (LAGO, ROTA, SFER and UCAD, see Figure 8.1) is calculated. In the same Figure, red star sites are in the land and correspond exactly to the current location of a GPS receiver. Blue circles are in the ocean, corresponding to the closest point in the water to the GPS site of the same name with respect to a land-sea grid of 0.005 deg spacing created by the Generic Mapping Tool (GMT), version 5, an open-source software package for the analysis and display of geoscience data [*Wessel and Smith*, 1991; *Wessel et al.*, 2013].

In order to simulate the subsidence at the different locations, SPOTL is used. Several tsunami surge height models are chosen to generate the input data for SPOTL in order to predict the subsidence that a given GPS station would undergo due to the water mass and the distance to it. The relation between predicted surge heights and vertical subsidence time series is studied in detail. More information on the tsunami models can be found in Section 4.3.2.

8.2 Tsunami Models 1. Best- and Worst-Case Scenarios for the Whole Region

The tsunami models studied here correspond to the best- and worst-case scenarios generated by M.Sc. Ricardo Tavares da Costa [personal communication]. The best-case scenario is related to an earthquake nucleated in the MPF, as computed by *Lima et al.* [2010], with a magnitude of M$_w$8.5. The worst-case scenario is obtained when calculating a combination of two different epicenters in two separate faults, HSF and MPB, as computed by *Matias et al.* [2013] with a M$_w$8.6 magnitude. Both scenarios give only information about water surge, not including flooding or tides, in a region between 39 and 33 degrees latitude and -12 and -6 degrees longitude. They are detailed in Section 4.3.2 and in [*Lima et al.*, 2010; *Matias et al.*, 2013].

There are GPS receivers currently located in LAGO, ROTA, SFER and UCAD. A map showing their emplacement can be seen in Figure 8.1, and their coordinates are listed in Table 8.1. The vertical subsidence at those sites has been predicted using SPOTL (see Section 4.3) for the different scenarios provided. The time of the maximum vertical subsidence is also computed.

Name	Description	Longitude	Latitude
LAGO	LAGO GPS site	-8.668^o	37.099^o
LAGO_AUX	Closest point to LAGO in water	-8.665^o	37.100^o
HUEL	HUEL GPS site	-6.920^o	37.200^o
HUEL_AUX	Closest point to HUEL in water	-6.935^o	37.205^o
HUEL_AUX2	Closest point to HUEL in water, outside Huelva estuary	-6.945^o	37.165^o
ROTA	ROTA GPS site	-6.354^o	36.629^o
ROTA_AUX	Closest point to ROTA in water	-6.345^o	36.625^o
UCAD	UCAD GPS site	-6.209^o	36.531^o
UCAD_AUX	Closest point to UCAD in water	-6.195^o	36.520^o
SFER	SFER GPS site	-6.206^o	36.464^o
SFER_AUX	Closest point to SFER in water	-6.220^o	36.470^o
CADIZ_AUX	Closest point to Cádiz city center in water, outside Cádiz bay	-6.310^o	36.530^o

Table 8.1: Points chosen to calculate vertical subsidence (GPS sites) and water height from tsunami models (closest water point to a GPS site with respect to a land-sea grid of 0.005 deg spacing created by GMT 5).

As GPS sites are placed on land, the water height can not be directly obtained at those locations. Therefore, a land-sea mask is created by GMT 5 with 0.005 deg spacing in latitude and longitude, similar to the spacing in the tsunami models. The closest point in the ocean is chosen for each station. For HUEL, the nearest point in the ocean is placed inside the Huelva estuary (HUEL_AUX), so a third location is taken outside it (HUEL_AUX2). The closest points in the ocean to SFER and UCAD are placed in the Cádiz Bay (SFER_AUX, UCAD_AUX). Thus, a complementary point is selected in the ocean, very close to the city of Cádiz, where the surge is also computed (CADIZ_AUX). For ROTA and LAGO, an auxiliary point is selected for each station as well (ROTA_AUX, LAGO_AUX). The auxiliary points are also shown in Figure 8.1, and their coordinates can be found in Table 8.1. For all the auxiliary points aforementioned, the time and value of the maximum surge height are detailed as well in Tables 8.2 and 8.3.

	Maximum subsidence predicted		**Maximum surge predicted**		**Arrival time difference**
Location	**Value (mm)**	**Time (min)**	**Value(m)**	**Time (min)**	**Time (min)**
LAGO	3.4	38	-	-	0
LAGO_AUX	-	-	1.482	38	
HUEL	0.4	2	-	-	88
HUEL_AUX	-	-	0.013	90	
HUEL_AUX2	-	-	0.421	78	76
ROTA	0.9	64	-	-	76
ROTA_AUX	-	-	0.554	78	
UCAD	0.3	2	-	-	94
UCAD_AUX	-	-	0	96	
SFER	0.3	10	-	-	66
SFER_AUX	-	-	0.045	76	
CADIZ_AUX	-	-	0.769	72	-

Table 8.2: Arrival time (minutes after the tsunami nucleation) and value of the maximum subsidence predicted from tsunami models. Arrival time and value for maximum water surge predicted from tsunami models. Difference in arrival times. Best-case scenario.

	Maximum subsidence predicted		**Maximum surge predicted**		**Arrival time difference**
Location	**Value (mm)**	**Time (min)**	**Value(m)**	**Time (min)**	**Time (min)**
LAGO	4.7	8	-	-	28
LAGO_AUX	-	-	4.106	36	
HUEL	1.4	10	-	-	160
HUEL_AUX	-	-	0.041	180	
HUEL_AUX2	-	-	1.678	76	66
ROTA	3.8	70	-	-	10
ROTA_AUX	-	-	2.029	76	
UCAD	1.4	42	-	-	54
UCAD_AUX	-	-	0.029	96	
SFER	1.4	44	-	-	28
SFER_AUX	-	-	0.11	72	
CADIZ_AUX	-	-	2.873	66	-

Table 8.3: Arrival time (minutes after the tsunami nucleation) and value of the maximum subsidence predicted from tsunami models. Arrival time and value for maximum water surge predicted from tsunami models. Difference in arrival times. Worst-case scenario.

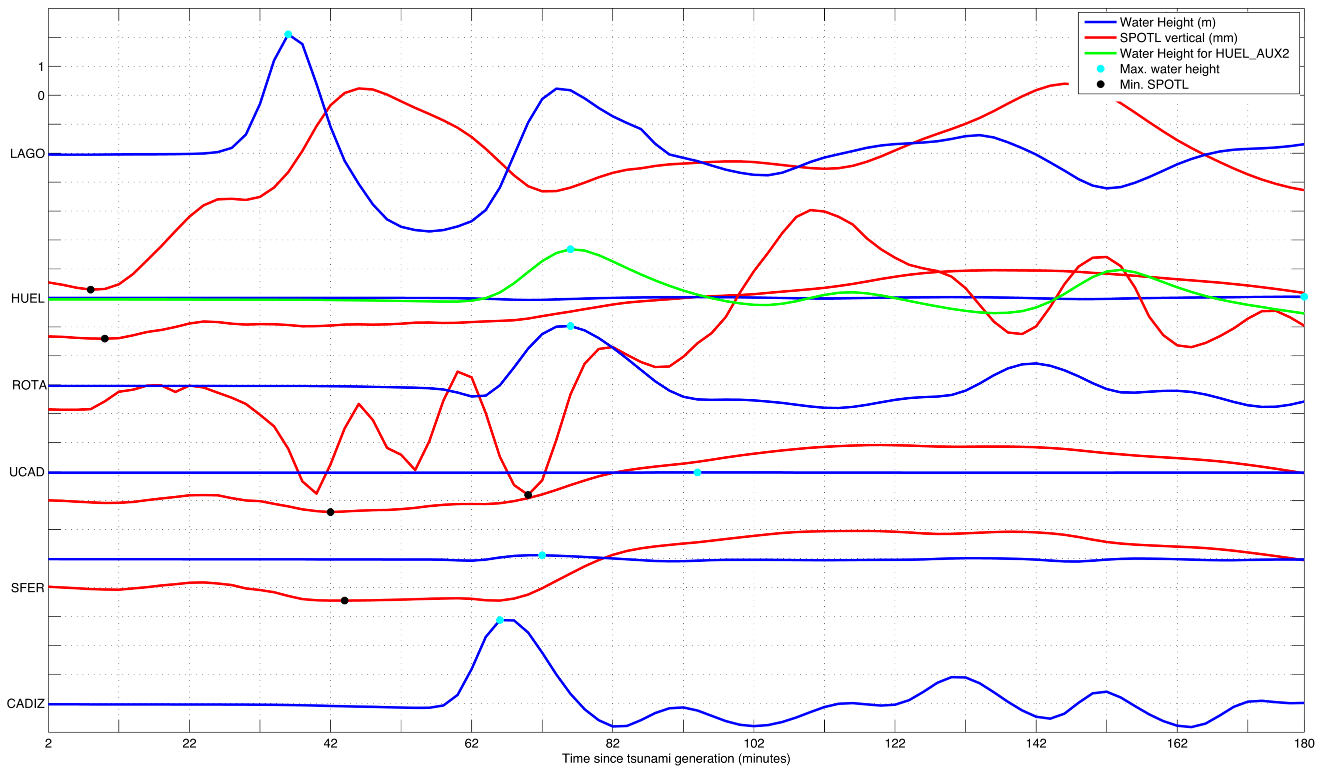

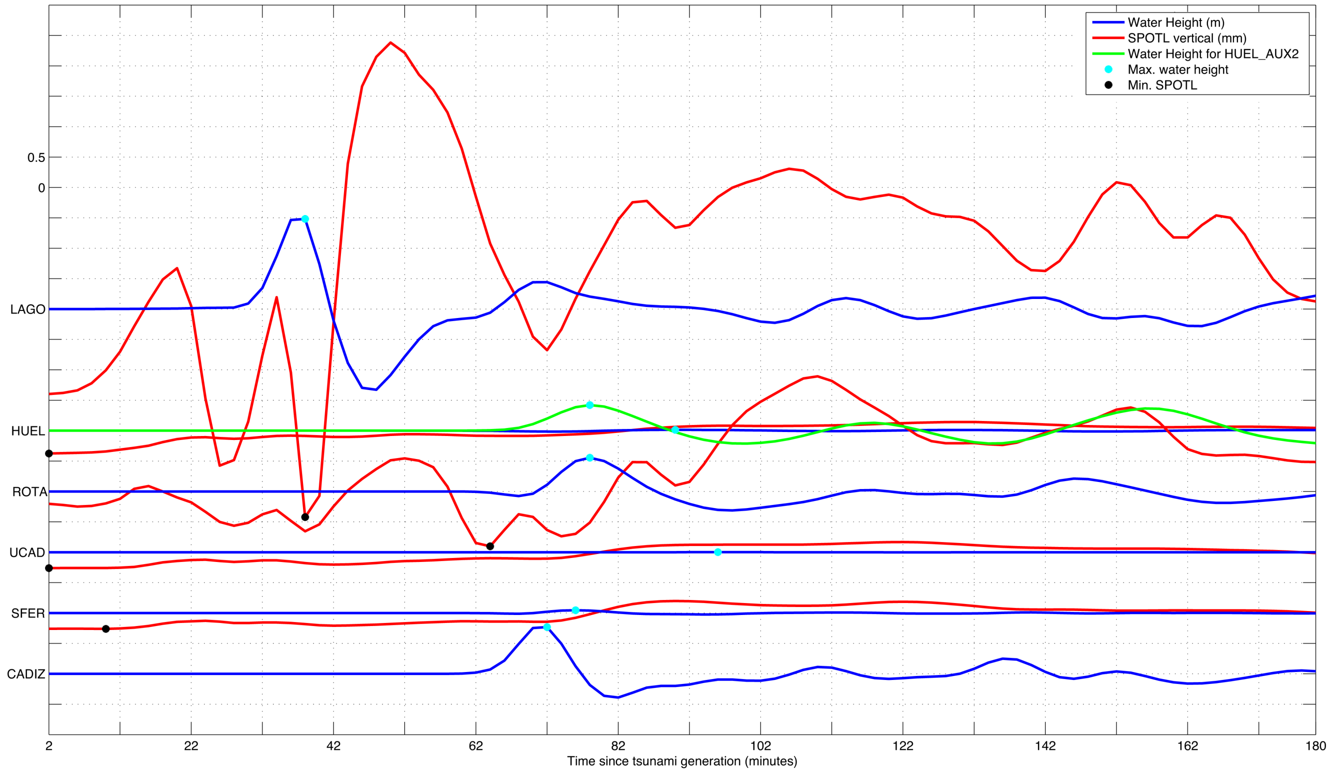

Figure 8.2: Subsidence predicted (blue, mm) in the different GPS stations. Surge height (red, m) in the closest points to such GPS sites. In green, water surge (m) obtained at the second auxiliary point to HUEL. See Table 8.1 for further explanation of the points and Figure 8.1 for their location. Upper figure: best-case scenario; Lower figure: worst-case scenario. Scale in Y axis is of 1 unit in the plot on the upper part side and 0.5 units on the lower part side, the units for surge height and subsidence are meters and millimeters, respectively.

For all the sites, the biggest surge is related to the arrival of the first tsunami wave. Also, the subsidence at each GPS site reaches its maximum some minutes before the first wave arrives: Tables 8.2 and 8.3 show this fact, as well as Figure 8.2. For LAGO, the maximum subsidence (3.4 mm) is obtained at the same moment as the maximum in water surge (1.5 m), 38 minutes after the earthquake nucleation for the best-case scenario. For the same scenario, the predicted subsidence in HUEL, ROTA, UCAD and SFER is less than 1 mm, and the water surge reaches up to 0.7 m. Note that the mean equinoctial high tide in the harbor of Cádiz is of 3.55 meters. Thus, in comparison, a tsunami of 0.7 meters should not endanger the population. However, if both are added, a big tide plus a tsunami of one meter can damage floating docks, aquaculture and beaches, among others.

On the other hand, for the worst-case scenario (Table 8.3), a subsidence ranging from 1.4 to up to 4.7 mm is predicted for the GPS locations. In LAGO, the maximum subsidence (4.7 mm) is predicted 8 minutes after the tsunami nucleation, which corresponds to 28 minutes before the maximum surge height (4 meters) reaches the city. This difference in time is enough to alert the population. The subsidence predicted in HUEL is only of 1.8 mm, and the maximum surge predicted for that location is 0.04 meters. However, in the auxiliary point chosen outside the Huelva estuary (HUEL_AUX2), the maximum of the predicted surge is 1.7 meters, which is considerable. Also, the warning time is enough, the difference in arrival times of both maximums is of 66 minutes. For ROTA, the maximum subsidence is 3.8 mm, reached 10 minutes before the maximum in surge (2 meters) is experienced. Because of the location of SFER and UCAD, the maximum in water height reaches only up to 0.11 meters. However, for the auxiliary point close to Cádiz city and in the open ocean, a surge close to 3 meters is predicted 66 minutes after the tsunami is nucleated.

Due to the location of ROTA and LAGO, see the map in Figure 8.1, the subsidence experienced by both stations is less smooth with respect to the rest of the sites (see Figure 8.2): the water coming from the west and the south of LAGO and ROTA influence the vertical subsidence because the two different subsidence patterns interfere with each other. This is opposite to what happens in HUEL, SFER and UCAD, where the water comes directly from only one direction, see the location of the epicenters in Figure 8.3. It must also be noted that the tsunami creates a signal in the GPS that arrives almost instantaneously after the tsunami nucleation, altering the vertical component in GPS time series. This outstands in Figure 8.2 for almost all the stations and both scenarios.

It must be pointed out that the comparisons shown in the aforementioned Figures and Tables can be achieved due to the use of tsunami modeled data which does not account for any other source of water like tides when induced water level can interfere with tsunami waves, increasing or decreasing the water height, or wind causing water accumulations. On the other hand, in Chapter 6, only a 40% correlation ratio was found between mareograph recordings and GPS measurements. A clear relationship between biggest water surge and maximum vertical subsidence was neither found in Chapter 7. Both can be explained by the redistribution of water due to the tides and the storm, respectively, and because a high rise in water level does not have to be directly linked to a rise in water mass in the vicinity.

The difference in maximum water height between the best- and worst-case accounts for up to 2.5 meters in LAGO, and is minimum in UCAD and SFER is due to their location inside the Cádiz Bay. Nevertheless, they do experience some subsidence related to the accumulation of water in the vicinity, closer to open ocean (up to 2.8 meters in CADIZ_AUX for the worst-case scenario). In theory, it is possible that the water retires from the coast before a tsunami arrives. This effect is only apparent for ROTA in the best-case scenario, where -0.5 m water level is found just before the arrival of the first wave. The interferences between water waves and local bathymetry and topography, and also among water waves, is distinct in Figure 8.2 after the first wave arrival.

8.2.1 Profile of the Load. Best- and Worst-Case Scenario

A profile is set-up for each scenario, from the epicenter of the event towards stations ROTA and LAGO. For the worst-case scenario, the start location for the profile is here chosen as the mean value of both epicenters and has coordinates [36.185, -9.902]. From that point towards ROTA (397 km distance), a profile has been selected consisting of 11 points with a $\sim$40 km step. The first location is the mean epicenter and the last is ROTA, as can

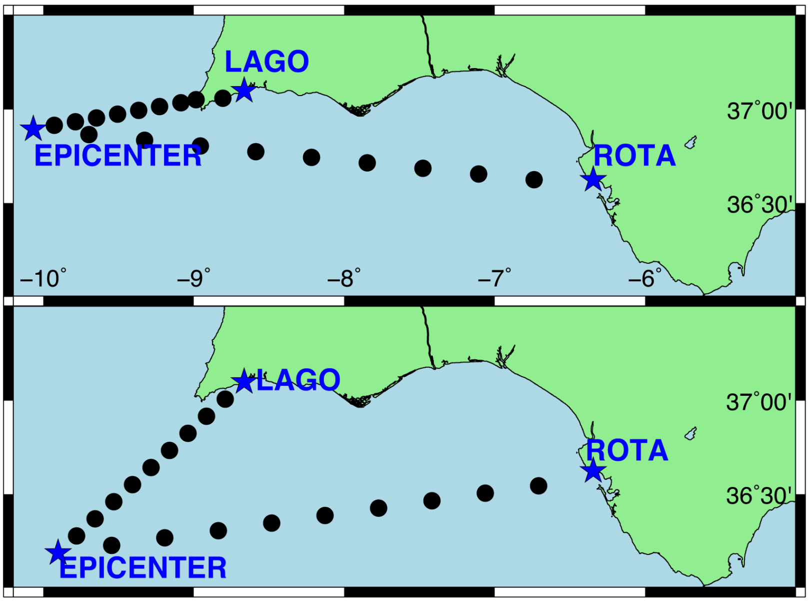

Figure 8.3: Profiles for best-case (top) and worst-case (bottom) tsunami scenarios. The coordinates of the points and the distance to the stations are listed in Tables 8.4 and 8.5.

be seen in Figure 8.3. Subsidence along the track has been computed, and maximum values and arrival time of such maximum are shown in Table 8.4.

A similar study is done for the best-case scenario, where the epicenter and the start location for the profile coincide and has coordinates [36.895, -10.067]. ROTA is placed only 157 km away from it, and an 11-locations profile towards ROTA is chosen with a point every 15.7 km, see Table 8.4.

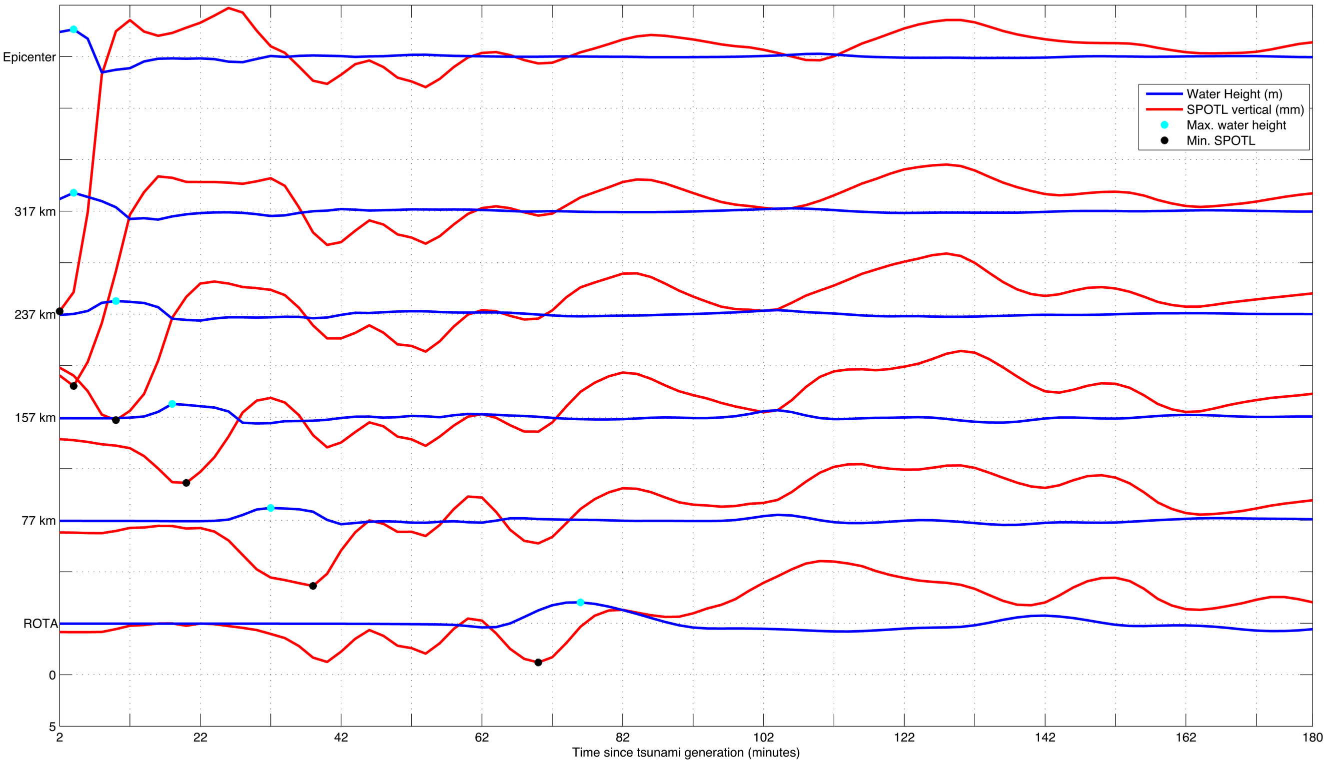

Figure 8.4: Time series for some stations chosen in the profile of the worst-case scenario, from the epicenter towards ROTA. Scale in Y axis is 5 mm for subsidence and 5 m for water height predicted, respectively. Black points correspond to the maximum subsidence; the cyan dots, to the maximum water height. Information detailed in Table 8.4.

Worst-case scenario					Best-case scenario				
Dist. to ROTA (km)	Time (min)	GPS (mm)	Time (min)	Water (m)	Dist. to ROTA (km)	Time (min)	GPS (mm)	Time (min)	Water (m)
397	2	24.7	2	2.645	**157**	2	8.5	2	1.395
357	2	22.3	4	2.298	**141**	2	9.1	2	1.539
317	4	17.0	4	1.789	**126**	4	5.9	6	1.243
277	6	13.0	6	1.572	**110**	10	3.4	12	1.547
237	10	10.3	10	1.279	**94**	16	1.9	16	0.880
197	14	8.3	14	1.264	**78**	20	1.4	20	0.573
157	20	6.4	18	1.293	**63**	26	1.8	24	0.433
117	26	5.2	26	1.179	**47**	28	1.8	30	0.433
77	38	6.4	32	1.190	**31**	38	1.6	36	0.448
37	40	8.2	42	1.682	**16**	40	1.0	46	0.529
0	70	3.8	76	2.029*	**0**	2	0.3	78	0.554*

Table 8.4: Maximum values for water height and predicted subsidence in the different points of a profile towards ROTA. Arrival times since the earthquake. Worst- and best-case scenarios. * water height indicated corresponds to the closest point in water to ROTA GPS station.

Table 8.4 shows the maximum surge height reached and its occurrence time in the several points of the two profiles created from the best- and worst-case scenarios epicenters towards ROTA. The results summarized there can be visually checked in Figure 8.4 for the profile corresponding to the worst-case scenario. The water height reached just at the epicenter is higher than in the coast for most of the points, and then flattens as it spreads. Normal tsunami waves range from 10 cm to 1 meter height in open ocean. They travel at a speed of 600 to 700 km/h in the open ocean, and lose velocity and gain height (energy remains constant) when arriving at the coast. This is clear in this profile, as the points are equally spaced: close to ROTA in the worst-case scenario, an increase in water level of up to 2 meters is found due to the local bathymetry. For the best-case scenario, the water that arrives at ROTA is much smaller, as it is in the open ocean. The energy is lost along the spatial spread of the tsunami. A similar evolution comes with the vertical subsidence predicted, which is much larger close to the epicenter for the worst-case scenario reaching down to -24.7 mm, and that attenuates along the profile. Despite the maximum surge height computed close to ROTA is bigger than 37 km away, the expected subsidence is smaller due to the influence of the water around that point.

The arrival of the maximum surge is parallel to the highest wave in the open ocean. However, while the water loses velocity, the vertical deformation related to the water redistribution does not, and the subsidence reaches its minimum some minutes before the maximum water height. Moreover, for the GPS in ROTA, the arrival time for the biggest subsidence (of 0.3 mm) is two minutes after the tsunami is nucleated. As can be seen in Figure 8.4, the evolution of the subsidence in such point is so tiny that the redistribution of waters attenuates the signal quickly and it does not affect the GPS in such place.

A similar profile is set up for the worst-case scenario, from the mean epicenter location towards LAGO, at 171 km from it. This time, the steps are of 17 km each and the profile consists of 11 points, the first coincides with the mean epicenter and the last with LAGO, first five columns of Table 8.5. The five last columns of such table correspond to the best-case scenario, at 413 km from LAGO, with 11 points separated by 41 km one to each other.

The profiles from best-case scenario epicenter and worst-case scenario mean epicenter towards LAGO are detailed in Table 8.5 and Figure 8.5. A similar pattern to the profiles to ROTA is found here, the redistribution of the water reaching the Peninsula highly attenuates the predicted subsidence for both scenarios. As the water height increases to up to 4 meters in the coast of LAGO, the predicted GPS signal decreases down to about -5 mm for the worst-case scenario. The water velocity decrease is also visible in this data.

One of the main disadvantages of using the models shown here is that the water surge is only given for the points in the grid that are water. This is, the expected run-up is not accounted for. It was introduced in Section 3.1.3.1

Worst-case scenario					Best-case scenario				
Dist. to LAGO (km)	**Time (min)**	**GPS (mm)**	**Time (min)**	**Water (m)**	**Dist. to LAGO (km)**	**Time (min)**	**GPS (mm)**	**Time (min)**	**Water (m)**
171	2	24.8	4	2.645	**413**	2	8.5	2	1.395
154	2	23.7	4	2.417	**372**	2	9.0	2	1.493
137	2	21.9	4	2.187	**331**	2	8.9	2	1.395
120	2	19.4	6	2.221	**290**	2	8.5	2	1.386
103	4	17.0	6	2.034	**249**	2	7.5	2	1.138
86	6	15.0	8	2.229	**208**	4	5.8	4	1.072
69	8	13.2	10	2.424	**167**	6	5.0	6	1.089
52	10	11.2	14	2.777	**126**	8	4.2	8	1.310
35	12	7.7	18	3.591	**85**	6	2.3	16	2.024
18	40	6.7	24	3.504	**44**	28	4.0	28	2.969
0	8	4.7	36	4.106*	**0**	2	1.5	38	2.98*

Table 8.5: Maximum values for water height and predicted subsidence in the different points of a profile towards LAGO. Arrival times since the earthquake. Worst- and best-case scenarios. * water height indicated corresponds to the closest point in water to LAGO GPS station.

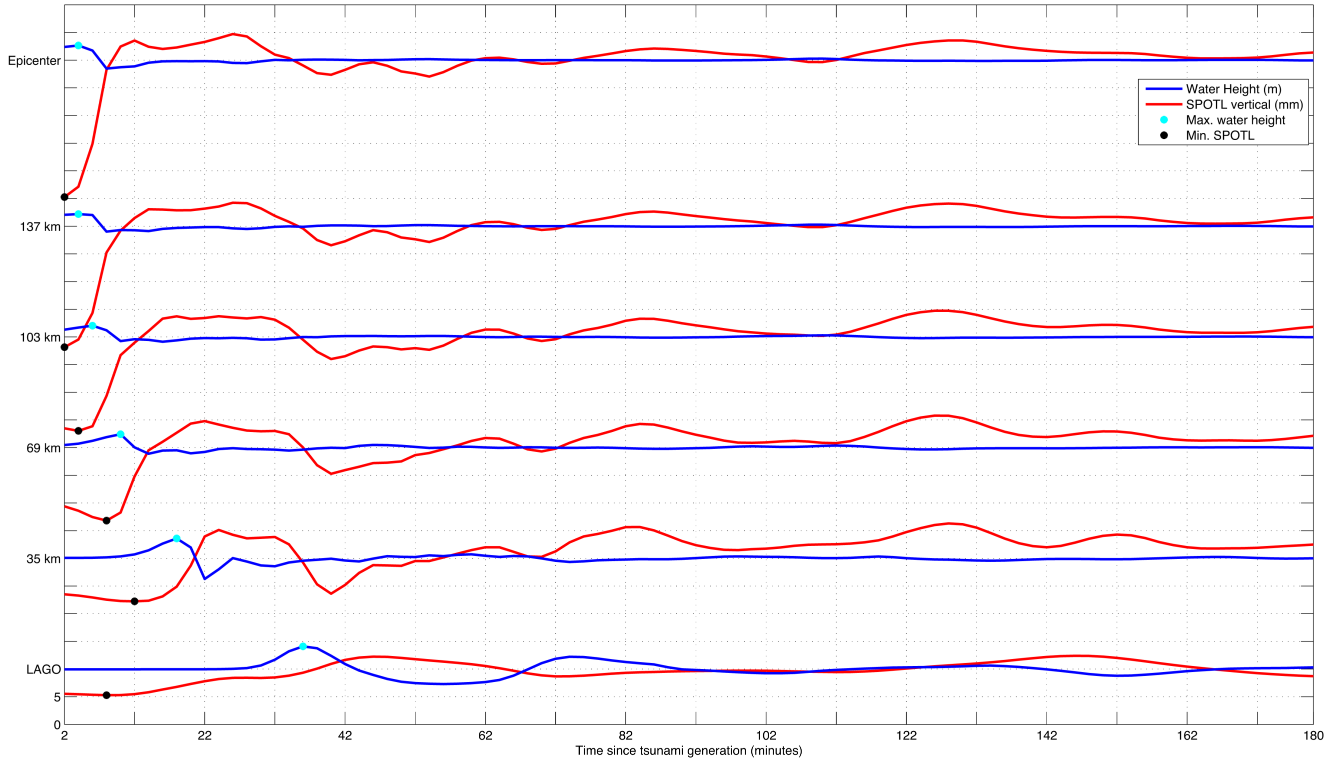

Figure 8.5: Time series for some stations chosen in the profile of the worst-case scenario, from the epicenter towards LAGO. Scale in Y axis is 5 mm for subsidence and 5 m for water height predicted, respectively. Black points correspond to the maximum subsidence; the cyan dots, to the maximum water height. Information detailed in Table 8.5.

that the expected flooding due to a tsunami of similar characteristics in the Province of Cádiz can reach up to 40 km inlands (Figure 3.6). This influences the predictions made by SPOTL.

Note also that the local and global oceanic tides are not included in the scenarios here studied. Thus, OTL is not included in the predicted subsidence. This is an advantage because GPS estimated time series are usually corrected by OTL as well, and the corrections are accurate for the GPS stations considered here. This was demonstrated in Chapter 6.

8.2.2 Worst-Case Scenario. Temporal Evolution

The complete time series of subsidence and surge heights predicted can be found in the additional material, hosted on http://tinyurl.com/mendoza-tsunami. Several snapshots corresponding to 120, 240, 360, 480, 840, 1440, 2040 and 4080 seconds after the earthquake nucleation are shown in Figure 8.6. The plots are sorted in pairs for each time stamp. On the left, predicted vertical subsidence; on the right, water height from the tsunami model. The temporal evolution of the water height (second and fourth columns) begins with a huge rise of water (up to 5 meters) in the faults where the epicenters are located. The water then spreads in all directions, reaching the Peninsula just two minutes after the nucleation. Due to the redistribution of water, its height decreases by -3 meters close to the epicenters, and continues spreading towards the Peninsula. 8 minutes after the earthquake, the water height close to LAGO is still small, around one meter. After 1440 seconds (first map in column 4), the water height on the coast near LAGO reaches its maximum, about 4 meters, and retracts just after that. The time series of the water height on the coast close to LAGO for this scenario can be seen in Figure 8.2 (below, blue lines). The arrival of the first wave in Cádiz happens in the minute 70 after the event and is of 3 meters height. Also, a second wave arrives at LAGO 76 minutes after the earthquake and is slightly higher than two meters. At the same time, a wave of approximately 2 meters height hits ROTA, and is the biggest wave reaching this coast. After that, due to the local topography and bathymetry, the water waves keep on interfering with themselves and gradually attenuate until the ocean comes back to its original state.

The vertical subsidence predicted by SPOTL from the aforementioned water height time series can be checked in parallel (first and third columns in Figure 8.6). In the first moments after the earthquake nucleation, a 3 cm subsidence is reached close to the epicenters. Later, this subsidence spreads slightly before the water waves, which could allow an early warning if it were detected. For example, 6 minutes after the earthquake, the wave still has not arrived to Portugal and the computed subsidence is of about 4 mm in LAGO. In ROTA, the arrival of the water is somewhat smooth, but the subsidence experienced in the region is highly influenced by the redistribution of the water close to it, what can be seen in Figure 8.2 below, red line.

The results discussed here in terms of water height depend strongly on the water level at the moment that the earthquake happens and the tsunami arrives: a hight tide could rise the water level in several meters, which increases the damaging effects of the tsunami. However, the effects in terms of vertical subsidence computed are very similar because GPS is corrected from tides very accurately in the area, as demonstrated in Chapter 6.

Also, it must be taken into account that an earthquake could create a co-seismic displacement in the crust that would also influence GPS recordings, close to 0.3 meters for the 2011 Japan earthquake [*Lin et al.*, 2012]. This should be eliminated from the time series in order to attain a more exact knowledge of the tsunami.

8.3 Tsunami Models 2: Worst-Case Scenarios for the City of Cádiz

Five tsunami models are used in this Section, computed for the TRANSFER project [*UCA and IGN*, 2009] and handed over by Prof. Mauricio González and Prof. Luis Otero [personal communication]. The time series of the event are not available, only a snapshot of the moment of maximum values for each case. The models consider the tidal level in the mean equinoctial high tide (3.55 meters in Cádiz harbor), which has been subtracted from the original data. The scenarios only comprise a small region around Cádiz city: between 36.37355 and 36.64105 deg Latitude, and from -6.40696 to -6.11946 deg Longitude. More information about the models can be found in Section 4.3.2 and in [*UCA and IGN*, 2009].

Figure 8.7 shows the water height (left) and the computed vertical subsidence (right) for CWF scenario, which is the worst possible case among all the scenarios computed for the city of Cádiz. The rest of the scenarios are plotted in the Appendix, see Figures J.3, J.4, J.5 and J.6. In all the Figures, it can be seen that the load computed by SPOTL is almost rectangular, which is the shape of the input grid. This can be explained by the fact that discarding the water state in farther regions highly influences SPOTL output. Therefore, the plots shown in this Section are only illustrative in terms of water height, and incorrect in terms of vertical deformation, and must not be taken into account for a global analysis.

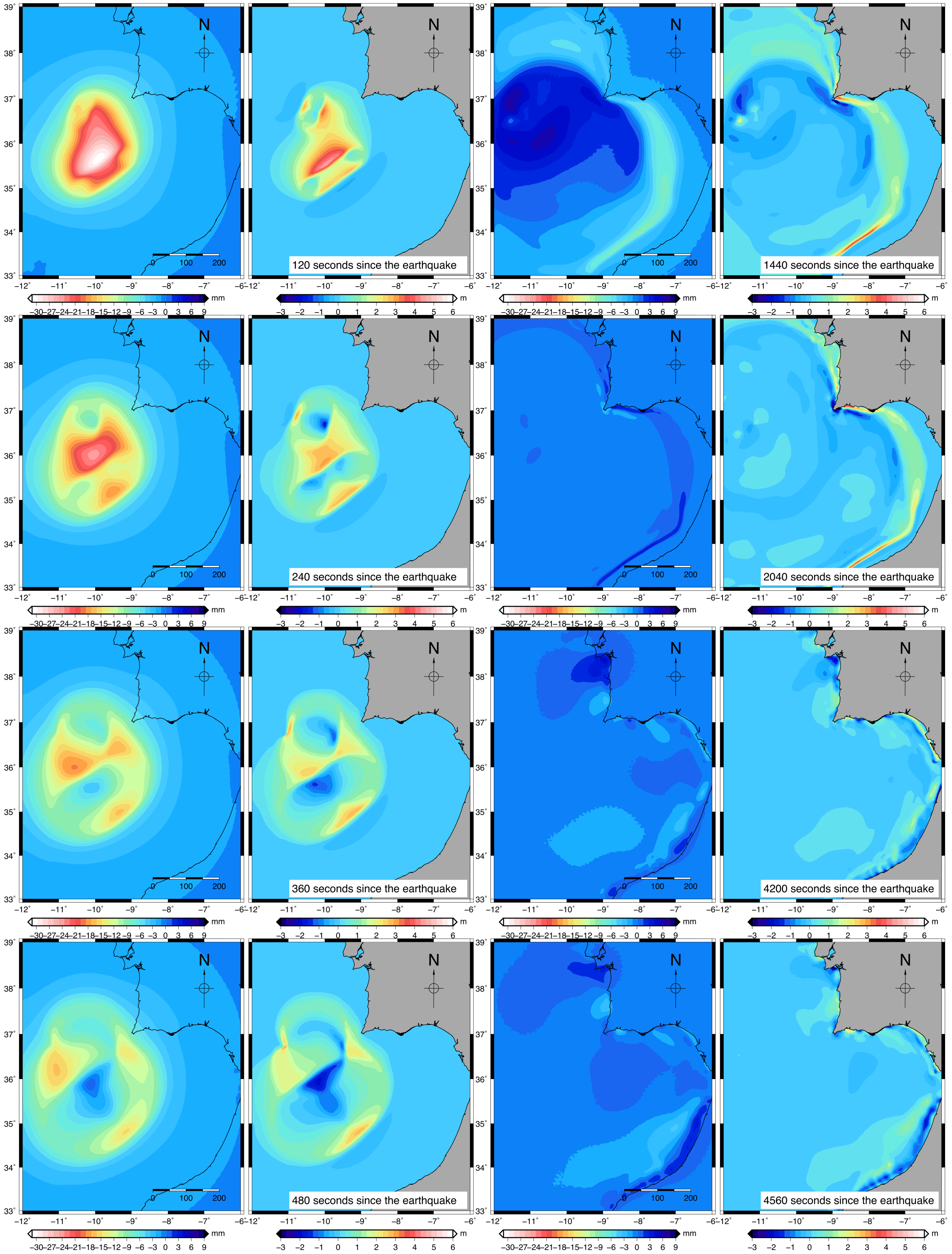

Figure 8.6: Pairs of figures, corresponding to the water height (right) and vertical subsidence computed by SPOTL (left), 120, 240, 360, 480, 840, 1440, 2040 and 4080 seconds after the earthquake. Worst-case scenario.

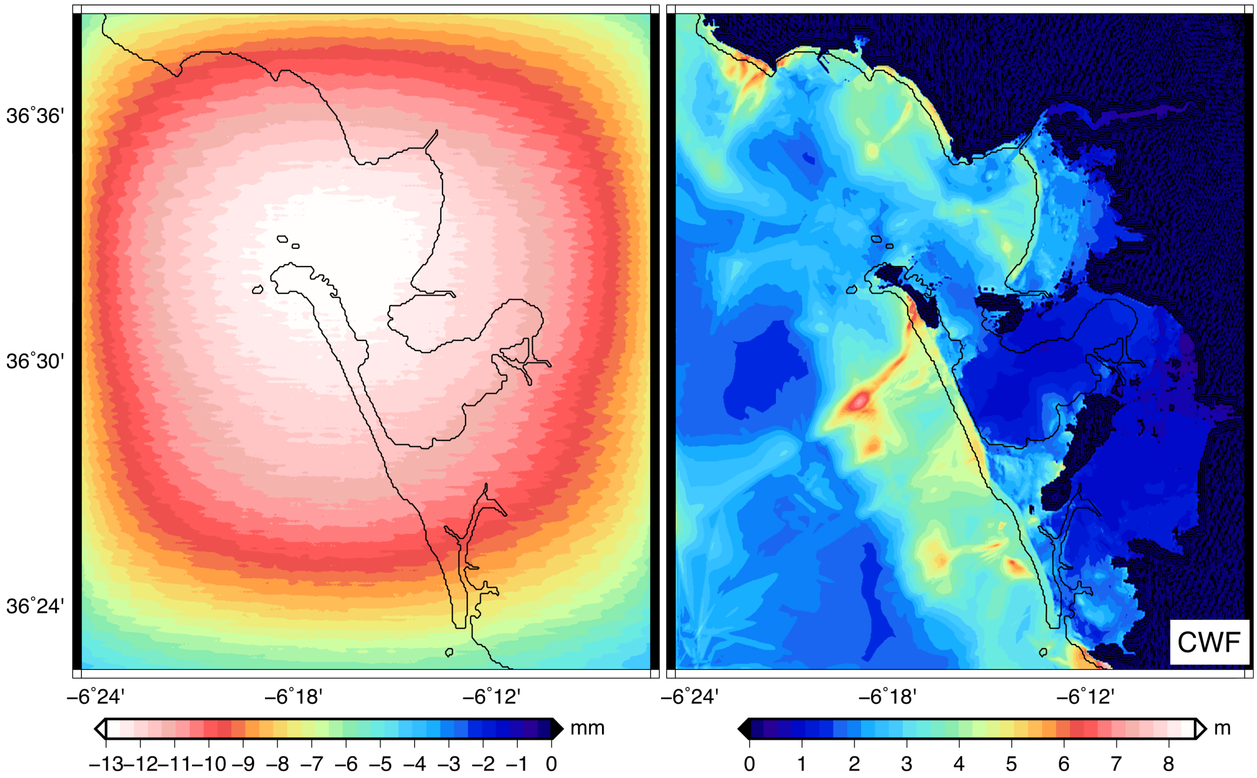

Figure 8.7: Tsunami model with epicenter in the Cádiz Wedge Fault and magnitude M_w8.6. Predicted subsidence (left) and water height (right).

8.4 Error Assessment

According to *Lima et al.* [2010], the water height modeled results are increased by a 40% with respect to the tidal level (1 meter tide increases the maximum water height in 0.4 meters). However, the run-up is only increased by a 10% of the tidal level in the moment of the flooding.

Also, the errors that SPOTL modeling induces in the data cannot be directly accounted for, but the reliability of SPOTL was assessed by comparing the results with similar softwares, and only a 5% difference was found, probably due to gridding discrepancies [*Agnew*, 1997]. As it was already discussed in Section 4.4, for a layer of 1 meter water in 100 km^2 deforms the crust only 12 mm. Therefore, if the model used as an input to SPOTL had a mismatch of 500 meters close to the coast, and if that surface was loaded by one meter of water, the total vertical displacement error derived to SPOTL would be of less than 1 mm.

The errors related to the models fed to SPOTL are detailed in the documentation from each model [*Matias et al.*, 2013; *Lima et al.*, 2010]: water density, local topography and bathymetry, the fault where the earthquake is produced, the type of earthquake and the propagation direction, among others. The errors that mismodeling such variables induce in the total is not the scope of this Thesis, but must be studied in further analysis.

The maximum subsidence predicted for the two stations and the two scenarios is only up to 4.7 mm. The sensitivity of GPS kinematic time series in the vertical component has been found to be about 10 mm for the stations used in this Thesis, as was detailed in 4.2. Therefore, the GPS receivers in LAGO and ROTA would not be able to detect a tsunami-induced loading with the characteristics here studied. However, for locations offshore, the subsidence can reach up to 24.8 mm, which is clearly above GPS noise level, thus detectable if a GPS was located in that point.

8.5 Summary

Results for vertical displacement obtained from SPOTL computation of the time series from best- and worst-case scenarios are below GPS noise level in all the stations considered (2 to 5 mm), thus the signal that precedes a tsunami could not be seen in current GPS time series. The maximum subsidence precedes the maximum wave height by up to 22 minutes in coastal stations like LAGO, that is the point that the tsunami first reaches. Thus, if the GPS sensitivity was improved, tsunamis could be alerted also by this method. It must be highlighted that this loading signal is not influenced in any matter by the shaking that an earthquake would produce. However, to extract it accurately, the GPS measurements have to be corrected by co- and post-seismic displacement.

In points like ROTA, the confluence of water from different directions induces a not very clear vertical signal (see Figure 8.3). The opposite happens to Cádiz, where the water comes only from the West. Also, the water interferes with itself after the first tsunami wave arrives to the coast. Moreover, local topography and bathymetry also meddles with the water signal. As the water loses velocity, its height is increased (energy remains constant). This is clear in Table 8.4 and also in the movie (http://tinyurl.com/mendoza-tsunami), where the water piling up in the direction towards Africa comes with the decrease in speed of that same wave.

Water arrives to the coast in the first minutes after the event, reaching its maximum in LAGO 36 minutes after the earthquake. A 3 meter height wave reaches Cádiz 70 minutes after the event, and six minutes after that, arrives to ROTA with 2 meters height. A second 2 meters wave hits LAGO at the same time. The vertical displacement related to the arrival of those waves reaches its maximum (in absolute terms) several minutes before the maximum wave, thus an alert could be set up (see last column in Tables 8.2 and 8.3).

The results obtained some kilometers far from the coast are more promising. Despite the fact that the water travels at the same time as the deformation, the vertical subsidence reaches the centimeter level for points along a track from the epicenter to the coast. If the seafloor subsidence could be monitored, this displacement could alert about a possible incoming tsunami.

An earthquake with similar characteristics to those studied here would surely create a co-seismic displacement which could reach up to several dozens of centimeters, as it was the case in the 2011 Japan Tohoku-Oki earthquake, where a co-seismic vertical signal of about 0.3 meters was found [*Lin et al.*, 2012]. This must be eliminated from the GPS signal in order to obtain only the deformation derived from the water redistribution.

Nowadays, noise level of GPS ranges from 7 to 10 mm in the vertical component for kinematic results. This does not allow for a very accurate detection of the signals studied here, that are below that level in most of the locations in the Peninsula. However, a GPS located in the St. Vincent Cape, which is the point in Portugal closest to the epicenter, could experience a subsidence of approximately 8 mm in the first minutes after the event, and this could be detected. Moreover, if the displacement of the ocean bottom could be monitored by installing very stable pillars in the open-ocean, a subsidence of up to 2.5 cm could be measured, even tens of minutes before the tsunami-induced water waves arrived to the coast. This could be achieved also by attaching GPS receivers to very stable offshore windmills or lighthouses. On the other hand, ocean-bottom pressure devices can estimate the water column over them, identifying the tsunami waves in open ocean but not the subsidence. GPS attached to buoys would do the same.

Also, the water threat related to the water height discussed here is just relative. This is, the effect of the local and global tides at the time of the earthquake highly influences the total water height: a high tide could increase the water level in several meters, which added to the water that the tsunami brings, can flood the coastal areas much more than if there was a low tide at the moment of the event. However, the comparison between the vertical subsidence computed by SPOTL with the expected GPS subsidence is much more direct, because GPS time series are commonly corrected by tidal effects.

In Section 8.3, five tsunami models are studied. The water height shown in them does include flooded areas inland. Alas, the area where the model is computed is too small to produce a reliable subsidence, because the rest of the water in the close ocean is not accounted for. However, the water height shown in the models go up to 10 meters in the coast and those models have been used for a tsunami risk assessment in the city of Cádiz [*UCA and IGN*, 2009].

The scenarios studied here are just a small part of all the possible tsunami scenarios, thus the results are very narrow among all the possibilities. The worst-case scenario accounts for two combined M_w8.6 magnitude earthquakes in two different faults, which is similar to the 1755 event. However, the possibility of a bigger earthquake also exists. Moreover, the best- and worst-case scenarios chosen for this study do not account for floods, i.e., water run-up, which can reach up to 40 km inlands, is not accounted for when calculating the related load.

However, the scope of this Chapter has been fulfilled: the possible application of GPS to TEWSs is shown: the crustal deformation arrives to the coastal GPS stations before the tsunami-induced waves reach the population, and such deformation can be detected by strategically located GPS receivers.

9 Conclusions

This Thesis details an automatic near real-time processing and post-processing methodology set up for a network of already-deployed GPS receivers in the Iberian Peninsula and surroundings. Its earthquake detection capability is validated, and its tsunami early warning potential is tested as well.

9.1 Summary

As this study is focused on application of several known processing strategies, only a quick overview of satellite positioning is provided. The processing methodology set up for a network of already-deployed GPS receivers in the Iberian Peninsula and surroundings is given in detail, particularized for a near real-time analysis technique. Processing time is shortened by parallelization of the different steps in the analysis.

Details on the natural processes that can be monitored are given: earthquakes, tides, storms and tsunamis. Also, a compendium of the necessary information to understand the threat imposed in the Iberian Peninsula is provided: geological and tectonic description of the study zones, as well as the characteristics of plausible events. A state of the art description of GPS used for tsunami and earthquake early warning is detailed in order to give an overview of the currently available possibilities. The available GPS receiver infrastructure and data used are studied as well, as it is focused on the region of interest.

The processing and post-processing strategy introduced is tested in several cases, using and particularizing the detailed methodology and software:

- An earthquake of magnitude $M_w5.1$ is monitored using a regional network and near real-time data, and the resulting time series is compared with a double-integration of seismic data from a seismograph placed close to the GPS. The outcome is validated through the comparison with results obtained from a different GPS data analysis approach (PPP).
- Two periods of extreme tides are used to assess the detecting capability of the different GPS receivers in the coast. It is demonstrated that the waves are correctly predicted and the OTL is eliminated within the standard GPS data processing for the network, even for extreme events.
- A storm surge is monitored by GPS, co-located tide gauges and satellite altimetry. The agreement between GPS recordings and tide gauge data is demonstrated through the comparison by modeled surge and derived crustal subsidence. Moreover, the results from the software used to translate water amount to crustal vertical displacement are validated by the comparison with recorded GPS data.
- Some tsunami models simulated from credible data are analyzed, obtaining the possible vertical displacement that a GPS device would experience if a tsunami of such characteristics arrived at the Iberian Peninsula. The maximum in the loading is found several minutes before the arrival of the first tsunami waves for the worst-case scenario studied.

9.2 Results and Application

The $M_w5.1$ magnitude earthquake studied here is one of the few medium-magnitude earthquakes registered by GPS up to date. The monitoring capabilities of this already-deployed network is therefore validated for similar events. Thus, the processing and post-processing strategy detailed in this Thesis can be used to monitor earthquakes with epicenters close to the deployed GPS receivers, with a magnitude equal or higher than $M_w5.1$.

The analysis of the extreme tides period leads to the conclusion that the signal recorded by a GPS in the coast of Southern Iberia and processed by Bernese is not influenced by ocean tides. This is, the ocean tidal model used, FES2004, is good enough to correct for OTL effects. From the cyclone water surge GPS monitoring it can be stated that an extreme event where a big mass of water is redistributed can be detected by GPS. If the data is corrected from OTL, the vertical deformation obtained must be due to the increase in water amount in the region and other sources excepting tides. The tsunami scenarios that have been analyzed show a vertical subsidence below GPS noise level for the coastal stations. On the other hand, the deformation begins long before the tsunami waves reach the coasts of Iberia. Furthermore, a deformation nowadays detectable is obtained in the points chosen in the ocean.

In conclusion, including this extreme events monitoring capabilities into an already-operative EWS can enhance early warning systems in terms of decreasing warning times and detecting false alerts. The further installation of coastal or inland GPS receivers would not be necessary.

9.3 Future Work

The processing and post-processing strategy detailed in this Thesis can be adapted to GLONASS or GALILEO satellites in a future, and also to a combined GPS+GLONASS+GALILEO satellite constellation.

The process of rapid detection of a natural event and the notification of an incoming hazard is the crucial part in risk management and population protection. The processing and post-processing here detailed is set-up for near real-time, which could be further improved. For example, the use of streaming data by NTRIP reduces the acquisition latency to less than seconds for raw data without corrections. If continuous GPS measurements are provided, PPP processing and filtering takes just a fraction of a second for one station, as tested by *Koppert* [2011] and later published in [*Mendoza et al.*, 2012], with accuracies of less than 3 cm in horizontal and 5 cm in vertical components. However, if the measurements are interrupted, PPP processing needs to converge again, which is a big drawback of this strategy. This real-time procedure would increase the population warning times. Moreover, the improvement in filtering methods can increase the noise reduction and thus the accuracy of the solutions.

The earthquake monitoring capability of this network and strategy has been assessed, but a better validation of the results by analyzing other events of similar or bigger magnitude is not possible due to the lack of suitable data. Rapid earthquake magnitude determination can be tested for the same event using GPS data and the strategy presented by *Colombelli et al.* [2013]. For earthquakes that are monitored by several GPS stations, an estimation of the epicenter can also be achieved by triangulation.

Due to the lack of real tsunami recordings from GPS in the Iberian Peninsula, a validation of the processing and post-processing techniques here introduced is impossible up to date. The use of different tsunami scenarios, either including scenarios between the best- and the worst-case, or increasing the magnitude of the earthquake, can also help to create an expected vertical deformation database in the GPS coastal stations. Using data from possible flooded areas can also improve the results. Also, if the subsidence in oceanic crust could be monitored using GPS data or modified ocean-bottom pressure gauges, this could help to increase warning times. On top of that, GPS receivers could be installed in offshore windmills, if was proved that they are not influenced by wind and waves.

Bibliography

Agnew, D. C., NLOADF: A program for computing ocean-tide loading, *Journal of Geophysical Research*, *102*(B3), 5109–5110, doi:10.1029/96JB03458, 1997.

Agnew, D. C., *SPOTL: Some Programs for Ocean-Tide Loading [online]*, http://escolarship.org/uc/item/954322pg, 2013.

Agnew, D. C., and K. Larson, Finding the repeat times of the GPS constellation, *GPS Solutions*, *11*, 71–76, doi:10.1007/s10291-006-0038-4, 2007.

Allen, R. M., and D. J. M. Greenslade, Model-based tsunami warnings derived from observed impacts, *Natural Hazards and Earth System Sciences*, *10*, 2631–2642, doi:nhess-10-2631-2010, 2010.

Allen, R. M., and A. Ziv, Application of real-time GPS to earthquake early warning, *Geophysical Research Letters*, *38*, L16,310, doi:10.1029/2011GL047947, 2011.

Altamimi, Z., P. Sillard, and C. Boucher, ITRF2000: A new release of the International Terrestrial Reference Frame for earth science applications, *Journal of Geophysical Research*, *107*(E10), ETG 2–1–ETG 2–19, doi:10.1029/2001JB000561, 2002.

Álvarez-Gómez, J. A., I. Aniel-Quiroga, M. González, and L. Otero, Tsunami hazard at the Western Mediterranean Spanish coast from seismic sources, *Natural Hazards and Earth System Sciences*, *11*, 227–240, doi:10.5194/nhess-11-227-2011, 2011.

Angermann, M., M. Guenther, and K. Wendlandt, Communication architecture of an early warning system, *Natural Hazards and Earth System Sciences*, *10*, 2215–2228, doi:10.5194/nhess-10-2215-2010, 2010.

Annunziato, A., The Tsunami Assessment Modelling System by the Joint Research Centre, *Science of Tsunami Hazards*, *26*(2), 70–92, 2007.

Astafyeva, E., S. Shalimov, E. Olshanskaya, and P. Lognonné, Ionospheric response to earthquakes of different magnitudes: larger quakes perturb the ionosphere stronger and longer, *Geophysical Research Letters*, *40*, 1675–1681, doi:10.1002/grl.50398, 2013.

Atillah, A., D. El Hadani, H. Moudni, O. Lesne, C. Renou, A. Mangin, and F. Rouffi, Tsunami vulnerability and damage assessment in the coastal area of Rabat and Salé, Morocco, *Natural Hazards and Earth System Sciences*, *11*, 3397–3414, doi:10.5194/nhess-11-3397-2011, 2011.

Babeyko, A. Y., A. Hoechner, and S. V. Sobolev, Source modeling and inversion with near real time GPS: a GITEWS perspective for Indonesia, *Natural Hazards and Earth System Sciences*, *10*, 1617–1627, doi:10.5194/nhess-10-1617-2010, 2010.

Baker, T. F., Tidal deformations of the Earth, *Sci. Prog. Oxford*, *69*, 197–233, 1984.

Balcerak, E., Studies provide new insights into Japan's March 2011 tsunami, *EOS*, *92*(50), 467, doi:2011EO500003, 2011.

Baptista, M. A., J. M. Miranda, R. Omira, and C. Antunes, Potential inundation of Lisbon downtown by a 1755-like tsunami, *Natural Hazards and Earth System Sciences*, *11*, 3319–3326, doi:10.5194/nhess-11-3319-2011, 2011.

Basher, R., Global early warning systems for natural hazards: systematic and people-centered, *Philosophical Transactions of the Royal Society*, *364*, 2167–2182, doi:10.1098/rsta.2006, 2006.

Behrens, A., and D. Schrader, The wave forecast system of the Deutscher Wetterdienst and the Bundesamt für Seeschiffahrt und Hydrographie: A verication using ers-1 altimeter and scatterometer data, *Deutsche Hydrographische Zeitschrift*, *46*(2), 131–149, 1994.

Behrens, J., A. Androsov, A. Y. Babeyko, S. Harig, F. Klaschka, and L. Mentrup, A new multi-sensor approach to simulation assisted tsunami early warning, *Natural Hazards and Earth System Sciences*, *10*, 1085–1100, doi:10.5194/nhess-10-1085-2010, 2010.

Benavent-Merchán, M. T., Estudio Metodológico del efecto oceánico indirecto y desarrollo de modelos de carga oceánica. Aplicaciones geodésicas para la Península Ibérica y Canarias, Ph.D. thesis, Universidad Complutense de Madrid, 2010.

Benito, B., J. M. Gaspar-Escribano, J. García-Mayordomo, and M. J. García, Peligrosidad sísmica y lecciones aprendidas de terremotos recientes en la región de Murcia: implicaciones para el diseño sismorresistente, *Tech. rep.*, Asociación Española de Ingeniería Sísmica, 2007.

Benito, M. B., M. Navarro, F. Vidal, J. Gaspar-Escribano, M. J. García-Rodríguez, and J. M. Martínez-Solares, A new seismic hazard assessment in the region of Andalusia (Southern Spain), *Bulletin of Eartquake Engenieering*, *8*, 739–766, doi:10.1007/s10518-010-9175-9, 2010.

Berrocoso, M., R. Páez, A. Sánchez-Alzola, J. Gárate, and A. Hermosilla, *Una red de estaciones permanentes GPS para Andalucía [online]*, http://tinyurl.com/qchnczq, 2006.

Bettinelli, P., J.-P. Avouac, M. Flouzat, L. Bollinger, G. Ramillien, S. Rajaure, and S. Sapkota, Seasonal variations of seismicity and geodetic strain in the Himalaya induced by surface hydrology, *Earth and Planetary Science Letters*, *266*, 332–344, doi:10.1016/j.epsl.2007.11.021, 2008.

Bezzeghoud, M., and E. Buforn, Source parameters of the 1992 Melilla (Spain, $M_w = 4.8$), 1994 Alhoceima (Morocco, $M_w = 5.8$), and 1994 Mascara (Algeria, $M_w = 5.7$) earthquakes and seismotectonic implications, *Bulletin of the Seismological Society of America*, *89*, 359–372, 1999.

Bilich, A. L., Improving the precision and accuracy of geodetic GPS: applications to multipath and seismology, Ph.D. thesis, University of Colorado, 2006.

Bilich, A. L., J. F. Cassidy, and K. M. Larson, GPS seismology: application to the 2002 M_w 7.9 Denali Fault Earthquake, *Bulletin of the Seismological Society of America*, *98*(2), 593–606, doi:10.1785/0120070096, 2008.

Birkmann, J., K. v. Teichman, T. Welle, M. González, and M. Olabarrieta, The unperceived risk to Europe's coasts: tsunami and the vulnerability of Cadiz, Spain, *Natural Hazards and Earth System Sciences*, *10*, 2659–2675, doi:10.5194/nhess-10-2659-2010, 2010.

Blaser, L., M. Ohrnberger, C. Riggelsen, A. Y. Babeyko, and F. Scherbaum, Bayesian networks for tsunami early warning, *Geophysical Journal International*, *185*, 1431–1443, doi:10.1111/j.1365-246X.2011.05020.x, 2011.

Blewitt, G., Carrier phase ambiguity resolution for the Global Positioning System applied to geodetic baselines up to 2000 km, *Journal of Geophysical Research*, *94*(B8), 10,187–10,203, doi:89JB00484, 1989.

Blewitt, G., Geodetic network optimization for geophysical parameters, *Geophysical Research Letters*, *27*(22), 2615–3618, doi:10.1029/1999GL011296, 2000.

Blewitt, G., M. B. Heflin, J. K. Hurst, D. C. Jefferson, F. H. Webb, and J. F. Zumberge, Absolute far-field displacements from the 28th June 1992 Landers earthquake sequence, *Nature*, *361*, 340–342, doi:10.1038/361340a0, 1993.

Blewitt, G., C. Kreemer, W. C. Hammond, H.-P. Plag, S. Stein, and E. Okal, Rapid determination of earthquake magnitude using GPS for tsunami warning systems, *Geophysical Research Letters*, *33*, L11,309, doi:10.1029/2006GL026145, 2006.

Blewitt, G., W. C. Hammond, C. Kreemer, H.-P. Plag, S. Stein, and E. Okal, GPS for real-time earthquake source determination and tsunami warning systems, *Journal of Geodesy*, *83*, 335–343, doi:10.1007/s00190-008-0262-5, 2009.

Bock, Y., Continuous monitoring of crustal deformation, *GPS World*, *2*(6), 40–47, 1991.

Bock, Y., R. M. Nikolaidis, P. J. de Jonge, and M. Bevis, Instantaneous geodetic positioning at medium distances with the Global Positioning System, *Journal of Geophysical Research*, *105*(B12), 28,223–28,253, doi:2000JB900268, 2000.

Bock, Y., L. Prawirodirdjo, and T. I. Melbourne, Detection of arbitrarily large dynamic ground motions with a dense high-rate GPS network, *Geophysical Research Letters*, *31*(4), L06,604, doi:10.1029/2003GL019150, 2004.

Bock, Y., D. Melgar, and B. W. Crowell, Real-time strong-motion broadband displacements from collocated GPS and accelerometers, *Bulletin of the Seismological Society of America*, *101*(6), 2904–2925, doi:10.1785/0120110007, 2011.

Boebel, O., M. Busack, E. R. Flueh, V. Gouretski, H. Rohr, A. Macrander, A. Krabbenhoeft, M. Motz, and T. Radtke, The GITEWS ocean bottom sensor packages, *Natural Hazards and Earth System Sciences*, *10*(8), 1759–1780, doi:10.5194/nhess-10-1759-2010, 2010.

Boese, M., and T. Heaton, Probabilistic prediction of rupture length, slip and seismic ground motions for an ongoing rupture: implications for early warning for large earthquakes, *Geophysical Journal International*, *183*, 1014–1030, doi:10.1111/j.1365-246X.2010.04774.x, 2010.

Boese, M., C. Ionescu, and F. Wenzel, Earthquake early warning for Bucharest, Romania: Novel and revisited scaling relations, *Geophysical Research Letters*, *34*, L07,302, doi:10.1029/2007GL029396, 2007.

Boese, M., H. T., and E. Hauksson, Real-time finite fault rupture detector (FinDer) for large earthquakes, *Geophysical Journal International*, *191*, 803–812, doi:10.1111/j.1365-246X.2012.05657.x, 2012.

Borges, J., A. Fitas, M. Bezzeghoud, and P. Teves-Costa, Seismotectonics of Portugal and its adjacent Atlantic area, *Tectonophysics*, *337*, 373–387, doi:10.1016/S0040-1951(00)00291-2, 2001.

Braile, L., *Seismic Wave Demonstrations and Animations*, http://tinyurl.com/2dt46e, 2004.

Bressan, L., and S. Tinti, Structure and performance of a real-time algorithm to detect tsunami-like alert conditions based on sea-level records analysis, *Natural Hazards and Earth System Sciences*, *11*, 1499–1521, doi:10.5194/nhess-11-1499-2011, 2011.

Bressan, L., and S. Tinti, Detecting the 11 March 2011 Tohoku tsunami arrival on sea-level records in the Pacific Ocean: application and performance of the Tsunami Early Detection Algorithm (TEDA), *Natural Hazards and Earth System Science*, *12*, 1583–1606, doi:10.5194/nhess-12-1583-2012, 2012.

Bruyninx, C., W. Gurtner, and A. Muls, The EUREF permanent GPS network, *EUREF Publication*, *5*, 123–130, 1996.

Buforn, E., A. Udias, and M. A. Colombas, Seismicity, source mechanisms and tectonics of the Azores-Gibraltar plate boundary, *Tectonophysics*, *152*, 89–118, doi:10.1007/978-3-0348-7899-9_9, 1988.

Buforn, E., C. Sanz de Galdeano, and A. Udías, Seismotectonics of the Ibero-Maghrebian region, *Tectonophysics*, *248*, 247–261, doi:10.1016/0040-1951(94)00276-F, 1995.

Buforn, E., M. Bezzeghoud, A. Udias, and C. Pro, Seismic sources on the Iberia-African plate boundary and their tectonic implications, *Pure and Applied Geophysics*, *161*, 623–646, doi:10.1007/s00024-003-2466-1, 2004.

Buforn, E., B. Benito, C. Sanz de Galdeano, C. Fresno, D. del Muñoz, and I. Rodríguez, Study of the damaging earthquakes of 1911, 1999, and 2002 in the Murcia, Southeastern Spain region: seismotectonic and seismic-risk implications, *Bulletin of the Seismological Society of America*, *95*, 549–567, doi:10.1785/0120040041, 2005.

Buforn, E., S. Cesca, T. Goded, C. del Fresno, and D. Muñoz, The Bullas (Murcia, SE Spain) earthquake, 29 January 2005, *Journal of Seismology*, *10*, 65–72, doi:10.1007/s10950-006-2536-9, 2006.

Cabañas-Rodríguez, L., E. Carreño-Herrero, A. Izquierdo-Álvarez, J. M. Martínez-Solares, R. C. del Villar, J. Martínez-Díaz, B. Benito-Oterino, J. Gaspar-Escribano, A. Rivas-Medina, J. García-Mayordomo, R. Perez-López, M. A. Rodríguez-Pascua, and P. Murphy-Corella, Informe del sismo de Lorca del 11 de mayo de 2011, *Tech. rep.*, Instituto Geográfico Nacional de España, 2011.

Cahyadi, M. N., and K. Heki, Ionospheric disturbances of the 2007 Bengkulu and the 2005 Nias earthquakes, Sumatra, observed with a regional GPS network, *Journal of Geophysical Research: Space Physics*, *118*(1777-1787), doi:10.1002/jgra.50208, 2013.

Calvert, A., E. Sandvol, D. Seber, M. Barazangi, S. Roecker, T. Mourabit, F. Vidal, G. Alguacil, and N. Jabour, Geodynamic evolution of the lythosphere and upper mantle beneath the Alborán region of the western Mediterranean: Constraints from travel time topography, *Journal of Geophysical Research*, *105*, 10,871–10,898, doi: 10.1029/2000JB900024, 2000.

Carreño Herrero, E., La peligrosidad de tsunamis en las costas españolas, *Simulaciones, Enseñanza de las Ciencias de la Tierra*, *13*(1), 60–64, 2005.

Ching, K.-E., R.-J. Rau, and Y. Zeng, Coseismic source model of the 2003 Mw 6.8 Chengkung earthquake, Taiwan, determined from GPS measurements, *Journal of Geophysical Research*, *112*, B06,422, doi:10.1029/2006JB004439, 2007.

Choi, K., A. L. Bilich, K. M. Larson, and P. Axelrad, Modified sidereal filtering: Implications for high-rate GPS positioning, *Geophysical Research Letters*, *31*, L22,608, doi:10.1029/2004GL021621, 2004.

Cirella, A., A. Piatanesi, E. Tinti, and M. Cocco, Rupture process of the 2007 Niigata-ken Chuetsu-oki earthquake by non-linear joint inversion of strong motion and GPS data, *Geophysical Research Letters*, *35*, L16,306, doi: 10.1029/2008GL034756, 2008.

Colombelli, S., R. M. Allen, and A. Zollo, Application of real-time GPS to earthquake early warning in subduction and strike-slip environments, *Journal of Geophysical Research: Solid Earth*, *118*, 3448–3461, doi:10.1002/jgrb.50242, 2013.

Comas, M. C., J. P. Platt, J. I. Soto, and A. B. Watts, The origin and tectonic history of the Alboran Basin, *Proceedings of the Ocean Drilling Program, Scientific Results*, *161*, 555–580, 1999.

Crowell, B. W., Y. Bock, and D. Melgar, Real-time inversion of GPS data for finite fault modeling and rapid hazard assessment, *Geophysical Research Letters*, *39*, L09,305, doi:10.1029/2012GL051318, 2012.

Dach, R., U. Hugentobler, P. Fridez, and M. Meindl, *Bernese GPS Software ver. 5.0 Manual [Online]*, www.bernese.unibe.ch/docs/DOCU50.pdf, 2007.

Dao, M. H., and P. Tkalich, Tsunami propagation modelling - a sensitive study, *Natural Hazards and Earth System Sciences*, *7*, 741–754, doi:10.5194/nhess-7-741-2007, 2007.

Dettmering, D., and G. Webber, The EUREF-IP Ntrip Broadcaster: Real-time GNSS data for Europe, Proceedings of the IGS2004 Workshop, 2004.

Dewey, J. F., Pitman, W. C., Ryan, W. B. F., and J. Bonnin, Plate tectonics and the evolution of the alpine system, *Bulletin of the Seismological Society of America*, *84*, 3137–3180, doi:10.1130/0016-7606(1975), 1973.

Dick, S., E. Kleine, K. H. Müller-Navarra, S, and H. Komo, The Operational Circulation Model of BSH (BSHcmod), *Berichte des Bundesamtes, für Seeschifahrt und Hydrographie*, *29*, 49, 2001.

Dong, D., and Y. Bock, Global positioning system network analysis with phase ambiguity resolution applied to crustal deformation studies in california, *Journal of Geophysical Research*, *94*(B4), 3949–3966, doi:0148-0227/89/88JB-041525, 1989.

Dow, J., R. Neilan, and G. Gendt, The International GPS Service (IGS): celebrating the 10th anniversary and looking to the next decade, *Advanced Space Research*, *3*(36), 320–326, doi:10.1016/j.asr.2005.05.125, 2005.

Dow, J., R. E. Neilan, and C. Rizos, The International GNSS Service in a changing landscape of Global Navigation Satellite Systems, *Journal of Geodesy*, *83*, 191–198, doi:10.1007/s00190-008-0300-3, 2009.

Elosegui, P., J. L. Davis, R. T. K. Jaldehag, J. M. Johansson, A. E. Niell, and I. I. Shapiro, Geodesy using the Global Positioning System: the effects of signal scattering on estimates of site position, *Journal of Geophysical Research*, *100*(B6), 9921–9934, doi:95JB00868, 1995.

Emore, G. L., J. S. Haase, K. Choi, K. M. Larson, and A. Yamagiwa, Recovering seismic displacements through combined use of 1-Hz GPS and strong-motion accelerometers, *Bulletin of the Seismological Society of America*, *97*, 357–378, doi:10.1785/0120060153, 2007.

Erdik, M., Y. Fahjan, O. Ozel, H. Alcik, A. Mert, and M. Gul, Istanbul earthquake rapid response and the early warning system, *Bulletin of Earthquake Engenieering*, *1*, 157–163, doi:10.1023/A:1024813612271, 2003.

Ergintav, S., U. Doganb, C. Gersteneckerc, R. Çakmaka, A. Belgena, H. Demirel, C. Aydin, and R. Reilinger, A snapshot (2003-2005) of the 3D postseismic deformation for the 1999, M_w = 7.4 Izmit earthquake in the Marmara Region, Turkey, by first results of joint gravity and GPS monitoring, *Journal of Geodynamics*, *44*, 1–18, doi:10.1016/j.jog.2006.12.005, 2007.

Falck, C., M. Ramatschi, C. Subarya, M. Bartsch, A. Merx, J. Hoeberechts, and G. Schmidt, Near real-time GPS applications for tsunami early warning systems, *Natural Hazards and Earth System Science*, *10*(2), 181–189, doi:10.5194/nhess-10-181-2010, 2010.

Farrell, W. E., Deformation of the Earth by surface loads, *Reviews of Geophysics and Space Physics*, *10*, 761–797, doi:10.1029/RG010i003p00761, 1972.

Fleming, K., M. Picozzi, C. Milkereit, F. Kühnlenz, B. Lichtblau, J. Fischer, C. Zulfikar, O. Ozel, and the SAFER and EDIM Working Groups, The Self-Organizing Seismic Early Warning Information Network (SOSEWIN), *Seismological Research Letters*, *80*(5), 755–771, doi:10.1785/gssrl.80.5.755, 2009.

Foster, J. H., B. Brooks, D. Wang, G. S. Carter, and M. A. Merrifield, Improving tsunami warning using commercial ships, *Geophysical Research Letters*, *39*, L09,603, doi:2012GL051367, 2012.

Fratepietro, F., T. F. Baker, S. D. P. Williams, and M. V. Camp, Ocean loading deformations caused by storm surges on the northwest European shelf, *Geophysical Research Letters*, *33*, L06,317, doi:10.1029/2005GL025475, 2006.

Freund, F., Toward a unified solid state theory for pre-earthquake signals, *Acta Geophysica*, *58*(5), 719–766, doi:10.2478/s11600-009-0066-x, 2010.

Fritz, H. M., W. Kongko, A. Moore, B. McAdoo, J. Goff, C. Harbitz, B. Uslu, N. Kalligeris, D. Suteja, K. Kalsum, V. Titov, A. Gusman, H. Latief, E. Santoso, S. Sujoko, D. Djulkarnaen, H. Sunendar, and C. Synolakis, Extreme runup from the 17 July 2006 Java tsunami, *Geophysical Research Letters*, *34*, 12, doi:10.1029/2007GL029404, 2007.

Gade, S., and H. Herlufsen, *Technical Review No 3-1987: Windows to FFT analysis (Part I)*, http://www.bksv.com/doc/Bv0031.pdf, 2013.

Gahalaut, V. K., S. Jade, J. K. Catherine, R. Gireesh, M. B. Ananda, P. D. Kumar, M. Narsaiah, S. S. H. Jafri, A. Ambikapathy, A. Bansal, R. K. Chadha, D. C. Gupta, B. Nagarajan, and S. Kumar, GPS measurements of postseismic deformation in the Andaman-Nicobar region following the giant 2004 Sumatra-Andaman earthquake, *Journal of Geophysical Research*, *113*, B08,401, doi:10.1029/2007JB005511, 2008.

García-Mayordomo, J., J. M. Gaspar-Escribano, and B. Benito, Seismic hazard assessment of the Province of Murcia (SE Spain): analysis of source contribution to hazard, *Journal of Seismology*, *11*, 453–471, doi:10.1007/s10950-007-9064-0, 2007.

Gaspar-Escribano, J. M., B. Benito, and J. García-Mayordomo, Hazard-consistent response spectra in the Region of Murcia (Southeast Spain): comparison to earthquake-resistant provisions, *Bulletin of Eartquake Engenieering*, *6*, 179–196, doi:10.1007/s10518-007-9051-4, 2008.

Ge, L., S. Dai, S. Han, C. Rizos, Y. Ishikawa, and Y. Yoshida, GPS seismometers: the implementing issues, *Proceedings of the 13th International Technical Meeting of the Satellite Division of The Institute of Navigation (ION GPS 2000), Salt Lake City, UT*(1), 75–83, 2000a.

Ge, L., S. Han, C. Rizos, Y. Ishikawa, M. Hoshiba, Y. Yoshida, M. Izawa, N. Hashimoto, and S. Himori, GPS seismometers with up to 20-Hz sampling rate, *Earth Planets Space*, *52*(10), 881–884, doi:10.1186/BF03352300, 2000b.

Geist, E. L., Implications of the 26 December 2004 Sumatra-Andaman earthquake on tsunami forecast and assessment models for great subduction-zone earthquakes, *Bulletin of the Seismological Society of America*, *97*(1A), S249–S270, doi:10.1785/0120050619, 2007.

Geller, R., D. Jackson, Y. Kagan, and F. Mulargia, Earthquakes cannot be predicted, *Science*, *275*(5306), 16,161–1617, doi:10.1126/science.275.5306.1616, 1997.

Geller, R. J., Shake-up time for Japanese seismology, *Nature*, *472*, 407–409, doi:10.1038/nature10105, 2011.

Geng, J., S. D. Williams, F. N. Teferle, and A. H. Dodson, Detecting storm surge loading deformations around the southern North Sea using subdaily GPS, *Geophysical Journal International*, *191*(2), 569–578, doi:10.1111/j.1365-246X.2012.05656.x, 2012.

Genrich, J., and Y. Bock, Rapid resolution of crustal motion at short ranges with the Global Positioning System, *Journal of Geophysical Research*, *97*, 3261–3269, doi:10.1029/91jb02997, 1992.

Genrich, J. F., and Y. Bock, Instantaneous geodetic positioning with 10-50 Hz GPS measurements: noise characteristics and implications for monitoring networks, *Journal of Geophysical Research*, *111*, B03,403, doi:10.1029/2005JB003617, 2006.

Godin, G., *The analysis of tides*, University of Toronto Press, 1972.

Godin, O. A., V. G. Irisov, R. R. Leben, B. D. Hamlington, and G. A. Wick, Variations in sea surface roughness induced by the 2004 Sumatra-Andaman tsunami, *Natural Hazards and Earth System Sciences*, *9*, 1135–1147, doi:10.5194/nhess-9-1135-2009, 2009.

Gonzalez, P. J., K. F. Tiampo, M. Palano, F. Cannavó, and J. Fernández, The 2011 Lorca Earthquake slip distribution controlled by groundwater crustal unloading, *Nature Geoscience Letters*, *5*(11), 821–825, doi:10.1038/NGEO1610, 2012.

Grapenthin, R., and J. T. Freymueller, The dynamics of a seismic wave field: Animation and analysis of kinematic GPS data recorded during the 2011 Tohoku-oki earthquake, Japan, *Geophysical Research Letters*, *38*, L18,308, doi:10.1029/2011GL048405, 2011.

Grimison, N. L., and W.-P. Chen, The Azores-Gibraltar plate boundary: focal mechanisms, depths of earthquakes, and their tectonic implications, *Journal of Geophysical Research*, *91*, 2029–2048, doi:10.1029/JB091iB02p02029, 1986.

Hamlington, B. D., R. R. Leben, O. A. Godin, J. F. Legeais, E. Gica, and V. V. Titov, Detection of the 2010 Chilean tsunami using satellite altimetry, *Natural Hazards and Earth System Sciences*, *11*, 2391–2406, doi:10.5194/nhess-11-2391-2011, 2011.

Hamlington, B. D., R. R. Leben, O. A. Godin, E. Gica, V. V. Titov, B. J. Haines, and S. D. Desai, Could satellite altimetry have improved early detection and warning of the 2011 Tohoku tsunami?, *Geophysical Research Letters*, *39*, L15,605, doi:10.1029/2012GL052386, 2012.

Hammond, W. C., B. A. Brooks, R. Bürgmann, H. T., M. Jackson, A. R. Lowry, and S. Anandakrishnan, Scientific value of the real-time Global Positioning System data, *EOS*, *92*(15), 125–132, doi:10.1029/2011EO150001, 2011.

Hanka, W., J. Saul, B. Weber, J. Becker, P. Harjadi, Fauzi, and G. S. Group, Real-time earthquake monitoring for tsunami warning in the Indian Ocean and beyond, *Natural Hazards and Earth System Science*, *10*(12), 2611–2622, doi:10.5194/nhess-10-2611-2010, 2010.

Hanks, T. C., and H. Kanamori, Moment Magnitude scale, *Journal of Geophysical Research*, *84*(B5), 2348–2350, doi:10.1029/JB084iB05p02348, 1979.

Harris, L., Characteristics of the Hurricane Storm Surge, *Technical Paper 48*, Department of Commerce USA, 1963.

Hayakawa, M., On the fluctuation spectra of seismo-electromagnetic phenomena, *Natural Hazards and Earth System Sciences*, *11*, 301–308, doi:10.5194/nhess-11-301-2011, 2011.

Hayakawa, M., Y. Sue, and T. Nakamura, The effect of earth tides as observed in seismo-electromagnetic precursory signals, *Natural Hazards and Earth System Sciences*, *9*, 1733–1741, doi:10.5194/nhess-9-1733-2009, 2009.

Heiki, K., and Y. Tamura, Short term afterslip in the 1994 Sanriku-Haruka-Oki Earthquake, *Geophysical Research Letters*, *24*(24), 3285–3288, doi:10.1029/97GL03316, 1997.

Herbert, H., and P. J. Alasset, The tsunami triggered by the 21 May 2003 Algiers Earthquake, *EMSC Newsletter*, *30*, 10–12, 2003.

Hill, E. M., J. C. Borrero, Z. Huang, Q. Qiu, P. Banerjee, D. H. Natawidjaja, P. Elosegui, H. M. Fritz, B. W. Suwargadi, I. R. Pranantyo, L. Li, K. A. Macpherson, V. Skanavis, C. E. Synolakis, and K. Sieh, The 2010 Mw 7.8 Mentawai earthquake: very shallow source of a rare tsunami earthquake determined from tsunami field survey and near-field GPS data, *Journal of Geophysical Research*, *117*, B06,402, doi:10.1029/2012JB009159, 2012.

Hiroo, and Kanamori, Mechanism of tsunami earthquakes, *Physics of the Earth and Planetary Interiors*, *6*(5), 346 – 359, doi:10.1016/0031-9201(72)90058-1, 1972.

Hofmann-Wellenhof, B., and H. Moritz, *Physical Geodesy*, Springer Wien New York, 2006.

Horiuchi, S., Y. Horiuchi, S. Yamamoto, H. Nakamura, C. Wu, P. A. Rydelek, and M. Kachi, Home seismometer for earthquake early warning, *Geophysical Research Letters*, *36*, L00B04, doi:10.1029/2008GL036572, 2009.

Hreinsdóttir, S., J. T. Freymueller, R. Bürgmann, and J. Mitchell, Coseismic deformation of the 2002 Denali Fault earthquake: insights from GPS measurements, *Journal of Geophysical Research*, *111*, B03,308, doi:10.1029/2006JB003676, 2006.

Hsiao, N.-C., Y.-M. Wu, T.-C. Shin, L. Zhao, and T.-L. Teng, Development of earthquake early warning system in Taiwan, *Geophysical Research Letters*, *36*, L00B02, doi:10.1029/2008GL036596, 2009.

IERS Technical Note n. 36, *IERS Conventions 2010. Chapter 4: Terrestrial reference systems and frames*, http://www.iers.org/IERS/EN/Publications/TechnicalNotes/tn36.html?nn=94912, 2010a.

IERS Technical Note n. 36, *IERS Conventions 2010. Chapter 8: Tidal variations in the Earth's rotation*, http://www.iers.org/IERS/EN/Publications/TechnicalNotes/tn36.html?nn=94912, 2010b.

IGS, IGS Products, http://igscb.jpl.nasa.gov/components/prods.html, 2015.

ITRF, Science background - General concepts, http://itrf.ensg.ign.fr/general.php, 2015.

Jelínek, R., and E. Krausmann, *Tsunami risk analysis applied to the city of Cádiz*, JRC Scientific and Technical Reports, 2009.

Ji, C., K. M. Larson, Y. Tan, K. W. Hudnut, and K. Choi, Slip history of the 2003 San Simeon earthquake constrained by combining 1-Hz GPS, strong motion, and teleseismic data, *Geophysical Research Letters*, *31*, L17,608, doi:10.1029/2004GL020448, 2004.

Jing, F., X. H. Shen, C. L. Kang, and P. Xiong, Variations of multi-parameter observations in atmosphere related to earthquake, *Natural Hazards and Earth System Sciences*, *13*, 27–33, doi:10.5194/nhess-13-27-2013, 2013.

Jolivet, L., and C. Faccenna, Mediterranean extension and the Africa-Eurasia collision, *Tectonics*, *19*, 1095–1106, doi:10.1029/2000TC900018, 2000.

Kagan, Y. Y., and D. D. Jackson, Global earthquake forecasts, *Geophysical Journal International*, *184*, 759–776, doi:10.1111/j.1365-246X.2010.04857.x, 2010.

Kakinami, Y., M. Kamogawa, Y. Tanioka, S. Watanabe, A. R. Gusman, J.-Y. Liu, Y. Watanabe, and T. Mogi1, Tsunamigenic ionospheric hole, *Geographical Research Letters*, *39*, L00G27, doi:10.1029/2011GL050159, 2012.

Kamigaichi, O., *Tsunami forecasting and warning*, vol. 9592-9618, springer ed., Meyers, R. A., 2009.

Kamigaichi, O., M. Saito, K. Doi, T. Matsumori, S. Tsukada, K. Takeda, T. Shimoyama, K. Nakamura, M. Kiyomoto, and Y. Watanabe, Earthquake early warning in Japan: warning the general public and future prospects, *Seismological Research Letters*, *80*(5), 717–726, doi:10.1785/gssrl.80.5.717, 2009.

Kato, T., Y. Terada, K. Ito, R. Hattori, T. Abe, T. Miyake, S. Koshimura, and T. Nagai, Tsunami due to the 2004 September 5th off the Kii Peninsula earthquake, Japan, recorded by new GPS buoy, *Earth Planets Space*, *57*, 297–301, doi:10.1186/BF03352566, 2005.

Kedar, S., G. A. Hajj, B. D. Wilson, and M. B. Heflin, The effect of second order GPS ionospheric correction on receiver positions, *Geophysical Research Letters*, *30*(16), 1929, doi:10.1029/2003GL017639, 2003.

Khazaradze, G., E. Suriñach, J. Gárate, and J. M. Davila, Crustal deformation in Eastern Betics from CuaTeNeo GPS network, *Geophysical Research Letters*, *9*(05314), 600–612, doi:10.1016/j.tecto.2013.08.020, 2007.

Koehler, N., G. Cua, F. Wenzel, and M. Boese, Rapid source parameter estimations of Southern California earthquakes using PreSEIS, *Seismological Research Letters*, *80*(5), 748–754, doi:10.1785/gssrl.80.5.748, 2009.

Koppert, A., GPS-Seismometer auf Basis von NTRIP-Datenströmen, Bachelor thesis, Institute of Geodesy, TU Darmstadt, 2011.

Kouba, J., Measuring seismic waves induced by large earthquakes with GPS, *Studia Geophysica et Geodaetica*, *47*, 741–755, doi:10.1023/A:1026390618355, 2003.

Kreemer, C., G. Blewitt, , and F. Maerten, Co- and postseismic deformation of the 28 March 2005 Nias Mw 8.7 earthquake from continuous GPS data, *Geophysical Research Letters*, *33*, L07,307, doi:10.1029/2005GL025566, 2006.

Langbein, H., and Y. Bock, High-rate real-time GPS network at Parkfield: Utility for detecting fault slip and seismic displacements, *Geophysical Research Letters*, *31*, L15S20, doi:10.1029/2003GL019408, 2004.

Lario, J., C. Zazo, J. Goy, P. Silva, T. Bardaji, A. Cabero, and C. Dabrio, Holocene palaeotsunami catalogue of SW Iberia, *Quatern. Int.*, *242*, 196–200, doi:10.1016/j.quaint.2011.01.036, 2011.

Larson, K., Gps seismology, *Journal of Geodesy*, *83*, 227–233, doi:10.1007/s00190-008-0233-x, 2009.

Larson, K. M., P. Bodin, and J. Gomberg, Using 1-Hz GPS data to measure deformations caused by the Denali Fault earthquake, *Science xpress*, *300*(5624), 1421–1424, doi:10.1126/science.1084531, 2003.

Larson, K. M., A. L. Bilich, and P. Axelrad, Improving the precision of high-rate GPS, *Journal of Geophysical Research*, *112*, B05,422, doi:10.1029/2006JB004367, 2007.

Lima, V. V., J. M. Miranda, M. A. Baptista, J. Catalão, M. Gonzalez, L. Otero, M. Olabarrieta, J. A. Álvarez-Gómez, and E. Carreño Herrero, Impact of a 1755-like tsunami in Huelva, Spain, *Natural Hazards and Earth System Sciences*, *10*, 139–148, doi:10.5194/nhess-10-139-2010, 2010.

Lin, A., R. Ikuta, and G. Rao, Tsunami run-up associated with co-seismic thrust slip produced by the 2011 Mw 9.0 off Pacific coast of Tohku earthquake, Japan, *Earth and Planetary Science Letters*, *337*(338), 121–132, doi:j.epsl.2012.04.047, 2012.

Liu, P., T. R. Wu, F. Raichlen, C. E. Synolakis, and J. C. Borrero, Runup and rundown generated by three-dimensional sliding masses, *Journal of Fluid Mechanics*, *536*, 107–144, doi:10.1017/S0022112005004799, 2005.

Liu, S., and A. Stuerze, An evaluation of the IGS real time service based on PPP, in *Geodätische Woche*, 2013.

López-Comino, J. A., F. d. L. Mancilla, J. Morales, and D. Stich, Rupture directivity of the 2011 Mw 5.2 Lorca Earthquake (Spain), *Geophysical Research Letters*, *31*, L03,301, doi:10.1029/2011GL050498, 2012.

Lyard, F., F. Lefevre, T. Letellier, and O. Francis, Modelling the global ocean tides: modern insignths from FES2004, *Ocean Dynamics*, *56*(5-6), 394–415, doi:10.1007/s10236-006-0086-X, 2006.

Mancilla, F., C. Ammon, R. Herrmann, and J. Morales, Faulting parameters of the 1999 Mula earthquake, south-eastern Spain, *Tectonophysics*, *354*, 139–155, 2002.

Maouche, S., M. Meghraoui, C. Morhange, S. Belabbes, Y. Bouhadad, and H. Haddou, Active coastal thrusting and folding, and uplift rate of the Sahel Anticline and Zemmouri earthquake area (Tell Atlas, Algeria), *Tectonophysics*, *509*, 69–80, doi:10.1016/j.tecto.2011.06.003, 2011.

Martínez-Solares, J. M., and A. López Arroyo, The great historical 1755 earthquake. Effects and damage in Spain, *Journal of Seismology*, *8*, 275–294, doi:10.1023/B:JOSE.0000021365.94606.03, 2004.

Masana, E., J. Martínez-Díaz, J. L. Hernández-Enrile, and P. Santanach, The Alhama de Murcia fault (SE Spain), a seismogenic fault in a diffuse plate boundary: seismotectonic implications for the Ibero-Magrebian region, *Journal of Geophysical Research*, *109*, B01,301, doi:10.1029/2002JB002359, 2004.

Masci, F., Brief Communication "On the recent reaffirmation of ULF magnetic earthquakes precursors", *Natural Hazards and Earth System Sciences*, *11*, 2193–2198, doi:10.5194/nhess-11-2193-2011, 2011.

Matias, L. M., T. Cunha, A. Annunziato, M. A. Baptista, and F. Carrilho, Tsunamigenic earthquakes in the Gulf of Cadiz: fault model and recurrence, *Natural Hazards and Earth System Sciences*, *13*, 1–13, doi:10.5194/nhess-13-1-2013, 2013.

McCaffrey, R., Global frequency of magnitude 9 earthquakes, *Geology*, *36*, 263–266, doi:10.1130/G24402A.1., 2008.

McCloskey, J., A. Antonioli, K. Piatanesi, K. Sieh, S. Steacy, S. S. Nalbant, M. Cocco, C. Giunchi, Huang, and P. Dunlop, Tsunami threat in the Indian Ocean from a future megathrust earthquake west of Sumatra, *Earth and Planetary Science Letters*, *265*, 61–81, doi:10.1016/j.epsl.2007.09.034, 2008.

Meijninger, B. M. L., Late-orogenic extension and strike-slip deformation in the Neogene of southeastern Spain, Ph.D. thesis, Utrecht University, 2006.

Melgar, D., Y. Bock, and B. W. Crowell, Real-time centroid moment tensor determination for large earthquakes from local and regional displacement records, *Geophysical Journal International*, *188*, 703–718, doi:10.1111/j.1365-246X.2011.05297.x, 2011.

Mendoza, L., A. Kehm, A. Koppert, J. Martín Dávila, J. Gárate, and M. Becker, The Lorca earthquake observed by GPS: a test case for GPS Seismology, *Física de la Tierra*, *24*, 129–150, 2012.

Mezcua, J., and J. Rueda, Seismological evidence for a delamination process in the lithosphere under the Alboran Sea, *Geophys. J. Int.*, *129*, 1–8, doi:10.1111/j.1365-246X.1997.tb00934.x, 1997.

Mitsui, Y., and K. Heki, Scaling of early afterslip velocity and possible detection of tsunami-induced subsidence by GPS measurements immediately after the 2011 Tohoku-Oki earthquake, *Geophysical Journal International*, *195*, 238–248, doi:10.1093/gji/ggt256, 2013.

Miyazaki, S., and K. M. Larson, Coseismic and early postseismic slip for the 2003 Tokachi-oki earthquake sequence inferred from GPS data, *Geophysical Research Letters*, *35*, L04,302, doi:10.1029/2007GL032309, 2007.

Miyazaki, S., T. Sagiya, T. Tada, and Y. Hatanaka, *One Hz sampling GPS as an ultra-long-period seismograph*, AGU Fall Meeting, San Francisco, California, 1997.

Miyazaki, S., K. M. Larson, K. Choi, K. Hikima, K. Koketsu, P. Bodin, J. Haase, G. Emore, and A. Yamagiwa, Modeling the rupture process of the 2003 September 25 Tokachi-Oki (Hokkaido) earthquake using 1-Hz GPS data, *Geophysical Research Letters*, *31*, L21,603, doi:10.1029/2004GL021457, 2004.

Morel, J. L., and M. Meghraoui, Goringe-Alboran-Tell tectonic zone; a transpression system along the Africa–Eurasia plate boundary, *Geology*, *24*(8), 755–758, doi:10.1130/0091-7613(1996), 1996.

Muhari, A., F. Imamura, S. Koshimura, and J. Post, Examination of three practical run-up models for assessing tsunami impact on highly populated areas, *Natural Hazards and Earth System Sciences*, *11*, 3107–3123, doi:nhess-11-3107-2011, 2011.

Muñoz-Martín, A., G. D. Vicente, J. Fernández-Lozano, S. Cloetingh, E. Willingshofer, D. Sokoutis, and F. Beekman, Spectral analysis of the gravity and elevation along the western Africa–Eurasia plate tectonic limit: continental versus oceanic lithospheric folding signals, *Tectonophysics*, *495*, 298–314, doi:10.1016/j.tecto.2010.09.036, 2010.

Newman, A. V., L. Feng, H. M. Fritz, Z. M. Lifton, N. Kalligeris, and Y. Wei, The energetic 2010 m_w 7.1 solomon islands tsunami earthquake, *Geophysical Journal International*, *186*, 775–781, doi:10.1111/j.1365-246X.2011.05057.x, 2011.

Niell, A., Global mapping functions for the atmosphere delay at radio wavelengths, *Journal of Geophysical Research*, *101*, 3227–3246, doi:10.1029/95JB03048, 1996.

Nikolaidis, R. M., Y. Bock, P. J. de Jonge, P. Shearer, D. Carr Agnew, and M. Van Domselaar, Seismic wave observations with the global positioning system, *Journal of Geophysical Research*, *106*(B10), 21,897–21,916, doi:10.1029/2001JB000329, 2001.

Nocquet, J.-M., Present-day kinematics of the Mediterranean: a comprehensive overview of GPS results, *Tectonophysics*, *579*, 220–242, doi:10.1016/j.tecto.2012.03.037, 2012.

Occhipinti, G., A. Komjathy, and P. Lognonné, Tsunami detection by GPS. How ionospheric observations might improve the global warning system, *GPS World*, *February 2008*, 50–53, 2008.

Ohta, Y., I. Meiano, T. Sagiya, F. Kimata, and K. Hirahara, Large surface wave of the 2004 Sumatra-Andaman earthquake captured by the very long baseline kinematic analysis of 1-Hz GPS data, *Earth Planets Space*, *58*, 153–157, doi:10.1186/BF03353372, 2006.

Ohta, Y., T. Kobayashi, H. Tsushima, S. Miura, R. Hino, T. Takasu, H. Fujimoto, T. Iinuma, K. Tachibana, T. Demachi, T. Sato, M. Ohzono, and N. Umino, Quasi real-time fault model estimation for near-field tsunami forecasting based on RTK-GPS analysis: Application to the 2011 Tohoku-Oki earthquake (Mw 9.0), *Journal of Geophysical Research: Solid Earth*, *117*(B2), 2156–2202, doi:10.1029/2011JB008750, 2012.

Okal, E., and C. E. Synolakis, Source discriminants for near-field tsunamis, *Geophysical Journal International*, *158*, 899–912, doi:10.1111/j.1365-246X.2004.02347.x, 2004.

Olivieri, M., and L. Scognamiglio, Toward a Euro Mediterranean tsunami warning system: the case of the February 12, 2007, Ml = 6.1 earthquake, *Geophysical Research Letters*, *34*, L24,309, doi:10.1029/2007GL031364, 2007.

Omira, R., M. A. Baptista, L. Matias, J. M. Miranda, C. Catita, F. Carrilho, and E. Toto, Design of a sea-level tsunami detection network for the Gulf of Cadiz, *Natural Hazards and Earth System Sciences*, *9*, 1327–1338, doi:10.5194/nhess-9-1327-2009, 2009.

O'Toole, T. B., A. P. Valentine, and J. H. Woodhouse, Earthquake source parameters from GPS-measured static displacements with potential for real-time application, *Geophysical Research Letters*, *40*, 1–6, doi:10.1029/2012GL054209, 2012a.

O'Toole, T. B., A. P. Valentine, and J. H. Woodhouse, Centroid-moment tensor inversions using high-rate GPS waveforms, *Geophysical Journal International*, *191*, 257–270, doi:10.1111/j.1365-246X.2012.05608.x, 2012b.

Pazos, A., J. Martin Davila, E. Buforn, J. Gárate Paquin, M. Catalán Morollón, W. Hanka, A. Udias, M. Benzzeghoud, M. Harnafi, and R. S. Team, Multi-parameter observations in the Ibero-Moghrebian region: the Western Mediterranean seismic network (WM) and ROA GPS geodynamic network, *Geophysical Research Abstracts*, *12*, EGU2010–9865, 2010.

Peng, H., Z. Wu, Y. M. Wu, S. Yu, D. Zhang, and W. Huang, Developing a prototype Earthquake Early Warning System in the Beijing Capital Region, *Seismological Research Letters*, *82*(3), 394–403, doi:10.1785/gssrl.82.3.394, 2011.

Plag, H. P., G. Blewitt, C. Kreemer, and W. C. Hammond, *Solid earth deformations induce by the sumatra earthquakes of 2004-2005: GPS detection of co-seismic displacements and tsunami-induced loading*, 549-556, 2006.

Pollitz, F. F., B. Brooks, X. Tong, M. G. Bevis, J. H. Foster, R. Bürgmann, J. Robert Smalley, C. Vigny, A. Socquet, J.-C. Ruegg, J. Campos, S. Barrientos, H. Parra, J. C. Baez-Soto, S. Cimbaro, and M. Blanco, Coseismic slip distribution of the February 27, 2010 M_w 8.8 Maule, Chile earthquake, *Geophysical Research Letters*, *38*, L09,309, doi:10.1029/2011GL047065, 2011.

Pro, C., E. Buforn, S. Cesca, C. Sanz de Galdeano, and A. Udías, Rupture process of the Lorca (southeast Spain) 11 May 2011 (Mw=5.1) earthquake, *Journal of Seismology*, *18*, 481–495, doi:10.1007/s10950-014-9421-8, 2014.

Probst, P., and G. Franchello, *Global storm surge forecast and inundation modeling*, Joint Research Centre, European Commission, eur 25233 ed., 2012.

Remondi, B. W., Global positioning system carrier phase: description and use, *Bulletin Géodésique*, *59*(4), 361–377, doi:10.1007/BF02521069, 1985.

Renou, C., O. Lesne, A. Mangin, F. Rouffi, A. Atillah, D. El Hadani, and H. Moudni, Tsunami hazard assessment in the coastal area of Rabat and Salé, Morocco, *Natural Hazards and Earth System Sciences*, *11*, 2181–2191, doi:10.5194/nhess-11-2181-2011, 2011.

Ribeiro, J., A. Silva, and P. Leitao, High resolution tsunami modelling for the evaluation of potentia risk areas in Setúbal (Portugal), *Natural Hazards and Earth System Sciences*, *11*, 2371–2380, doi:10.5194/nhess-11-2371-2011, 2011.

Roger, J., H. Hébert, J.-C. Ruegg, and P. Briole, The El Asnam 1980 October 10 inland earthquake: a new hypothesis of tsunami generation, *Geophysical Journal International*, *185*, 1135–1146, doi:10.1111/j.1365-246X.2011.05003.x, 2011.

Rolandone, F., M. Dreger, D an Murray, and R. Bürgmann, Coseismic slip distribution of the 2003 Mw 6.6 San Simeon earthquake, California, determined from GPS measurements and seismic waveform data, *Geophysical Research Letters*, *33*, L16,315, doi:10.1029/2006GL027079, 2006.

Rosenau, M., R. Nerlich, S. Brune, and O. Oncken, Experimental insights into the scaling and variability of local tsunamis triggered by giant subduction megathrust earthquakes, *Journal of Geophysical Research*, *115*, B09,314, doi:10.1029/2009JB007100, 2010.

Rudloff, A., J. Lauterjung, U. Münch, and S. Tinti, Preface The GITEWS Project (German-Indonesian Tsunami Early Warning System), *Natural Hazards and Earth System Sciences*, *9*, 1381–1382, doi:10.5194/nhess-9-1381-2009, 2009.

Rundle, J. B., J. R. Holliday, M. Yoder, M. K. Sachs, A. Donnellan, D. L. Turcotte, K. F. Tiampo, W. Klein, and L. H. Kellogg, Earthquake precursors: activation or quiescence?, *Geophysical Journal International*, *187*, 225–236, doi:10.1111/j.1365-243X.2011.05134.x, 2011.

Saradjian, M. R., and M. Akhoondzadeh, Prediction of the date, magnitude and affected area of impending strong earthquakes using integration of multi precursors earthquake parameters, *Natural Hazards and Earth System Sciences*, *11*, 1109–1119, doi:10.5194/nhess-11-1109-2011, 2011.

Sarri, A., S. Guillas, and F. Dias, Statistical emulation of a tsunami model for sensitivity analysis and uncertainty quantification, *Natural Hazards and Earth System Sciences*, *12*, 2003–2018, doi:nhess-12-2003-2012, 2012.

Scharroo, R., and L. Fenoglio, *Cyclone Xaver seen by SARAL/AltiKa [online]*, http://tinyurl.com/pokztsm, 2013.

Scharroo, R., W. Smith, and J. Lillibridge, Hurricane storm surge seen with altimetry, *EOS*, *86*, 40, 2005.

Schmid, R., M. Rothacher, D. Thaller, and P. Steigenberger, Absolute phase center corrections of satellite and receiver antennas – impact on global GPS solutions and estimation of azimuthal phase center variations of the satellite antenna, *GPS Solutions*, *9*, 283–293, doi:10.1007/s10291-005-0134-x, 2005.

Schoene, T., C. Subarya, P. Manurung, C. Nölte, S. Roemer, R. Galas, J. Illigner, A. Kloth, M. Köppl, T. Queisser, C. Selke, N. Storlarczuk, and M. Bartsch, Offshore and onshore sea level measurements, *Proceedings of the International Conference on Tsunami Warning*, *Bali*(Indonesia), 2008.

Schoene, T., W. Pandoe, I. Mudita, S. Roemer, J. Illigner, C. Zech, and R. Galas, GPS water level measurements for Indonesia's Tsunami Early Warning System, *Natural Hazards and Earth System Sciences*, *11*, 741–749, doi:10.5194/nhess-11-741-2011, 2011.

Segall, P., and J. L. Davis, GPS applications for geodynamics and earthquake studies, *Earth Planets Science*, *25*, 301–336, doi:10.1146/annurev.earth.25.1.301, 1997.

Shearer, P., *Introduction to Seismology*, Cambridge University Press, 2009.

Sobolev, G. A., and A. A. Lyubushin, Microseismic impulses as earthquake precursors, *Physics Solid Earth*, *42*(9), 721–733, doi:10.1134/S1069351306090023, 2006.

Sobolev, S. V., A. Y. Babeyko, R. Wang, R. Galas, M. Rothacher, D. Sein, J. Schröter, J. Lauterjung, and C. Subarya, Towards real-time tsunami amplitude prediction, *Eos*, *87*(37), 374–378, 2006.

Sobolev, S. V., A. Y. Babeyko, R. Wang, A. Hoechner, R. Galas, M. Rothacher, D. V. Sein, J. Schröter, J. Lauterjung, and C. Subarya, Tsunami early warning using GPS-Shield arrays, *Journal of Geophysical Research*, *112*, B08,415, doi:10.1029/2006JB004640, 2007.

Song, Y. T., Detecting tsunami genesis and scales directly from coastal GPS stations, *Geophysical Research Letters*, *34*, L19,602, doi:10.1029/2007GL031681, 2007.

Song, Y. T., *NASA Demonstrates Tsunami Prediction System [online]*, http://www.jpl.nasa.gov/news/news.cfm?release=2010-198, 2010.

Sørensen, M. B., M. Spada, A. Babeyko, S. Wiemer, and G. Grünthal, Probabilistic tsunami hazard in the Mediterranean Sea, *Journal of Geophysical Research*, *117*, B01,305, doi:10.1029/2010JB008169, 2012.

Steblov, G. M., M. G. Kogan, B. V. Levin, N. F. Valisenko, A. S. Prytkov, and D. I. Frolov, Spatially linked asperities of the 2006-2007 great kuril earthquakes revealed by gps, *Geophysical Research Letters*, *35*, L22,306, doi:10.1029/2008GL035572, 2008.

Stich, D., C. Ammon, and J. Morales, Moment tensor solutions for small and moderate earthquakes in the ibero–maghreb region, *Journal of Geophysical Research*, *108*, 21–48, doi:10.1029/2002JB002057, 2003.

Stich, D., E. Serpelloni, F. Mancilla, and J. Morales, Kinematics of the Iberia-Maghreb plate contact from seismic moment tensors and GPS observations, *Tectonophysics*, *426*, 295–317, doi:10.1016/j.tecto.2006.08.004, 2006.

Suárez, G., D. Novelo, and E. Mansilla, Performance evaluation of the seismic alert system (SAS) in Mexico City: A seismological and a social perspective, *Seismological Research Letters*, *80*(5), 707–714, 2009.

Synolakis, C. E., J.-P. Bardet, J. C. Borrero, H. L. Davies, E. A. Okal, E. A. Silver, S. Sweet, and D. R. Tappin, The slump origin of the 1998 papua new guinea tsunami, *Proceedings of the Royal Society of London*, *458*, 763–789, 2002.

Takasu, T., *RTKLIB ver. 2.4.1 manual [online]*, http://www.rtklib.com/prog/manual_2.4.1.pdf, 2011.

Tang, L., V. V. Titov, E. Bernard, Y. Wei, C. Chamberlin, J. C. Newman, H. Mofjeld, D. Arcas, M. Eble, C. Moore, B. Uslu, C. Pells, M. C. Spillane, L. M. Wright, and E. Gica, Direct energy estimation of the 2011 japan tsunami using deep-ocean pressure measurements, *Journal of Geophysical Research*, *117*, C08,008, doi:10.1029/2011JC007635,2012, 2012.

Thio, H. K., R. W. Graves, P. G. Sommerville, T. Sato, and T. Ishii, A multiple time window rupture model for the 1999 chi-chi earthquake from a combined inversion of teleseismic, surface wave, strong motion, and gps data, *Journal of Geophysical Research*, *109*, B08,309, doi:10.1029/2002JB002381, 2004.

Tinti, S., A. Maramai, and L. Graziani, A new version of the european tsunami catalogue: updating and revision, *Natural Hazards and Earth System Sciences*, *1*, 255–262, doi:10.5194/nhess-1-255-2001, 2001.

Tinti, S., A. Armigliato, G. Pagnoni, and F. Zaniboni, Scenarios of giant tsunamis of tectonic origin in the mediterranean, *Journal of Earthquake Technology*, *42*(4), 171–188, 2005.

Tinti, S., L. Graziani, B. Brizuela, A. Maramai, and S. Gallazzi, Applicability of the decision matrix of north eastern atlantic, mediterranean and connected seas tsunami warning system to the italian tsunamis, *Natural Hazards and Earth System Sciences*, *12*, 843–857, doi:10.5194/nhess-12-843-2012, 2012.

Titov, V. V., *Tsunami forecasting in the sea*, Harvard University Press, 2009.

UCA, and IGN, Scenario flooding and risk maps, probabilistic risk maps for Cádiz city and Huelva community. Risk reduction measures for Cádiz, *Deliverable D8.2 of project TRANSFER*, *5th European Framework Programme*, 2009.

Valencia, N., A. Gardi, A. Gauraz, F. Leone, and R. Guillande, New tsunami damage functions developed in the framework of schema project: application to european-mediterranean coasts, *Natural Hazards and Earth System Sciences*, *11*, 2835–2846, doi:10.5194/nhess-11-2835-2011, 2011.

van Dam, T., X. Collilieux, J. Wuite, Z. Altamimi, and J. Ray, Nontidal ocean loading: amplitudes and potential effects in gps height time series, *Journal of Geodesy*, *86*, 1043–1057, doi:10.1007/s00190-012-0564-5, 2012.

Vigny, C., A. Socquet, S. Peyrat, J.-C. Ruegg, M. Métois, R. Madariaga, S. Morvan, M. Lancieri, R. Lacassin, J. Campos, D. Carrizo, M. Bejar-Pizarro, S. Barrientos, R. Armijo, C. Aranda, M.-C. Valderas-Bermejo, I. Ortega, F. Bondoux, S. Baize, H. Lyon-Caen, A. Pavez, J. P. Vilotte, M. Bevis, B. Brooks, R. Smalley, H. Parra, J.-C. Baez, M. Blanco, S. Cimbaro, and E. Kendrick, The 2010 m_w 8.8 maule megathrust earthquake of central chile, monitored by gps, *Science*, *332*(6036), 1417–1421, doi:10.1126/science.1204132, 2011.

Vilanova, S. P., J. F. B. D. Fonseca, and C. S. Oliveira, Ground-motion models for seismic-hazard assessment in western iberia: constraints from instrumental data and intensity observations, *Bulletin of the Seismological Society of America*, *102*(1), 169–184, doi:10.1785/0120110097, 2012.

Vissers, R. L. M., and B. M. L. Meijninger, The 11 may 2011 earthquake at lorca (se spain) viewed in a structural-tectonic context, *Solid Earth*, *2*(2), 199–204, doi:10.5194/se-2-199-2011, 2011.

Wang, G.-Q., D. M. Boore, G. Tang, and X. Zhou, Comparisons of ground motions from colocated and closely spaced one-sample-per-second Global Positioning System and accelerograph recordings of the 2003 m 6.5 san simeon, california, earthquake in the parkfield region, *Bulletin of the Seismological Society of America*, *97*, 76–90, doi:10.1785/0120060053, 2007.

Wang, R., S. Parolai, M. Ge, M. Jin, T. Walter, and J. Zschau, The 2011 m_w 9.0 tohoku earthquake: comparison of gps and strong-motion data, *Bulletin of the Seismological Society of America*, *103*(2b), 1336–1347, doi:10.1785/0120110264, 2012.

Welch, P. D., The use of fast fourier transform for the estimation of power spectra: A method based on time averaging over short, modified periodograms, *IEEE Transactions on Audio Electroacoustics*, *AU-15*, 70–73., doi:10.1109/TAU.1967.1161901, 1967.

Wessel, P., and W. H. F. Smith, Free software helps map and display data, *EOS Transactions, American Geophysical Union*, *72*(441), 445–446, doi:10.1029/90EO00319, 1991.

Wessel, P., W. H. F. Smith, R. Scharroo, J. Luis, and F. Wobbe, Generic Mapping Tools: Improved Version Released, *EOS Transactions, American Geophysical Union*, *94*(45), 409, doi:10.1002/2013EO450001, 2013.

Willetts, H., Storm surge warning for mainland Europe, http://www.bbc.com/news/world-europe-25242991, 2013.

Williams, S. D. P., N. T. Penna, F. N. Teferle, and J. Geng, *Storm surge and non-tidal ocean loading effects on geodetic GPS observations*, American Geophysical Union, Fall Meeting, 2009.

Wright, T. J., N. Houlié, M. Hildyard, and T. Iwabuchi, Real-time, reliable magnitudes for large earthquakes from 1 Hz GPS precise point positioning: The 2011 Tohoku-Oki (Japan) earthquake, *Geophysical Research Letters*, *39*, L12,302, doi:10.1029/2012GL051894, 2012.

Wu, T. R., and T. C. Ho, High resolution tsunami inversion for 2010 Chile earthquake, *Natural Hazards and Earth System Sciences*, *11*, 3251–3261, doi:nhess-11-3251-2011, 2011.

Yamagiwa, A., Y. Hatanaka, T. Yutsudo, and B. Miyahara, Real time capability of GEONET system and its application to crust monitoring, *Bulletin of the Geographical Survey Institute*, *53*, 27–33, 2006.

Yao, Y. B., P. Chen, S. Zhang, J. J. Chen, F. Yan, and W. F. Peng, Analysis of pre-earthquake ionospheric anomalies before the global M = 7.0+ earthquakes in 2010, *Natural Hazards and Earth System Sciences*, *12*, 575–585, doi: 10.5194/nhess-12-575-2012, 2012.

Yelles, K., K. Lammali, A. Mahsas, E. Calais, and P. Briole, Coseismic deformation of the May 21st, 2003, Mw=6.8 Boumerdes earthquake, Algeria, from GPS measurements, *Geophysical Research Letters*, *31*, L13,610, doi:10.1029/2004GL019884, 2006.

Yokota, Y., K. Koketsu, K. Hikima, and S. Miyazaki, Ability of 1-Hz GPS data to infer the source process of a medium-sized earthquake: the case of the 2008 Iwate-Miyagi Nairiku, Japan, earthquake, *Geophysical Research Letters*, *36*, L12,301, doi:10.1029/2009GL037799, 2009.

Yue, H., and T. Lay, Inversion of high-rate (1 sps) GPS data for rupture process of the 11 March 2011 Tohoku earthquake (Mw 9.1), *Geophysical Research Letters*, *38*, L00G09, doi:10.1029/2011GL048700, 2011.

Zheng, Y., J. Li, Z. Xie, and M. H. Ritzwoller, 5 Hz GPS seismology of the El Mayor-Cucapah earthquake: estimating the earthquake focal mechanism, *Geophysical Journal International*, *190*, 1723–1732, doi:10.1111/j.1365-246X.2012.05576.x, 2012.

Zitellini, N., E. Gràcia, L. Matias, P. Terrinha, M. Abreu, G. DeAlteriis, J. Henriet, J. Dañobeitia, D. Masson, T. Mulder, R. Ramella, L. Somoza, and S. Diez, The quest for the Africa-Eurasia plate boundary west of the Strait of Gibraltar, *Earth and Planetary Science Letters*, *280*(1-4), 13 – 50, doi:10.1016/j.epsl.2008.12.005, 2009.

Zollo, A., G. Iannaccone, M. Lancieri, L. Cantore, V. Convertito, A. Emolo, G. Festa, F. Gallovic, M. Vassallo, C. Martino, C. Satriano, and P. Gasparini, Earthquake early warning system in southern Italy: methodologies and performance evaluation, *Geophysical Research Letters*, *36*, L00B07, doi:10.1029/2008GL036689, 2009.

Zumberge, J. F., M. B. Heflin, D. C. Jefferson, M. M. Watkins, and F. H. Webb, Precise Point Positioning for the efficient and robust analysis of GPS data from large networks, *Journal of Geophysical Research*, *102*(B3), 5005–5017, doi:0148-0227/97/96JB-03860, 1997.

Appendix

A List of Figures

C List of Acronyms

AMF	Alhama de Murcia Fault
ART	Aspect Repeat Time
ASPREP	Program to calculate the ART
BARD	Bay Area Regional Deformation Network
BeiDou	GNSS Chinese regional network
BfG	Bundesanstalt für Gewässerkunde (German Federal Institute of Hydrology)
BSH	German Federal Maritime and Hydrographic Agency
BSHcmod	Ocean model from the BSH
BPE	Bernese Processing Engine
C/A	Coarse Acquisition code
CaF	Carboneras Fault
CDDIS	Crustal Dynamics Data Information System
CODE	Center for Orbit Determination in Europe
COMPASS	China GNSS
COSMO	Consortium for Small scale Modeling
COSMO-EU	COSMO Europe water model
CrF	Carrascoy Fault
CRF	Celestial Reference Frame
CRS	Conventional Celestial Reference System
CRTN	California Real-Time Network
CWF	Cádiz Wedge Fault
DD	Double Differencing
DOY	Day of Year
DWD	German Weather Service
ECMWF	European Center for Medium-Range Weather Forecasts
EEW	Earthquake Early Warning
EEWS	Earthquake Early Warning System
ERA Interim	Global atmospheric reanalysis from 1979, continuously updated in real time
ERP	Earth Rotation Parameters
ETRF	European Terrestrial Reference Frame
EUREF	Reference Frame Sub Commission for Europe
EWMA	Exponentially Weighted Moving Average filter
FES2004	Finite Element Solution tide model
FTP	File Transfer Protocol
GALILEO	European GNSS
GBF	Gorringe Bank Fault
GFS	Global Forecast System
GITEWS	German Indonesian Tsunami Early Warning System
GLONASS	Russian Global Navigation Satellite System
GME	Operational global numerical weather prediction model of the DWD
GMT	Global Mapping Tools
GNSS	Global Navigation Satellite System
GPS	Global Positioning System
GPS@TG	GPS co-located with TG
GPST	GPS Time
HSF	Horseshoe Fault
Hz	Hertz
IAG	International Association of Geodesy
IGN	Instituto Geográfico Nacional (National Geographical Institute, Spain)

IGS	International GNSS Service
IGS05	Establishment of the IGS TRF in 2005
IGS08	Establishment of the IGS TRF in 2008
InSAR	Interferometric Synthetic Aperture Radar
IRNSS	Indian Regional Navigational Satellite System
ITRF	International Terrestrial Reference Frame
JRC	European Commission Joint Research Center
LSM	Local Wave Model
Meristemum	GPS network of the Consejería de Agricultura y Agua of the Murcia Region, Spain
MPF	Marqués de Pombal Fault
MSF	Modified Sidereal Filter
NAVSTAR GPS	NAVigation Satellite Timing And Ranging Global Positioning System
NCEP	National Centers for Environmental Prediction
NOAA	National Oceanic and Atmospheric Administration
NTRIP	Networked Transport of RTCM Data via Internet Protocol
OTL	Oceanic Tide Loading
PANGA	Pacific Northwest Geodetic Array
PBF	Portimao Bank Fault
PDGPS	Precise/Phase Differential GPS
PF	Palomares Fault
PPP	Precise Point Positioning
QIF	Quasi-Ionosphere Free
RAP	Red Andaluza de Posicionamiento, positioning network in Andalusia
REDMAR	RED de MAReógrafos, mareograph network
RINEX	Receiver-INdependent EXchange
RF	Regional Filter
RMS	Root Mean Square
RNSS	Regional Navigation Satellite System
ROA	San Fernando Naval Observatory (Real Instituto y Observatorio de la Armada)
RTCM	Radio Technical Commission for Maritime Services
RTKLib	Real-Time Kinematic Library
SAT NAV	Satellite Navigation System
SCHEMA	SCenarios for Hazard-induced Emergencies Management
SF	Sidereal Filter
S_N	Empirical Standard Deviation
SP3-c	Extended Standard Product 3 orbit format
SPOTL	Some Programs for Ocean Tidal Loading
SWIM	South West Iberia Margin
TEW	Tsunami Early Warning
TEWS	Tsunami Early Warning System
TG	Tide Gauge
TRANSFER	Tsunami Risk ANd Strategies For the European Region
TRF	Terrestrial Reference Frame
TRS	Terrestrial Reference System
UCA	Universidad de Cádiz
UCM	Universidad Complutense de Madrid (Madrid Complutense University)
UTC	Coordinated Universal Time
WGS-84	World Geodetic System 84
WSV	German Wasser- und Schiffahrtsverwaltung des Bundes

4-CHAR ID	Station name	X	Y	Z	Receiver type	Antenna type	
ACOR	Coruña	4594489.7502	-678367.8509	4357066.0698	LEICA GRX1200PRO	LEIAT504	LEIS
ALAC	Alicante	5009051.2400	-42072.2974	3935057.6843	LEICA GR10	LEIAR25.R3	LEIT
ALBA	Albacete	4962848.0370	-160854.1939	3990884.3753	LEICA GR10	LEIAR25.R3	LEIT
ALBO	Alborán	5162825.1872	-273808.5198	3722691.9591	TRIMBLE NETRS	TRM29659.00	NONE
ALGC	Algeciras	5135570.4880	-489449.4030	3738221.9930	LEICA GRX1200PRO	LEIAT504	LEIS
ALME	Almería	5105220.1362	-219278.6169	3804387.0582	TRIMBLE NETRS	TRM29659.00	NONE
BELL	Bellmunt	4775849.4545	116814.2736	4213018.9161	TRIMBLE NETRS	TRM29659.00	NONE
BORR	Borriana	4899519.1451	-7115.6426	4069961.5956	TRIMBLE R7	TRM29659.00	NONE
CACE	Cáceres	4899866.6823	-544567.4130	4033769.9683	TRIMBLE NETRS	TRM29659.00	NONE
CAGZ	Cagliari	4893380.0369	772650.3803	4004179.9583	TPS E GGD	JPSREGANT DD E	NONE
CANT	Santander	4625924.5347	-307096.6109	4365771.3453	TRIMBLE NETRS	TRM29659.00	NONE
CART	Cartagena	5059821.9926	-89383.4128	3869254.8646	TRIMBLE 4700	TRM29659.00	NONE
CASC	Cascais	4917536.9864	-815726.3100	3965857.3158	LEICA GRX1200GGPRO	LEIAT504GG	NONE
CEU1	Ceuta	5150907.8966	-478414.8197	3718518.3948	TRIMBLE NETRS	TRM29659.00	NONE
CEUD	Ceuta	5150954.8848	-476121.1055	3718812.1389	TRIMBLE NETRS	TRM29659.00	NONE
COBA	Córdoba	5021255.9226	-414684.9061	3898182.3635	LEICA GRX1200PRO	LEIAT504	LEIS
CREU	Cap de Creus	4715420.3587	273177.6828	4271946.6103	TRIMBLE NETRS	TRM41249.00	NONE
CRTG	Cartagena	5058509.6516	-86467.3858	3870990.6791	TRIMBLE NETR5	TRM55971.00	NONE
CRVC	Caravaca de la Cruz	5022498.0050	-163861.8500	3915914.3650	TRIMBLE NETR5	TRM55971.00	NONE
GAIA	Gaia	4759095.5217	-718818.7249	4171491.3305	LEICA GRX1200GGPRO	LEIAT504	NONE
HUEL	Huelva	5049613.0408	-612885.4564	3835144.0432	TRIMBLE NETRS	TRM29659.00	NONE
IZAN	Izana	5390243.4909	-1596630.2381	3007752.6319	LEICA GRX1200GGPRO	LEIAT504GG	LEIS
JUMI	Jumilla	4999149.2220	-115817.5410	3946872.6330	TRIMBLE NETR5	TRM55971.00	NONE
LAGO	Lagos	5035246.5701	-767657.1981	3826194.2697	LEICA GRX1200GGPRO	LEIAT504GG	NONE

4-CHAR ID	Station name	X	Y	Z	Receiver type	Antenna type	
LORC	Lorca	5054087.3434	-148834.1246	3875323.8116	TRIMBLE NETR5	TRM55971.00	NONE
MAHO	Mahón	4886508.5839	364717.2457	4069311.4851	TRIMBLE 4000SSE	TRM29659.00	NONE
MALA	Málaga	5103282.2803	-392096.5709	3793147.0749	LEICA GRX1200GGPRO	LEIAT504GG	LEIS
MALL	Palma de Mallorca	4919369.5215	225499.7682	4039849.7887	LEICA GRX1200GGPRO	LEIAT504GG	LEIS
MELI	Melilla	5205105.6255	-267253.7158	3664201.4875	TRIMBLE 4000SSE	TRM22020.00+GP	NONE
MURC	Murcia	5032093.8550	-98790.0140	3904835.4640	TRIMBLE NETR5	TRM55971.00	NONE
ONSA	Onsala	3370658.6088	711877.0661	5349786.8941	JPS E GGD	AOAD/M B	OSOD
PDEL	Ponta Delgada	4551595.9808	-2186893.2002	3883410.7772	LEICA GRX1200GGPRO	LEIAT504GG	NONE
REYK	Reykjavik	2587384.4122	-1043033.5080	5716563.9972	TPS E GGD	TPSCR.G3	TPSH
RIOJ	Rioja	4708688.4529	-205761.5469	4283609.5383	TRIMBLE NETRS	TRM29659.00	NONE
ROAP	San Fernando	5105509.7776	-555200.7815	3769790.1285	SEPT POLARX3ETR	LEIAR25.R4	NONE
ROTA	Rota	5094359.4651	-565180.8732	3783258.2247	TRIMBLE NETRS	TRM29659.00	NONE
SALA	Salamanca	4803054.6771	-462131.4510	4158378.8487	LEICA GRX1200+GNSS	LEIAR25	NONE
SALI	San Pedro del Pinatar	5043277.9450	-68531.9270	3891028.8048	TRIMBLE NETRS	TRM41249.00	NONE
SFER	San Fernando	5105519.0348	-555145.9394	3769803.2964	TRIMBLE NETRS	TRM29659.00	NONE
SONS	Sonseca	4904660.3755	-339867.8574	4050823.6893	LEICA GRX1200GGPRO	LEIAT504GG	NONE
TERU	Teruel	4867391.5256	-95523.7263	4108341.4531	LEICA GRX1200GGPRO	LEIAT504GG	LEIS
UCAD	Universidad de Cádiz	5101036.2450	-555095.5630	3775797.9850	LEICA GRX1200PRO	LEIAT504	LEIS
VALA	Valladolid	4753521.5569	-391505.4642	4221500.7309	LEICA GRX1200+GNSS	LEIAR25.R3	NONE
VALE	Valencia	4929533.8822	-29050.5045	4033710.0998	LEICA GR10	LEIAR25.R3	LEIT
VELE	Velez de la Gomera	5204788.8643	-391394.4519	3653634.1360	TRIMBLE NETRS	TRM29659.00	NONE
VIGO	Vigo	4677480.9408	-725204.9127	4260827.3628	TRIMBLE NETRS	TRM29659.00	TCWD
YEBE	Yebes	4848724.7451	-261632.3062	4123094.0778	TRIMBLE NETRS	TRM29659.00	NONE
ZARA	Zaragoza	4773803.3831	-73506.3560	4215453.8751	TRIMBLE NETRS	TRM29659.00	NONE

Table D.1: GPS receivers and antennas used for the Iberian Peninsula network.

4-CHAR ID	Station name	X	Y	Z	Receiver type	Antenna type	
BOR1	Borowiec	3738358.30320	1148173.85428	5021815.82324	TRIMBLE NETRS	AOAD/M_T	NONE
BORJ	Borkum-Südstrand	3769402.86362	440564.38017	5109099.13869	JPS LEGACY	LEIAR25.R3	LEIT
BUDP	Kobenhavn	3513638.12005	778956.53705	5248216.49198	LEICA GRX1200GGPRO	ASH701941.B	UNAV
DELF	Delft	3924687.32056	301133.13548	5001911.04248	TRIMBLE 4700	TRM29659.00	UNAV
DENT	Dentergem	4020711.35582	238851.26200	4928949.70927	SEPT POLARX2E	ASH701945C_M	NONE
DIEP	Diepholz	3842152.94998	563402.02064	5042888.48992	JPS LEGACY	LEIAR25.R4	LEIT
FFMJ	Frankfurt/Main	4053455.75224	617729.81528	4869395.78369	JPS LEGACY	LEIAR25.R4	LEIT
FLDW	Frontlight Dwarsgat	3742849.14242	546531.50469	5118321.31154	LEICA GRX1200+GNSS	LEIAT504GG	LEIS
GRAZ	Graz	4194423.66911	1162702.85660	4647245.48115	LEICA GRX1200+GNSS	LEIAR25.R3	LEIT
HEL2	Helheim Glacier	3705182.87378	512589.88299	5148980.86124	LEICA GRX1200+GNSS	LEIAR25.R3	LEIT
HELG	Helgoland Island	3706067.05770	513804.02038	5148174.53057	JPS LEGACY	LEIAT504GG	LEIS
HERS	Hailsham	4033469.98168	23673.04141	4924301.36929	SEPT POLARX3ETR	LEIAR25.R3	NONE
HOBU	Hohenbuenstorf	3778219.65278	698635.58357	5074054.27865	LEICA GRX1200+GNSS	LEIAR25.R4	LEIT
HOE2	Hörnum / Sylt	3650022.54942	532050.69592	5185984.54882	LEICA GRX1200+GNSS	LEIAR25.R4	LEIT
HOFN	Hoefn	2679689.95416	-727951.08639	5722789.44671	LEICA GR25	LEIAR25.R4	LEIT
HOL2	Kiel Holtenau	3665228.96363	656626.11365	5161071.81504	JPS LEGACY	LEIAR25.R4	LEIT
INVR	Inverness	3427172.05066	-252833.99143	5355255.77465	LEICA GRX1200+GNSS	LEIAR25	LEIT
LEIJ	Leipzig	3898736.25553	855345.40982	4958372.51276	JPS LEGACY	LEIAR25.R3	LEIT
LHAW	Leuchtturm Alte Weser	3731697.54222	532937.56752	5127835.98613	LEICA GRX1200+GNSS	LEIAT504GG	LEIS
MORP	Morpeth	3645667.72627	-107277.09065	5215053.59433	TRIMBLE NETR8	AOAD/M_T	NONE
ONSA	Onsala	3370658.42028	711877.27290	5349787.01989	JPS E_GGD	AOAD/M_B	OSOD
OSLS	Oslo	3169981.76052	579956.89658	5485936.76414	TRIMBLE NETR8	TRM55971.00	NONE
POTS	Postdam	3800689.49583	882077.53195	5028791.37926	JAVAD TRE_G3TH DELTA	JAV_RINGANT_G3T	NONE

4-CHAR ID	Station name	X	Y	Z	Receiver type	Antenna type
PTBB	Braunschweig	3844059.82295	709661.46743	5023129.61157	ASHTECH Z-XII3T	ASH700936E SNOW
SASS	Sassnitz Island of Ruegen	3606145.93688	875303.48810	5170193.99713	JPS LEGACY	TPSCR3_GGD CONE
SMID	Smidstrup, Vejle	3557911.09708	599176.82015	5242066.50284	LEICA GR25	ASH701941.B UNAV
STAS	Stavanger	3275753.50776	321111.17061	5445042.13621	TRIMBLE NETR8	TRM55971.00 NONE
SULD	Suldrup	3446394.08124	591713.28362	5316383.51673	LEICA GR25	ASH701945E_M UNAV
TERS	West-Terschelling	3798580.48685	346994.21098	5094781.07641	SEPT POLARX4	TRM29659.00 UNAV
TGBF	Borkum - Fischerbalje	3770680.22913	446150.58299	5107675.84167	LEICA GRX1200+GNSS	LEIAT504GG LEIS
TGBH	Bremerhaven Alter Leuchtturm	3755709.39619	565864.61374	5106854.18826	LEICA GRX1200+GNSS	LEIAT504GG LEIS
TGBU	Büsum	3701580.86874	576950.05691	5144738.12797	LEICA GRX1200+GNSS	LEIAT504GG LEIS
TGCU	Cuxhaven - Steubenhöft	3725602.11495	571259.70982	5128116.01733	LEICA GRX1200+GNSS	LEIAT504GG LEIS
TGDA	Dagebüll	3648811.86664	557503.08958	5184159.47676	LEICA GRX1200GGPRO	LEIAT504GG LEIS
TGEM	Emden - Neue Seeschleuse	3786730.54632	477454.29379	5093051.76536	LEICA GRX1200+GNSS	LEIAT504GG LEIS
TGME	Mellumplate	3740164.99656	531813.99857	5121826.81471	LEICA GRX1200+GNSS	LEIAT504GG LEIS
TGWH	Wilhelmshaven Neuer Vorhafen	3760139.51757	539846.40502	5106411.93337	LEICA GRX1200+GNSS	LEIAT504GG LEIS
TITZ	Titz / Jackerath	3993780.48261	450206.87287	4936136.96909	JPS LEGACY	LEIAR25.R4 LEIT
TRO1	Tromsoe	2102928.33094	721619.54665	5958196.30805	TRIMBLE NETR8	TRM59800.00 SCIS
WARN	Rostock-Warnemuende	3658785.66259	784471.02053	5147870.65052	JPS LEGACY	LEIAR25.R3 LEIT
WSRT	Westerbork	3828735.72969	443305.10351	5064884.77058	AOA SNR-12 ACT	AOAD/M_T DUTD
WTZR	Bad Koetzting	4075580.40661	931853.95510	4801568.19116	LEICA GRX1200+GNSS	LEIAR25.R3 LEIT
ZIM2	Zimmerwald	4331299.75545	567537.48605	4633133.79919	TRIMBLE NETR5	TRM59800.00 NONE
ZIMM	Zimmerwald	4331296.94269	567556.04369	4633134.01385	TRIMBLE NETRS	TRM29659.00 NONE

Table D.2: GPS receivers and antennas used for the northern Germany network.

4-CHAR ID	Station name	Longitude	Latitude
ABER	Aberdeen	-2.080^o	57.114^o
LOWE	Lowestoft	1.751^o	52.473^o
BORJ	Borkum-Südstrand	6.653^o	53.575^o
TGBF	Borkum-Fischerbalje	6.736^o	53.558^o
TGEM	Emden Neue Seeschleuse	7.186^o	53.337^o
HELG	Helgoland	7.903^o	54.175^o
TGME	Leuchtturm Mellumplate	8.097^o	53.775^o
LHAW	Leuchtturm Alte Weser	8.125^o	53.858^o
TGWH	Wilhelmshaven - Neuer Vorhafen	8.181^o	53.542^o
FLDW	Dwarsgat	8.319^o	53.725^o
HOE2	Hörnum	8.319^o	54.758^o
TGBH	Bremerhaven - Alter Leuchtturm	8.569^o	53.542^o
TGDA	Dagebüll	8.681^o	54.725^o
TGCU	Cuxhaven - Steubenhöft	8.708^o	53.875^o
TGBU	Büsum	8.847^o	54.125^o

Table D.3: Coordinates of the tide gauges co-located with GPS in Northern Germany.

E Additional Tables: Bernese Input Parameters

Input sampling rate	1 second
Processing interval	6 hours
Orbits, ERP	IGS Ultra-Rapid
Elevation cutoff angle	7 degrees
A priori troposphere model	Niell dry
Tropospheric zenith delay model	Niell wet, estimated each 2 hours
OTL model	FES2004
Coordinates and velocities	IGS05, IGS08 (from 2012)
Baseline strategy	MAX-OBS
Ambiguity resolution strategy	Baseline length dependent
Output kinematic rate	1 second

Table E.1: Parameters used for a near real-time Bernese processing.

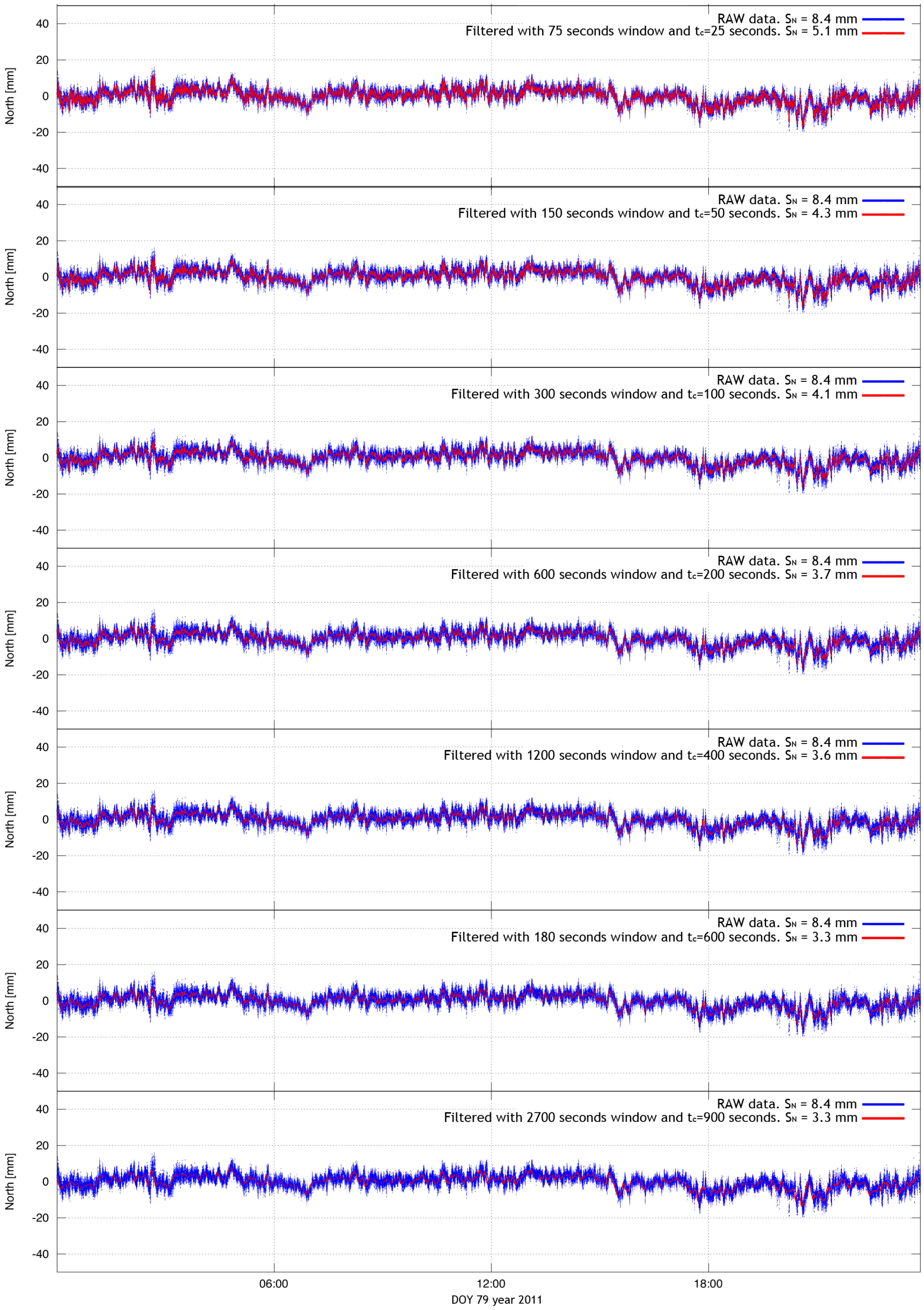

Figure F.1: Different window lengths for the EWMA filter with t_c=25, 50, 100, 200, 400, 600 and 900 seconds and a window length of 3 times t_c. Station UCAD, North component corrected by OTL.

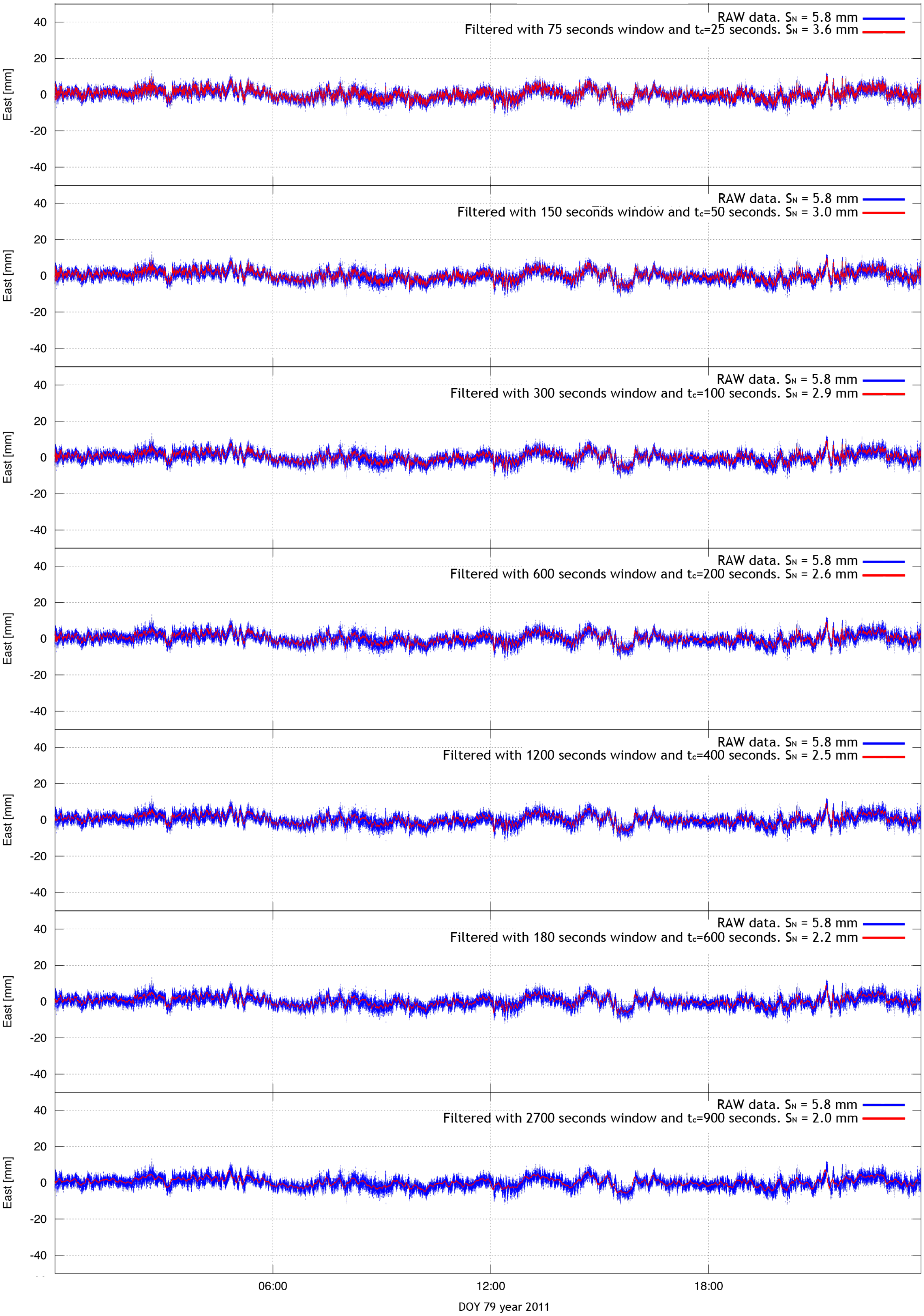

Figure F.2: Different window lengths for the EWMA filter with t_c=25, 50, 100, 200, 400, 600 and 900 seconds and a window length of 3 times t_c. Station UCAD, East component corrected by OTL.

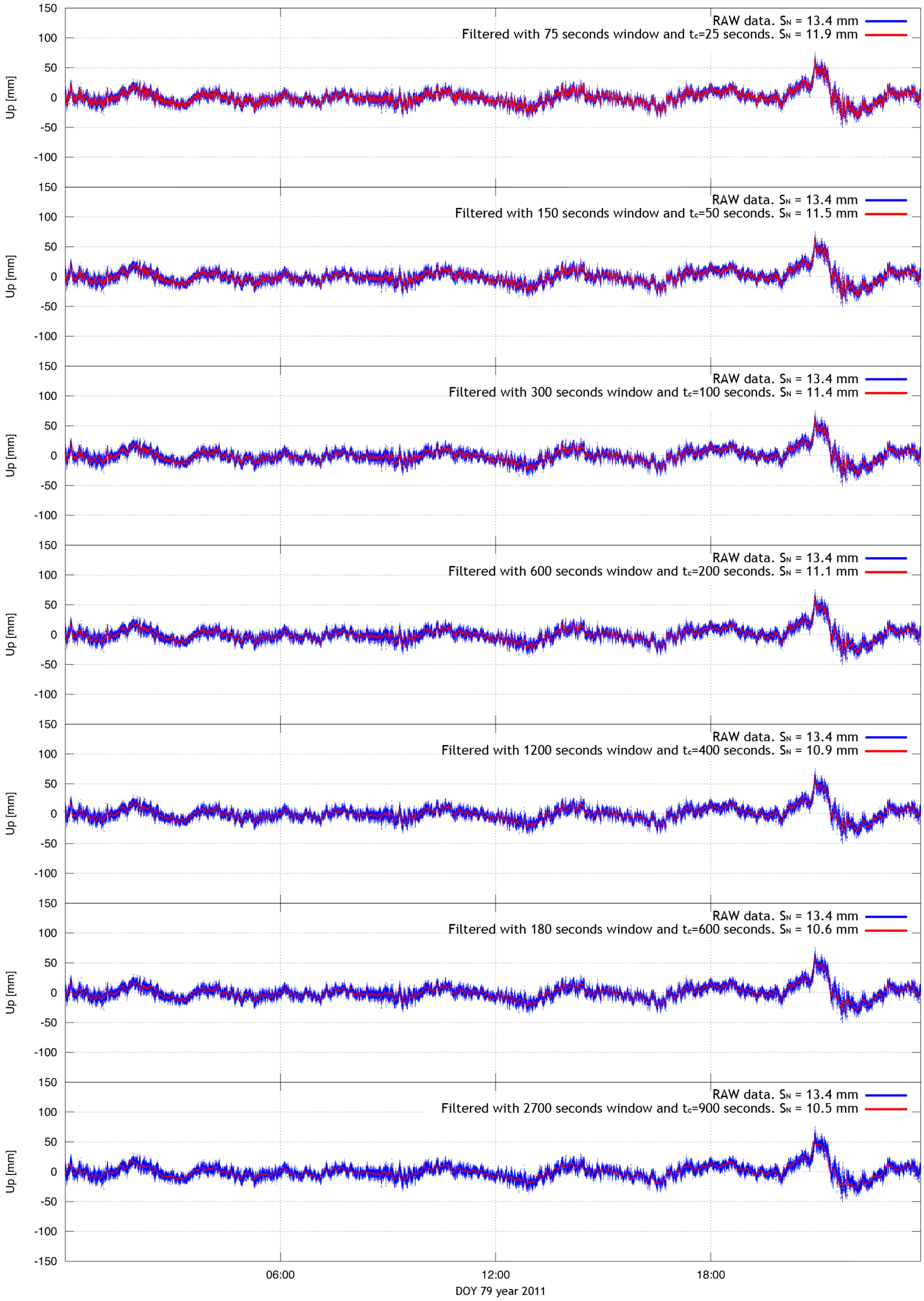

Figure F.3: Different window lengths for the EWMA filter with t_c=25, 50, 100, 200, 400, 600 and 900 seconds and a window length of 3 times t_c. Station UCAD, vertical component corrected by OTL.

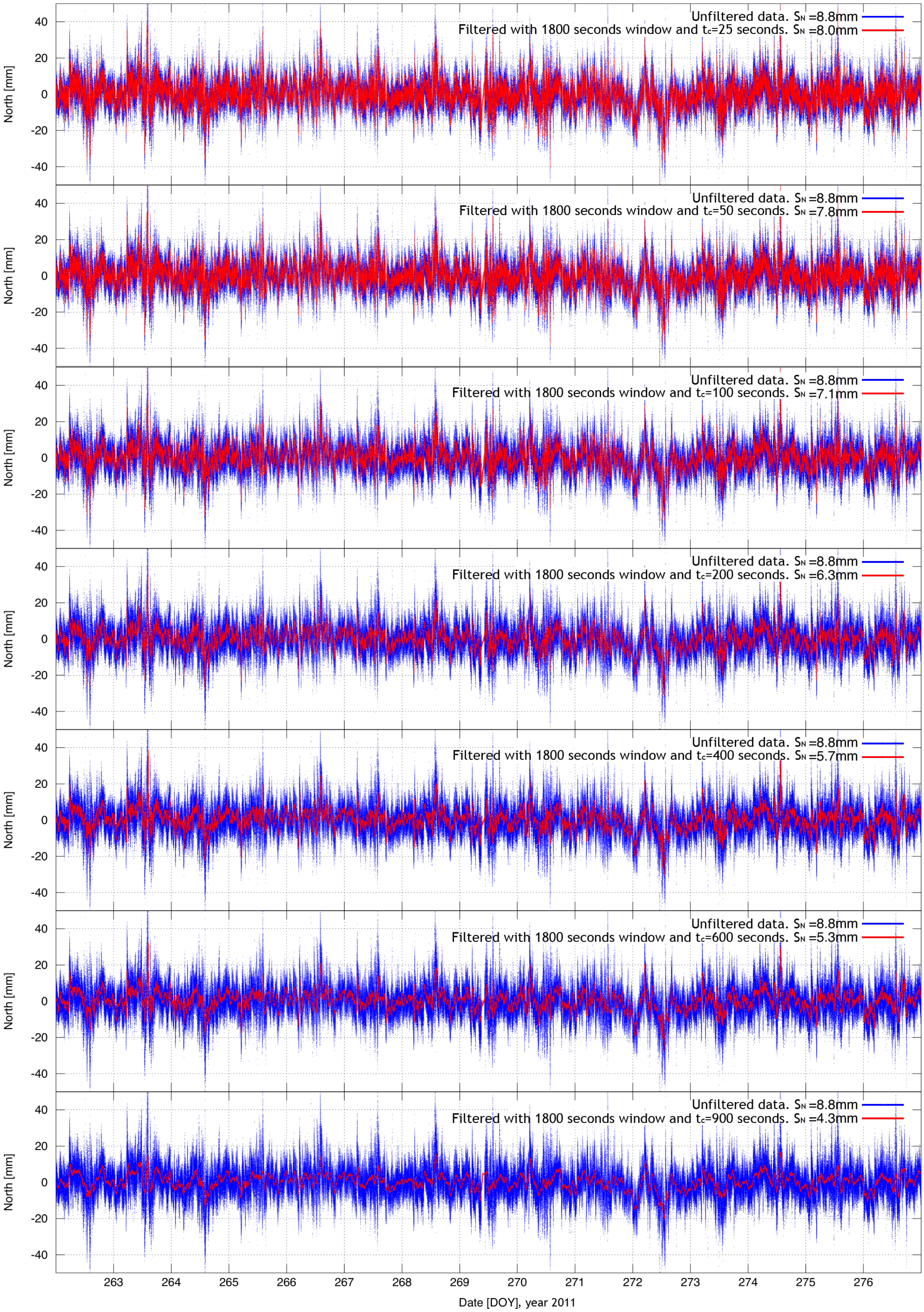

Figure F.4: Different characteristic times for the EWMA filter with a window length of 1800 seconds. Station ROTA, North residual not corrected by OTL. 25, 50, 100, 200, 400, 600 and 900 seconds characteristic time.

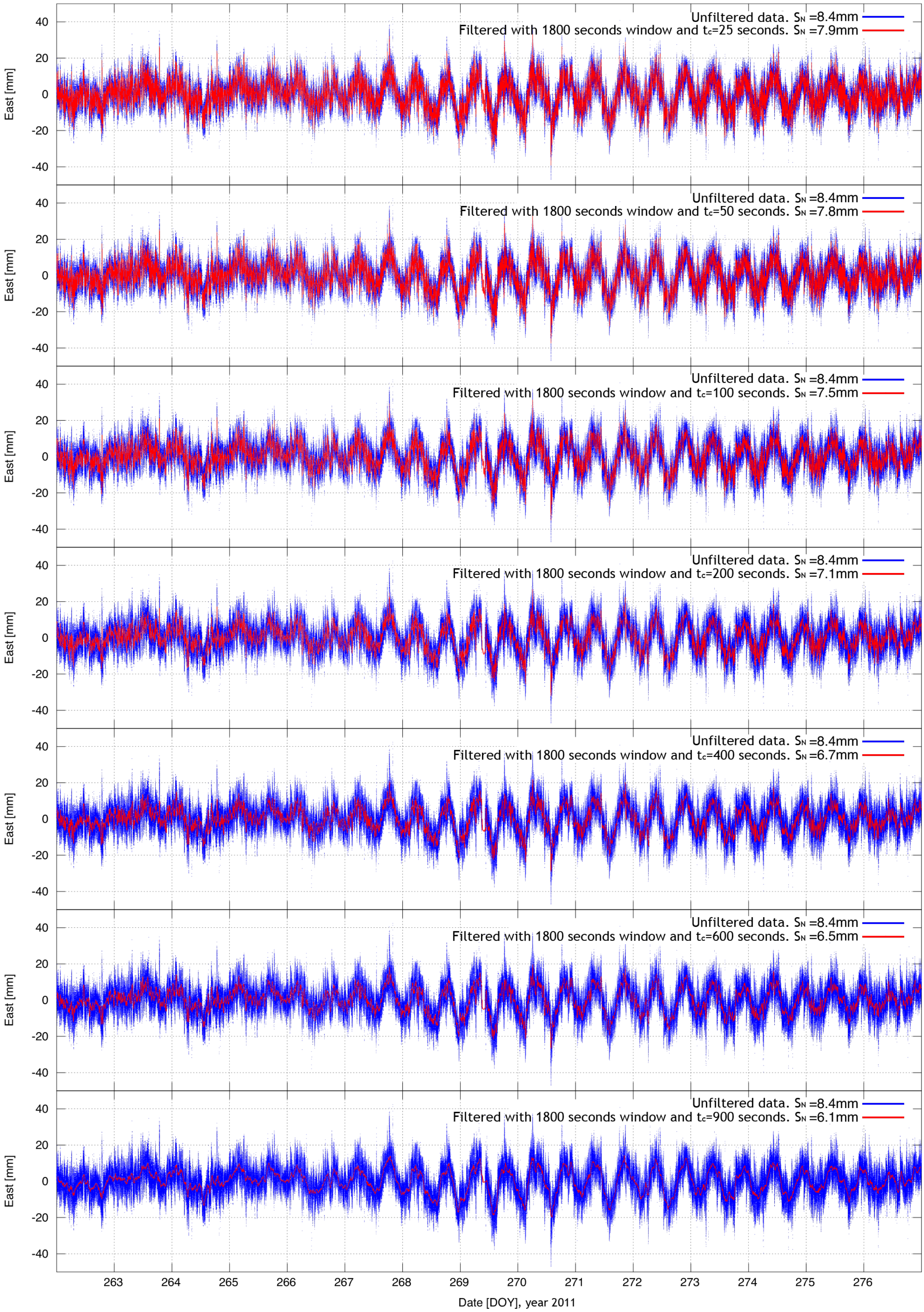

Figure F.5: Different characteristic times for the EWMA filter with a window length of 1800 seconds. Station ROTA, East residual not corrected by OTL. 25, 50, 100, 200, 400, 600 and 900 seconds characteristic time.

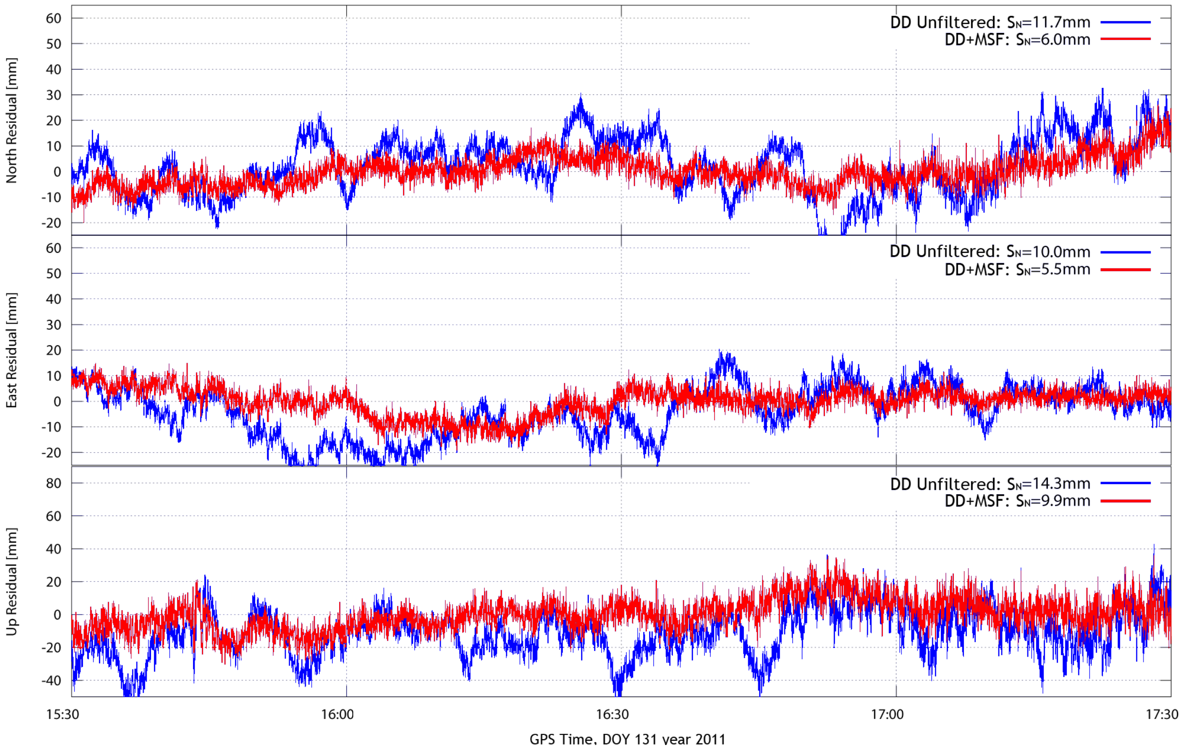

Figure G.1: Time series for station MURC, unfiltered (blue) and filtered by a MSF (red).

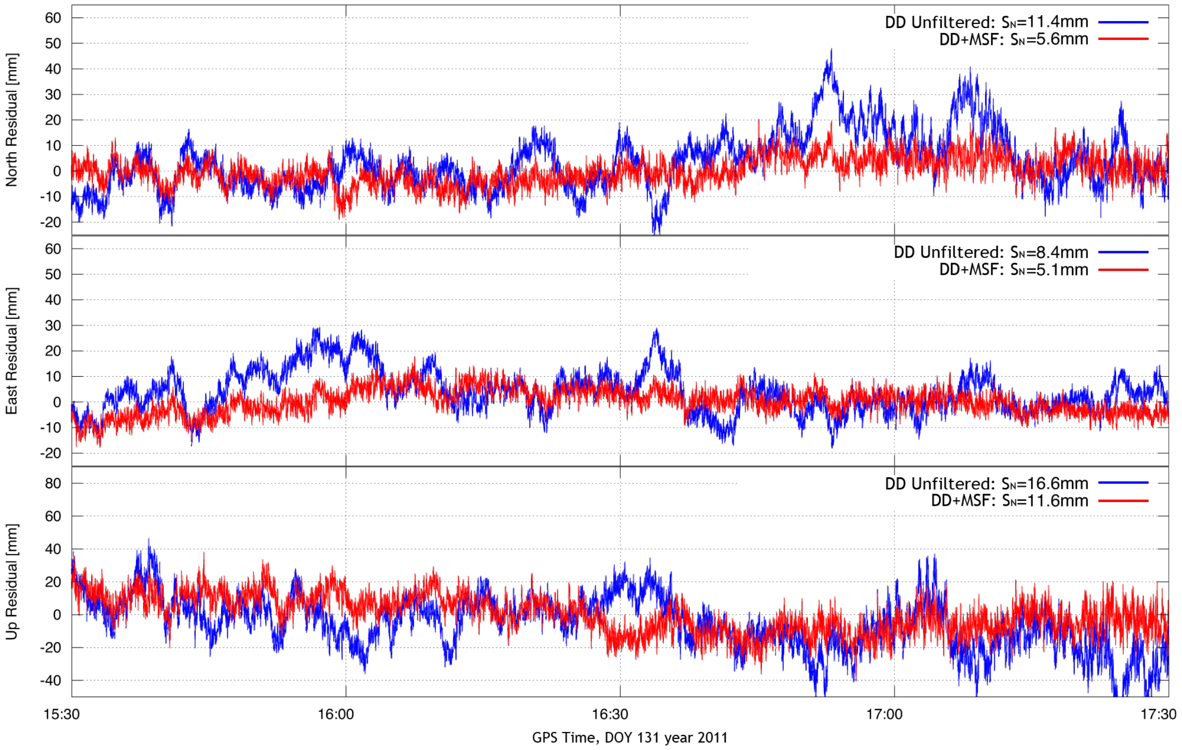

Figure G.2: Time series for station CRTG, unfiltered (blue) and filtered by a MSF (red).

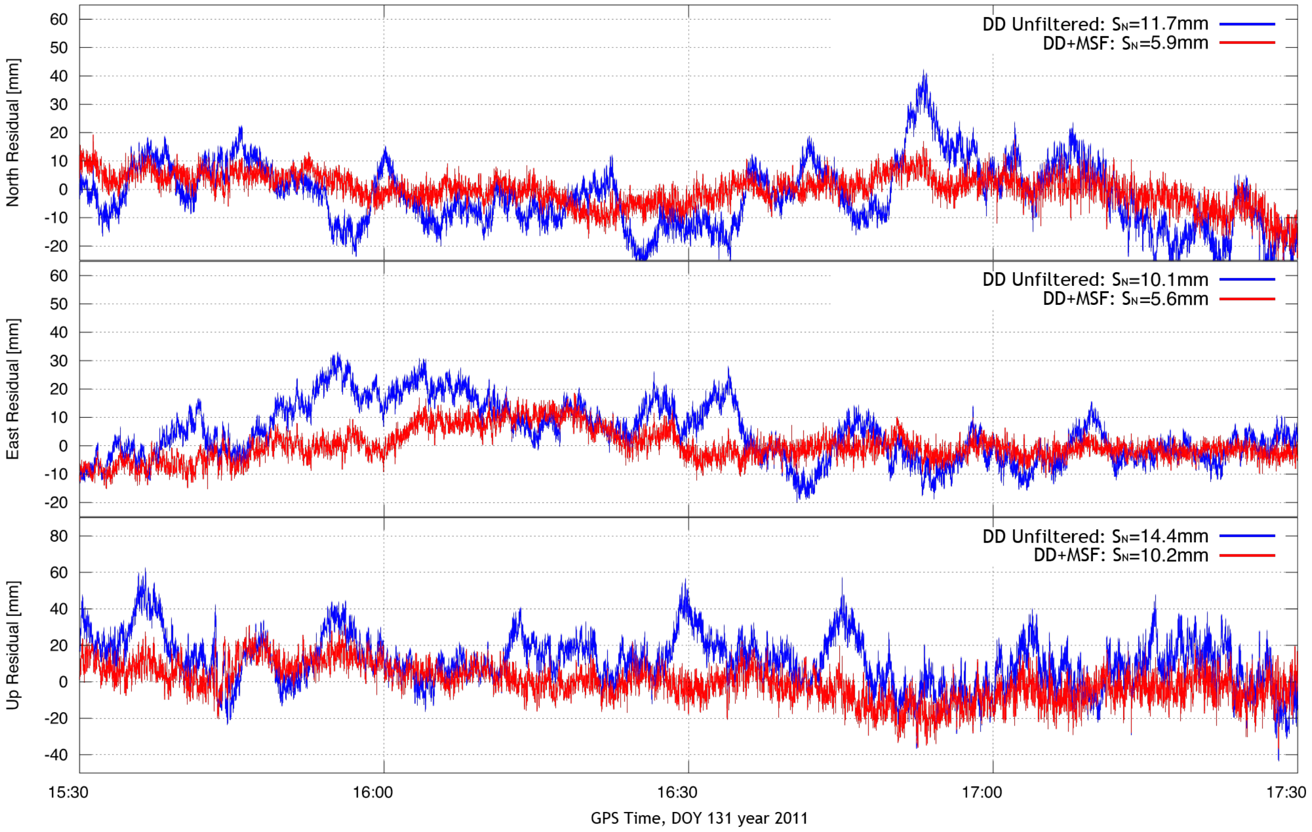

Figure G.3: Time series for station CRVC, unfiltered (blue) and filtered by a MSF (red).

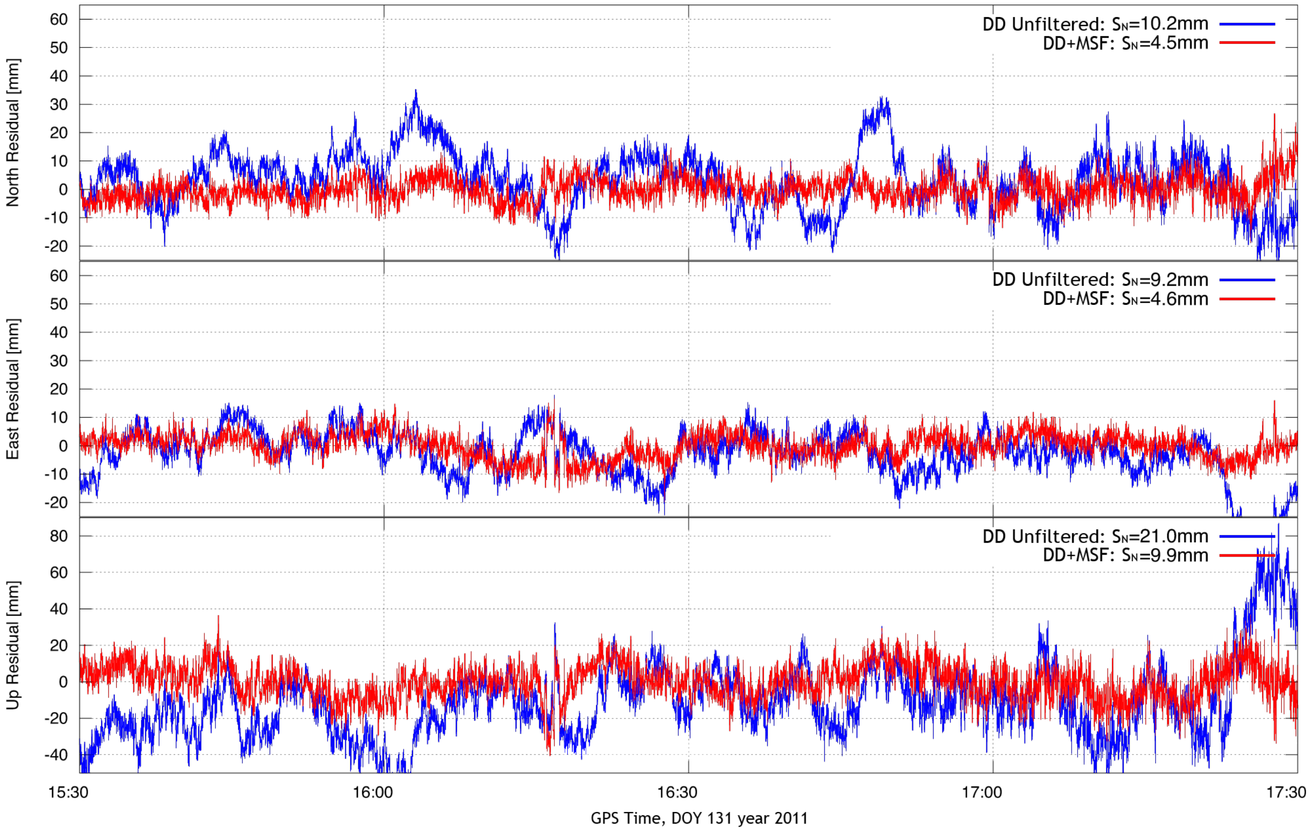

Figure G.4: Time series for station JUMI, unfiltered (blue) and filtered by a MSF (red).

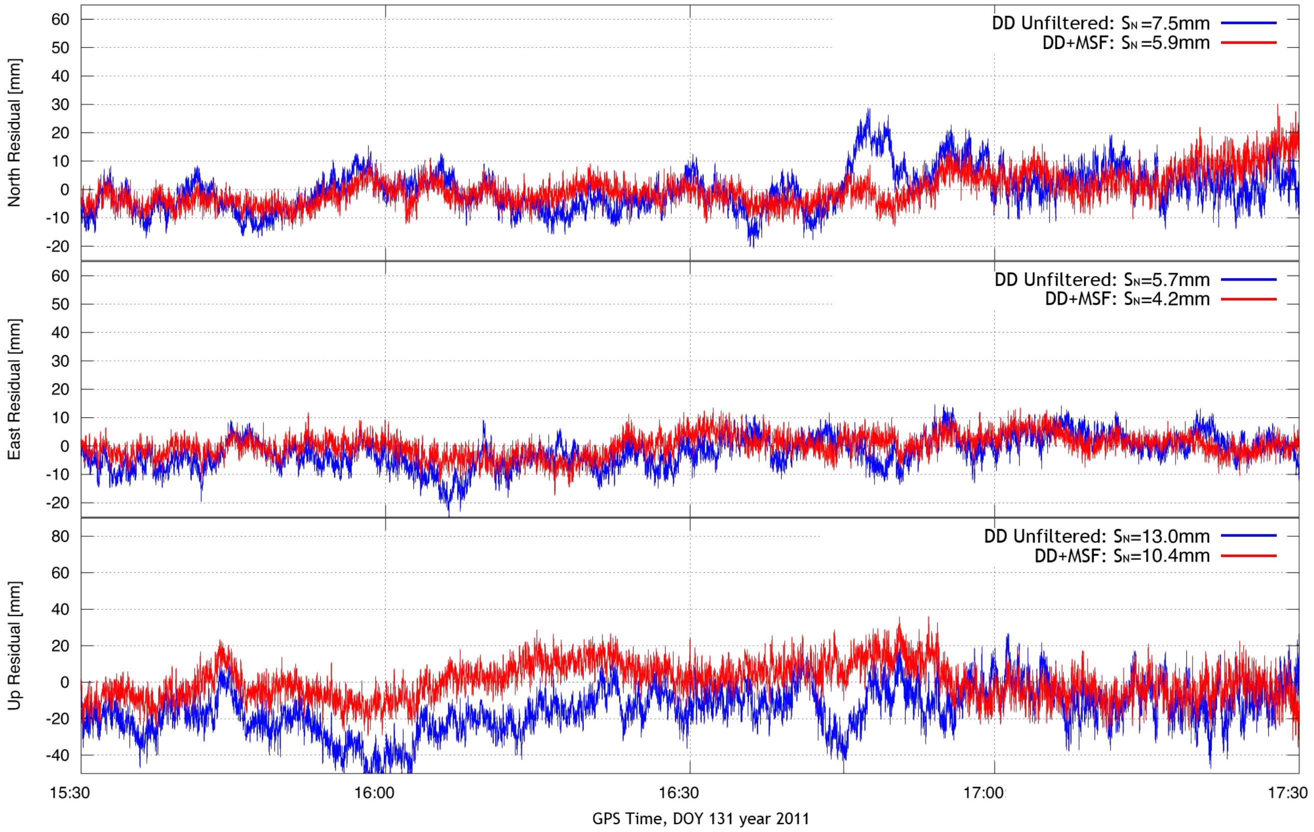

Figure G.5: Time series for station SALI, unfiltered (blue) and filtered by a MSF (red).

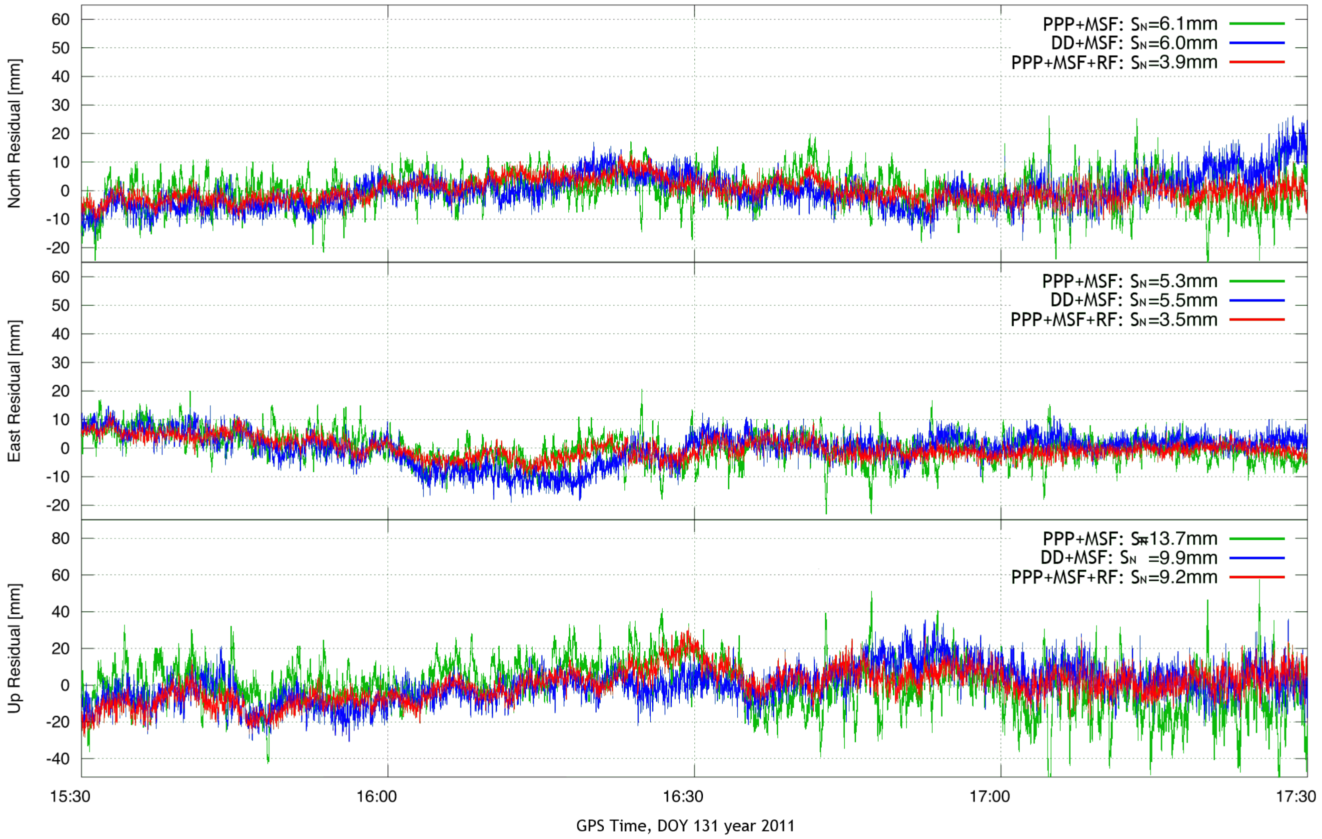

Figure G.6: Time series for station MURC, MSF results from PPP (green PPP+MSF, red PPP+MSF+RF) and DD (blue, DD+MSF).

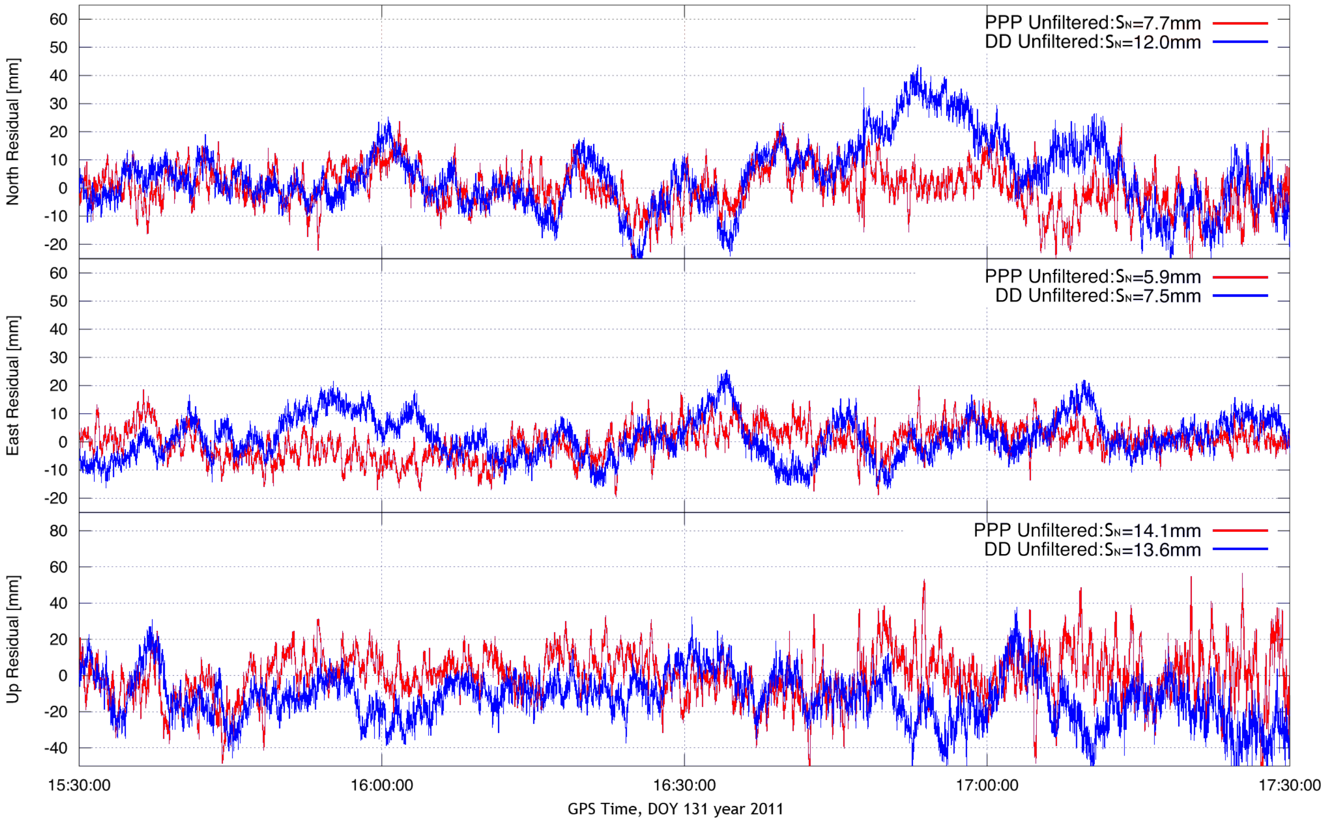

Figure G.7: Time series for station LORC, unfiltered results from PPP (red) and DD (blue).

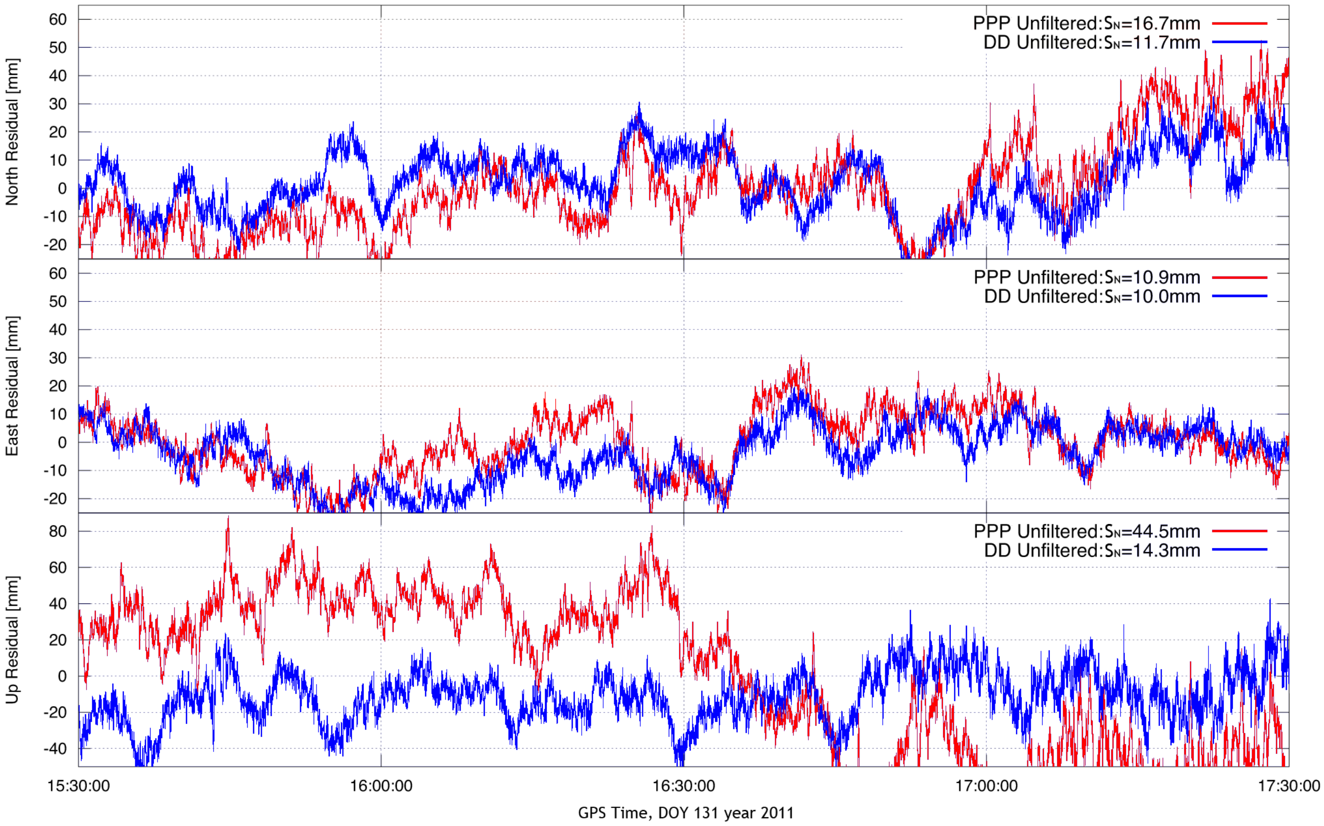

Figure G.8: Time series for station MURC, unfiltered results from PPP (red) and DD (blue).

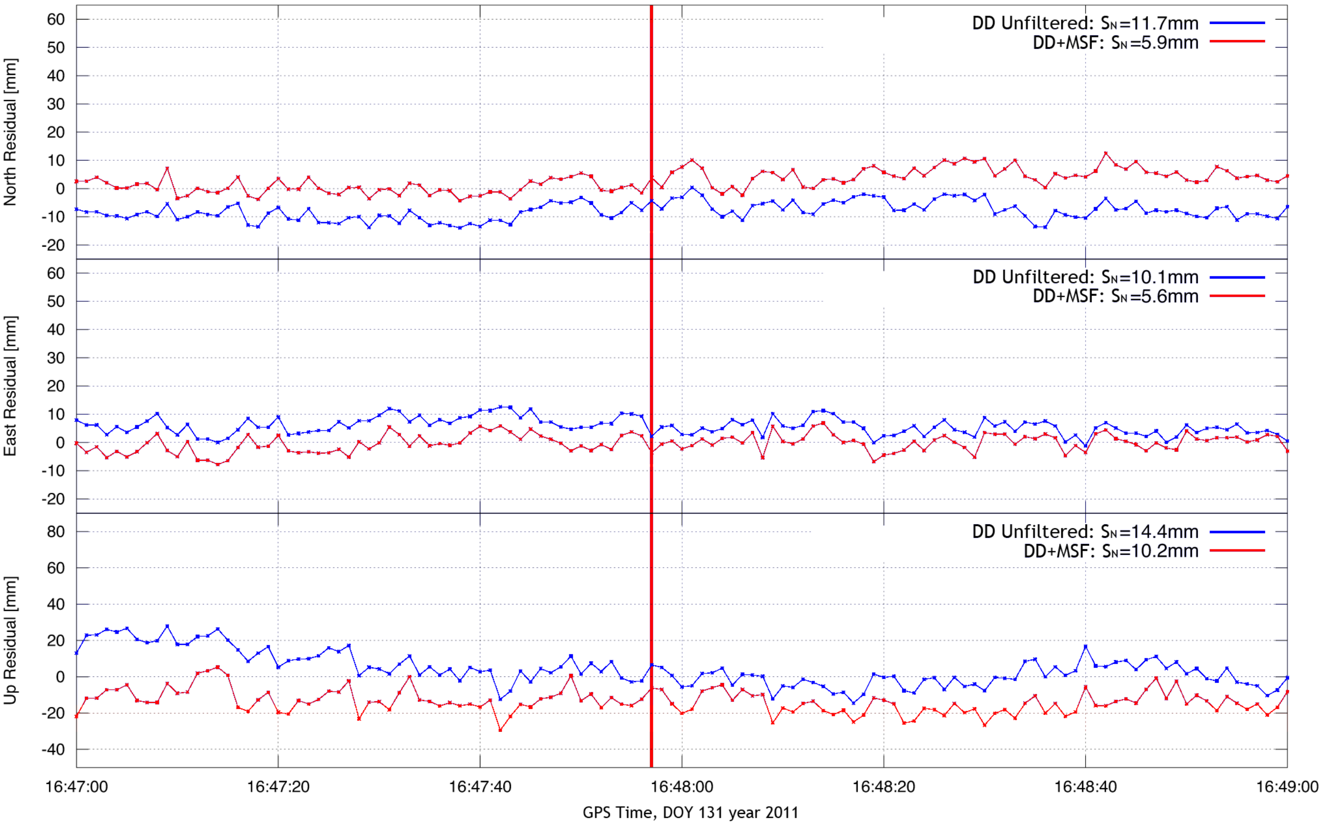

Figure G.9: CRVC time series, DD unfiltered (blue) and after SF (blue), for the estimated time of arrival of the earthquake at 16:47:57 GPST (red vertical line).

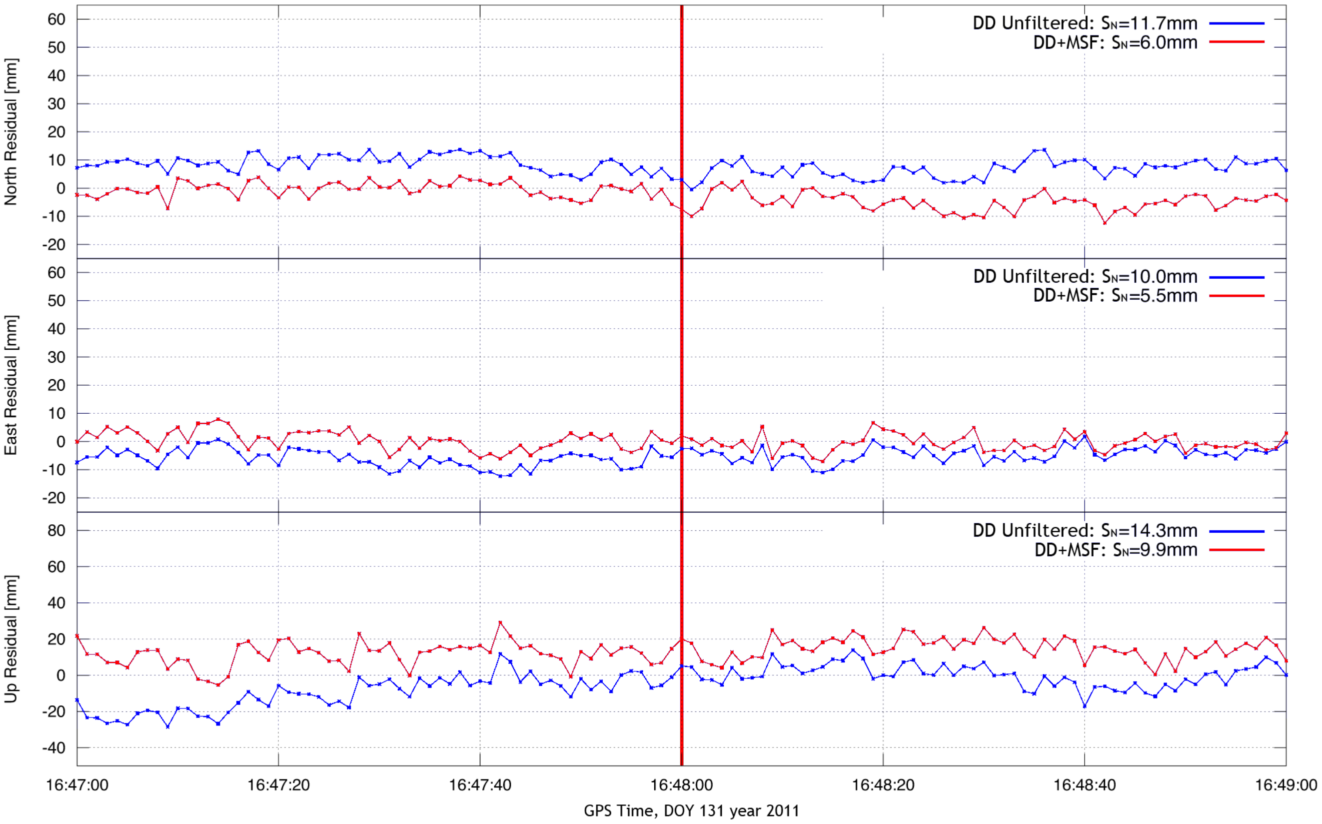

Figure G.10: MURC time series, DD unfiltered (blue) and after SF (blue), for the estimated time of arrival of the earthquake at 16:48:00 GPST (red vertical line).

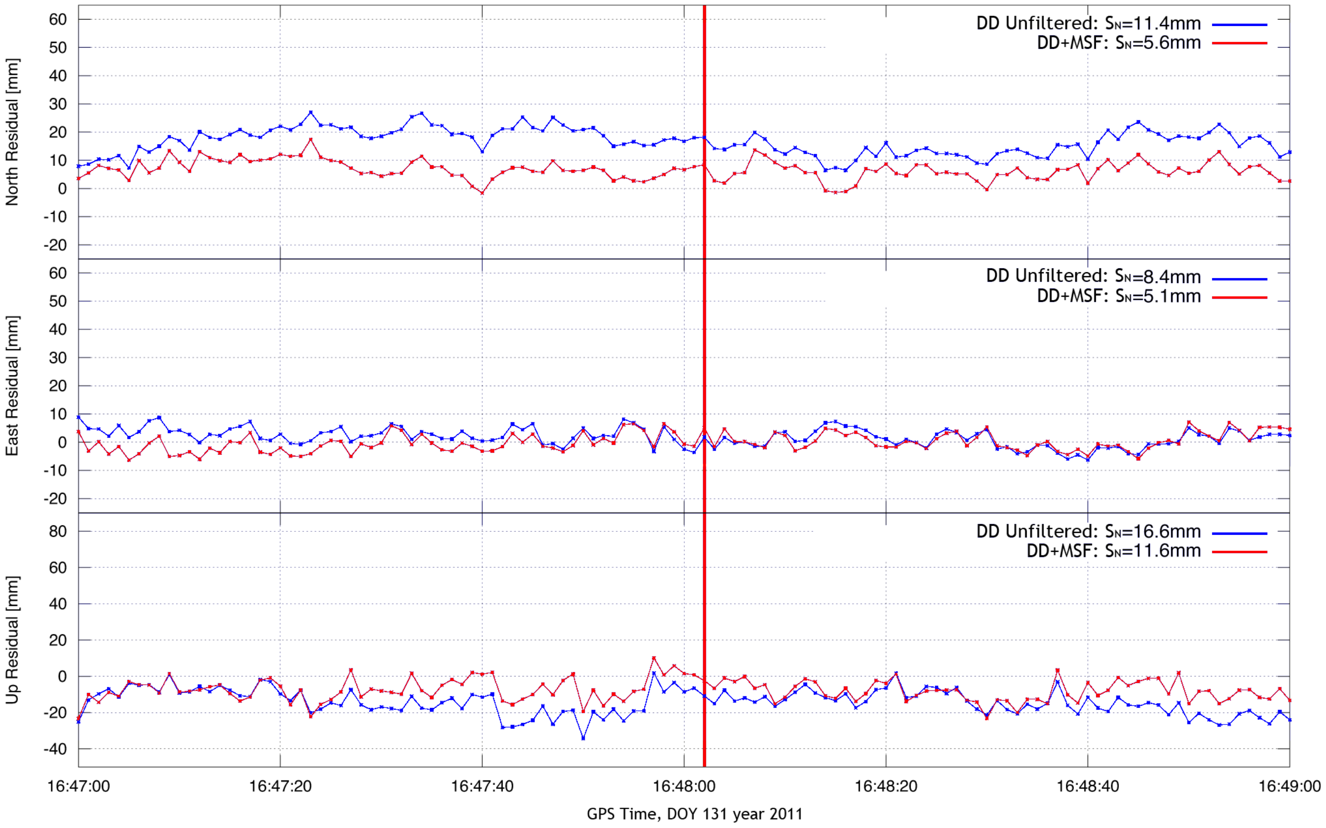

Figure G.11: CRTG time series, DD unfiltered (blue) and after SF (blue), for the estimated time of arrival of the earthquake at 16:48:02 GPST (red vertical line).

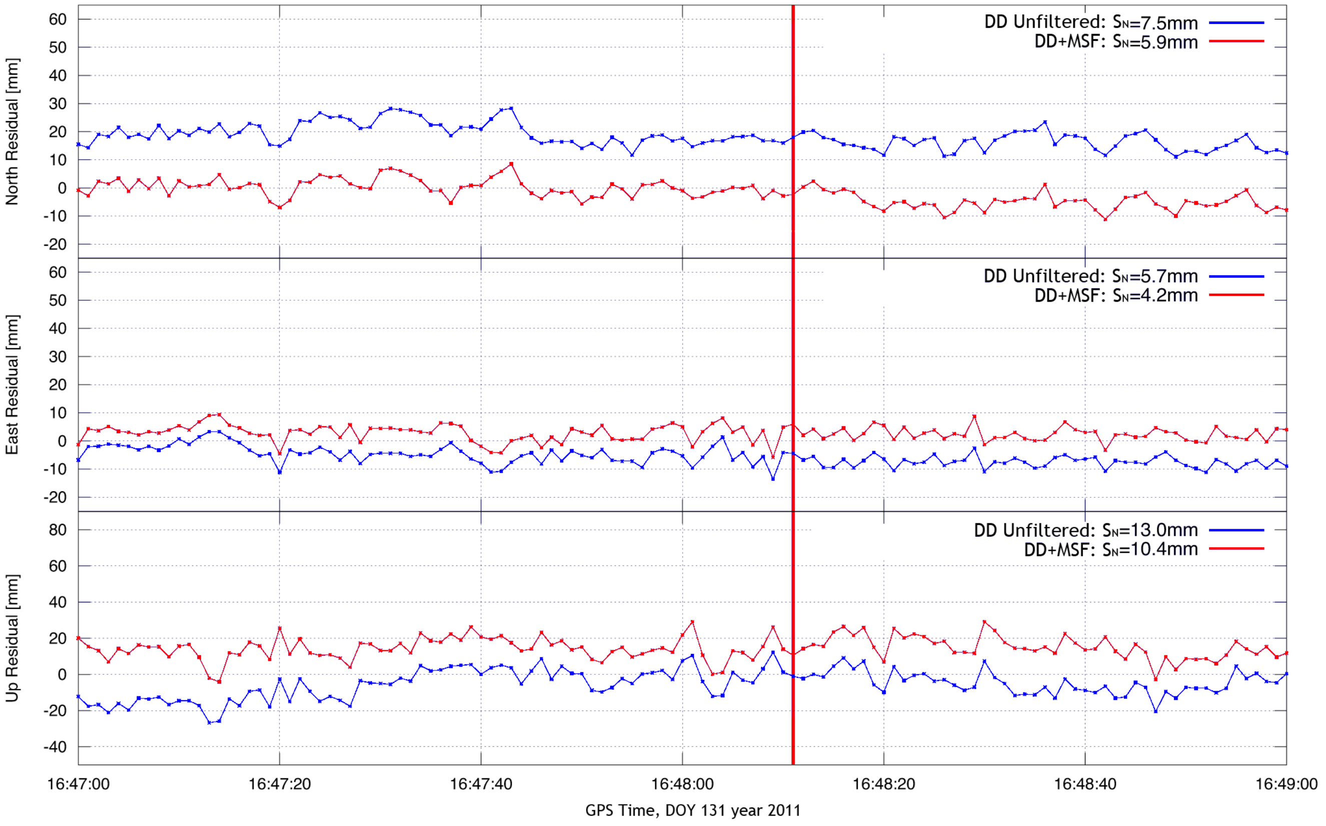

Figure G.12: SALI time series, DD unfiltered (blue) and after SF (blue), for the estimated time of arrival of the earthquake at 16:48:11 GPST (red vertical line).

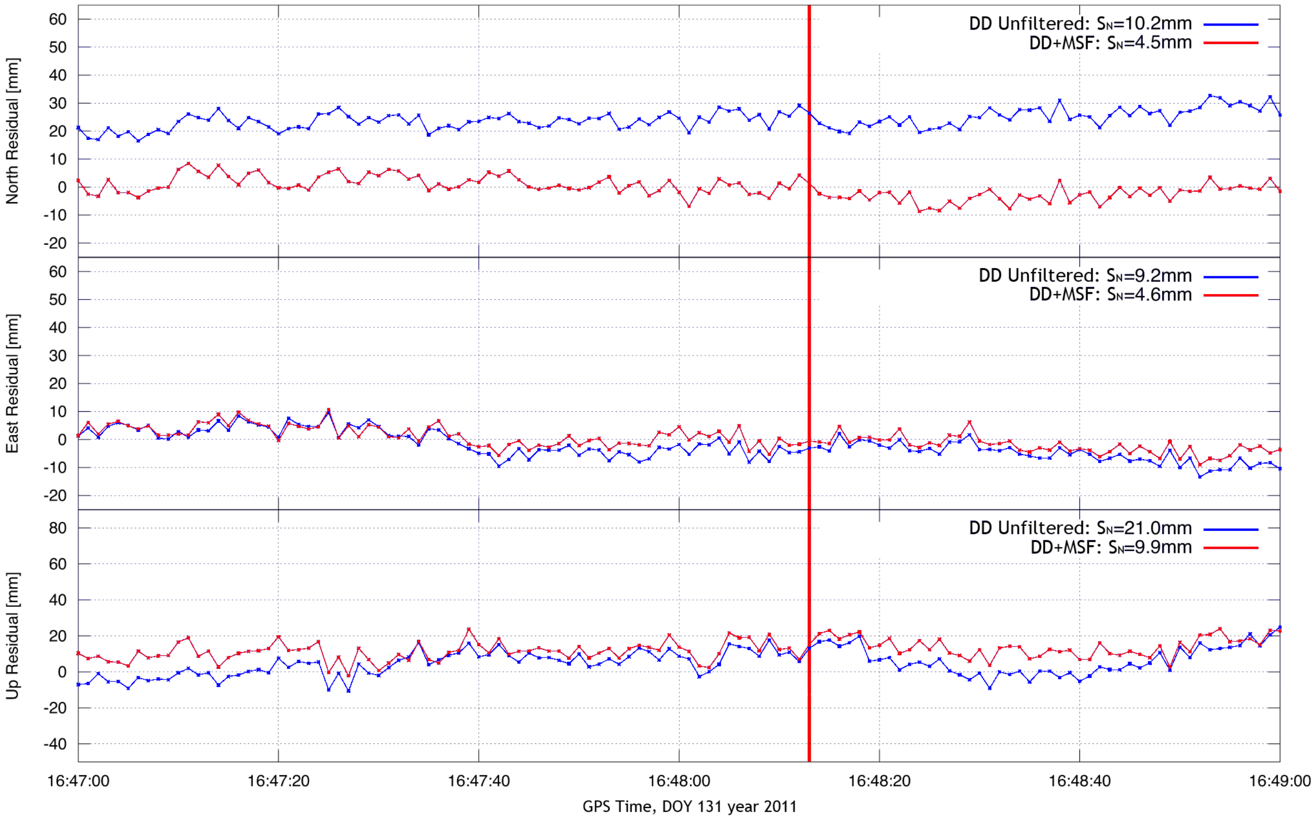

Figure G.13: JUMI time series, DD unfiltered (blue) and after SF (blue), for the estimated time of arrival of the earthquake at 16:48:13 GPST (red vertical line).

Mareograph	Longitude	Latitude	X(m)	Y(m)	Z(m)
CADIZ	36^{o}32’25”N	6^{o}17’11”W	5099682.1679	-561783.9492	3776526.5047
CARRACA	36^{o}29’51”N	6^{o}11’1”W	5103490.1330	-552939.4653	3772711.5406
PTO STA MARIA	36^{o}35’54”N	6^{o}13’19”W	5096495.0771	-555631.6342	3781700.6377
PUNTALES	36^{o}30’23”N	6^{o}15’40”W	5102154.2923	-559778.0984	3773504.4312
ROTA	36^{o}36’56”N	6^{o}19’47”W	5094308.1552	-565091.8993	3783234.8121

Table H.1: Coordinates of the mareographs[6]in the Province of Cádiz. Mareographs with recorded data are in bold.

		DOY 77				**DOY 81**			
Station	**Length (km)**	**Resolved amb.**	S_NN **(mm)**	S_NE **(mm)**	S_NU **(mm)**	**Resolved amb.**	S_NN **(mm)**	S_NE **(mm)**	S_NU **(mm)**
ACOR	769.4	76%	10.1	7.4	23.8	82%	12.5	8.2	25.2
ALGC	97.3	93%	8.4	6.9	19.9	94%	8.5	6.6	21.3
BELL	866.8	78%	13.3	11.6	36.4	90%	11.8	9.8	38.3
CACE	**317.8**	**91%**	**8.5**	**7.0**	**20.6**	**93%**	**8.9**	**6.9**	**20.4**
CANT	790.8	87%	11.0	7.6	21.3	91%	12.1	7.5	22.5
CASC	356.9	92%	8.2	7.4	19.2	89%	10.4	8.3	27.9
CEU1	122.1	90%	9.1	7.7	23.1	89%	9.0	7.5	22.7
COBA	203.0	87%	8.7	6.8	21.3	90%	15.2	11.8	50.3
CREU	1041.8	86%	12.5	10.7	26.7	86%	10.7	8.8	36.8
GAIA	535.5	75%	16.8	9.4	44.2	74%	36.4	49.8	107.5
HUEL	83.5	89%	8.3	6.9	21.5	85%	9.4	6.5	22.3
LAGO	215.3	94%	8.3	7.6	20.7	90%	8.4	7.7	24.0
LEON	665.5	90%	8.5	6.6	19.8	89%	14.5	13.4	31.3
MALA	173.6	93%	13.8	13.0	40.1	89%	16.2	15.8	64.2
RIOJ	726.8	88%	8.1	7.0	22.7	87%	8.9	6.8	23.2
ROAP	20.1	91%	36.3	14.6	39.8	89%	11.4	10.2	63.0
SALA	486.0	88%	9.4	7.2	22.6	93%	10.2	7.5	28.9
SONS	397.9	89%	9.5	7.7	29.0	89%	12.1	8.5	35.8
TERU	**614.6**	**91%**	**9.0**	**7.1**	**21.2**	**90%**	**8.6**	**6.8**	**21.3**
UCAD	14.2	87%	8.3	6.9	20.4	87.9	7.8	6.1	18.9
VALA	581.7	93%	8.6	6.6	20.1	88%	7.8	6.1	19.2
VIGO	653.8	83%	8.6	7.3	20.6	78%	11.0	7.0	20.7
YEBE	517.7	81%	10.2	7.7	28.2	83%	9.9	7.2	23.1
ZARA	728.9	87%	8.6	6.9	22.7	88%	9.0	7.0	21.0

Table H.2: Baselines with ROTA in an end. GPS stations outside the Peninsula are not listed. Year 2011.

---

[6] The vertical coordinate are referred to the Hydrographical Zero in each harbor, used as a vertical reference for the nautical cartography derived in the Spanish Hydrographic Institute. In the recorded data, the vertical zero is referred to each sensor, respectively. Therefore, corrections to the coordinates must be made to match the Hydrographical Zero. For the stations with recorded data the corrections are the following: Cádiz, 0.09 meters; Rota, 0 meters and Puntales, 1.806 meters (Moreno, S. & Quijano, J.; personal communication).

		DOY 77				**DOY 81**			
Station	**Length (km)**	**Resolved amb.**	S_NN **(mm)**	S_NE **(mm)**	S_NU **(mm)**	**Resolved amb.**	S_NN **(mm)**	S_NE **(mm)**	S_NU **(mm)**
ACOR	780.8	79%	8.1	5.7	20.2	83%	15.2	8.7	32.2
ALGC	83.2	91%	28.6	13.2	49.2	89%	9.1	4.8	18.7
BELL	865.1	80%	11.8	19.3	32.9	91%	15.8	12.9	62.8
BORR	653.8	86%	7.2	5.1	19.1	81%	8.1	7.4	27.7
CACE	**327.3**	**90%**	**6.7**	**5.4**	**17.7**	**86%**	**6.9**	**5.2**	**17.7**
CAGZ	1363.2	87%	6.7	7.1	23.2	85%	11.3	25.1	215.1
CANT	797.1	84%	10.4	5.8	20.4	87%	10.8	6.1	20.3
CASC	371.1	91%	6.4	5.1	17.3	89%	9.3	6.8	21.8
CEU1	107.9	88%	8.2	6.1	23.1	84%	7.2	5.7	19.3
COBA	202.6	90%	8.0	9.0	20.1	88%	51.9	77.5	162.5
CREU	1039.7	86%	9.7	7.5	26.0	88%	8.3	6.1	41.6
GAIA	548.0	75%	19.4	7.7	40.9	78%	33.6	13.1	70.1
HUEL	97.5	87%	6.3	5.5	17.2	80%	7.6	5.5	21.5
IZAN	1326.0	79%	18.2	10.2	30.8	82%	14.0	10.6	48.2
LAGO	228.1	92%	6.0	5.2	17.3	89%	5.5	5.2	22.1
LEON	673.9	89%	5.9	4.7	16.1	87%	49.7	56.7	115.4
LPAL	1389.7	82%	10.3	8.8	20.8	81%	17.4	15.9	69.0
MALA	163.9	93%	46.7	75.3	114.2	91.0	80.0	119.2	274.3
MALL	843.8	90%	7.1	5.9	19.9	87%	6.8	6.1	22.6
ONSA	2660.2	85%	13.8	7.2	32.6	94%	121.0	44.1	65.5
PDEL	1725.2	83%	49.8	20.0	100.7	87%	22.4	54.3	164.6
REYK	3213.0	81%	79.9	10.0	47.3	86%	231.9	61.1	215.0
RIOJ	730.6	88%	6.7	5.4	21.7	89%	6.4	5.3	20.6
ROAP	7.5	95%	21.9	6.5	36.1	89%	32.8	27.7	278.5
ROTA	14.2	86%	21.9	6.5	36.1	89%	7.8	6.1	18.8
SALA	493.8	90%	7.4	5.3	15.2	89%	21.4	24.8	91.2
SONS	400.7	89%	7.4	6.4	25.5	87%	15.6	20.2	68.0
TERU	**613.5**	**89%**	**6.6**	**4.6**	**16.7**	**91%**	**6.7**	**4.5**	**18.3**
VALA	588.4	85%	6.9	5.1	18.8	87%	32.9	40.2	167.6
VIGO	666.0	84%	6.5	5.0	20.2	78%	51.7	8.3	97.0
YEBE	520.0	82%	9.0	6.2	27.6	81%	8.4	5.5	23.7
ZARA	729.6	87%	6.8	6.4	19.0	90%	7.5	5.4	19.5

Table H.3: Baselines with UCAD in an end. Year 2011.

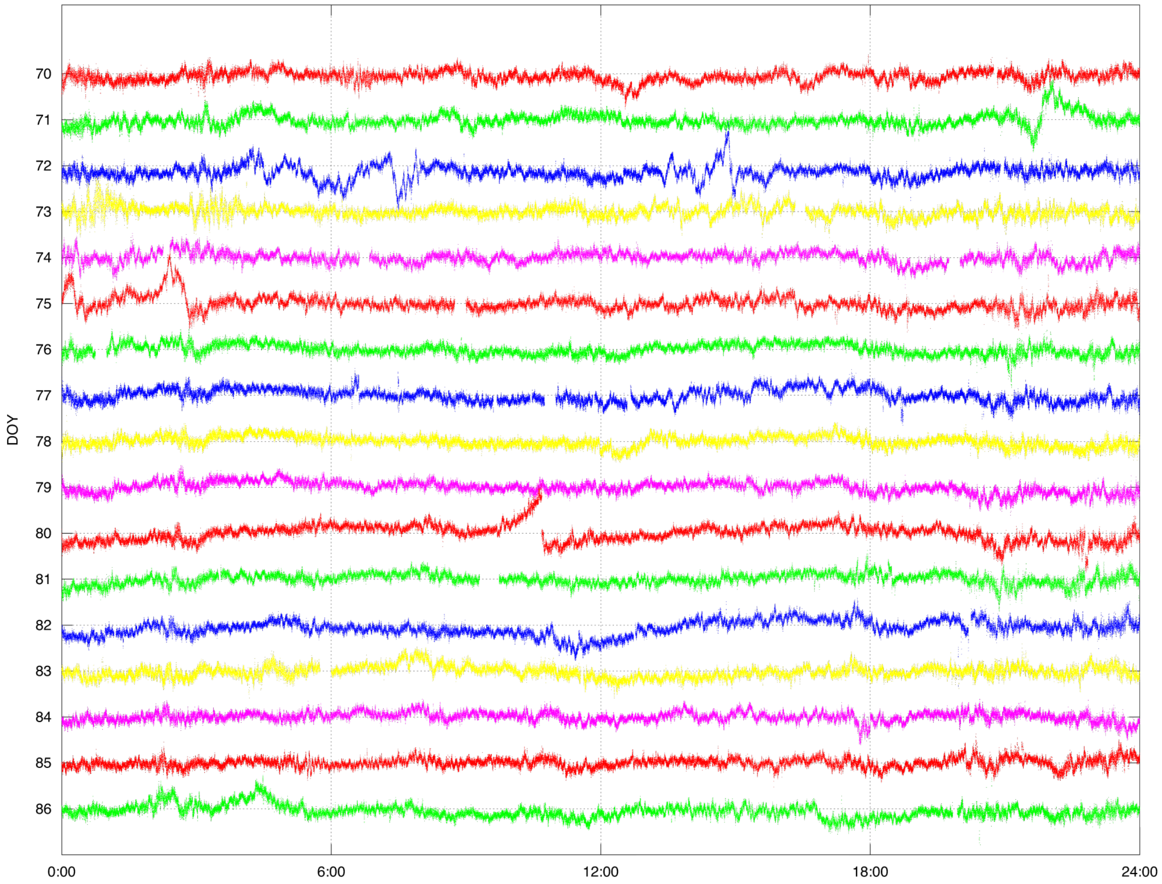

Figure H.1: Stacking for March 2011 GPS data from UCAD station. North residual. Scale in Y axis is 5 cm.

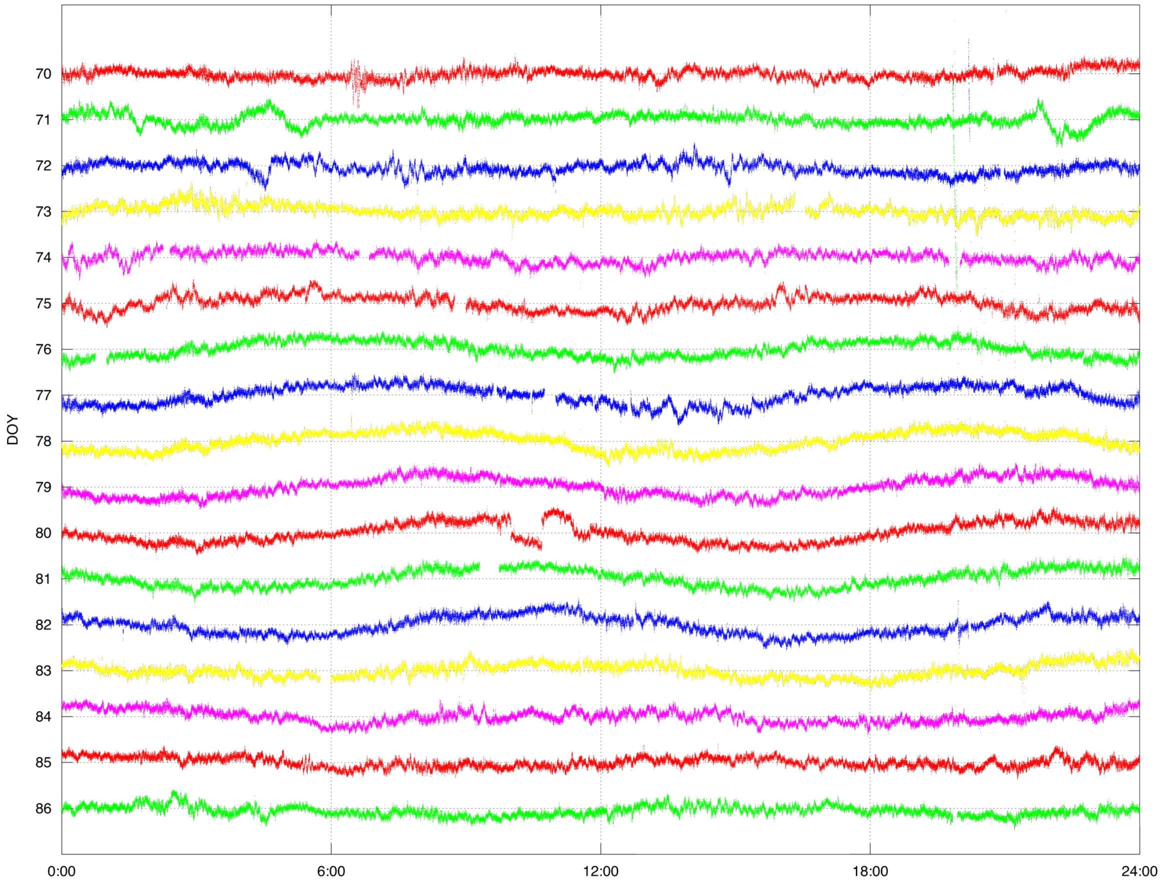

Figure H.2: Stacking for March 2011 GPS data from UCAD station. East residual. Scale in Y axis is 5 cm.

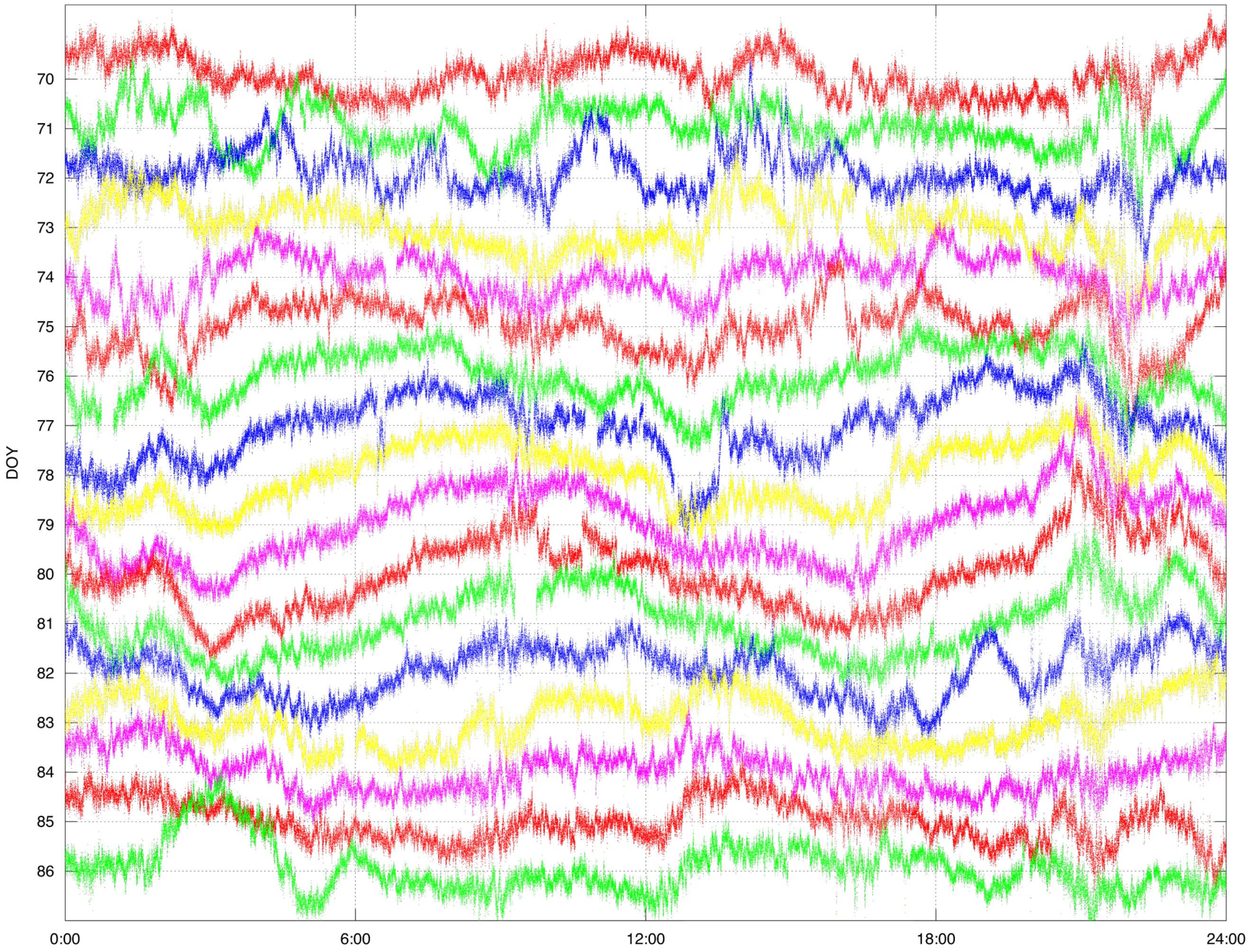

Figure H.3: Stacking for March 2011 GPS data from UCAD station. Up residual. Scale in Y axis is 5 cm.

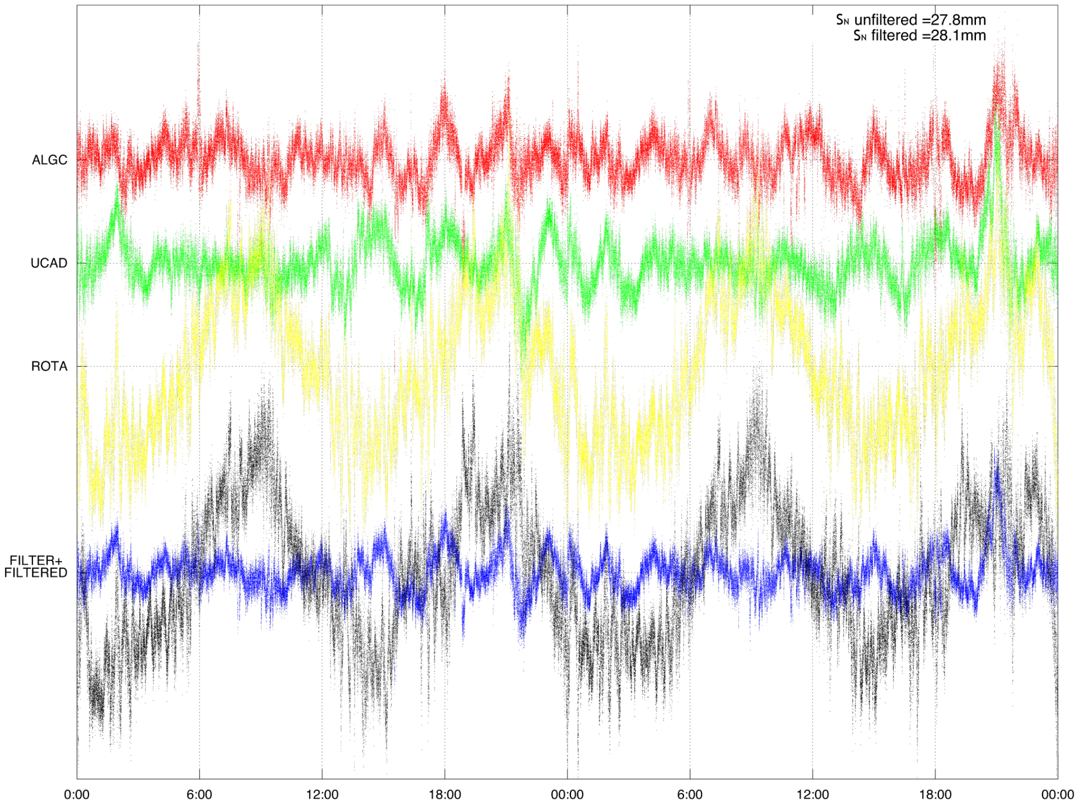

Figure H.4: Regional filter applied to ROTA (yellow) without ocean loading corrections applied, during DOY 78 and 79 2011. It is composed by stations ALGC (red) and UCAD (green), with ocean loading corrections applied. The filter is in blue and ROTA filtered data is plotted in black.

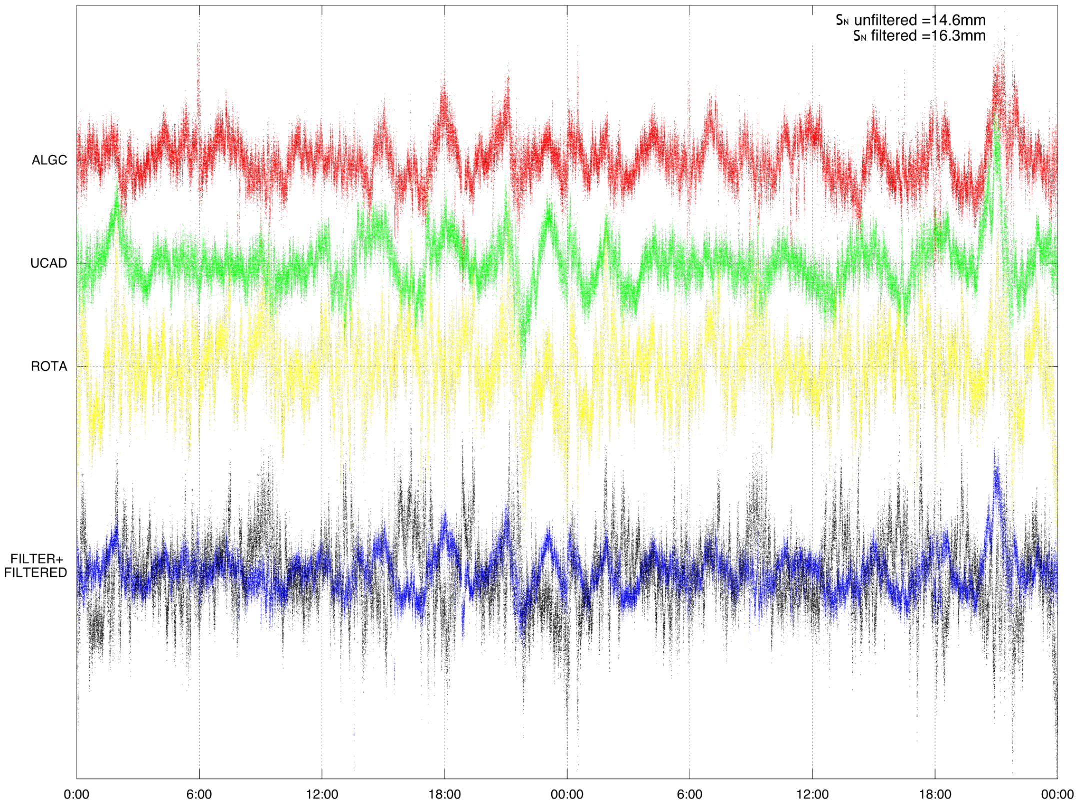

Figure H.5: Regional filter applied to ROTA (yellow), during DOY 78 and 79 2011. It is composed by stations ALGC (red) and UCAD (green). The filter is in blue and ROTA filtered data is plotted in black. All stations used are corrected for ocean loadings.

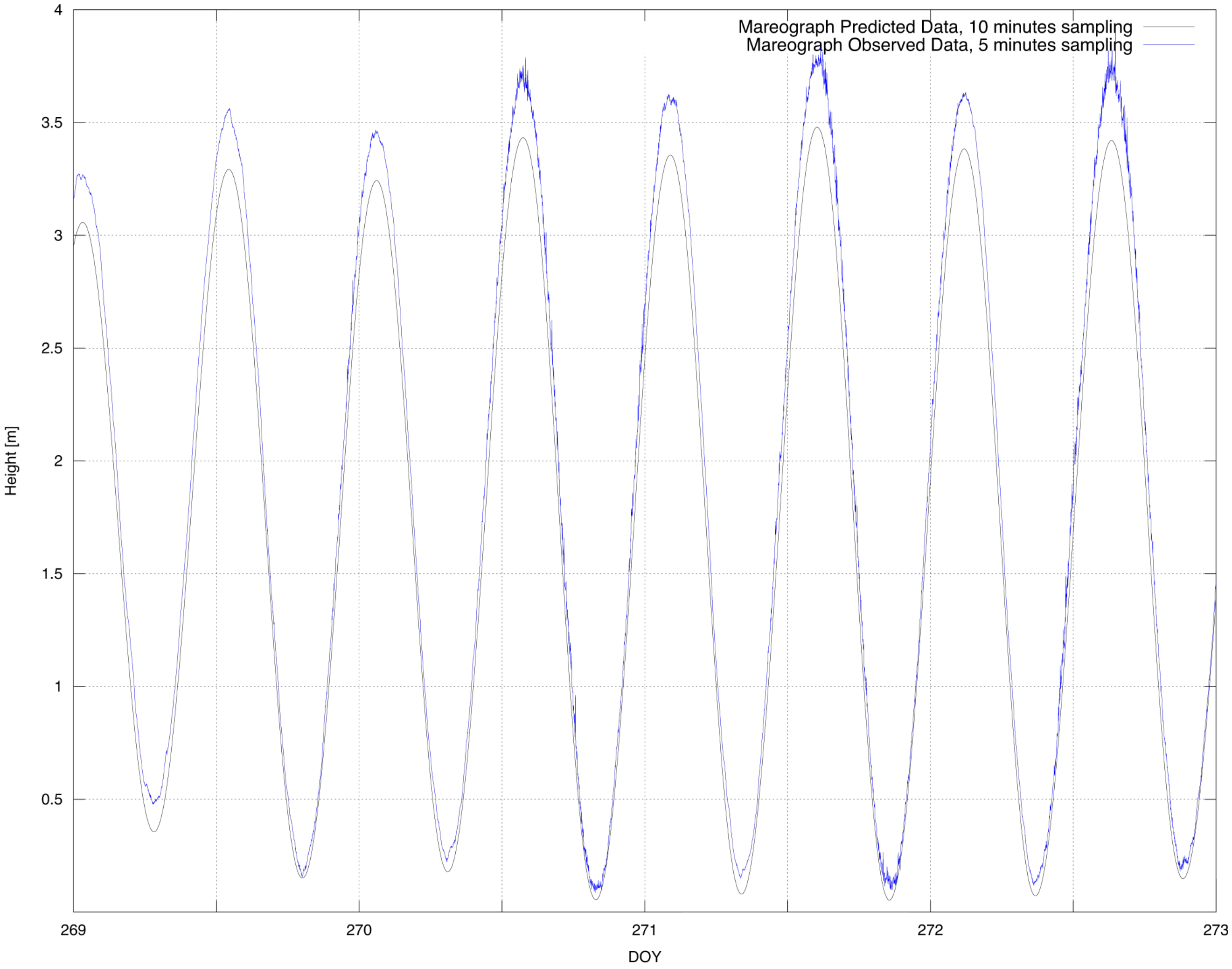

Figure H.6: Mareograph data, observed versus predicted. Year 2011.

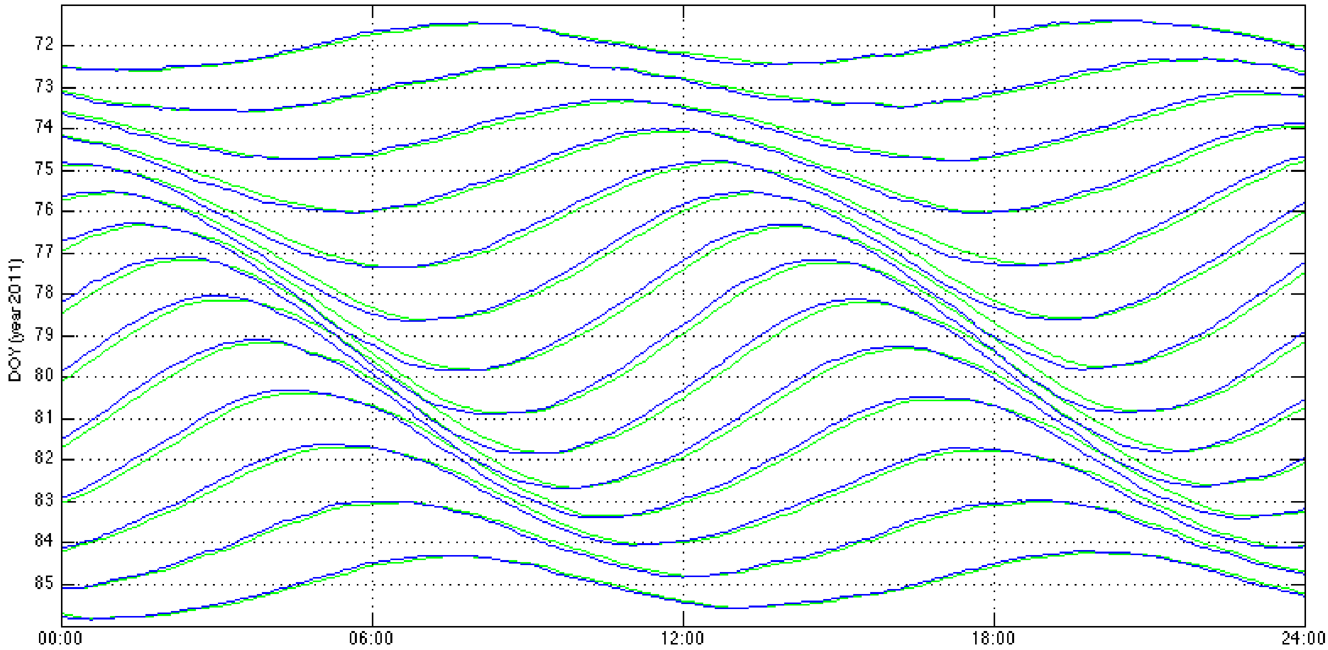

Figure H.7: Stacking for March data from Puntales (in blue) and Cádiz (in green) mareographs. DOY 79, year 2011. Scale in Y axis is 1 meter.

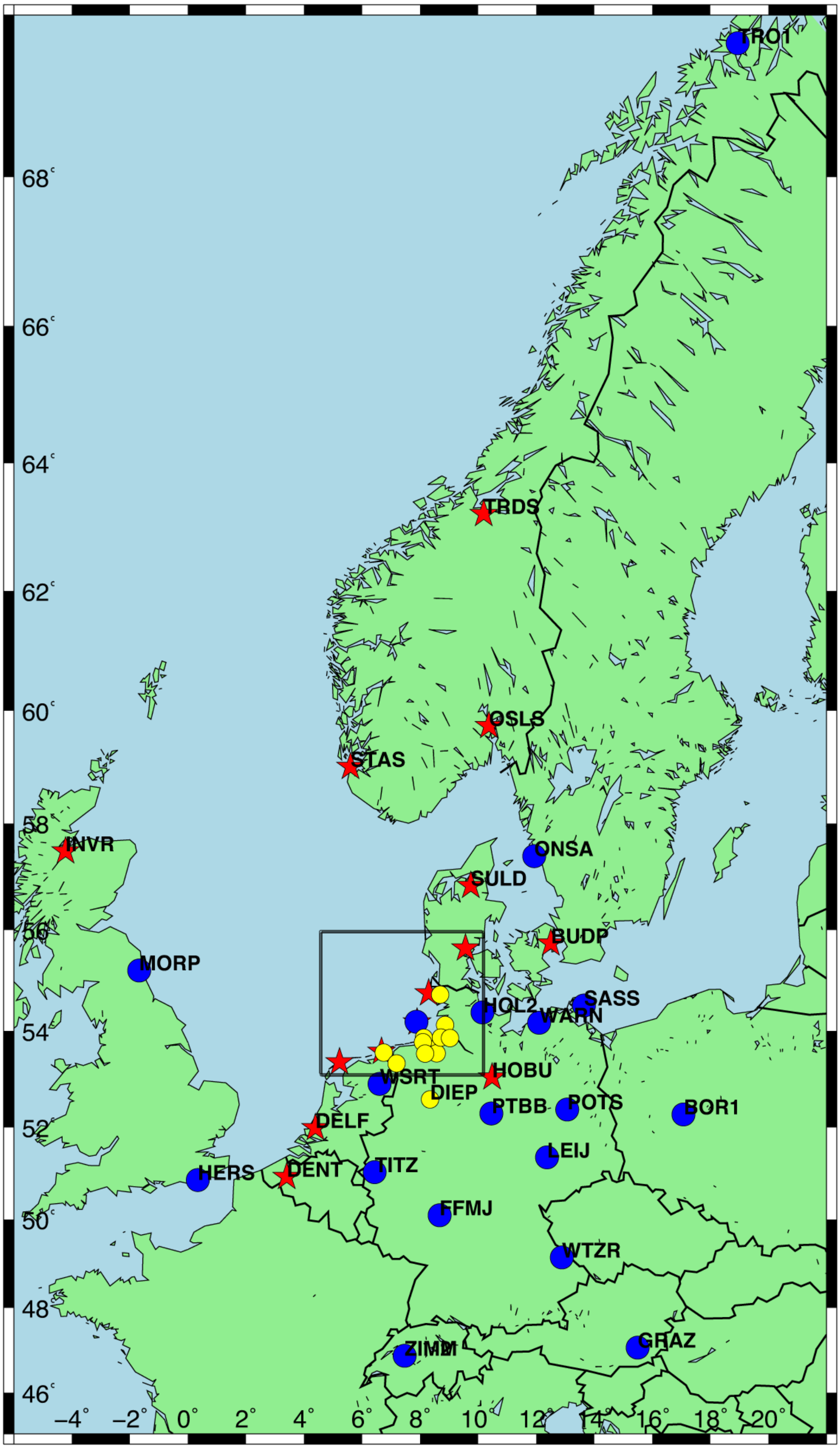

Figure I.1: IGS (blue), EUREF (red) and BfG (yellow) permanent GNSS stations from the selected GPS network

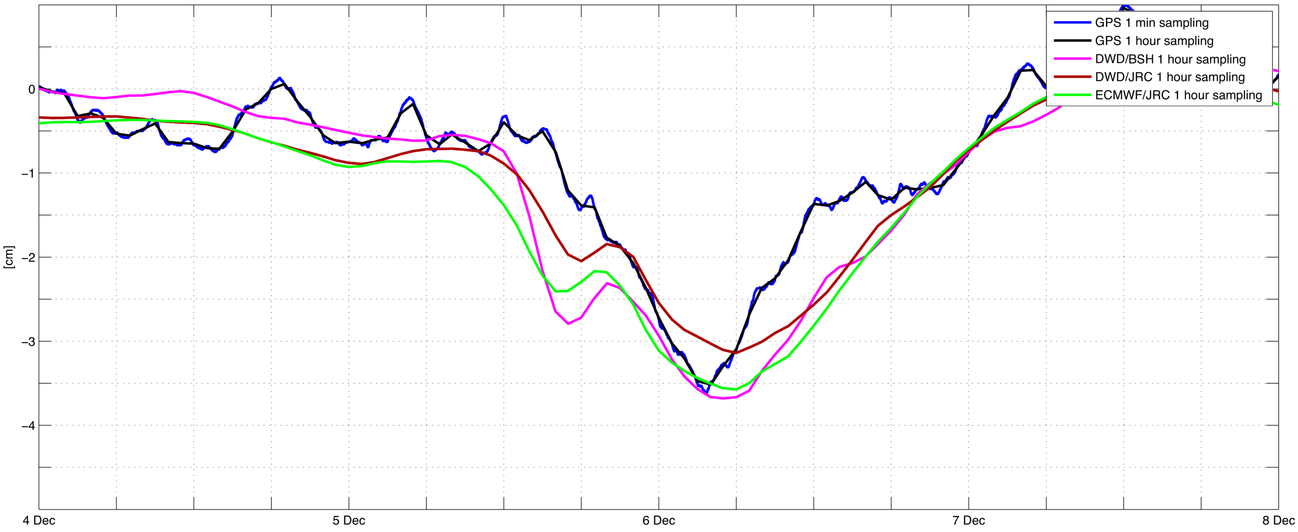

Figure I.2: Comparison for the different models in BORJ, also for 1 and 60 minutes GPS vertical residuals. December 2013.

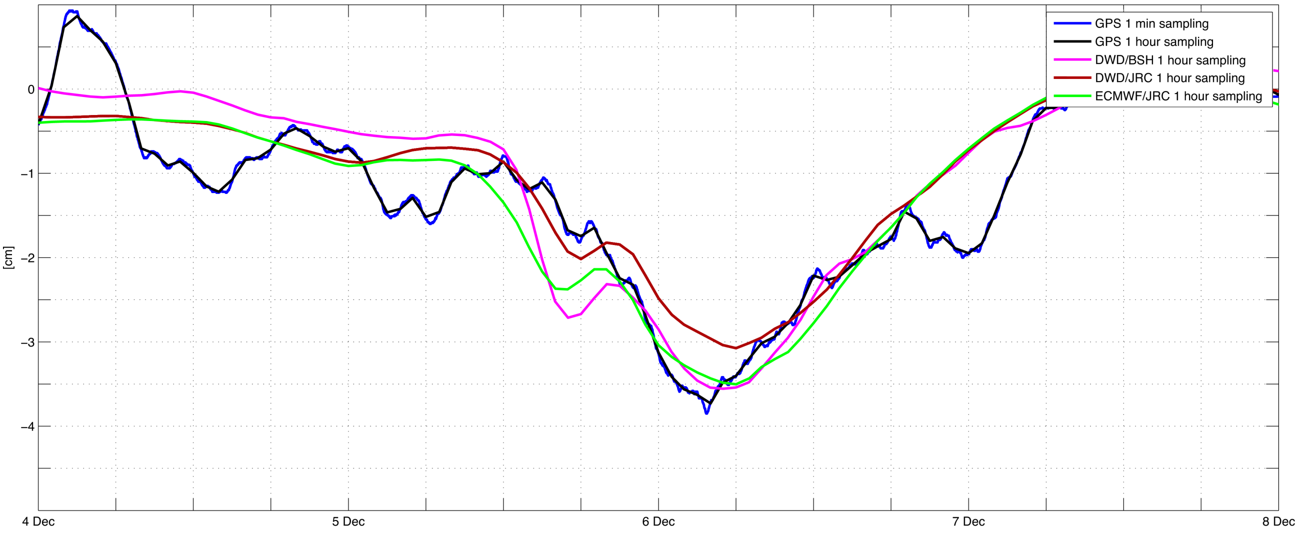

Figure I.3: Comparison for the different models in TGBF, also for 1 and 60 minutes GPS vertical residuals. December 2013.

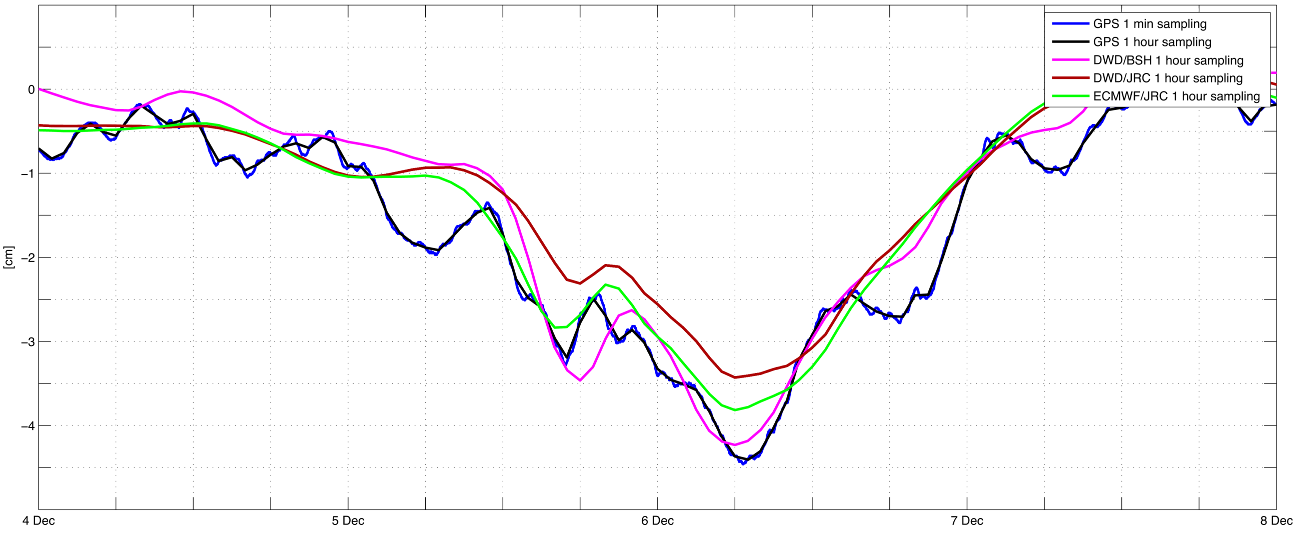

Figure I.4: Comparison for the different models in HELG, also for 1 and 60 minutes GPS vertical residuals. December 2013.

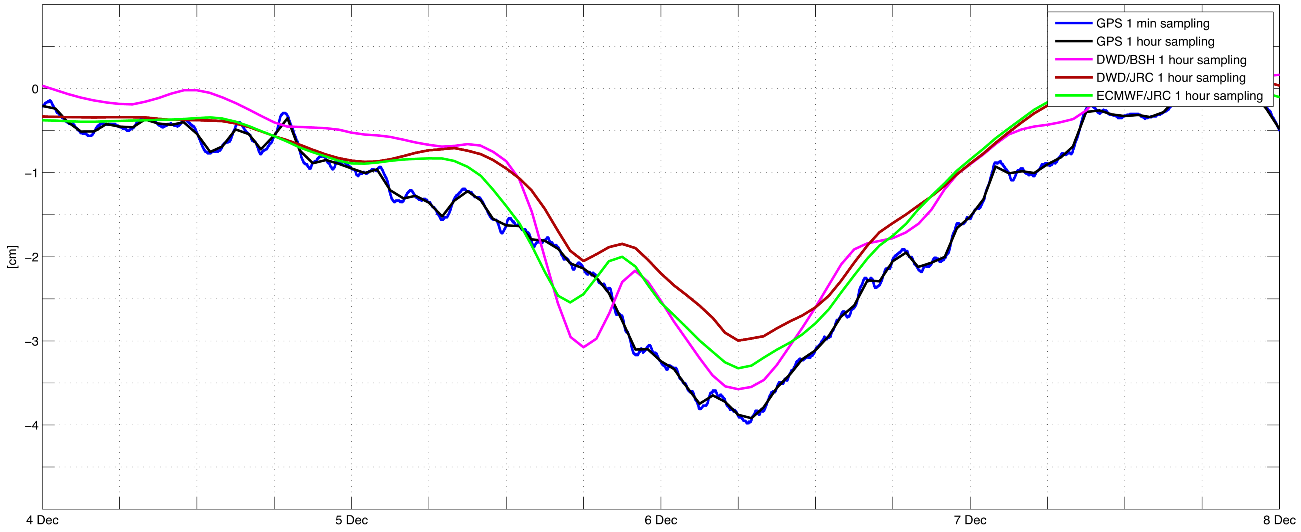

Figure I.5: Comparison for the different models in TGME, also for 1 and 60 minutes GPS vertical residuals. December 2013.

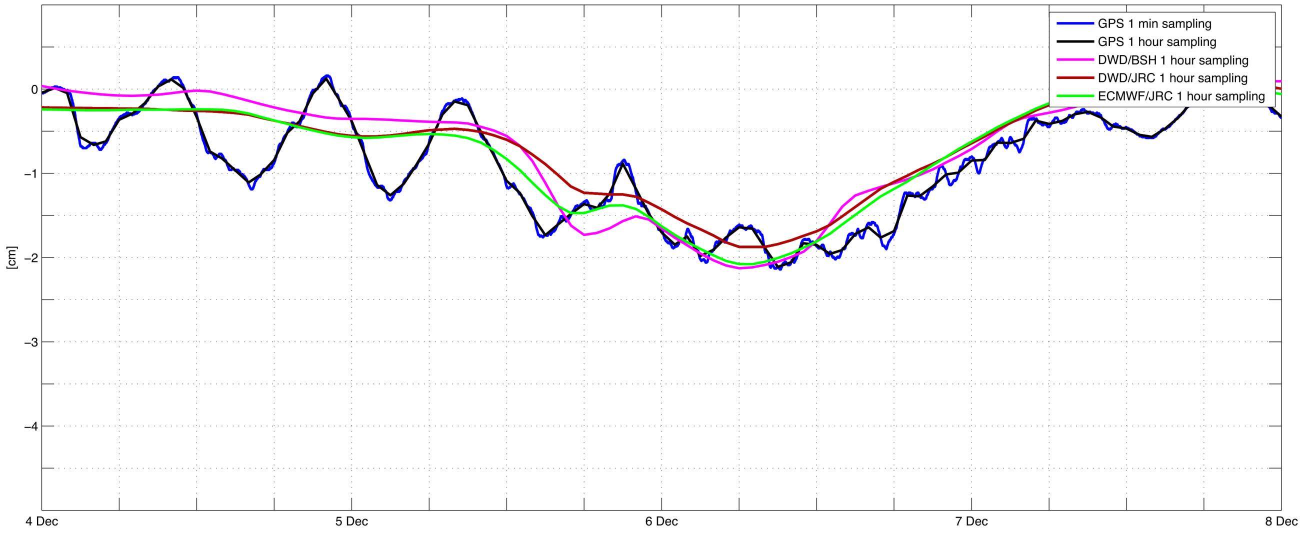

Figure I.6: Comparison for the different models in TGBH, also for 1 and 60 minutes GPS vertical residuals. December 2013.

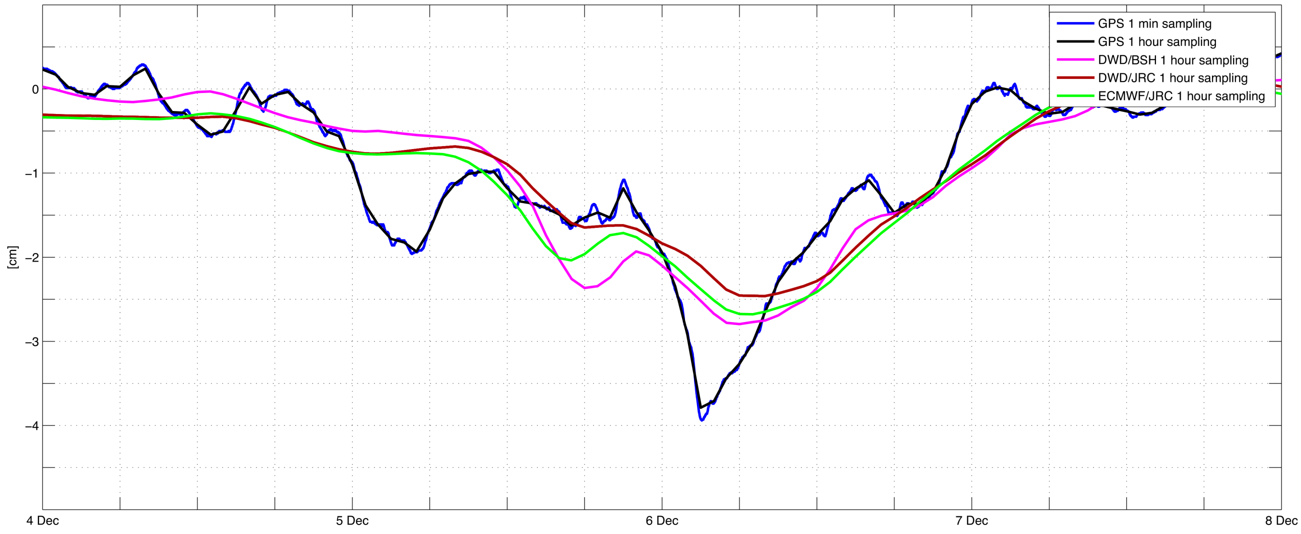

Figure I.7: Comparison for the different models in TGBU, also for 1 and 60 minutes GPS vertical residuals. December 2013.

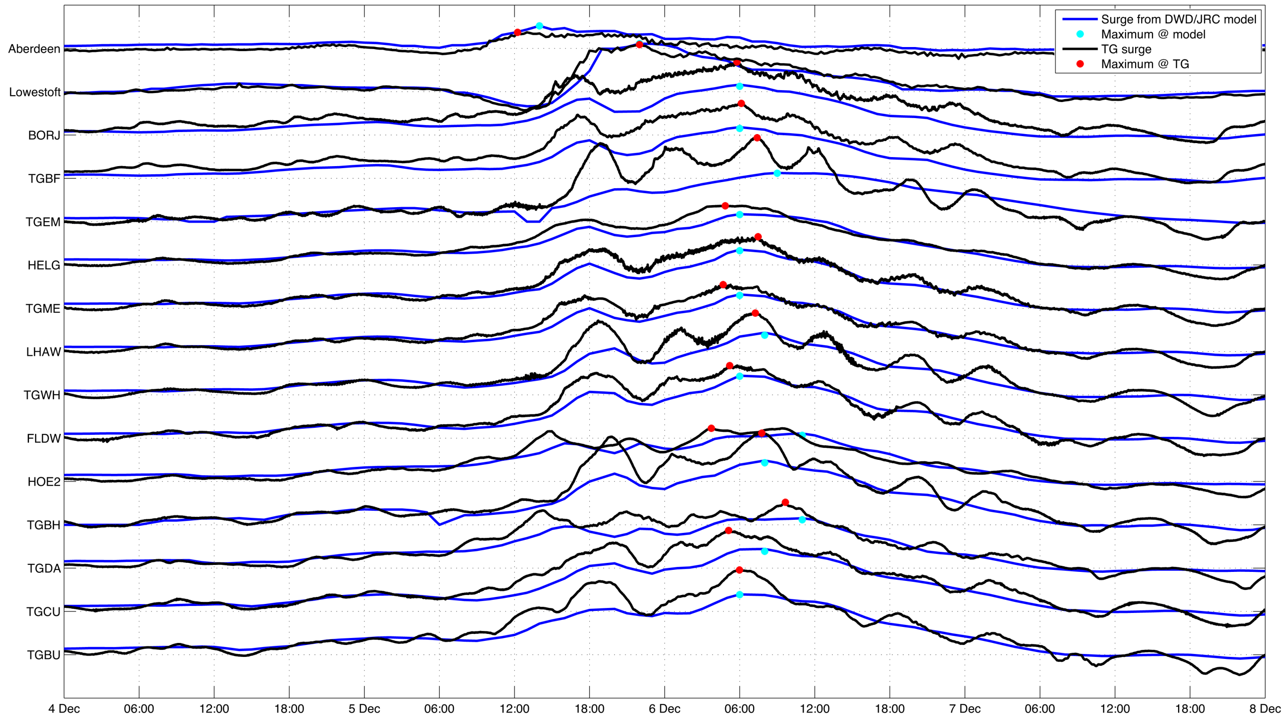

Figure I.8: Stacking of 1 minute tide gauge time series (except for Aberdeen and Lowestoft whose sampling is 15 minutes), in black. Red dots show the maximum value for each station. In blue, DWD/JRC surge with 60 minutes sampling. Cyan dots show the maximum value for each station. Stations sorted by longitude. Scale in Y axis is 2 meters. December 2013.

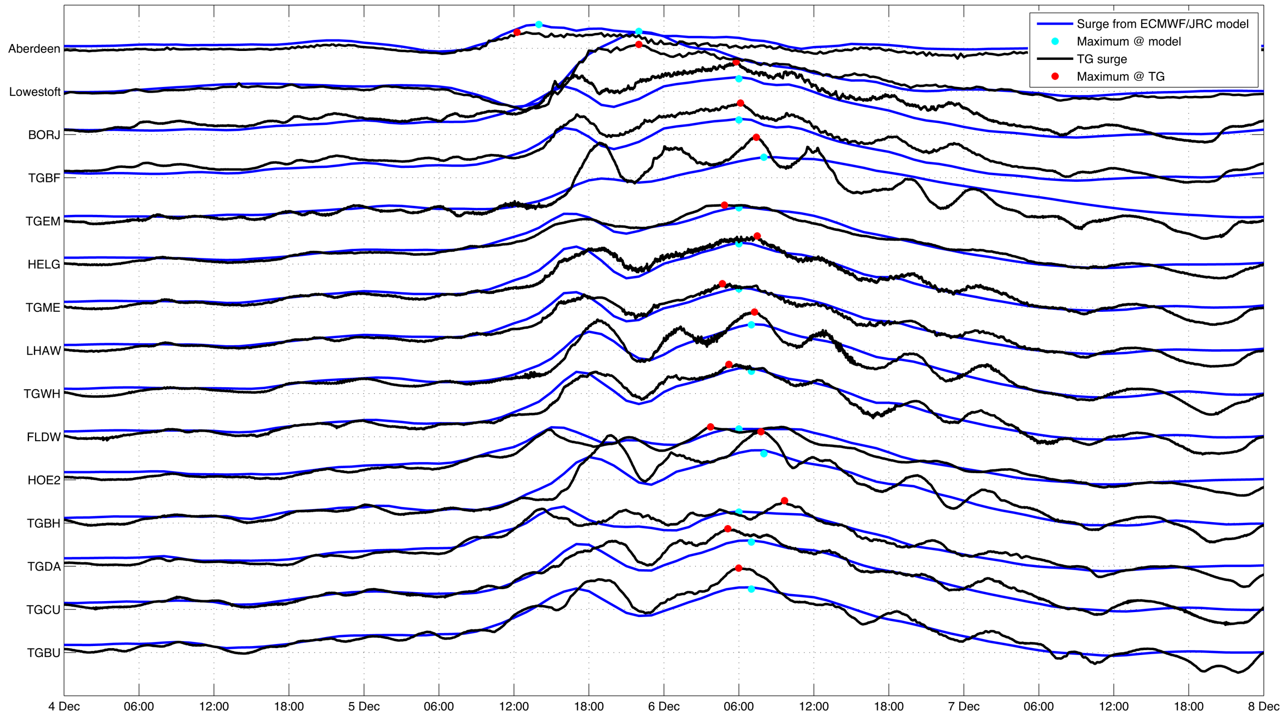

Figure I.9: Stacking of 1 minute tide gauge time series (except for Aberdeen and Lowestoft whose sampling is 15 minutes), in black. Red dots show the maximum value for each station. In blue, ECMWF/JRC surge with 60 minutes sampling. Cyan dots show the maximum value for each station. Stations sorted by longitude. Scale in Y axis is 2 meters. December 2013.

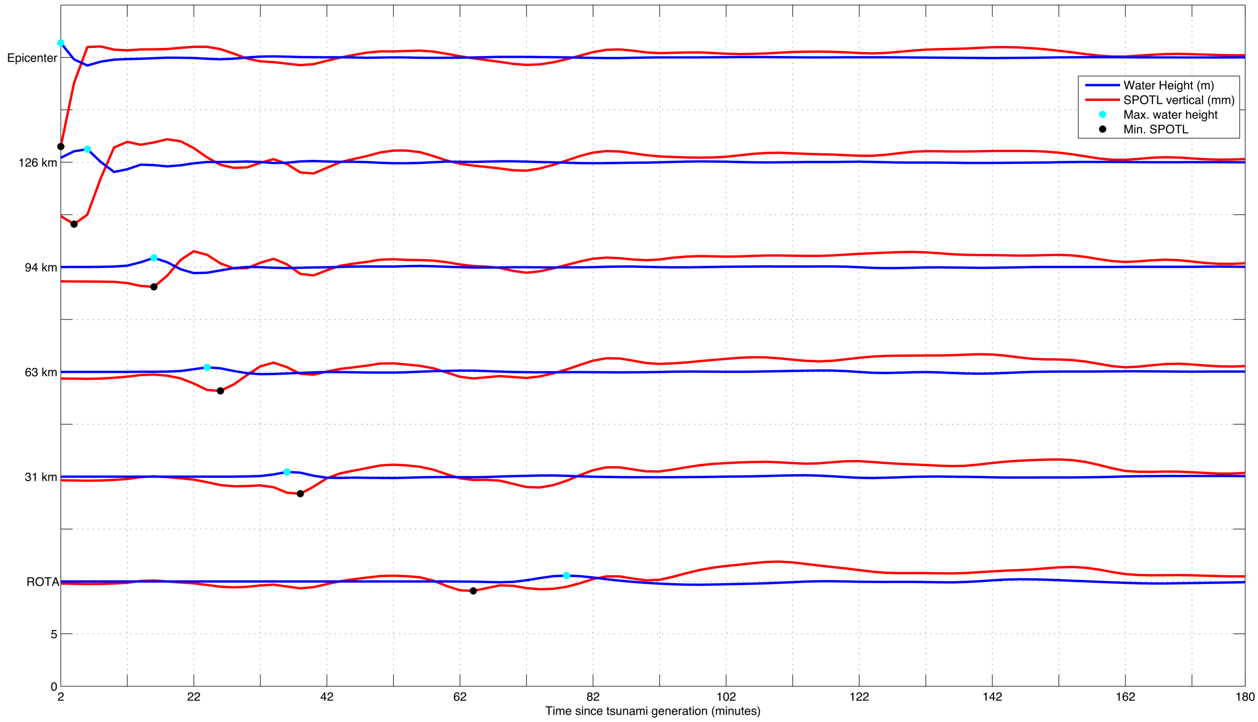

Figure J.1: Time series for some stations chosen in the profile of the best-case scenario, from the epicenter towards ROTA. Scale in Y axis is 5 mm for subsidence and 5 m for water height predicted, respectively. Black points correspond to the maximum subsidence; the cyan dots, to the maximum water height. Information detailed in Table 8.4.

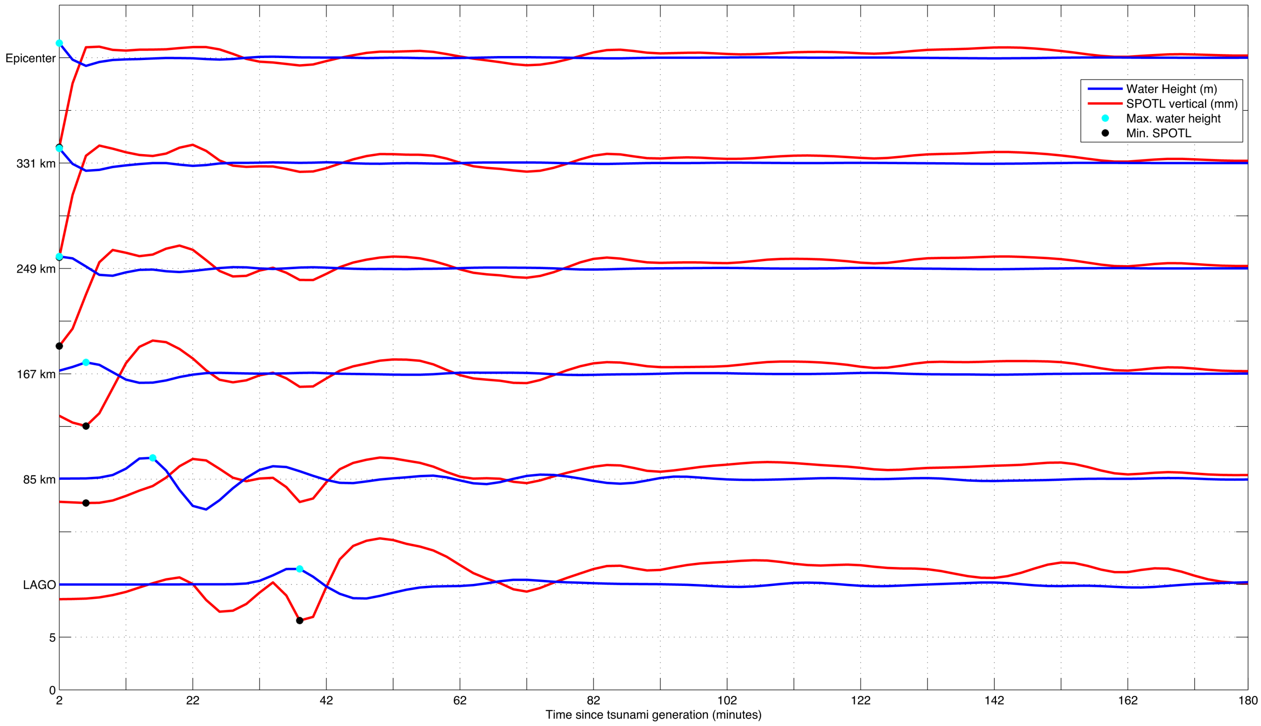

Figure J.2: Time series for some stations chosen in the profile of the best-case scenario, from the epicenter towards LAGO. Scale in Y axis is 5 mm for subsidence and 5 m for water height predicted, respectively. Black points correspond to the maximum subsidence; the cyan dots, to the maximum water height. Information detailed in Table 8.5.

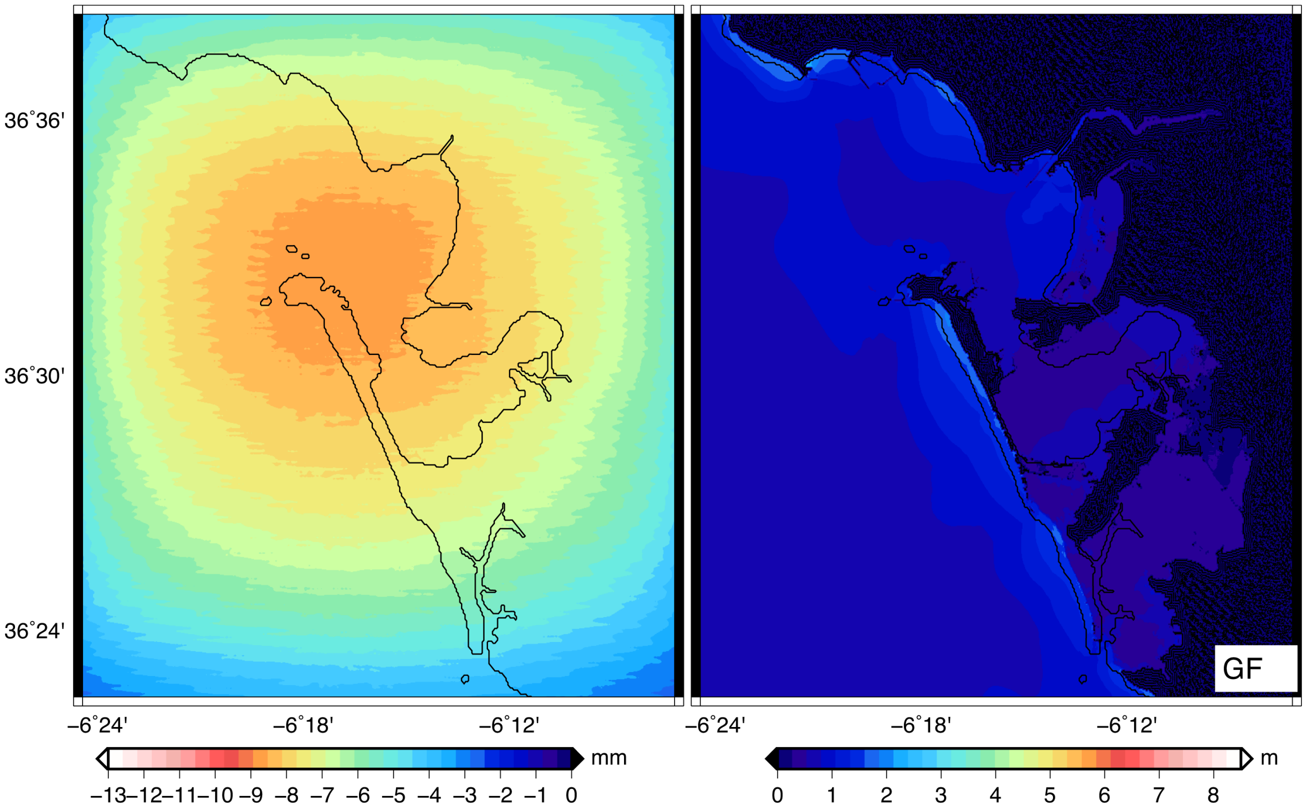

Figure J.3: Tsunami model with epicenter in the Gorringe Bank Fault and magnitude $M_w 8.2$. Predicted subsidence (left) and water height (right).

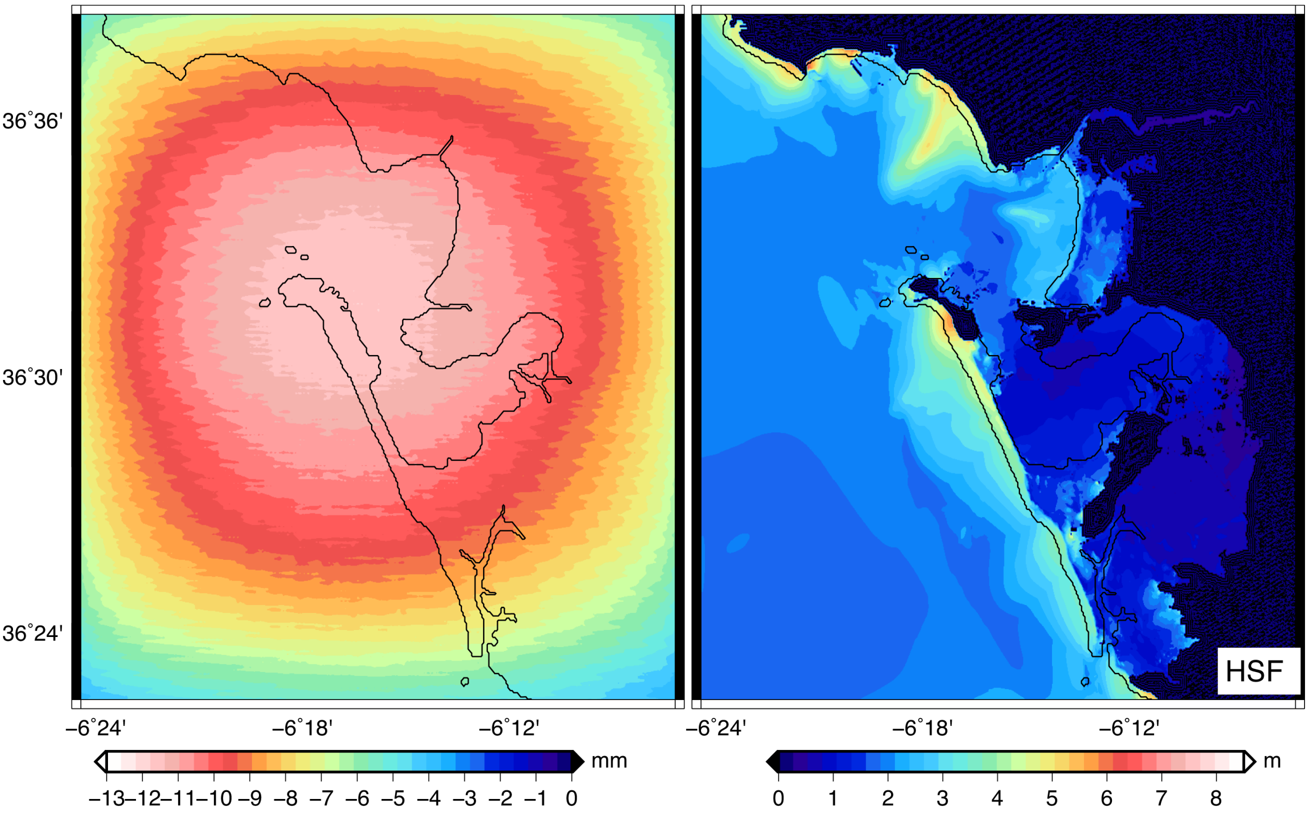

Figure J.4: Tsunami model with epicenter in the Horseshoe Fault and magnitude $M_w 8.3$. Predicted subsidence (left) and water height (right).

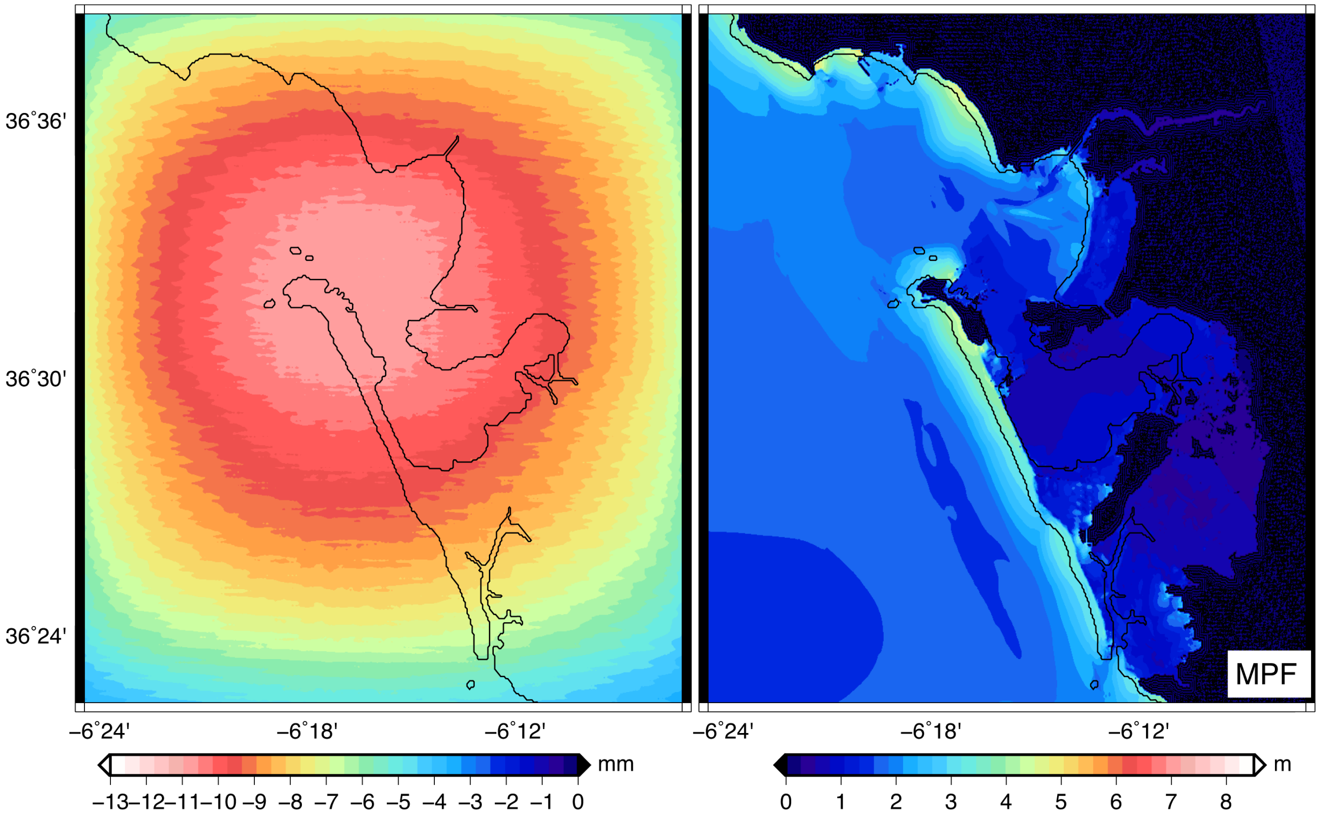

Figure J.5: Tsunami model with epicenter in the Marqués de Pombal Fault and magnitude $M_w 8.1$. Predicted subsidence (left) and water height (right).

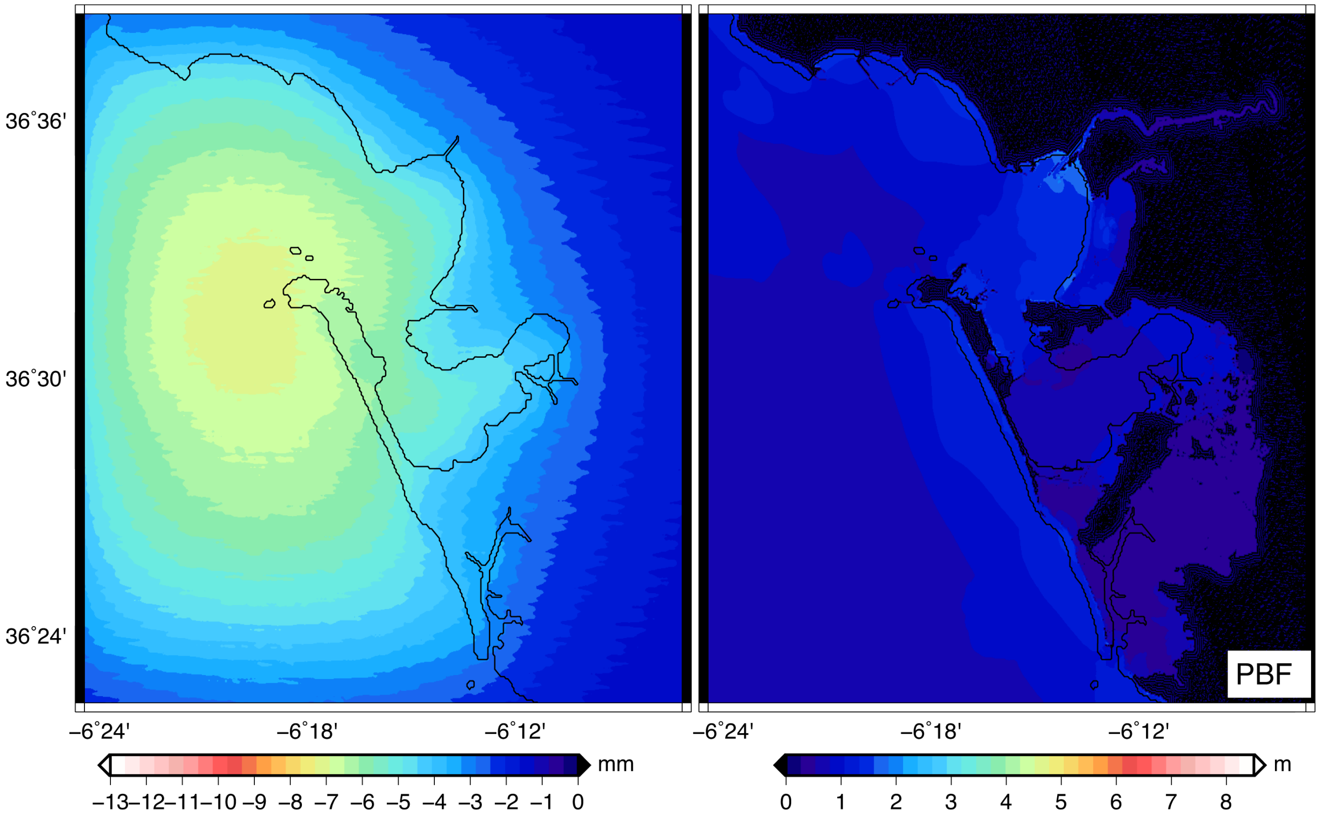

Figure J.6: Tsunami model with epicenter in the Portimao Bank Fault and magnitude $M_w 8.0$. Predicted subsidence (left) and water height (right).

K Acknowledgements

This Thesis has been partially supported by the Spanish research projects TOPOIBERIA (CSD2006-00046), ALERT-ES (CGL2010-19803-C03-02) and ALERTES-RIM (CGL2013-45724-C3-3-R). Also, by the Spanish Alvargonzález foundation grant and Technische Universität Darmstadt Stibet Promotionsabschlussstipendium (end of ph.D. studies grant).

I would also like to thank:

- the Consejería de Agricultura y Agua of the Murcia Region, for their public FTP service,
- the Red Andaluza de Posicionamiento,for their public FTP service,
- the Bundesanstalt für Gewässerkunde, Germany (BfG), and especially Dr. Robert Weiss, for the GPS data provided,
- the International GNSS Service (IGS) for their public ftp service,
- the Spanish Hydrographic Institute, and especially M.Sc. Salvador Moreno Soba, for the mareograph data provided,
- the Red de Puertos del Estado, and especially Dr. Begoña Pérez Gómez, for the Huelva mareograph data provided,
- the European Commission Joint Research Centre (JRC), for its storm surge model data provided. And especially M.Sc. Ricardo Tavares da Costa, for providing several tsunami scenarios.
- the German Federal Maritime and Hydrographic Agency (BSH), for their regional operational numerical circulation ocean model and wind model provided.
- Prof. Mauricio González from the Universidad de Cantabria, Spain; and Prof. Luis Jesús Otero Díaz, from the Universidad del Norte in Barranquilla, Colombia, for providing several tsunami scenarios, calculated in the frame of the TRANSFER project [*UCA and IGN*, 2009],
- the San Fernando Naval Observatory in Spain, for the partial stay during this investigation, and the use of their data and resources,
- and the Technische Universtät Darmstadt in Germany, and in particular the Institute for Physical and Satellite Geodäsie, for the almost 7 years of stay, using software and resources.

L Curriculum Vitae

Name	Leonor Mendoza Malia
Date of birth	5th June 1985
Place of birth	Cádiz, Spain
Nationality	Spanish

Education

Sep. 2008 -	**Technische Universität. Darmstadt, Germany** Ph.D. Student
Sep. 2003 - Jul. 2008	**Cádiz University, Spain** BSc & MSc in Mathematics Specialization in Astronomy and Geodesy Awarded with the Extraordinary End-Of-Degree First Prize
Sep. 2006 - Jul. 2007	**Complutense University. Madrid, Spain** Exchange student SICUE mobility program

Experience

Dec. 2014 -	**Fachgebiet für Physikalische Geodäsie und Satellitengeodäsie. TU Darmstadt, Germany** GPS data analyst
2009 - 2012	**San Fernando Naval Observatory, Spain** Researcher RISTE project: seismic and tsunami risk in the Cádiz Bay ALERT-ES project: early warning seismic alert applied to Southern Spain TOPO-IBERIA project: geosciences in Iberia. Topography and 4-D evolution studies
2008 - 2009	**Institut für Physikalisches Geodäsie und Satellitengeodäsie. TU Darmstadt, Germany** Researcher. Application of high-rate GPS data for natural hazard mitigation
Sep. 2007 - Jul. 2008	**Laboratory of Astronomy and Geodesy. Cádiz University, Spain** Help and support of the researchers during data acquisition and analysis
Jul. 2007	**Spanish Hydrographic Institute and San Fernando Naval Observatory, Spain** Magnetometer observations, data acquisition and analysis ZEEE 07 campaign in the BIO Hespérides
Jun. 2006 - Sep. 2006	**San Fernando Naval Observatory, Spain** Internship, 300 hours SLR observations and data analysis